IPICYT

INSTITUTO POTOSINO DE INVESTIGACIÓN CIENTÍFICA Y TECNOLÓGICA, A.C.

POSGRADO EN CIENCIAS APLICADAS

Synthesis and New Properties of Nanostructured Zinc Oxide, Carbon and other Layered Materials

Tesis que presenta

Andrés Rafael Botello Méndez

Para obtener el grado de

Doctor en Ciencias Aplicadas

En la opción de

Nanociencias y Nanotecnología

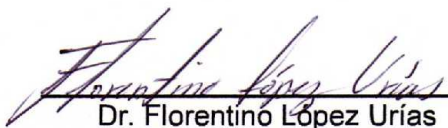**Codirectores de la Tesis:**
Dr. Florentino López Urías
Dr. Mauricio Terrones Maldonado
Dr. Humberto Terrones Maldonado

IPICYT

Constancia de aprobación de la tesis

La tesis "**Synthesis and New Properties of Nanostructured Zinc Oxide, Carbon and other Layered Materials**" presentada para obtener el Grado de Doctor en Ciencias Aplicadas en la opción de Nanociencias y Nanotecnología fue elaborada por **Andrés Rafael Botello Méndez** y aprobada el **17 de diciembre de 2009** por los suscritos, designados por el Colegio de Profesores de la División de Materiales Avanzados del Instituto Potosino de Investigación Científica y Tecnológica, A.C.
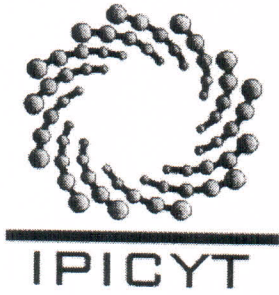

Dr. Florentino López Urías
(Codirector de la tesis)

Dr. Mauricio Terrones Maldonado
(Codirector de la tesis)

Dr. Humberto Terrones Maldonado
(Codirector de la tesis)

iii

Créditos Institucionales

Instituto Potosino de Investigación Científica y Tecnológica, A.C.

Acta de Examen de Grado

El Secretario Académico del Instituto Potosino de Investigación Científica y Tecnológica, A.C., certifica que en el Acta 031 del Libro Primero de Actas de Exámenes de Grado del Programa de Doctorado en Ciencias Aplicadas en la opción de Nanociencias y Nanotecnología está asentado lo siguiente:

En la ciudad de San Luis Potosí a los 17 días del mes de diciembre del año 2009, se reunió a las 17:00 horas en las instalaciones del Instituto Potosino de Investigación Científica y Tecnológica, A.C., el Jurado integrado por:

Dr. Fernando Jaime Rodríguez Macías	Presidente	IPICYT
Dr. Mauricio Terrones Maldonado	Secretario	IPICYT
Dr. Florentino López Urías	Sinodal	IPICYT
Dr. Humberto Terrones Maldonado	Sinodal	IPICYT
Dr. Jean-Christophe Charlier	Sinodal externo	UCLouvain
Dr. Vincent Meunier	Sinodal externo	ORNL

a fin de efectuar el examen, que para obtener el Grado de:

DOCTOR EN CIENCIAS APLICADAS
EN LA OPCIÓN DE NANOCIENCIAS Y NANOTECNOLOGÍA

sustento el C.

Andrés Rafael Botello Méndez

sobre la Tesis intitulada:

Synthesis and New Properties of Nanostructured Zinc Oxide, Carbon and Other Layered Materials

que se desarrolló bajo la dirección de

Dr. Florentino López Urías
Dr. Humberto Terrones Maldonado
Dr. Mauricio Terrones Maldonado

El Jurado, después de deliberar, determinó

APROBARLO

Dandose por terminado el acto a las 19:30 horas, procediendo a la firma del Acta los integrantes del Jurado. Dando fe el Secretario Academico del Instituto.

A petición del interesado y para los fines que al mismo convengan, se extiende el presente documento en la ciudad de San Luis Potosí, S.L.P., México, a los 17 días del mes de diciembre de 2009.

Dr. Marcial Bonilla Marín
Secretario Académico

INSTITUTO POTOSINO
DE INVESTIGACIÓN
CIENTÍFICA Y TECNOLÓGICA, A.C.
IPICYT
SECRETARIA ACADEMICA

Mtra. Ivonne Lizette Cuevas Vélez
Jefa del Departamento de Asuntos Escolares
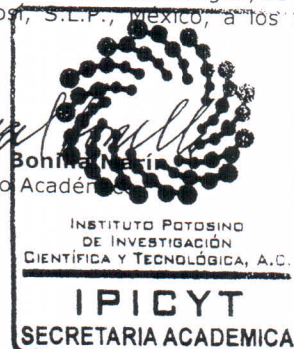
It would be impossible for me to have reached this point without the help of all the people *behind the courtains*. Of course, help comes in many flavours. It may come from the guiding words of an advisor, from a discussion with collaborators, from technical support, from inspiring talks, from supporting friends, from a loving companion, or from a lifelong encouragement for dream persual from family. I thank and dedicate this work to all who have helped me in this journey.

Acknowledgments

I am grateful to Daniel Ramírez, Grisel Ramírez, Gabi Pérez, and Karla Gómez, and the technicians of the National Laboratory for Research in Nanoscience and Nanotechnology (LINAN) for technical support.

Also, I would like to acknowledge the support of the Mexican Society of Nanoscience and Nanotechnology (SOMENANO) to attend the 9th International Conference on the Science and Technology of Nanotubes.

Additionally, part of the work presented in this Thesis was carried out through collaboration with other groups. Therefore part of the credit is shared with them. I give special thanks to:

Murali Kota from Motorola Labs. In Bangalore, India.

Pulickel M. Ajayan and Ashavani Kumar from Rice University, Texas.

David Kylcone in Advanced Light Source, Berkeley National Laboratory.

Vincent Meunier and Bobby G. Sumpter from Oakridge National Laboratory.

I would also like to thank the European Theoretical Spectroscopy Facility (ETSF) for the grant to attend the "Workshop on Electronic Excitations" in September, 2009.

Contents

Resumen

Existe una gran expectativa de que la Nanotecnología impacte de manera positiva la calidad de vida a través de las nuevas aplicaciones que se deriven de esta. Dichas aplicaciones estarán basadas en fenómenos y características de los materiales que sólo es posible encontrar a escalas nanométricas. Quizás las más importantes aplicaciones sean en 1) medicina, desde mejores herramientas de diagnóstico, hasta mejores medicinas con blancos específicos y hechas a la medida; 2) en problemas de alto impacto social, como remediación de agua, aire y suelo; 3) en materiales para fuentes alternas de energía; y 4) en la industria de semiconductores para sostener la llamada Ley de Moore del escalamiento del tamaño y la capacidad de los elementos de procesamiento.

En este trabajo de tesis se han atendido problemas específicos que de alguna u otra manera contribuyen al desarrollo de las aplicaciones esperadas de la Nanotecnología. En particular, se ha contribuido al desarrollo de dos áreas principalmente: 1) la ciencia del óxido de zinc a nanoescala, y 2) la ciencia del carbono a nanoescala. El carbono, sin lugar a dudas, es el material que más ha sido estudiado en el área de Nanociencias y Nanotecnología, debido, en parte, a la flexibilidad de su química. Tal vez, el segundo material más estudiado es el óxido de zinc (ZnO). Esto es debido a la combinación de sus propiedades: es un semiconductor de brecha prohibida ancha con propiedades ópticas interesantes; presenta propiedades mecánicas interesantes; y es, en principio, un material inofensivo para la salud humana y para el medio ambiente.

En este trabajo se optimizó la síntesis de nanoestructuras de ZnO en una dimensión utilizando un método limpio de baja temperatura y de bajo costo. Esta técnica de síntesis y este material se utilizó para hacer un compósito de ZnO con celulosa, del cual se investigaron sus propiedades piezoeléctricas y piroeléctricas. Los dispositivos construidos a partir de este material compósito son capaces de generar energía eléctrica cuando se someten a excitación mecánica por medio de ondas ultrasónicas, o a gradientes de temperatura.

A través de cálculos de primeros principios, se contribuyo al entendimiento del ferromagnetismo observado por otros grupos en ZnO y en ZnO dopado con elementos no magnéticos. Los resultados presentados en este trabajo sugieren que las propiedades magnéticas observadas son muy sensibles al entorno de los átomos en la superficie.

Además, se estudiaron las propiedades de nanolistones de ZnO. Se ha encontrado en este trabajo que los nanolistones de ZnO muestran propiedades electrónicas que dependen de la morfología de los bordes, pero no del ancho. En particular, los nanolistones de ZnO con bordes con morfología tipo zigzag muestran estados de borde y son metálicos, mientras que los que tienen bordes con morfología tipo armchair son semiconductores con un ancho de brecha prohibida de cerca de 3eV. Además, los nanolistones de ZnO tipo zigzag muestran propiedades ferromagnéticas interesantes y metalicidad polarizada cuando los bordes son manipulados adecuadamente. Por último otros grupos han hecho estudios basados en nuestros resultados en los que se muestra que los nanolistones de ZnO tipo armchair exhiben una regulación de ancho de la brecha prohibida cuando son sometidos a un campo eléctrico.

Los estados de borde no son exclusivos de los nanolistones de ZnO. Los nanolistones de grafeno (una capa mono-atómica de grafito) y sus estados de borde han sido estudiados por más de una década. Sin embargo, la síntesis controlada y a gran escala de estos sistemas sigue siendo un reto. En este trabajo, se ha contribuido al entendimiento de la estructura y de las propiedades químicas de nanolistones de carbono sintetizados por el método de deposición química de vapores sintetizados en el Laboratorio de Nanociencias y Nanotecnología del IPICYT. Se muestra que este material puede presentar una rica e interesante química en los bordes. También se contribuyó a la producción de grafeno de algunas capas a partir del desdoblamiento de nanotubos a través de la hidrogenación asistida por catalizadores. Este método es particularmente interesante porque abre la posibilidad de sintetizar nanolistones de grafeno dopados al desdoblar nanotubos de carbono dopados.

Por último, se propone que los nanolistones podrían jugar un papel importante en la electrónica del futuro. Se estudian y comparan las propiedades de nanolistones de ZnO, grafeno y otros materiales. Estos materiales son más prometedores que los nanotubos porque son compatibles con las actuales técnicas litográficas. Por esto, en este trabajo se llama la atención no solo la los nanolistones de carbono, sino a nanolistones de otros materiales laminares que pueden exhibir nuevas, diferentes e interesantes propiedades que pueden complementar a las que muestra el carbono.

Abstract

Nanotechnology is expected to impact the quality of life through many of the novel applications that it will enable. These applications will take advantage of features that are only feasible at the nanoscale. The most important applications are in medicine from better tools for diagnosis, to improved, custom-made, and specifically targeted drugs; in problems of high social impact such as water, air and soil remediation, and alternative sources of renewable energy; and in the semiconductor industry to try to keep up with the so-called Moore's Law of the scaling of the size and power of processing units.

In this Thesis work we have addressed punctual problems that in some way or another try to contribute to the development of the expected applications of nanotechnology. In particular, we have contributed to the development of mainly two areas: 1) nanoscale zinc oxide science, and 2) nanoscale carbon science. Carbon is, without a doubt, the material which has the most intense research activity in nanoscience and nanotechnology, because of its flexible chemistry. The second most studied material in nanoscience and nanotechnology is probably zinc oxide (ZnO). This is due to the combination of mainly three facts: it is a wide band gap semiconductor with interesting optical properties; it has interesting mechanical properties; and it is, in principle, innocuous to human health and to the environment.

We optimized a method for the synthesis of ZnO nanorods using a low temperature, low cost and clean approach. We used this material to make a composite with cellulose and probed its piezoelectric and pyroelectric response. The constructed devices are capable of generating electricity when excited with ultrasonic waves or temperature gradients.

Through first principles calculations, we have contributed to the understanding of ferromagnetism in non-doped ZnO and in ZnO doped with non-magnetic atoms. Our results suggest that the observed properties are very sensitive to the environment of the atoms at the surface.

In addition, we have studied the properties of ZnO nanoribbons. We found that ZnO nanoribbons show edge dependent (but not width dependent) electronic properties: zigzag ZnO nanoribbons are metallic, while armchair ZnO nanoribbons are semiconducting with a constant band gap regardless of the width (c.a. 3eV). ZnO zigzag nanoribbons show interesting ferromagnetic properties, and half metallicity after proper manipulation of the edges. Finally, other groups have shown that armchair ZnO nanoribbons exhibit gap modulation under an electric field.

Edge effects are not exclusive to ZnO. Graphene nanoribbons and their edge effects have been studied for more than a decade. However, the large scale and controlled synthesis of such systems remains a challenge. In this work, we have contributed to the understanding of the structure and the properties of chemical-vapor-deposition grown graphitic nanoribbons. We show that there could be an interesting chemistry underneath their complex structure at the edges. We also contributed to the production of few layer graphenes from the unzipping of carbon nanotubes through catalyst assisted hydrogenation. This method is interesting particularly because it opens the possibility of synthesizing doped nanoribbons through the unzipping of already doped carbon nanotubes.

Finally, we propose that nanoribbons might hold the future of electronics. In particular, nanoribbons show better future than nanotubes because they are compatible with current lithographic techniques, since the former are planar systems. In this work we call the attention not only to carbon nanoribbons, but also to other layered materials that exhibit different and interesting properties which complement those of carbon.

Preface

CONTENTS

Nanoscience: what is it about?

Considering the amount of attention that nanoscience and nanotechnology (N&N) is getting from society, it would be convenient for researchers in this area to have a clear definition of what it actually is. However, a single definition is hard to construct because it involves different concepts in a wide area of study with unforeseen applications. Most of the definitions have it clear that nanoscience involves the study of materials of 100 nm or smaller in size in at least one dimension [1]. However, this rather common definition has two flaws. First, it is too rigid for such a diverse field. It is very common to synthesize a material which has size dispersion. For instance in a typical synthesis of carbon nanotubes, the diameters range from tens to hundreds of nanometers (see, for example Ref. 2). Is such a sample then a mixture of carbon microtubes and nanotubes? What if the properties of interest of the tubes in the sample is the same, regardless of their dimension within this range? Then, it does not make sense to make any distinction. This brings up the second flaw: if nanoscience is only a matter of scale, then why make up names by adding a "nano" prefix to any word? There should be something more to it. In fact, there is. The National Science Foundation (NSF) definition for N&N explicitly states that for a research work to be considered as nanoscience, it should *"have novel properties and functions because of their small and/or intermediate size"* [3]. This means, for instance, that the processors of our computers do not have nanotechnology, despite of the fact that they use 45nm transistors. As a matter of fact, the people in the semiconductor industry do all kinds of clever things to avoid the effect of size (particularly of the dielectric material) and retain the properties of the original micron sized transistors. However, the NSF definition still has the 1 to 100 nm flaw [3]. It is clear then that a deep discussion on the definition and scope of N&N is imperative, not only for the epistemology of the discipline, but also because it would help for facing some of the challenges of this research area (*e.g.* metrology, regulation).

Challenges

Nanotechnology is expected to impact the quality of life through many of the novel applications that it will enable. These applications, consistent with the definition above, will take advantage of features that are only feasible at the nanoscale. For

instance, there has been an increasing expectancy of the impacts of nanotechnology in medicine: from better tools for diagnosis, to improved, custom-made, and specifically targeted drugs [4]. In addition to medical science, there is considerable hope in nanotechnology to solve problems of high social impact such as water, air and soil remediation [5], and alternative sources of renewable energy [6]. Also, there is hope in nanotechnology to aid the semiconductor industry in keeping up with the so-called Moore's Law of the scaling of the size and power of processing units [7]. In any case, the use of nanotechnology will have an impact in the efficient use of materials, since in principle, the properties of nanomaterials can be tailored to fit the needs of specific applications with minimal loss due to imperfections. In fact, this is the idea behind the most successful application of N&N to date: composites. In these materials a small amount of a nanomaterial is used to change or enhance the properties (mechanical or electrical) of a large matrix.

No matter what the application is, there are common challenges in the development of N&N, which can be divided in two: experimental and theoretical. From the experimental point of view, there is strong need for the control of the properties and dimensions of the nanomaterials. Although there has been some progress, there are still unsolved puzzles, like the control of the electronic properties of a carbon nanotube sample. Another challenge is the development of scalable and environmentally clean production methods. From the theoretical point of view, there is a strong need for the development, and most importantly, the implementation of theories that can reproduce and explain the experimental observations. For this, a multi-scale approach is often required, since the quantum phenomena might play a crucial role in the macroscopic properties of a material.

Another kind of challenges that N&N face are of human character. First, there is a strong need for a systematic and standardized characterization procedures for nanomaterials. For this, of course, a consensus on the definition of nanoscience must be reached first. Metrology institutes and organisms should play a crucial role on this point. Second, the interaction between experimentalists and theoreticians should be encouraged. It is my perception that the deep understanding of many new observed phenomena, which can only be gained by proper theories, is far behind the rate of new discovered phenomena. However, there are also many situations in which theoretical predictions (mostly based on calculations and

simulations) of new interesting properties are still pending for an experimental confirmation. Hence, many times the two areas seem to be out of phase.

Finally, there are the challenges and demands from the society. Addressing the potential risks of nanomaterials in health and on the environment is a particularly serious challenge. This challenge involves researchers, but also transcends the scientific community. So far, the position of researchers is based on the "new deficit model" which has the hypothesis that the difficulty for handling the introduction of nanomaterials into society through products is due to a deficit on the knowledge of their impact in health and the environment; should that deficit be covered, proper policies will be created [8]. Instead, both researchers and policy makers should learn how to handle uncertainty, and make "elastic policies" that can rapidly change as new data is available.

POSSIBLE PATHWAYS

Of course, it is impossible to address each and every of the challenges of N&N as it was stated before, the applications of N&N are now unforeseen. Also this area of research is interdisciplinary and multidisciplinary. Therefore, the researcher in this discipline should be open to work with many different materials and in different approaches (*e.g.* experimental and theoretical).

In this thesis work we have addressed punctual problems that in some way or another try to contribute to the development of the expected applications of nanotechnology. The original objective of this thesis was to contribute to the science of nanoscale zinc oxide (ZnO). That was the main motivation behind Chapters 1 and 2. However, as we were working with the properties of the edges in planar ZnO, it came to our attention that there were some unanswered questions on the properties of the edges in graphene (an isolated layer of graphite) and other single layer materials. These new possibilities were studied in Chapters 3 and 4. Also, we tried to combine the study of these materials from an experimental and theoretical point of view, since we think is the way to go for researchers in this area.

This work is organized as follows: Chapter 1 introduces ZnO and nanoscale ZnO. Special attention is paid to one-dimensional ZnO structures and in particular to nanorods and nanowires. In Chapter 2, we present an optimized method for the synthesis of ZnO nanorods using a low temperature, low cost and clean approach.

Despite being a low temperature method (*c.a.* 80°C) the nanorods are of high quality, *i.e.*, highly crystalline. The produced ZnO nanorods, as any ZnO crystal, exhibit interesting piezoelectric properties. We used this material to make composite with cellulose which we called ZnO-paper and then probed its piezoelectric and pyroelectric response. The constructed devices are capable of generating electricity when excited with ultrasonic waves or temperature gradients. Although the efficiency of these devices is still very low, they could be useful for powering small scale devices in unreachable places. For instance, a micro or nanoscale sensor inside the body could be powered from the outside through ultrasonic waves.

At the beginning of this thesis work two reports appeared (both in 2007) in the literature that influenced its course. First, the work by Garcia *et al.*, which reported the observation of a ferromagnetic response at room temperature in ZnO nanoparticles capped with organic molecules [9]. ZnO in bulk is a wide band gap semiconductor with no magnetic properties; therefore this observation raises the question of the origin of the observed magnetic properties in the nanoscale. Second, the work by Tusche *et al.*, in which they report the observation of new planar phase for ZnO [10]. Since it is a new crystal phase, the properties of this material were unknown. Furthermore, since it is a planar layered material, it would inevitably show edges. Edges in layered materials play a very important role, just as surfaces play important roles in crystals. Therefore the observation of this planar phase raises the question of the properties of its edges. These two problems are the main motivation of Chapter 3.

As mentioned above, the properties of edges have a very important role in planar layered materials. The properties of these edges in graphene have been known for more than a decade. However, the recent isolation of graphene and the investigation of its peculiar properties has brought the problem alive. Chapter 4 introduces nanoscale carbon, and in particular the properties of graphene and graphene nanoribbons. Despite the importance and interest in graphene and graphene nanoribbons, the most common techniques for producing graphene are not easily scalable. In our group we have proposed two approaches to develop a more scalable way to produce nanoribbons. The first, is based on a chemical vapor deposition (CVD) method, and yields a completely new material that share the properties of carbon nanotubes and graphene nanoribbons. The second is a top

down approach in which carbon nanotubes are somehow treated to make them unzip into nanoribbons. The contribution to these methods done in this thesis work are presented in Chapter 5.

In Chapter 6 we propose that nanoribbons might hold the future of electronics. Nanoscale carbon based electronics are already a topic in the semiconductor industry road map because of the high mobilities these materials exhibit. In particular, nanoribbons show better future than nanotubes because they are compatible with current lithographic techniques. In this work we call the attention not only to carbon nanoribbons, but also to other layered materials that exhibit different and interesting properties which complement those of carbon. The Semiconductor Industry was for a long time based only on silicon. However, as the dimensions scaled down there was an increasing need to incorporate new elements (*e.g.* high dielectrics) into the technology and adapt the processing and fabrication techniques to fit them. A carbon based electronics future might be doomed to eventually need other elements. Therefore, we propose that a more versatile layered-nanoelectronics might hold the key for the future of electronics.

REFERENCES

[1]. Wikipedia contributors. Nanotechnology. Wikipedia, The Free Encyclopedia (2009) at http://en.wikipedia.org/w/index.php?title=Nanotechnology&oldid=324550145. Retrieved on November 8, 2009.

[2]. Botello-Méndez, A. et al. Controlling the dimensions, reactivity and crystallinity of multiwalled carbon nanotubes using low ethanol concentrations. *Chem. Phys. Lett.* **453**, 55-61 (2008).

[3]. Nanotechnology definition (NSET, February 2000). The National Science Foundation. http://www.nsf.gov/crssprgm/nano/reports/omb_nifty50.jsp. Retrieved on November 8, 2009.

[4]. Wagner, V., Dullaart, A., Bock, A. & Zweck, A. The emerging nanomedicine landscape. *Nat. Biotechnol.* **24**, 1211-1217 (2006).

[5]. Wiesner, M.R. & Bottero, J. *Environmental nanotechnology.* (McGraw-Hill Professional: 2007).

[6]. Whittingham, M.S. Materials challenges facing electrical energy storage. *MRS Bulletin* **33**, (2008).

[7]. Emerging Research Materials. International Technology Roadmap for semiconductors 2007. http://www.itrs.net/Links/2007ITRS/2007_Chapters/2007_ERM.pdf

[8]. Brown, S. The New Deficit Model. *Nat. Nanotechnol.* **4**, 609-611 (2009).

[9]. García, M. A.; Merino, J. M.; Fernández Pinel, E.; Quesada, A.; de la Venta, J.; Ruíz

González, M. L.; Castro, G. R.; Crespo, P.; Llopis, J.; González Calbet, J. M.; Hernando, A. Magnetic Properties of ZnO Nanoparticles. *Nano Lett.* **7**, 1489-1494 (2007).

[10]. Tusche, C., Meyerheim, H.L. & Kirschner, J. Observation of Depolarized ZnO(0001) Monolayers: Formation of Unreconstructed Planar Sheets. *Phys. Rev. Lett.* **99**, 026102-4 (2007).

Chapter 1

ZnO Nanostructures

CONTENTS

1.1. INTRODUCTION

Zinc oxide (ZnO) is a mineral that was discovered in 1810 by Bruce Franklin. It is naturally found as a mineral known as zincite that often exhibits red color due to manganese impurities [1]. However, pure zinc oxide (ZnO) is usually a white powder produced from the oxidation of metallic zinc, which is one of the most abundant elements on the surface of the earth. Today, most of the zinc oxide powder produced worldwide is used in applications such as vulcanization activator (in rubber production), for de-sulfuration of gases, fabrication of phosphates, paints, in agriculture, ceramics, fungicides, etc [1].

However, in the last decades, most of the interest on ZnO has been focused on the mechanical, optical, and electronic properties of this mineral. For example, ZnO has now been increasingly used in applications for high technological industrial areas such as piezoelectric transducers, optical waveguides, acousto-optic media, conductive gas sensors, transparent conductive electrodes, and varistors [2,3].

Nanoscale ZnO structures have brought new applications to this material. In particular, ZnO one-dimensional materials have been proposed for a wide variety of applications. It is worth noting that ZnO has played an important role in the search for materials for alternative energy harvesting devices, such as solar cells, fuel cells, and scavenging devices through the piezoelectric or pyroelectric effect [3]. According to the philosophy of green alternative energy, the materials used for the construction of harvesting devices should be produced at a low cost, with low environmental footprint, and produce minimal waste before and after their use lifetime; all of this, without loosing their functionality. In this sense, ZnO is very attractive.

1.2. PROPERTIES OF ZnO

1.2.1. CRYSTAL STRUCTURES OF BULK ZnO

The most stable crystal structure for ZnO at standard temperature and pressure conditions is the hexagonal Wurtzite (WZ) structure. However, as most of the II-VI binary compounds, it can also be crystallized in the cubic Zinc-Blende (ZB)

structure. Both WZ and ZB structures are characterized by a four-fold coordination in which each anion is bonded to four cations, or vice versa. This bonding is similar to a sp³ bonding; nevertheless, these compounds have also a strong ionic component. In particular, ZnO is a compound that lies in the borderline between a covalent and ionic semiconductor, and shares characteristics of both. Another phase of ZnO, which behaves as an ionic semiconductor, is the rock salt structure (RS), similar to NaCl. In the last decade, several studies regarding the polar surfaces of ZnO revealed that for a small number of layers, the Wurtzite structure would become planar, resulting in a fourth phase of ZnO, which was only recently confirmed experimentally. In this section we will analyze the characteristics and properties of each of these structures to set the background for the following sections. The analysis is carried out with the help of first principles calculations using the density functional theory described in appendix B.2.

Color	white
Structure	Wurtzite(P6₃mc) a=b 3.249 Å c 5.206 Å u 0.374 α=β 90° γ 120°
Composition	O 19.66%wt; Zn 80.34%wt
Fusion Temperature	1975°C
Boiling Point	sublimes at 1800°C
Density	5600kg/m³

Table 1.1: Physical Properties of the naturally found WZ structure of ZnO [2,3].

1.2.1.1. WURTZITE STRUCTURE

ZnO is usually crystallized in the WZ structure (see figure 1.1). This structure has a hexagonal cell with parameters *a=b*, and *c*. and belongs to the space group P6₃mc (see table 1.1). It is composed of two hexagonal close packed sublattices displaced from each other on the *c*-axis by an amount *u*. Each of the sublattices contains only one atomic specie. In an ideal WZ crystal, *c/a*= $\sqrt{(8/3)}$, and *u*=3/8. However, a real ZnO WZ crystal will deviate from these values. This phase, as well as the other phases is a wide band gap semiconductor with an experimental

electronic band gap of *c.a.* 3.4eV. The electron and hole effective masses are $0.28m_0$ and $0.59m_0$, respectively, where m_0 is the mass of a free electron. WZ-ZnO exhibits an exciton binding energy of 60meV, which makes it very competitive for optoelectronic applications. The lack of inversion symmetry in WZ structure causes an ionic displacement when the structure is under stress, thus, leading to a piezoelectric behavior with a relevant piezoelectric constant d_{33}=12 mp/V [1].

The properties of WZ-ZnO have been widely studied both from the theoretical and experimental standpoints. However, the properties of the other different phases are not as widely known. In table 1.2, we compare the properties of the different ZnO phases with first principles density functional calculations under the local density approximation (LDA) (see appendix B.2). It is well known that the LDA underestimates the band gap for insulators up to more than 30%. For ZnO the underestimation goes from 3.4eV to 0.84eV. However, other relevant properties are well described under the LDA and will help in the discussion of the different phases in ZnO. Generalized gradient approximations usually exhibit larger deviations from the lattice parameters, and do not improve significantly the underestimation of the calculated band gap [3]. Therefore, the LDA is the most common choice in DFT calculations for ZnO.

1.2.1.2. ZINC-BLENDE STRUCTURE

The ZB structure is metastable and can be achieved by growing zinc oxide epitaxially on a cubic crystal such as ZnS. The symmetry of the ZB structure is given by the F-4$_3$m space group. It consists of two face centered cubic sublattices of one atomic specie displaced from each other by ¼ along the body diagonal (see figure 1.1). The main difference between the WZ and the ZB structures is the stacking sequence of the diatomic planes. The WZ structure consists of triangularly arranged alternating diatomic close-packed (0001) planes, thus the stacking sequence of the (0001) plane is AaBbAaBbA in the *c* axis, where the small and large letters stand for the two different kinds of constituent atoms. In contrast, the ZB structure consists of triangularly arranged atoms in the closed-packed (111) planes along the body diagonal that causes a stacking order of AaBbCcAaBbCcA. The band structure of ZB-ZnO is very close to that of the WZ phase, and the character of the bonding is also very similar. Therefore, the electronic properties of ZB-ZnO and WZ-ZnO are much alike. However, the ZB phase has a slightly more
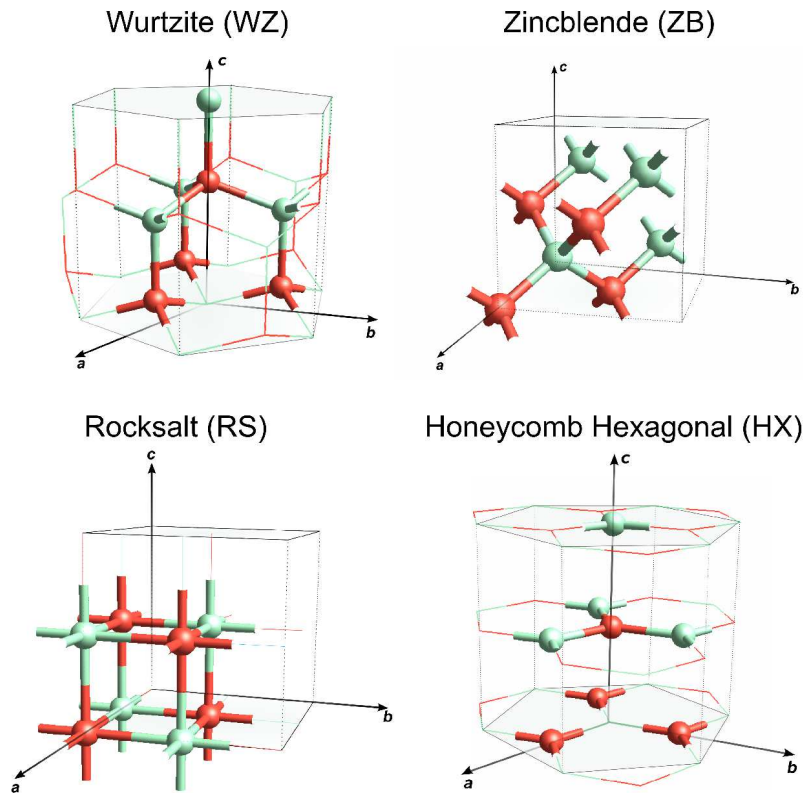
Figure 1.1: Molecular models of the different phases of zinc oxide. In the WZ and the ZB the atoms are four-fold coordinated in a sp^3-like tetrahedrical bonding. In the RS structure, the atoms are six-fold coordinated and is the most ionic phase of ZnO. The honeycomb hexagonal phase is three-fold coordinated, and is the most covalent phase of ZnO. The red (dark) and green (light) spheres represent oxygen and zinc, respectively.

covalent bonding, and is mechanically more robust when compared to the other phases.

1.2.1.3. ROCKSALT STRUCTURE

The RS structure of ZnO is found at relatively low hydrostatic pressures (~10GPa) [2,3]. Once ZnO is stabilized in this phase, the structure is metastable for long periods of time and for a wide range of temperatures (above 300K). This structure is a simple cubic with symmetries described by the Fm_3m space group, and exhibits a six-fold coordination. The change of the lattice dimensions in ZnO, causes the inter-ionic Coulomb interaction to favor the ionicity more over its covalent nature, being this the phase the most ionic bonding for ZnO. The Zn-O distance is increased considerably with respect to the WZ and ZB cases (see table

1.2). The electronic properties are also affected by the change of phase leading to a LDA band gap of several electron-volts higher than the WZ and ZB cases. There is an important difference in the electromechanical properties: due to symmetry considerations, there is no relative ionic displacement under stress, and therefore, no piezoelectricity.

	Lattice Parameters(Å)	LDA Gap (eV)	d_{Zn-O} (Å)	$\sum_{\alpha} \langle \varphi^{KS}_{i,\alpha} \| \varphi^{KS}_{i,\alpha} \rangle - \langle \varphi^{Atom}_{i,\alpha} \| \varphi^{Atom}_{i,\alpha} \rangle$	$\sum_{\alpha} \langle \varphi^{KS}_{i \in O,\alpha} \| \varphi^{KS}_{j \in Zn,\alpha} \rangle$
WZ	$a=b=3.244$, $c=5.21$	0.8353	1.982 1.974	0.5	0.131 0.134
ZB	$a=b=c=4.55$	0.7306	1.971	0.485, $i \in Zn$; 0.310, $i \in O$	0.153
RS	$a=b=c=4.25$	1.053 (ind)	2.128	0.463, $i \in Zn$; 0.556, $i \in O$	0.091, 0.011
HX	$a=b=3.259$	1.9082	1.881	0.606, $i \in Zn$; 0.372, $i \in O$	0.196

Table 1.2: Calculated properties of the different phases of ZnO within the LDA: optimized LDA lattice parameters, electronic band gap (ind=indirect gap), distance between a nearest neighbors Zn-O (d_{ZnO}), charge transfer to the atom with respect to a free atom, and overlap charge, or charge at the bond. It is clear from the data shown that the planar hexagonal (HX) phase shows a Zn-O bond of more covalent nature, while the Rocksalt (RS) phase shows a Zn-O bond of more ionic nature, and the Zinc-Blende (ZB) and Wurtzite (WZ) phases lie in between.

1.2.1.4. HEXAGONAL PLANAR STRUCTURE

The WZ structure of ZnO is formed by alternating planes of oxygen and Zn ions stacked along the *c*-axis, so that any cut of the crystal perpendicular to this direction would result in a single-ion dominated surface. Hence, a polar surface occurs. However, according to the Tasker ionic model, this arrangement would result in a dipole that drives to a divergence in energy as the number of planes increases [4]. Since thin films of ZnO grown in the [0001] direction have been observed in experimental setups [5], the stabilization mechanism of the surface was a problem that received considerable attention over the last decades. Originally, three main mechanisms were proposed: 1) the creation of surface states and charge transfer from the anion to the cation surface [6]; 2) the appearance of Zn vacancies on the cation surface [5,7]; and 3) removal of negative charge on the
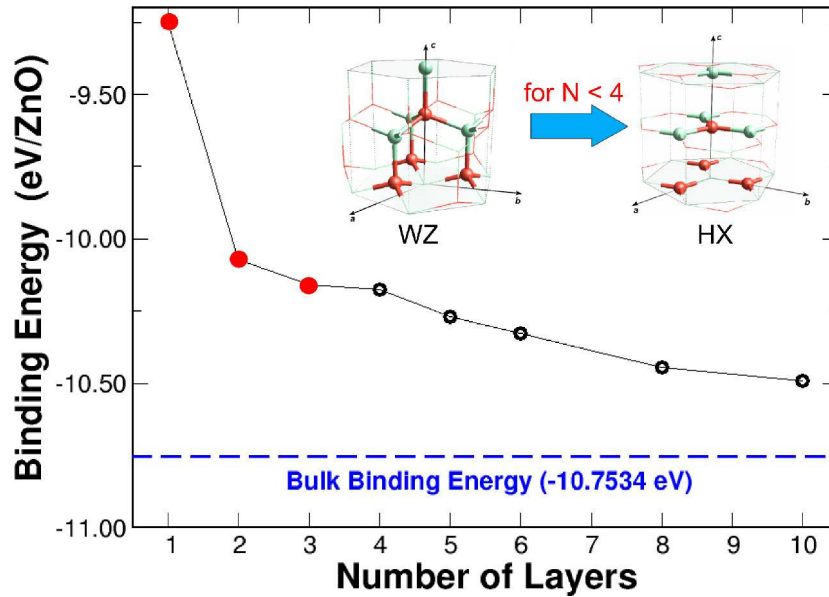
Figure 1.2: Binding energy per formula (eV/ZnO) for ZnO WZ layers calculated within LDA-DFT. The structures were constructed by cutting a the bulk WZ with two planes perpendicular to the c axis. For slabs with number of layers (N) less than 4, there is a structural change form WZ to HX structures.

oxygen dominated surface [5,8]. Recently, however, triangular shaped reconstructions were proposed for a stabilization mechanism for setups in which the surface is changed form the ideal case [5,7,9]. Freeman *et al.* proposed a boron-nitride like transition to remove the dipole [10] (see figure 1.2). In this transition, the Zn and O atoms share the same plane, thus eliminating the dipole.
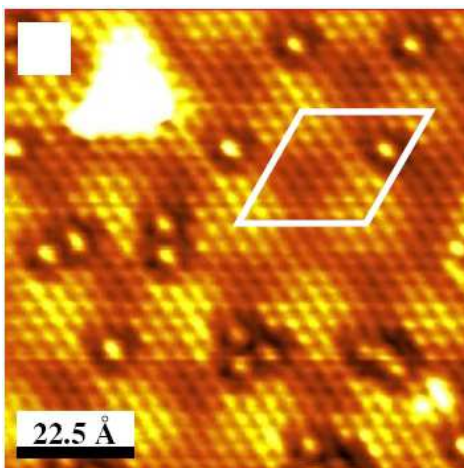
Figure 1.3: High resolution 9×9 nm² STM image of a bilayer of ZnO grown on Ag (111) by Tusche, *et al.* [11].

Recently, Tusche and collaborators have synthesized for the first time this predicted planar ZnO [11]. They have grown 2-5 layers of ZnO using laser ablation on a silver (111) substrate (see figure 1.3). Their surface x-ray diffraction and scanning tunneling microscopy studies reveal that when the number of layer is less than 4, the structure suffers a severe inward relaxation, changing the bulk four-fold tetrahedral for a trigonal planar coordination. Our calculations, as well as those reported before confirm this theoretically (see figure 1.2).

16

The electronic properties of this new phase of ZnO are quite different from the other phases. As opposed to the rocksalt case, in the HX phase, the bond length is decreased and the bond is significantly more covalent. The LDA band gap increases considerably with respect to the other phases by almost 1eV. The band structure shows that the electron and hole effective masses have a similar value.

1.2.2. PHYSICAL PROPERTIES OF WURTZITE ZnO

1.2.2.1. ELECTRONIC PROPERTIES

The band structure of a given semiconductor determines to a large degree its potential utility. As a direct and wide-band-gap material, ZnO is attracting a lot of attention for a variety of electronic and optoelectronic applications. Advantages associated with a large band gap for these applications include higher breakdown voltages, ability to sustain large electric fields, lower noise generation, and high temperature and high-power operation. However, the correct description of the band structure of ZnO and its band gap has been difficult because of the large discrepancy between experiment and the most common theoretical calculations.

WZ ZnO conduction band is mainly constructed from the s-like state, whereas the valence band is a p-like state. Photoemission spectra for WZ ZnO revealed a band gap of 3.4eV, with the cation *3d*-band positioned 7.8eV below the valence band maximum, and an anion *2p* valence bandwidth of 5.3eV [3,12]. It was accepted very early that for a fair qualitative theoretical description of the band structure of ZnO, most of them based on the LDA, *3d* states should be included as valence electrons [13,14]. This is because there is a non-negligible influence of *3d* states on the *s* and *p* valence bands. Contrarily, if the *3d* states are considered as core electrons, the calculated lattice constant underestimates the experimental values by as much as 18%. However, even if *3d* states are considered as valence electrons, there is still quantitative disagreement with experiments for the values of band gap and band positions [15]. For example, our calculations using DFT-LDA shows a band gap of 0.78eV, a *d* band position of ~5eV and a *p* valence bandwidth of ~4.8eV (see figure 1.4). In this case, the position of the *d* bands and the bandwidth of the O-*p* valence bands are not clearly distinguished, since there is an overestimated *p-d* interaction, that leads to some hybridization. Nevertheless, DFT-LDA band structures including *3d* states, often show very good agreement for the
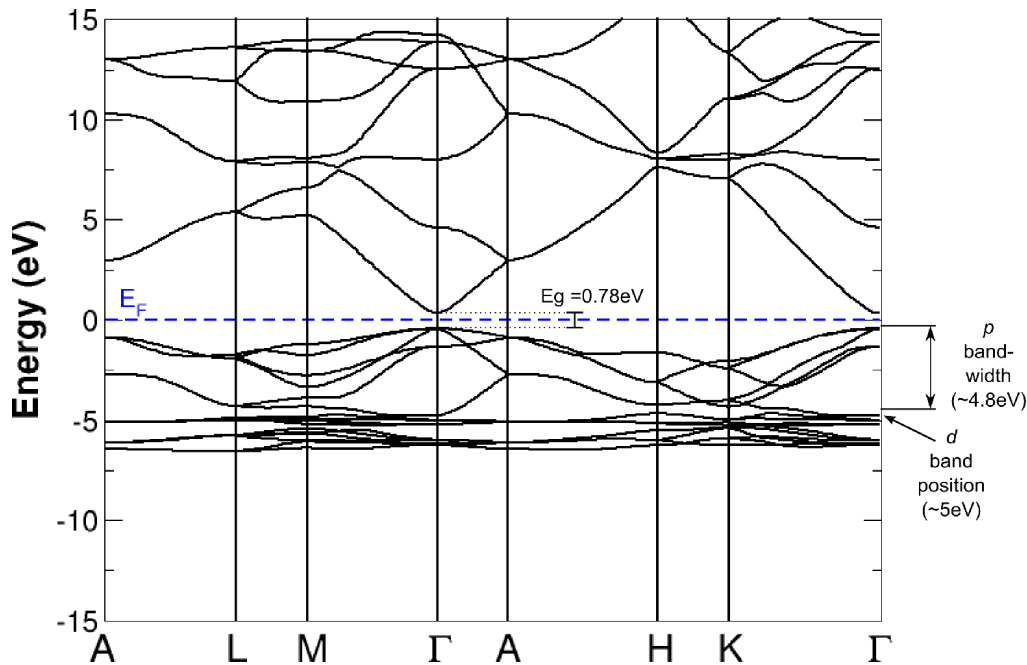
Figure 1.4: DFT-LDA band structure of bulk WZ ZnO showing an underestimated band gap (exp.: 3.34eV), p band-width (exp.: 5.8eV), and 3d band position (exp.:7.8eV).

valence and conduction edge bands and wavefunction shape, which is good enough for the calculations of different properties of ZnO.

It has been previously reported that the use of a generalized gradient approximation (GGA) (see appendix B.2) functional underestimates even more the electronic band gap, and overestimates the cell parameters (1.6% as compared to -0.8% in LDA for the cell parameter c).

Electron-electron interactions in narrow bands originating from spatially localized atomic-like states are not well described by a homogeneous electron gas as described by with DFT-LDA. Therefore, calculations that include electron-electron interactions improve significantly the quantitative agreement between theory and experiment for ZnO band structure. Self interaction correction pseudopotential approaches correct the non-physical self-interaction intrinsic in DFT, and give close agreement with the experimental band gap. However the d bands are 1eV too low [15]. Another, more accurate, semi-empirical approach, DFT+U (see appendix B.3), introduces a Hartree-Fock like term with a Coulomb interaction parameter U. This approximation gives a better description of the $3d$ bands and could be very important for describing impurities. Although the electronic band gap is closer to
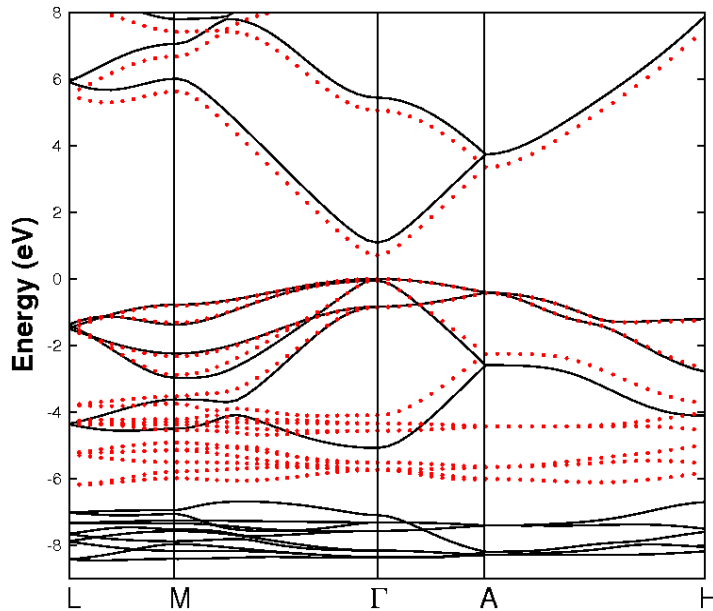
Figure 1.5: LDA+U (solid line) compared to LDA bands structure (dotted line). The band gap is still underestimated (1.0eV), but the *p* bandwidth (5.2eV) and the position of the *3d* bands (7.5eV) agree well with experiment.

the experimental gap, the underestimation persists (see figure 1.5). The determination of U is rather difficult, nevertheless, Janotti and coworkers have proposed a method for the *ab-initio* determination of the otherwise empirical parameter $U = U^{at}/\varepsilon_\infty$, where U^{at} is the atomic correlation energy obtained by the energy difference between the addition and the removal of an electron from the atomic *d* subshell (the reference in this case is a configuration with 9 electrons in the *d* subshell), and ε_∞ is the macroscopic dielectric constant [16]. Following this approach we have obtained a value of U=4.7 eV for the case of bulk WZ ZnO using the experimental value for ε_∞ .

First principles approaches including electron-electron interactions are significantly more expensive in terms of computational time. In order of complexity and computational time, non self-consistent G_0W_0, partial self-consistent GW_0 and full self-consistent GW calculations (see appendix B.4) on top of DFT obtain increasingly better results for band gap energies (2.86, 3.02 and 3.33eV, respectively) [17,18].

The electronic properties of ZnO, and specifically the conductivity, can be controlled to a great extent by doping with Al or Ga (n-doping). However, p-type doping has been a challenge. Nevertheless, some efforts have been successful for doping ZnO with Li, Na, K, N, P, As, and Sb [2,3].

1.2.2.2. OPTICAL PROPERTIES

ZnO has gained much interest in part because its optical properties are superior

to currently used materials. For instance, ZnO alloys might be an alternative to GaN based alloys which are currently used in UV optoelectronic devices. This is because its band gap is similar to GaN (*c.a.* 3.2eV), but the exciton binding energy is more than two times larger than that of GaN. Therefore, opposite to GaN, stimulated excitonic emission is possible even above room temperature. The optical properties of a semiconductor are connected with both intrinsic and extrinsic effects. Intrinsic optical transitions take place between the electrons in the conduction band and holes in the valence band, including excitonic effects due to the Coulomb interaction. Excitons are classified into free and bound excitons. In high-quality samples with low impurity concentrations, the free exciton can also exhibit excited states, in addition to their ground-state transitions. Extrinsic properties are related to dopants or defects, which usually create discrete electronic states in the band gap, and therefore influence both optical-absorption and emission processes [2].

1.2.2.3. MECHANICAL PROPERTIES

The mechanical properties of materials involve various concepts such as hardness, stiffness, and piezoelectric constants, Young's and bulk moduli, and yield strength. In hexagonal crystals, there exist five independent elastic constants: C_{11}, C_{33}, C_{12}, C_{13}, and C_{44}.

Among the tetrahedrally bonded semiconductors, it has been stated that ZnO has the highest piezoelectric tensor or at least one comparable to that of GaN and AlN. This property makes it a technologically important material for many applications, which require a large electromechanical coupling. The piezoelectric tensor has three independent components in WZ phase and one (e_{14}=0.69C/m^2) in the cubic Zinc-blende phase, which characterize the full piezoelectric tensors of such crystals. Two of these
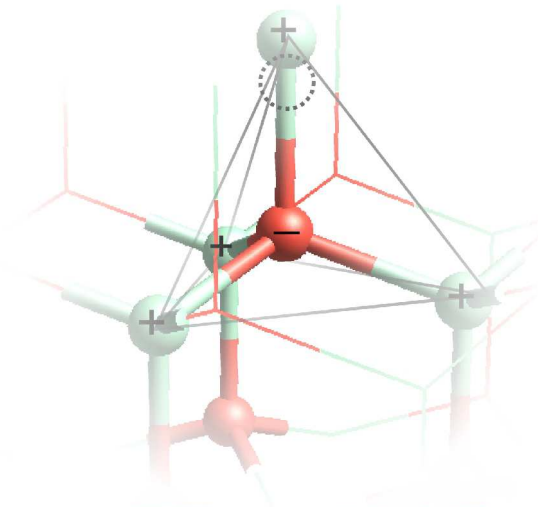
Figure 1.6: Electric dipole created upon ionic displacement in WZ ZnO, leading to a piezoelectric effect.

components in WZ phase measure the polarization induced along the c axis, at zero electric field, by a uniform strain either along the c axis or in the basal plane. The relevant relationship is $^zP_{piezo} = e_{33}\varepsilon_z + e_{31}\varepsilon_\perp$, where ε_z and $\varepsilon_\perp$ are the strain along the c axis and in the basal plane, respectively. e_{33} and e_{31} are the piezoelectric coefficients. The third independent component of the piezoelectric tensor, e_{15}, describes the polarization induced by a shear strain. The lack of inversion symmetry in WZ structure causes an ionic displacement when the structure is under stress (see figure 1.6), leading to spontaneous polarization. The combination of this spontaneous polarization and the low mobility of charges at zero bias results in a piezoelectric behavior with relevant piezoelectric constants d_{33}=12 pm/V, or e_{33}= 1.2C/m^2, e_{31}=-0.5C/m^2, e_{15}=-0.40C/m^2, (for example d_{11}=2.3, and d_{15}=117 pm/V for quartz and PZT, respectively) [19,20].

1.2.3. SIZE EFFECTS IN ZnO NANOSTRUCTURES

The structural, electronic, optical and mechanical properties of ZnO change when the dimensions scale down. These changes or size effects are entangled with the increase of surface area. Atoms at the surface have different environment than the bulk atoms, leading to different chemical and physical properties. As the surface to volume ratio increases, these surface properties become more and more important. In addition, symmetries are broken and properties such as mechanical properties are affected. Also, new properties arise from these new atomic environment. For instance, ZnO nanoparticles can exhibit unusual magnetic properties not seen in the bulk in any of its phases. This phenomenon is studied in detail in §3.2. Also, there are several reports on the observation of a blue shift (*i.e.* increase of the band gap) in the photoluminescence spectra of crystalline ZnO nanoparticles of few nm of diameter due to quantum confinement and surface passivation[21]. This blue shift has been used to monitor the growth of ZnO nanoparticles [22].

The loss of symmetry due to the increase of surface in ZnO 1D nanostructures such as nanorods, nanowires or nanobelts is responsible for the increased piezoelectric response. As stated above, the piezoelectric response requires that the spontaneous polarization lasts longer than the chances for recombination. The large surface area of nanostructured ZnO can cause more unintentional n-doping with hydrogen, and therefore an increase of carriers mobility, which in turn could

diminish the piezoelectric response. However, the large surface area could also lead to a large amount of charge traps which could increase the recombination lifetimes and thus, increase the piezoelectric response. Theoretically, it has been shown that the piezoelectric properties of ZnO are dependent on the size for both one-dimensional structures and for nanostructured thin films [23,24]. Initially, the piezoelectric response increases as the dimensions decrease, and then falls drastically when the dimensions keep decreasing.

The structural change from the WZ structure to a HX structure when the number of layers, or the thickness of a thin film decreases to less than four monolayers is a consequence of the change of the environment of the atomic species and the interaction between the (0001) and (000-1) surfaces. This new phase of ZnO, the HX ZnO was described in detail in §1.2.1.4. This quasi-2D phase can again have size effects. In this case, instead of surfaces, we have edges. These edges appear in different flavors, and have different properties to the bulk. The study of these edges is the focus of §3.3, and the general study of edges in other systems is the focus of §6.

1.3. SYNTHESIS OF ZnO NANOSTRUCTURES AND THEIR PROPERTIES

ZnO nanostructures have received a great deal of attention in the last few years. Since the 1960's there has been interest in the synthesis of thin films of zinc oxide for opto-electronic applications [1]. Recently, research on one-dimensional (1D) ZnO nanostructures has become a very active field due to different properties that these systems exhibit with respect to the bulk.

ZnO usually crystallizes in the Wurtzite (WZ) structure (figure 1.7), although as described above, it can be found in three other phases: Zinc-Blende (ZB), Rocksalt (RS) and
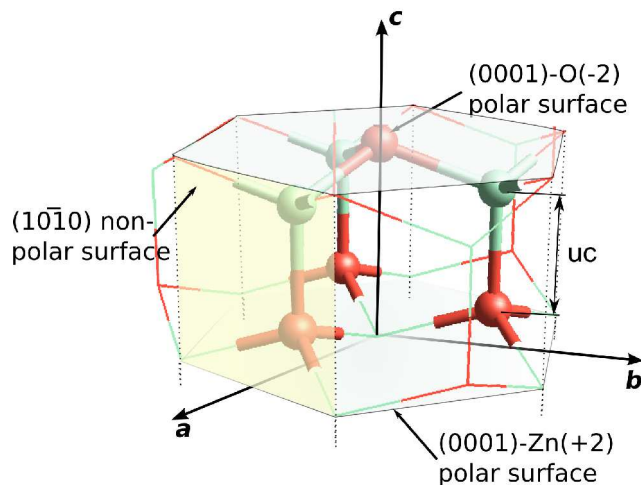
Figure 1.7: Crystal structure of Wurtzite ZnO showing the different polar and non-polar surfaces and directions.
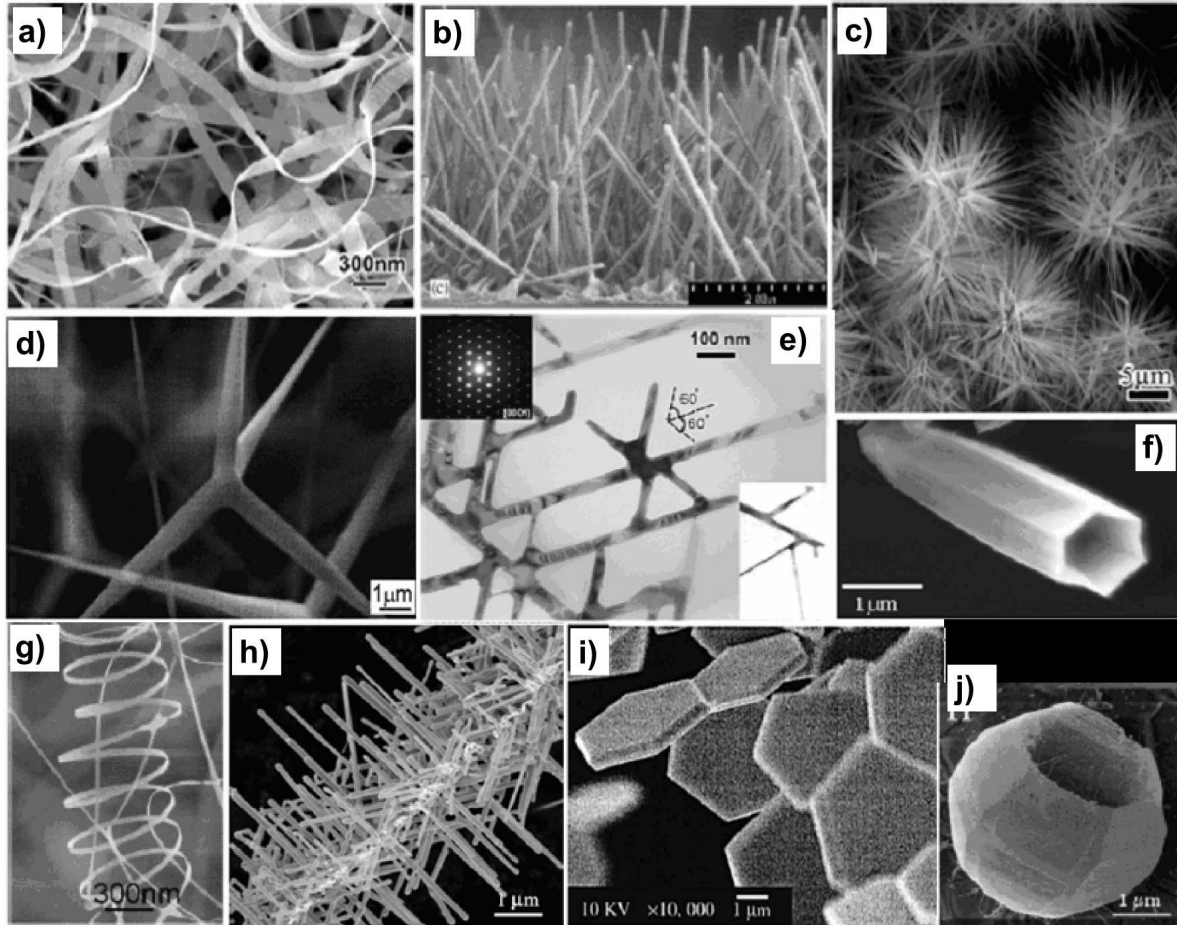
Figure 1.8: Different ZnO nanostructures reported in the literature: a) nanobelts [25], b) nanowires [27], c) flower-like structures [28], d) tetrapods [29], e) 2D dendritic structures [30], f) nanopipes [31], g) nanosprings [32], h) 3D dendritic structures [35], i) nanoplates [33], and j) nanocages [34].

Planar-Hexagonal (HX).The WZ structure is composed of two hexagonal close packed sub-lattices displaced from each other on the *c*-axis by an amount *u*. According to this structure, and to the stabilities of its surfaces, ZnO has three fast growth directions: $< 2\bar{1}\bar{1}0 >$, $< 01\bar{1}0 >$, and <0001>. Therefore, ZnO has a very broad family of nanostructures, which grow in one or several of these directions. Macroscopically, a crystal has different kinetic growth parameters associated to its planes. After nucleation, a structure usually grows with well defined crystal planes depending on the experimental conditions. In ZnO, the growth conditions have been controlled during synthesis favoring a specific direction, giving as result a wide range of nanostructures, such as: nanobelts [25,26], nanowires [27], flowerlike structures [28], tetrapods [29], dendritic structures in two [30] and three dimensions [25], nanopipes [31], nanosprings, nanohelixes [32], nanodisks [33], and

23

nanocages [34] (see figure 1.8).

Of particular relevance in this work, are nanorods or nanowires, and nanobelts. These one-dimensional nanostructures are related to the work presented in §2, and to the theoretical work presented in §3. Therefore, the next two subsections will be devoted to a review of the literature of the growth mechanisms and properties of these systems.

1.3.1. NANORODS AND NANOWIRES

ZnO one dimensional nanostructures are of great interest to researchers because of the different properties they exhibit due to the intrinsic properties of ZnO and the novel properties brought by the low dimensionality. In the literature three types of 1D ZnO nanostructures can be found: nanowires, nanorods, and nanobelts. These three 1D nanostructures are differentiated by their aspect ratio. It is generally accepted that nanorods are cylinders of radius of a few tens of nanometers and lengths of a few hundred of nanometers. On the other hand, nanowires usually have a diameter around 100 nm or more, and length of a few micrometers. Nanobelts are not cylinders, but rather rectangular prisms with high length to width to thickness ratio, and a few micrometers long. ZnO nanowires and nanorods grow in the [0001] direction as shown in figure 1.9; nanobelts, however, can show other growth directions, and will be described in the next subsection.
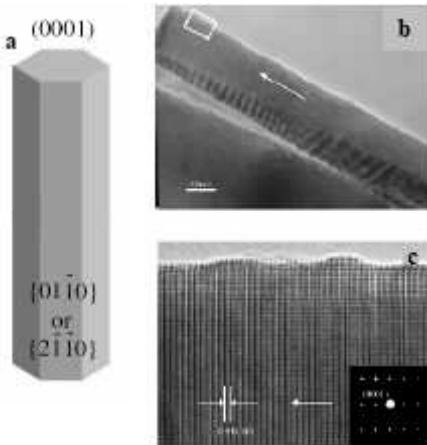
Figure 1.9: Growth direction of nanowires and nanorods. a) Schematic diagram of a typical ZnO nanostructure growing in the [0001] direction [25]. b) Low magnification Transmission Electron Microscopy (TEM) micrograph of a nanowire, and a c) high resolution TEM (HR-TEM) micrograph showing the growth direction spacing correspondig to the parameter c of WZ ZnO.

Without a doubt, ZnO nanowires and nanorods have been the most studied ZnO nanostructures because of their numerous potential applications. These nanostructures have been synthesized to characterize their properties as devices for applications in photodetectors [35], photodiodes[36], transistors [37], sensors [38,39], field emission [40], spintronics [41], actuators [1], transparent conductors [2], and piezoelectric generators [42-45].

The synthesis of high quality ZnO nanorods and nanowires has been achieved through various routes, such as laser ablation [46], organo-metallic chemical vapor deposition [47-50], electrodeposition [51,52], sputtering [53,54], sol-gel methods [55,36], through templates [46], spin coating [57], vapor-liquid-solid synthesis (VLS) [58-73], and solution based methods [74-80].

The most common method for the synthesis of ZnO nanostructures is VLS because of the large yield, and the high purity of the obtained samples. However, the yield of a pure ZnO nanowire sample is very sensitive to the experimental conditions. The VLS method consists in generating through heat, a zinc vapor under a controlled oxygen atmosphere. This mix is deposited through a carrier gas onto a substrate with a previously planted catalyst. Common sources of zinc are zinc powder and bulk ZnO powder with graphite, which reduces ZnO. The most used catalysts are gold, and tin, and are previously deposited on a substrate of Si, GaN, quartz, or sapphire. The synthesis temperature is usually above 1000°C, since Zn sublimes at 907°C.
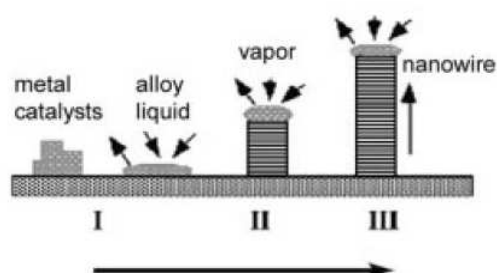

Figure 1.10: Growth mechanism for ZnO nanowires and nanorods grown by the VLS method proposed by Y. Xia et al. The zinc vapor and oxygen in the controlled atmosphere diffuse through metal catalyst in liquid phase forming the nanowire and pushing up the solid liquid interphase [81].

Y. Xia and coworkers have proposed a growth mechanism for VLS synthesis of nanorods or nanowires [81]. This mechanism is based on a bottom-up approach in which the precursors diffuse into the molten catalyst pushing up the liquid solid interface. Other methods are based on this same growth mechanism (see figure 1.10). For instance, the laser ablation method usually hits a zinc or zinc oxide target in an oxygen controlled atmosphere, generating a zinc vapor which is again deposited on a substrate with a catalyst [46]. Similarly, a catalyst can be deposited on a template which is then used for electrodeposition of ZnO, VLS reaction or chemical vapor deposition with organometallic compounds (*i.e.*, dietil zinc, zinc acetate or zinc acetyl-acetonate). These methods have several advantages: high crystallinity, aligned sample with the possibility of patterning by controlling the deposition of the catalyst.

Chemical methods have also been successful in the synthesis of ZnO nanostructures. These methods have been used extensively for the synthesis of nanoparticles. In this case the growth mechanism is usually mediated by nucleation through a reaction of a zinc salt and a base. Since the process is very slow and driven by precipitation of ZnO dimers, all faces grow uniformly and particles tend to agglomerate and coalescence is often observed. In order to avoid this, a capping agent that preferentially reacts with one specific face of ZnO is needed to grow one dimensional nanostructures. Although reactions take longer (more than 10 hours versus 2 or 3 hours for a VLS synthesis), these methods are very attractive because they are carried out at low temperatures (~100°C versus ~1000°C in VLS methods), and the quality of the samples is not compromised. Therefore, these methods seem to be highly scalable for many applications. This kind of synthesis is described in detail and explored in §2.
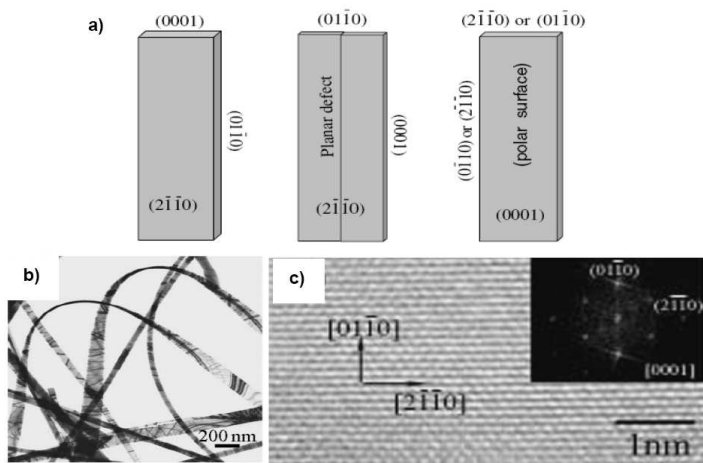
Figure 1.11: a) schematic diagram of the different growht directions and the resulting faces in ZnO nanobelts [25]. b) and c) show TEM micrographs at low and high resolution showing a nanobelt with a (0001) surface [82].

1.3.2. NANOBELTS

ZnO nanobelts grow with a dominant surface. This surface can be the (0001) or ($2\bar{1}\bar{1}0$). When grown in the [$01\bar{1}0$] direction (figure 1.11), with the large surface corresponding to the ($2\bar{1}\bar{1}0$) plane while the short direction corresponds to the (0001) plane, then this polar surface can cause a deformation of the structure forming the so-called ZnO nanohelixes or nanosprings [82].

The synthesis of these type of nanobelts is usually carried out through VLS. However, in contrast to nanowires, nanobelts generally grow without the need of a catalyst [82] (figure 1.12). In this case the precursor (zinc source) is evaporated in oxygen atmosphere such that small ZnO dimers are formed. These small clusters are driven by a carrier gas through a gradient of temperature. When the temperature is low enough, these small clusters or molecules are deposited on a
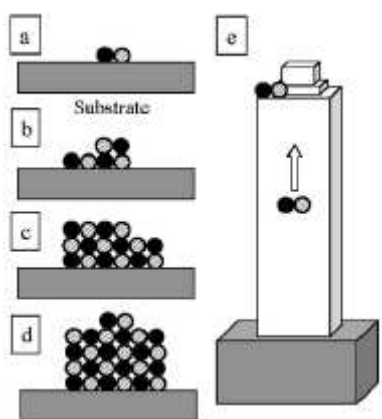
Figure 1.12: Schematic diagram of the growth mechanism for ZnO nanobelts proposed by Wang [82]. The ionic molecules tend to move and find a position where the electrostatic forces are minimized.

substrate. The charges due to the small ZnO polar molecules cause such an ordering that the coordination is preserved and the total net charge is zero. As new molecules arrive, they are pushed to the place where they minimize the unbalanced charge. Since the temperature is still high at these colder substrates (~600-800°C) the mobility of the molecules is large and no agglomeration is observed. Other methods for the synthesis of ZnO nanobelts have been tried, but have not been very successful.

The properties of nanobelts have been studied as a function of the size, observing interesting size effects. In particular the decrease of the width of nanoribbons has proved to be important in their optical properties, since there is a blue shift in the photoluminescence spectra [83]. Mechanical and thermal properties have also been probed, and there is a direct dependence of size and thermal conductivity [84]. On the other hand, theoretical work by Kulkarni and coworkers has shown that there can be a change in phase from WZ to HX when a nanobelt with {0001} faces is subject to high tension loads (~4.5GPa) [85]. This particular result is important for the work presented in §3.

1.4. Conclusions

ZnO is a wide band gap semiconductor that has attracted considerable attention of researchers from many disciplines because of the peculiar electronic, opto-electronic and mechanical properties which have been presented in this chapter. A large band gap of *c.a.* 3.4eV and an excitonic binding energy of 60meV make of ZnO a good candidate for photocatalytic processes, optoelectronic devices, solar cells, and transparent conductors [1,3]. When doped with some transition metals, or when synthesized as nanoparticles, ZnO could exhibit unusual magnetic properties. On top of this, ZnO is abundant in the Earth's surface and is an environmental- and bio- friendly material. Some of the structural, electronic and magnetic properties described in this chapter will be studied in detail in §3.

ZnO is also a unique material that combines semiconductor and piezoelectric properties with its biocompatibility and the ease of a low cost synthesis. This makes it an ideal candidate for applications dedicated to power nanoscale devices, *in-vivo* sensors, actuators, monitors, or drug delivers with remote control and wireless communication. These characteristics of ZnO are used in the work presented in §2.3.

1.5. REFERENCES

[1]. Nickel, N. H.; Terukov, E. *Zinc Oxide – A Material for Micro- and Optoelectronic Applications*. Springer, The Netherlands, 2005, Chapter 1.

[2]. Elmer, K.; Klein, A.; Rech, B. *Transparent Conductive Zinc Oxide: Basics and Applications in Thin Film Solar Cells*. Springer-Verlag Berlin Heidelberg 2008, Chapter 1.

[3]. Ozgur, U. et al. A comprehensive review of ZnO materials and devices. *J. Appl. Phys.* **98**, 041301-103 (2005).

[4]. Tasker, P.W. The stability of ionic crystal surfaces. *J. Phys. C: Solid State Phys.* **12**, 4977-4984 (1979).

[5]. Dulub, O., Boatner, L.A. & Diebold, U. STM study of the geometric and electronic structure of ZnO (0001)-Zn,(0001)-O,(1010), and (1120) surfaces. *Surf. Sci.* **519**, 201-217 (2002).

[6]. Wander, A. et al. Stability of Polar Oxide Surfaces. *Phys. Rev. Lett.* **86**, 3811 (2001).

[7]. Kresse, G., Dulub, O. & Diebold, U. Competing stabilization mechanism for the polar ZnO(0001)-Zn surface. *Phys. Rev. B* **68**, 245409 (2003).

[8]. Meyer, B. First-principles study of the polar O-terminated ZnO surface in thermodynamic equilibrium with oxygen and hydrogen. *Phys. Rev. B* **69**, 045416 (2004).

[9]. Dulub, O., Diebold, U. & Kresse, G. Novel Stabilization Mechanism on Polar Surfaces: ZnO(0001)-Zn. *Phys. Rev. Lett.* **90**, 016102 (2003).

[10]. Freeman, C.L., Claeyssens, F., Allan, N.L. & Harding, J.H. Graphitic Nanofilms as Precursors to Wurtzite Films: Theory. *Phys. Rev. Lett.* **96**, 066102-4 (2006).

[11]. Tusche, C., Meyerheim, H.L. & Kirschner, J. Observation of Depolarized ZnO(0001) Monolayers: Formation of Unreconstructed Planar Sheets. *Phys. Rev. Lett.* **99**, 026102-4 (2007).

[12]. Vesely, C.J., Hengehold, R.L. & Langer, D.W. uv Photoemission Measurements of the Upper d Levels in the IIB-VIA Compounds. *Phys. Rev. B* **5**, 2296 (1972).

[13]. Bloom, S. & Ortenburger, I. Pseudopotential Band Structure of ZnO. *Physica Status Solidi (b)* **58**, 561-566 (1973).

[14]. Ivanov, I. & Pollmann, J. Electronic structure of ideal and relaxed surfaces of ZnO: A prototype ionic wurtzite semiconductor and its surface properties. *Phys. Rev. B* **24**, 7275 (1981).

[15]. Vogel, D., Krüger, P. & Pollmann, J. Ab initio electronic-structure calculations for II-VI

semiconductors using self-interaction-corrected pseudopotentials. *Phys. Rev. B* **52**, R14316 (1995).

[16]. Janotti, A., Segev, D., & Van de Walle, C. G. Effects of cation d states on the structural and electronic properties of III-nitride and II-oxide wide-band-gap semiconductors. *Phys. Rev. B* **74**, 045202 (2006).

[17]. Zakharov, O., Rubio, A., Blase, X., Cohen, M.L. & Louie, S.G. Quasiparticle band structures of six II-VI compounds: ZnS, ZnSe, ZnTe, CdS, CdSe, and CdTe. *Phys. Rev. B* **50**, 10780 (1994).

[18]. Fuchs, F., Furthmuller, J., Bechstedt, F., Shishkin, M. & Kresse, G. Quasiparticle band structure based on a generalized Kohn-Sham scheme. *Phys. Rev. B* **76**, 115109-8 (2007).

[19]. Polla, D.L.; Francis, L. F. Processing and Characterization of Piezoelectric Materials and Integration into Microelectromechanical Systems. *Annu. Rev. Mater. Sci.* **28**, 563 (1998).

[20]. Hill, N. A.; Waghmare, U. First-principles study of strain-electronic interplay in ZnO: Stress and temperature dependence of the piezoelectric constants. *Phys. Rev. B* **62**, 8802 (2000).

[21]. Xiong, G., Pal, U. & Serrano, J.G. Correlations among size, defects, and photoluminescence in ZnO nanoparticles. *J. Appl. Phys.* **101**, 024317-6 (2007).

[22]. Viswanatha, R., Amenitsch, H., & Sarma, D. D. Growth Kinetics of ZnO Nanocrystals: A Few Surprises. *J. Am. Chem. Soc.* **129**, 4470 (2007).

[23]. Li, C., Guo, W., Kong, Y. & Gao, H. Size-dependent piezoelectricity in zinc oxide nanofilms from first-principles calculations. *Appl. Phys. Lett.* **90**, 033108-3 (2007).

[24]. Xiang, H. J., Yang, J., Hou, J. G., & Zhu, Q. Piezoelectricity in ZnO nanowires: A first-principles study. *Appl. Phys. Lett.* **89**, 223111 (2006).

[25]. Wang, Z. L. Zinc oxide nanostructures: growth, properties and applications. *J. Phys. Condens. Matter.* **16**, R829-R858 (2004).

[26]. Wen, J.G. et al. Self-assembly of semiconducting oxide nanowires, nanorods, and nanoribbons. Chem. Phys. Lett. **372**, 717-722 (2003).

[27]. Li, S.Y., Lee, C.Y. & Tseng, T.Y. Copper-catalyzed ZnO nanowires on silicon (1 0 0) grown by vapor-liquid-solid process. J. Cryst. Growth. **247**, 357-362 (2003).

[28]. Du, G.H., Xu, F., Yuan, Z.Y. & Van Tendeloo, G. Flowerlike ZnO nanocones and nanowires: Preparation, structure, and luminescence. Appl. Phys. Lett. **88**, 243101-3 (2006).

[29]. Ronning, C., Shang, N.G., Gerhards, I., Hofsass, H. & Seibt, M. Nucleation mechanism of the seed of tetrapod ZnO nanostructures. *J. Appl. Phys.* **98**, 034307 (2005).

[30]. Fan, H. J., Scholz, R., Kolb, F. M., & Zacharias, M. Two-dimensional dendritic ZnO nanowires from oxidation of Zn microcrystals. *Appl. Phys. Lett.* **85**, 4142 (2004)

[31]. Wang, R. M., Xing, Y. J., Xu, J., & Yu, D. P. Fabrication and microstructure analysis on zinc oxide nanotubes. *New Journ. Phys.* **5**, 115.1 (2003).

[32]. Wang, Z. L. Functional Oxide Nanobelts: Materials, properties and Potential Applications in Nanosystems and Biotechnology. *Annu. Rev. Phys. Chem.* **55**, 159 (2004).

[33]. Xu, C. X., Sun, X. W., Dong, Z. L., & Yu, M. B. Zinc oxide nanodisk. *Appl. Phys. Lett* **85**, 3878 (2004).

[34]. Gao, P. X., & Wang, Z. L. Mesoporous Polyhedral Cages and Shells Formed by Textured Self-Assembly of ZnO Nanocrystals. *J. Am. Chem. Soc.* **125**, 11299 (2003).

[35]. Law, J. B. K., & Thong J. T. L. Simple fabrication of a ZnO nanowire photodetector with a fast photoresponse time. *Appl. Phys. Lett.* **88**, 133114 (2006).

[36]. Huang, M. H., Mao, S., Feick, H., Yan, H., Wu, Y., Kind, H., Weber, E., Russo, R., & Yang P. Room Temperature Ultraviolet Nanowire Nanolasers. *Science* **292**, 1897 (2001).

[37]. Fan, Z., & Lu, J.G. Chemical Sensing with ZnO Nanowire Field-Effect Transistor. *IEEE Trans. Nanotech.* **5**, 393 (2006).

[38]. Al-Hilli, S. M., Al-Mofarji, R. T., & Willander, M. Zinc oxide nanorod for intracellular pH sensing. *Appl. Phys. Lett.* **89**, 173119 (2006).

[39]. Wei, A., Sun, X. W., Wang, J. X., Lei, Y., Cai, X. P., Li, C. M., Dong, Z. L., Huang, W. Enzymatic glucose biosensor based on ZnO nanorod array grown by hydrothermal decomposition. *Appl. Phys. Lett.* **89**, 123902 (2006).

[40]. Jo, S. H., Lao, J. Y., Ren, Z. F., Farrer, R. A., Baldacchini, T., & Fourkas, T. Field-emission studies on thin films of zinc oxide nanowires. *Appl. Phys. Lett.* **83**, 4821 (2003).

[41]. Pearton, S. J., Norton, K. P., Heo, Y. W., Tien, L. C., Ivill, M. P., Li, Y., Kang, B. S., Ren, F., Kelly, J., & Hebard, A. F.. ZnO Spintronics and Nanowire Devices. *J. Elect. Mater.* **35**, 862 (2006).

[42]. Zhao, M. H., Wang, Z. L., & Mao, S. X. Piezoelectric Characterization of Individual Zinc Oxide Nanobelt Probed by Peizoresponse Force Microscope. *Nano Lett.* **4**, 587 (2004).

[43]. Wang, X., Song, J., Liu, J., Wang, Z. L. Direct Current Nanogenerator Driven by Ultrasonic Waves. *Science* **316**, 102 (2007).

[44]. Gao, P. X., Song, J., Liu, J., Wang, Z. L. Nanowire Piezoelectric Nanogenerators on Plastic Substrates as Flexible Power Sources for Nanodevices. *Adv. Mater.* **19**, 67 (2007).

[45]. Fan, Z., Dutta, D., Chien, C. J., Chen, H. Y., Brown, E. C., Chang, P. C., & Lu, J. G. Electrical and photoconductive properties of vertical ZnO nanowires in high density arrays. *Appl. Phys Lett.* **89**, 213110 (2006).

[46]. Zhang, G., Nakamura, A., Aoki, T., Temmyo, J., & Matsui, Y. Au-assisted growth approach for vertically aligned ZnO nanowires on Si Substrate. *Appl. Phys. Lett.* **89**, 113112 (2006).

[47]. Liu, J. J., Yu, M. H., & Zhou, W. L. Fabrication of Mn-doped ZnO diluted magnetic semiconductor nanostructures by chemical vapor deposition. *J. Appl. Phys.* **99**, 08M119 (2006).

[48]. Park,W., Yi, G. C., Kim, M., & Pennycook, S. ZnO Nanoneedles Grown Vertically on Si Substrates by Non-Catalytic Vapor-Phase Epitaxy. *Adv. Mater.* **14**, 1841 (2002).

[49]. Muthukumar, S., Sheng, H., Zhong, J., & Emanetoglu, N. W. Selective MOCVD Growth of ZnO Nanotips. *IEEE Trans. Nanotech.* **2**, 50 (2003).

[50]. Cui, J., Gibson, U. Termal modification of magnetism in cobalt-doped ZnO nanowires grown at low temperatures. *Phys. Rev. B.* **74**, 045416 (2006).

[51]. Cui, J., Zheng, Q., & Gibson, U. Synthesis and magnetic properties of Co-doped ZnO nanowires. *J Appl. Phys.* **99**, 08M113 (2006).

[52]. Pauporté, T., Lincot, D., Ciana, B., & Pellé, D. Toward laser emisión of epitaxial nanorod

arrays of ZnO grown by electrodeposition. *Appl. Phys. Lett* **89**, 233113 (2006).

[53]. Shin, J. W., Lee, J. Y., Kim, T. W., No, Y. S., Cho, W. J., & Choi, W. K. Growth mechanisms of thin-film columnar structures in zinc oxide on p-type silicon substrates. *Appl. Phys. Lett.* **88**, 091911 (2006).

[54]. Kwon, S. J., Park, J. G. Theoretical analysis of growth of ZnO nanorods on the amorphous surfaces. *J. Chem. Phys.* **122**, 214714 (2005).

[55]. Chen, Y. W., Liu, Y. C., Lu, S. X., Xu, C. S., Shao, C. L., Wang, C., Zhang, J. Y., Lu, Y. M., Shen, D. Z., & Fan X. W. Optical properties of ZnO and ZnO:In nanorods assembled by sol-gel method. *J. Chem. Phys.* **123**, 134701 (2005).

[56]. Pradhan, B., Batabyal, S., & Pal, A. J. Rectifying junction in a single ZnO vertical nanowire. *Appl. Phys. Lett.* **89**, 233109 (2006).

[57]. Fan, H.J., et al. Patterned growth of aligned ZnO nanowire arrays on sapphire and GaN layers. *Superlatt. Microstruct.* **36**, 95 2004

[58]. Dai, Y., Zhang, Y., Bai, Y.Q., & Wang, Z.L. Bicrystalline zinc oxide nanowires. *Chem. Phys. Lett.* **375**, 96 (2003)

[59]. Kouklin, N. & Sen, S. Towards controlled manipulation and assembly of ZnO nanowires for nanoscale imaging applications. *Appl. Phys. Lett.* **89**, 123114 (2006).

[60]. Zhao, Q., et al. Enhanced field emission from ZnO nanorods via thermal annealing in oxygen. *Appl. Phys. Lett.* **88**, 033102 (2006).

[61]. Hoffmann, S., et al.Fracture strength and Young's modulus of ZnO nanowires. ArXiv: cond-mat/0611409

[62]. JrH He, CS Lao, LJ Chen, D Davidovic, ZL Wang. Large-Scale Ni-Doped ZnO Nanowire Arrays and Electrical and Optical Properties. *J. Am. Chem. Soc.* **127**, 16376 (2005).

[63]. Ding, Y., Gao, P.X., & Wang, Z.L. Catalyst-Nanostructure Interfacial Lattice Mismatch in Determining the Shape of VLS Grown Nanowires and Nanobelts: A Case of Sn/ZnO. *J. Am. Chem. Soc.* **126**, 2066 (2004).

[64]. Hsu, H.C., et al. Luminescence of selective area growth of epitaxial ZnO nanowires and random-growth-oriented nanobelts. *Nanotechnol.* **17**, 1404 (2006).

[65]. Li, Y., et al. Au-catalized growth processes and luminescence properties of ZnO nanopillars on Si. *J. Appl. Phys.* **99**, 054307 (2006).

[66]. Wang, D., et al. Effects of postgrowth annealing treatment on the photoluminescence of zinc oxide nanorods. *J. Appl. Phys.* **99**, 113509 (2006).

[67]. Wen, J.G., et al. Self-assembly of semiconducting oxide nanowires, nanorods, and nanoribbons. *Chem. Phys. Lett.* **372**, 717 (2003).

[68]. Shalish, I., Temkin, H., & Narayanamurti, V. Size-dependent surface luminescence in ZnO nanowires. *Phys. Rev. B* **69**, 245401 (2004).

[69]. Song, J., Wang, X., Riedo, E., Wang, Z.L. Systematic Study on Experimental Conditions for Large- Scale Growth of Aligned ZnO Nanowires on Nitrides. *J Phys. Chem. Lett. B.* **109**, 9869 (2005).

[70]. Huang, M.H., et al. Room- Temperature Ultraviolet Nanowire Nanolasers. *Science* **292**,

1897 (2001).

[71]. Gao, P.X., Ding, Y., & Wang, Z.L. Crystallographic Orientation-Aligned ZnO Nanorods Grown by a Tin Catalyst. *Nano Lett.* **3**, 1315 (2003).

[72]. HJ Fan, et al. Self-assembly of ZnO nanowires and the spatial resolved characterization of their luminescence. *Nanotechnol.* **15**, 1401 (2004).

[73]. Chang, P.C, et al. ZnO. Nanowires Synthesized by Vapor Trapping CVD Method. *Chem. Mater* **16**, 5133 (2004).

[74]. Chang, C.Y.,et al. Electroluminescence from ZnO nanowire/polymer composite p-n junction. *Appl. Phys. Lett.* **88**, 173503 (2006).

[75]. Kim, Y.J., et al. Controlled selective growth of ZnO nanorod and microrod arrays on Si substrates by wet chemical method. *Appl. Phys. Lett.* **89**, 163128 (2006).

[76]. Cheng, B. & Samulski, E.T. Hydrothermal synthesis of one-dimensional ZnO nanostructures with different aspect ratios. *Chem. Comm.* **2004**, 986 (2004).

[77]. Hirano, S., et al. Room-temperature nanowire ultraviolet lasers: An aqueous pathway for zinc oxide nanowires with low defect density. *J. Appl. Phys.* **98**, 094305 (2005).

[78]. Lv, Y., Guo, L., Xu, H., Ding, L., Yang, C., Wang, J., Ge, W., Yang, S., & Wu, Z. Low temperature synthesis and optical properties of small-diameter ZnO nanorods. *J Appl. Phys.* **99**, 114302 (2006).

[79]. Govender, K., Boyle, D.S., O'Brien, P., Binks, D., West, D., & Coleman, D. Room-Temperature Lasing Observed from ZnO Nanocolumns Grown by Aqueous Solution Deposition. *Adv. Mater.* **14**, 1221 (2002).

[80]. Hsu, J.W.P., Tallant, D.R., Simpson, R.L., Missert, N.A., & Copeland R.G. Luminescent properties of soluition-grown ZnO nanorods. *Appl. Phys. Lett.* **88**, 252103 (2006).

[81]. Xia, Y. One-Dimensional Nanostructures: Synthesis, Characterization, and Applications. *Adv. Mater.* **15**, 353 (2003).

[82]. Wang, Z.L. Functional Oxide Nanobelts: Materials, Properties and Potential Applications in Nanosystems and Biotechnology. *Ann. Rev. Phys. Chem.* **55**, 159 (2004).

[83]. Wang, X., Ding, Y., Summers, C.J., & Wang, Z.L. Large-Scale Synthesis of Six-Nanometer-Wide ZnO Nanobelts. J. Phys. Chem. B. **108**, 8773 (2004).

[84]. Kulkarni, A.J. & Zhou, M. Size-dependent thermal conductivity of zinc oxide nanobelts. *Appl. Phys. Lett.* **88**, 141921 (2006).

[85]. Kulkarni, A.J., Zhou, M., Sarasamak, K., & Limpijumnong, S. Novel Phase Transformation in ZnO Nanowires under Tensile Loading. *Phys. Rev. Lett.* **97**, 105502 (2006).

Chapter 2

Synthesis And Applications Of ZnO Nanostructures

CONTENTS

2.1. Introduction

As described in §1.3, there have been several synthesis methods for the production of ZnO nanostructures. Some of these approaches are very clean processes, with low cost materials and innocuous by-products, while keeping the quality of the material. One of such processes has been developed during this work and is described in §2.2.

Of particular interest in this work has been the use of ZnO nanostructures in energy scavenging devices. In other words, the piezoelectric effect of ZnO and residual mechanical energy to power small devices in places where it is difficult to receive power from the grid, the sun, or even from batteries. The simple, low cost and scalable method presented in §2.2 was then used to produce a ZnO-cellulose composite. The composite was then used as main component of a piezoelectric and pyroelectric nanogenerator which could also be used as a sensor. The resulting device showed similar efficiency at a significantly lower cost and effort than similar contemporary devices. The characterization and results of this nanocomposite are presented in §2.3.

We believe this work will contribute to the development of ZnO as a key material for energy harvesting devices. The challenges of energy we face are huge, and increase continuously; thus, further understanding of the materials and mechanisms involved in energy generation are important for the development of our society.

2.2. Synthesis and characterization of ZnO nanorods

The synthesis and growth methods of nanostructured ZnO can be classified according to the temperature of the synthesis. The high temperature processes often yields long nanowires and nanobelts and samples with low homogeneity [1]. As mentioned before, these synthesis methods heat a zinc source or zinc oxide with a reducing agent, and collect the sample in plates, where a catalyst is placed. The range of temperatures is greater than 1000°C, and is considered as a high cost process. On the other hand, the low temperature methods produce small nanoparticles and nanorods with high homogeneity when purified. These processes are based on the hydrolysis of zinc salts in basic alcohol solutions. The

temperatures of reaction are usually *c.a.* 80°C, and thus, constitute a low cost synthesis. Another low temperature method is electrodeposition on templates. In this case, a hard template (commonly anodized alumina or polycarbonate membranes with diameter < 200nm) is put on top of the collecting electrode of an electrolytic cell. The nanowires are formed on the pores of the templates with high homogeneity in terms of both diameter and length.

Solution methods for the synthesis of crystalline semiconductor nanoparticles have been widely used, mainly because these are processes carried out at low temperature, with low cost and have a high yield. Koch et al. [2], Bahnemann *et al.* [3], and Haase *et al.* [4] first used the colloidal method to prepare ZnO nanoparticles by hydrolyzing zinc salts in basic alcoholic solutions. Usually, the synthesis of ZnO nanostructures through the solution route is carried out in alcohol (methanol, ethanol, or propanol) with a strong base (NaOH, LiOH or KOH) as the oxygen source and a zinc salt (zinc acetate, $Zn(CH_3CO_2)_2$, zinc bromide, $ZnBr_2$, zinc perchlorate, $Zn(ClO_4)_2$, or zinc nitrate, $Zn(NO_3)_2$). The nucleation of the metal oxide is fairly well understood, and it occurs by precipitation, involving the reaction of the soluble metal salt with the hydroxide ions or water, such that:

$$MX_2 + 2YOH \rightarrow MO(s) + 2Y^+ + 2X^- + H_2O \ ,$$
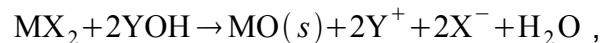
where X represents the anion and Y corresponds to the hydroxide cation (Na^+, etc.) [5].

However, the mechanism by which the nanoparticles grow after nucleation is still unclear. Trying to address this problem, some groups have studied the effect of the anion, the Zn-OH concentrations, the alcohol, along with the temperature and reactant concentrations. However, accurate investigations of these systems are more complicated than expected. The problem has been the absence of appropriate techniques to probe the *in-situ* growth of nanocrystals. While transmission electron microscopy (TEM) is the most direct probe to observe the size and morphology of any sample, it is not possible to carry out the measurement under reaction conditions. Also, the nanocrystals tend to agglomerate on the grid and present low contrast, making the determination of size of individual particles very difficult. Therefore, indirect methods have been used to investigate the growth process of nanoparticles. The measurement of the shift in absorption emission compared to that for bulk samples has been used extensively to understand the

growth, specially the UV-absorption spectra, where the surface states do not contribute. The size of the nanocrystal is determined from the shift in the absorption edge using the effective mass model. However, this approximation cannot be used for nanoparticles larger than the Bohr exciton diameter (~4nm). Some groups have used small angle X-ray scattering measurements which are directly related to the size and crystallinity of the sample to corroborate the diameter measurements having a positive result.

Hu and coworkers investigated the role of the zinc source on the growth of nanoparticles [5]. They used different zinc salts with NaOH as the oxygen source and probed with different temperatures. They found that ZnO nanoparticles synthesized from $Zn(ClO_4)_2$ grow faster, followed by zinc acetate and finally by zinc bromide. They argued that this is because halide ions adsorb more strongly on surfaces than acetate ions, and perchlorate ions exhibit very weak surface interactions.

Viswanatha and coworkers have made an extensive study of the growth kinetics of ZnO nanoparticles with NaOH as the oxygen source and zinc acetate as the zinc source [6]. They found that NaOH not only is a source of hydroxyl ions, but also provides the counter ion Na+ which acts as a capping agent. When concentrations are higher than 0.35mmol of NaOH in the synthesis, the growth of ZnO nanoparticles is inhibited. Therefore, the growth of ZnO nanoparticles is not only diffusion limited, but also the role of the reactants is important.

Hu and coworkers also investigate the growth of ZnO nanoparticles by reaction with water, without the use of any alcohol [7]. According to them, the incorporation of ions (Na^+, K^+) results in recombination centers, which affect negatively the optical response of the sample. Therefore, they suggest that the use of water as reactant is desirable for the synthesis of nanoparticles for optical applications. They study the effect of H_2O concentration on isopropanol on the growth rate of ZnO nanocrystals. The rate increases as the amount of H_2O increases. However, this rate is always smaller than that observed when NaOH is used. The nucleation process is also slower, taking between 30-60min to take place, whereas for the case of NaOH is almost instantaneous.

Solution based techniques have also been used to grow zinc oxide nanostructures with controlled aspect ratio, *i.e.*, nanorods. The use of a surfactant

with affinity to certain surfaces reduces the growth in the corresponding directions. In particular, Yang and coworkers use polyvinyl pyrrolidone (PVP) which passivates the {1010} surfaces, resulting in a growth velocity of [0001] direction larger than other directions [8].

S. P. García and coworkers also studied the effect of passivating surfaces on the growth of ZnO nanostructures with different surfactants [9]. They used sodium poly(styrene sulfonate) (PSS), poly(diallyldimethylammonium chloride) (PDADMAC) and trisodium citrate in solution synthesis with zinc nitrate as the zinc source and NaOH and H_2O as the oxygen sources in methanol. They show that in all cases, high concentrations of the surfactants decreases the aspect ratio, although is much faster for the citrate, followed by PSS and slower for PDADMAC.

In order to contribute to the advance of the understanding of the growth process, the reproduction of the most interesting experiments found in the literature was attempted. Here, an optimization of the parameters of the experiment was carried out.

The synthesis method was based on that reported by Yang and coworkers [8]. As stated before, the method consists on the hydrolysis of a zinc salt in the presence of PVP. In a first experiment, PVP (1.25g) was added to absolute ethanol (etOH) (60 ml) and magnetically stirred for 20 mins. Then, 0.25g zinc acetate ($Zn(AcO)_2$) was slowly added to the EtOH solution while heating the solution to 50ºC while still stirring. After the solution was completely clear, 1.5g NaOH was added and was stirred for another 30 min. Finally, the solution was heated for 24hrs at 75ºC. For washing the resulting solution, the solvent (brownish color) was extracted with a pipette to get ~5ml. Clean EtOH was added to the solution (~60ml), stirred and left until the precipitates appeared (~2hrs later). The solvent was removed using a pipette, and again clean ethanol was added, stirred and left to rest until precipitates appeared. In the third cleaning cycle, the solvent extracted was kept and considered as residues. The precipitates were mixed with 20ml EtOH and stored.

From this procedure, five main variables were identified:

- PVP concentration
- NaOH concentration
- Zn(AcO)2 concentration
- Temperature

- Time

Since the reaction involves the salt, the basic solution, and the basic agent, the concentrations of the different reagents can be varied relative to one of the compounds. In this case, we fixed the concentration of Zn(AcO)$_2$. Also, we noted that the temperature could not be increased, since 74.5°C was the observed boiling temperature of the solution. Therefore, we could only change three of the variables. In order to understand the effect of each of these variables, and their correlation, a set of experiments was carried out in which all of the variables were varied as in a 2^k experimental design. The experiments are summarized in the table 2.1.

Label	Time (h)	PVP (g)	NaOH (g)
0000	25	1.0	1.0
0001	25	1.0	1.5
0010	25	1.25	1.0
0011	25	1.25	1.5
0100	50	1.0	1.0
0101	50	1.0	1.5
0110	50	1.25	1.0
0111	50	1.25	1.5

Table 2.1. Summary of the parameters of the experiments carried out to determine the optimal conditions and the effect of the different variables in the growth of ZnO nanorods.

For the evaluation of each of the samples, scanning electron micrographs were acquired and the diameter and length of the nanorods were measured using a graphics editor. Around a hundred rods were measured for diameter distribution from at least 5 different scanning electron micrographs. As can be noted from figure 2.1, the length of most of the specimens cannot be appreciated, due to the agglomeration of the nanorods; therefore only 50 measurements were made for the length. The results are summarized in table 2.2.

The effect of each of these variables can be evaluated by taking the average of each parameter (diameter and length) from the different runs using each variable. For example, the effect of the increase of PVP concentration (E_{PVP}) on the diameter is the sum of average of the four runs using large concentration of PVP minus the average of the four runs using low concentration of PVP. Namely,

$$E_{PVP} = \frac{\left(d_{0001} + d_{0011} + d_{0101} + d_{0111}\right)}{4} - \frac{\left(d_{0000} + d_{0010} + d_{0100} + d_{0110}\right)}{4} = -1.33$$

Sample	Diameter			Length			
	Average (nm)	Variance (nm)^2	Std. Dev. (nm)	Average (nm)	Variance (nm)^2	Std. Dev. (nm)	Av. Aspect Ratio
0000	21.38	59.78	7.73	291.22	60490.76	245.95	13.62
0001	20.44	23.56	4.85	217.22	27118.89	164.68	10.63
0010	18.27	18.79	4.33	168.08	10539	102.66	9.2
0011	19.56	15.99	4	200.34	12518.03	111.88	10.24
0100	20.73	102.77	10.14	297.32	49167.23	221.74	14.35
0101	18.18	13.73	3.7	330.63	62525.83	250.05	18.19
0110	20.53	31.87	5.65	322.41	41833.06	204.53	15.7
0111	17.39	17.05	4.13	199.57	14796.67	121.64	11.47

Table 2.2. Results of the variation of the different parameters in the distribution of length and diameters of ZnO nanorods grown through the solvothermal method.
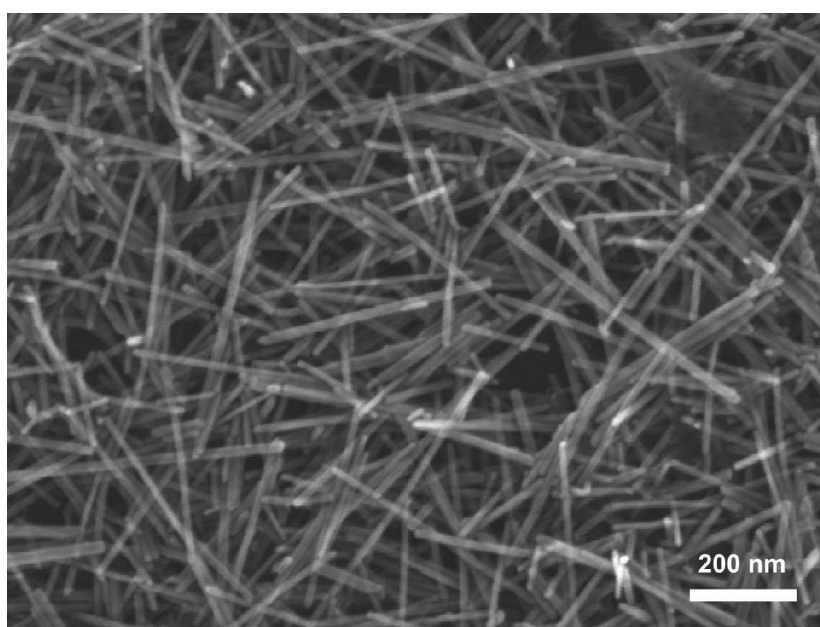

Figure 2.1: Scanning Electron Microscopy (SEM) of the typical synthesized ZnO nanorods (sample 0101) showing a high yield and homogeneity.

Therefore, the effect of increasing the concentration of PVP leads to a slight decrease of diameter. Also, if we take the effect of the PVP concentration on the standard deviation of the diameter (σE_{PVP}) we get a value of σE_{PVP}=-2.79, which means that the increase of the concentration of PVP not only reduces slightly the diameter of the rods, but also, reduces the standard deviation in the distribution of diameters, which is also very important for a good control. The summary of the effects of the different variables are summarized on table 2.3.

	Diameter		Length		
	Average	Std. Dev.	Average	Std. Dev.	Av. Aspect Ratio
E_{PVP}	-1.33	-2.79	-32.82	-31.66	-0.58
E_{NaOH}	-1.24	-2.08	-61.5	-85.42	-2.54
E_T	-0.71	0.67	68.27	43.2	4.01

Table 2.3. Effect of the different variables on the diameter, length and their distribution of the ZnO nanorods.
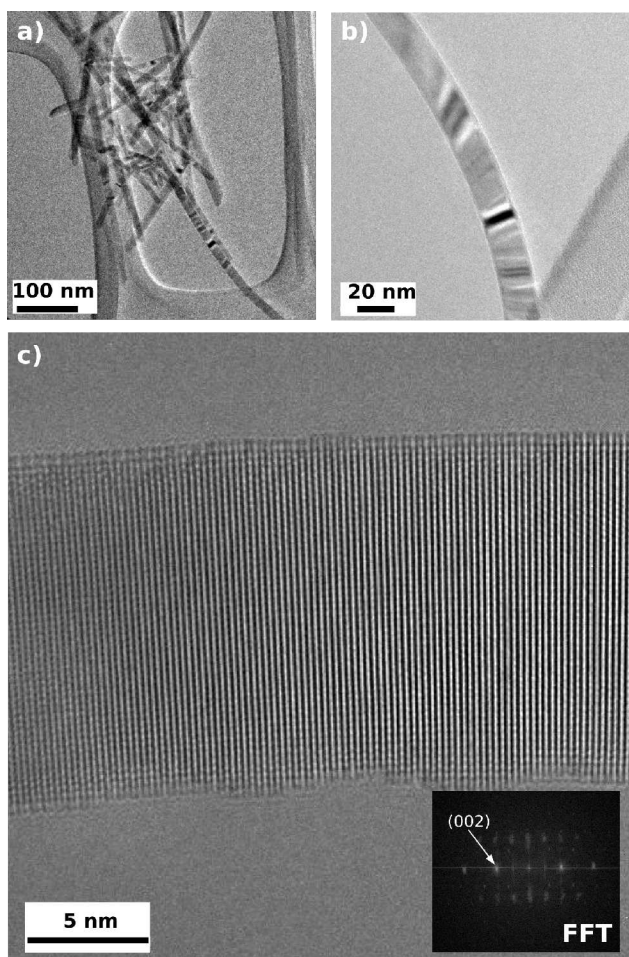
Figure 2.2: TEM images of the synthesized nanorods at low and high magnification. a) Low magnification image showing a good diameter dispersion of the nanorods. b) Fringes in a single nanorod due to strain in the lattice. c) High magnification image of a nanorod. The micrographs show that even though this is a low temperature method, the samples are very crystalline and show little amount of defects. The samples were not heat treated.

From table 2.3, we note that the effect of the increase in PVP concentration is to

reduce the diameter, its standard deviation, and also reduce the length of the nanorods. In the case of the NaOH, the effect is similar, but the reduction of the diameter is less and the decrease of the length is pronounced. The effect of time is negligible in the diameter and in the length, and thus in the aspect ratio. From these data, it can be concluded that the best sample would be achieved with increased concentrations of PVP, low concentrations of NaOH and longer times. In this case, the best sample would be the one labeled as 0101.

Figure 2.2 shows that the samples are highly crystalline and are grown in the [0001] direction. From the high resolution TEM image (figure 2.2c) it can be seen that there is some surface reconstruction. This kind of reconstructions might be due to the doping with hydrogen due to the synthesis methods, and could have some effect on the optical properties of the resulting material, but little effect on the mechanical properties. This method has been proved to yield very high quality nanostructures and is the basis of the method used for the synthesis of a nanocomposite material in §2.3 for energy scavenging taking advantage of the piezoelectric and pyroelectric properties of ZnO.

2.3. Synthesis and properties of a novel ZnO-paper nanocomposite

The growing need for renewable alternative sources of energy has motivated significant effort to develop new forms of energy conversion and storage devices for portable and wearable electronic devices [10]. The most attractive feature of such devices is their capability of capturing various forms of ambient energy surrounding a system (*e.g.* vibrations, thermal, flowing water, wind, human motion, shock waves, thermal gradient, temporal thermal fluctuations) and provide electrical power to devices making them independent of external power source [11]. The ambient energy is mostly in the form of mechanical and thermal energy [11] and their conversion into electrical energy could play a key role in developing remote access electronic devices, self-powered sensors or implantable medical devices. Recently, pyroelectric and piezoelectric materials have been devised as potential candidates for building scavenging (collect from residues) devices. In this section, we evaluate and describe a scavenging device based on ZnO nanostructures.

2.3.1. PYROELECTRIC AND PIEZOELECTRIC HARVESTING DEVICES

In 1960 the discovery of ZnO as a good piezoelectric material led to the first electronic application of zinc oxide as a thin layer for surface acoustic wave devices [12,13]. This piezoelectricity is caused by the polarity of ZnO, *i.e.,* the absence of inversion symmetry in this crystal lattice (see §1.2.2.3). Any displacement of the ions would result in a dipole which leads to spontaneous polarization (see figure 1.6). This displacement can be created through a mechanical strain (piezoelectric effect) or through an inhomogeneous thermal dilatation due to a thermal gradient and the thermal anisotropy of the system (pyroelectric effect). The combination of this spontaneous polarization and the low mobility of charges at zero bias results in a piezoelectric behavior with relevant piezoelectric constants d_{33}=12 pm/V, or e_{33}= 1.2C/m^2, e_{31}=-0.5C/m^2, e_{15}=-0.40C/m^2 (for example d_{33}=2.3, and d_{33}=117 pm/V for quartz and PZT, respectively) [14, 15].

Thermal energy in the environment is a potential source of energy for low power electronics. This energy can be converted into electrical energy based on thermoelectric modules due to the Seebeck effect, or to thermal expansion of the crystal lattice (pyroelectric effect) [16]. Some commercial products like wristwatches already work at the expense of thermoelectric modules that generate enough power to run their mechanical components [17]. However, thermoelectric modules find applications only in very specific cases, because of their limited efficiency. This efficiency is usually measured by the dimensionless parameter ZT, which is a function of the Seebeck coefficient or thermoelectric power, and of the electrical and thermal conductivities [18]. In an ideal scavenging device, the thermal energy would come as temporal temperature fluctuation in ambient environment due to residual or waste heat, as opposed to a constant thermal gradient. Therefore, harvesting energy from temporal temperature fluctuation rather than spatial temperature gradients would be a more useful and potential approach for future research [18].

Both mechanical and thermal energy can be harvested using piezoelectric materials. Several types of piezoelectric materials such as ceramics (lead zirconium titanate and barium titanate), polymers (poly vinylidene fluoride) and macro fiber composites have been successfully used for harvesting thermal as well as mechanical energy [14,16-18]. Ferroelectric ceramic/polymer composites have also been used for piezoelectric and pyroelectric sensor applications as the

composites can combine the mechanical compliance and flexibility of polymers with the high piezoelectric and pyroelectric properties of ceramics [16].

### 2.3.2. ZnO AS A PIEZOELECTRIC AND PYROELECTRIC DEVICE

ZnO is a unique material that combines semiconductor and piezoelectric properties [12,13] and the ease of low cost manufacturing. This makes it an ideal candidate for energy harvesting applications [19-22]. The piezoelectric and pyroelectric properties of both bulk and nanostructured ZnO have been thoroughly studied [15,23,24]. Recently, Wang and coworkers have developed aligned arrays of ZnO nanowires by a VLS process on GaN and sapphire substrates and have utilized them for energy generation based on the deflection/vibration of the nanowires [20-22]. In all these systems, the fabrication procedure involves multi step material processing and a difficult device assembly using precise manipulators, making it challenging for scalability and cost. Another drawback of such approaches is their limitation of harvesting energy only from mechanical excitations. Even though these reports have made significant contributions and set benchmarks, it is important to explore innovative, inexpensive, scalable technologies based on new materials and engineering approaches wherein a single device can be used to transform more than one form of ambient energy (e. g. mechanical and thermal).

2.3.3. ZnO – CELLULOSE COMPOSITE

An interesting scaffold material that could be used in designing an energy harvesting device is cellulose (main component of common paper) since it combines many attributes such as low cost, light-weight, abundance, eco-friendliness and availability [25-27]. Recent work shows the use of this material in making flexible energy storage devices such as batteries and supercapacitors [28].

Here we will demonstrate a simple procedure for the synthesis of a ZnO nanostructure-embedded cellulose film (ZnO-cellulose nanocomposite, hitherto called as the piezo-paper). This is achieved using a scalable, low cost, low temperature solvothermal method as the one described in the previous section. The piezo-paper is used as an energy harvesting device and the performance is analyzed. The efficiency of this piezo-paper generator is evaluated and compared to the devices reported so far using VLS grown nanowire generators.

(a)

(b)

(c)
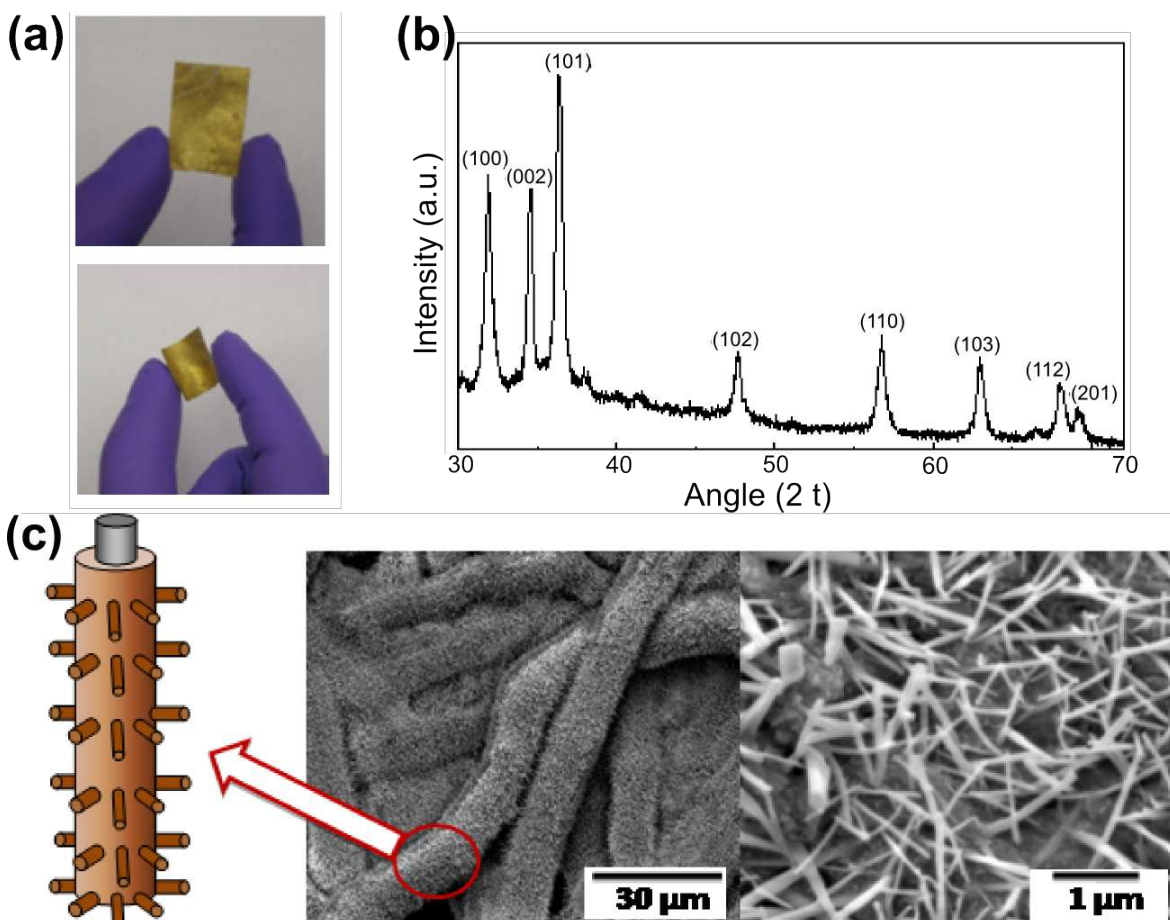
Figure 2.3: (a) Photographs of the piezo-paper demonstrating mechanical flexibility. (b) Powder X-ray diffraction spectrum of the ZnO coated paper composite. The peaks correspond to ZnO WZ structure, and confirm the crystallinity of the growth film and nanowires. (c) SEM images of ZnO coated paper at different magnification and a schematic diagram of the composite fibers.

The synthesis of the piezo-paper is carried out as follows: a 70mm diameter 0.47mm thick Whatman Grade No. 1 Filter Paper is soaked drop wise several times with solutions of zinc acetate and sodium hydroxide at 60°C alternately, with drying periods in between. It is clear that this method is similar to the synthesis presented in the previous section. However, in this case a thin layer of ZnO nanoparticles is first deposited on the surface of the micrometric cellulose fibers.

Thermo-gravimetric analysis was carried out on plain paper and ZnO embedded paper yielded ~36% (weight percent) ZnO in the paper (figure 2.3). X-ray diffraction is used to confirm the structure of the ZnO phase present in the paper. Figure 2.3b shows the XRD spectra of the ZnO coated paper revealing the ZnO Wurtzite structure. Morphology and chemical composition of the ZnO coated paper was observed by scanning electron microscopy (figure 2.3c). The ZnO nanorods formed

45

during synthesis coated uniformly the cellulose fibers and have typical diameters in the range of 40-100 nm and lengths between 500-1000 nm. These ZnO nanorods are notably larger in diameter than the ZnO nanorods presented in the previous section. However, it is important to note that in this case there is no capping agent (PVP) to stop the growth in all directions. The 1D growth in this case is dictated by the exposed faces of the ZnO nanoparticles initially deposited onto the cellulose fibers. The low and high magnification images shown in figure 2.3c clearly reveal the uniform coating on the paper over large areas of the filter paper.

2.3.4. PIEZOELECTRIC RESPONSE

For the fabrication of the devices, gold was sputtered over both sides of the paper until getting a ~500nm continuous film. A small piece (1.0✕1.0 cm^2) of the Au coated piezo-paper was placed between two copper current collectors and laminated with a commercial ID-card laminating sleeve for isolation from the environment. The photograph of a typical piezo-paper device is shown in figure 2.4. The same procedure was repeated for the paper without ZnO, as control.

The current and voltage response of the devices were measured with a Keithley source meter and DAS1414 intelligent data acquisition system with a gain/input range of ±0.1V. The typical I-V curves of the resulting device and plain paper are shown in figure 2.5. The characteristic I-V curve of plain paper shows a typical insulating behavior (black curve). The different response between forward and reverse bias of ZnO paper is an indication of good Schottky contact (red curve). The electrical behavior is in good agreement with previous reports which indicate that the Au-ZnO system forms a Schottky junction [22], which is very important for the performance of the energy generator device.
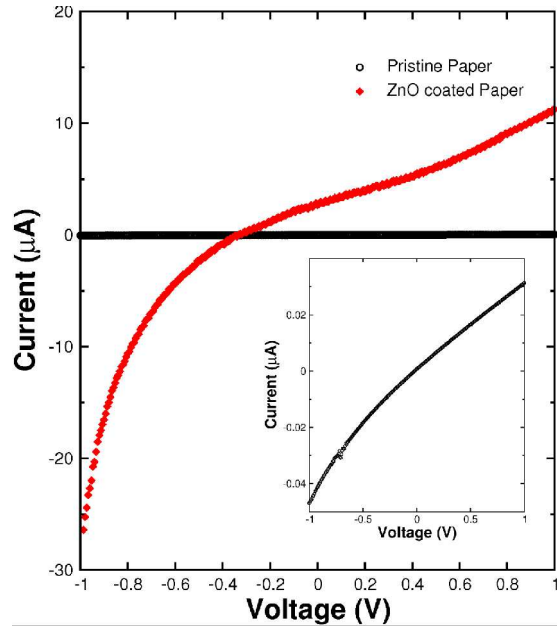
Before any response measurement, and for all the devices presented here, the I-V curve was taken to verify good Schottky diode behavior and to align the otherwise randomly polarized domains in the material. These devices were short circuited for half an hour to avoid any residual charge accumulated in the devices

Figure 2.4: Photograph of the gold coated piezo-paper placed between two copper foils for current collection.

due to polling. Despite of this, we always observed a decaying background current when measuring due to the internal capacitance of the device. Measurements were taken under both polarities to rule out any possible artifact caused by the measurement setup.
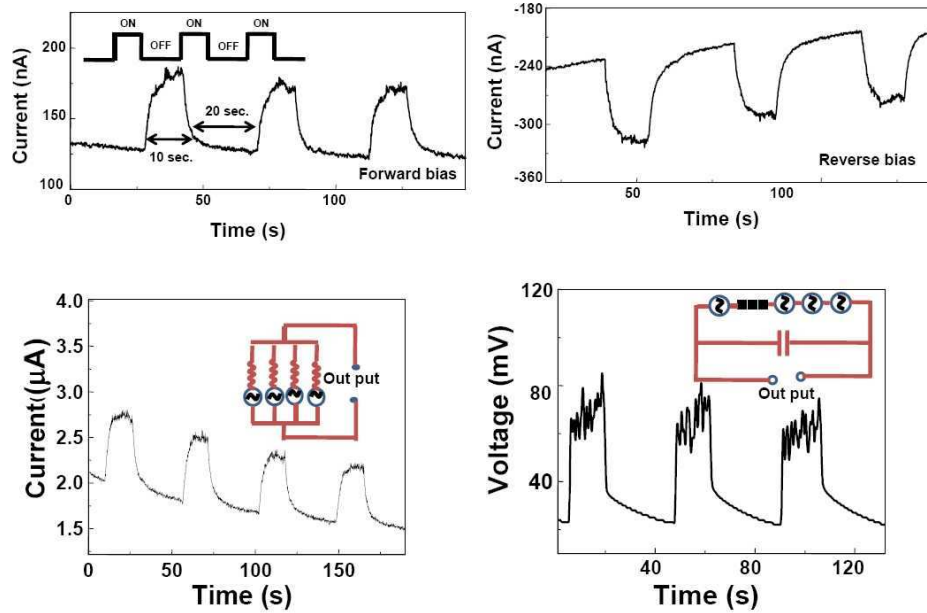
The piezoelectric response of the prepared samples was tested by measuring the closed circuit current when the device was immersed in an ultrasonic bath (frequency ~40kHz) (see figure 2.6a). The current response of a typical 0.5cm^2 device, when exposed to ultrasonic waves in pulsed intervals of 10 s, is *c.a.* 100 nA (figure 2.6a) leading to a current density of 0.2 µA/cm^2. We measured the forward current and the reverse current (by inverting the probes of the source meter) to verify that the observed response was

Figure 2.5: Current versus voltage curves for the zinc oxide coated paper (red) compared to plain paper (black). Note that the shape of the piezo-paper reveals a good Schottky contact with the electrodes. The inset reveals that the cellulose behaves as a non linear conductor but with a conductance of several orders of magnitude lower than the piezo-paper.

not an artifact. The device was tested under continuous excitation for 180 seconds showing an almost constant response; however, a slight decrease of the response current of ~10% was observed over the amount of time tested. It is important to note that the baseline of the plots shown in figure 2.6 are shifted from zero due to the internal capacitance of the device. The current output was measured from the baseline.

In order to prove the scalability of the proposed device, we stacked N numbers of the typical device (0.5 cm^2) in series or in parallel, named a N-stack. For instance, the in-set of figure 2.6b shows a schematic drawing of a 4-stack. Each of the individual devices was tested to make sure their response to mechanical vibration was consistent. For a 4-stack connected in parallel, the currents add up, giving a total of ~500nA during operation in similar conditions as mentioned above (see figure 2.6b). In another experiment, a device having 25 mm^2 area with ten stacks of individual piezo-paper connected in series, was used to measure the scalability on

Figure 2.6: Current output showing the performance of the piezo-paper device when subjected to pulsed excitations of ultrasonic waves in forward and reverse bias. The figure also shows closed circuit current response and open circuit voltage of a stack of different piezo-paper devices connected in series or in parallel showing that the response is scalable.
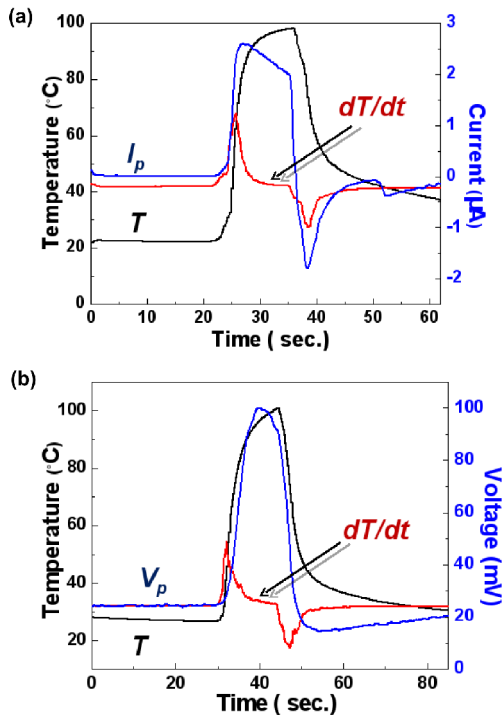
voltage. The voltage measurement circuit involves a capacitive filter (0.22 µF) in parallel to the device in order to obtain a stable DC voltage as shown in figure 2.6c. The output is monitored using DAS1414 intelligent data acquisition system with a gain/input range of ±0.1V and a 350 kHz maximum sample rate, which is much higher than the frequency of excitation of the device (40 kHz). The initial output from the device without capacitive filtering is observed to be a series of highly fluctuating pulses of single polarity. By introducing the capacitive filter, these pulses are averaged out to produce a stable DC voltage. The voltage is measured in the differential mode for better accuracy. The device is excited for a pulse of 15 seconds at regular intervals of 30 seconds. The arrays of piezo-paper devices show a voltage output of ~ 40mV (figure 2.6c). It is clear from the graph that the time taken for charging and discharging of the capacitor is 10 and 30 seconds, respectively. Stable outputs are observed for about 10 cycles after which the output is gradually reduced.

The mechanism for charge collection in the VLS grown ZnO nanogerator was proposed by Wang and co-workers [22]. The ZnO nanowires bend due to the external excitation by a tip or by a zigzag electrode, inducing a displacement of the

48

cations with respect to the anions, and a voltage is generated along the nanowire diameter. A current is driven through the external circuit to neutralize the ionic charges in the nanowires and to reduce the created voltage only when the top electrode touches the inner part of the deflected nanowire. The Schottky contact between the nanowire and the top electrode rectifies the signal, therefore showing a DC current on the external circuit. Recently, Gösele and his group thoroughly analyzed this mechanism [29]. They suggested that the high carrier concentration and high electron mobility of the presumably unintentionally doped ZnO would cancel out the difference of potential caused by the ion displacement along the nanowire diameter after straining it in less than 1 picoseconds. Furthermore, they point out that there is no Schottky barrier at room temperature for voltages below 25mV, so there is no real rectification of current for the voltages harvested in such experiments.

In the device we have proposed here, the energy harvesting mechanism is slightly different from what has been suggested earlier [22], and can be explained as follows. The mechanical waves make the fibers vibrate, thus creating two types of stresses on the ZnO coated paper: a) as contiguous fibers vibrate, the nanorods on their surface are rubbed against each other, causing them to deflect, and generating a potential difference (or piezoelectric potential) along the nanowire diameter; and b) since the fibers are coated with a ZnO thin film, there is a strain due to the vibration of the fibers. The ion displacement due to this strain creates a difference of potential along the thin film, therefore increasing the time for potential screening due to the intrinsic carriers in the ZnO film. This increase in the time for potential screening allows the current to flow through the external circuit. In this case, the potential difference that drives the current from one electrode to the other is in the ZnO thin film, and the difference of potential within individual nanorods barely contributes. Now, the electrodes always make contact with the sample, so that the response observed cannot be accounted for short circuit.

The maximum power output for our typical single layer devices presented in this work are ~11.3 nW/cm^2 for conversion of mechanical energy into electrical energy. The best power output achieved in previous reported work using vapor grown ZnO nanowire devices is reported to be 83 nW/cm^2 [22]. Same configuration of ZnO paper devices shows power output (~75 nW/cm^2) for conversion of thermal energy into electrical energy. The output power for conversion of mechanical energy is less

Figure 2.7: (a) closed circuit current as a function of temperature showing that the rate of change of temperature corresponds to a signal in the current measurement. Similarly (b) shows an open circuit voltage measurement across an external capacitor.
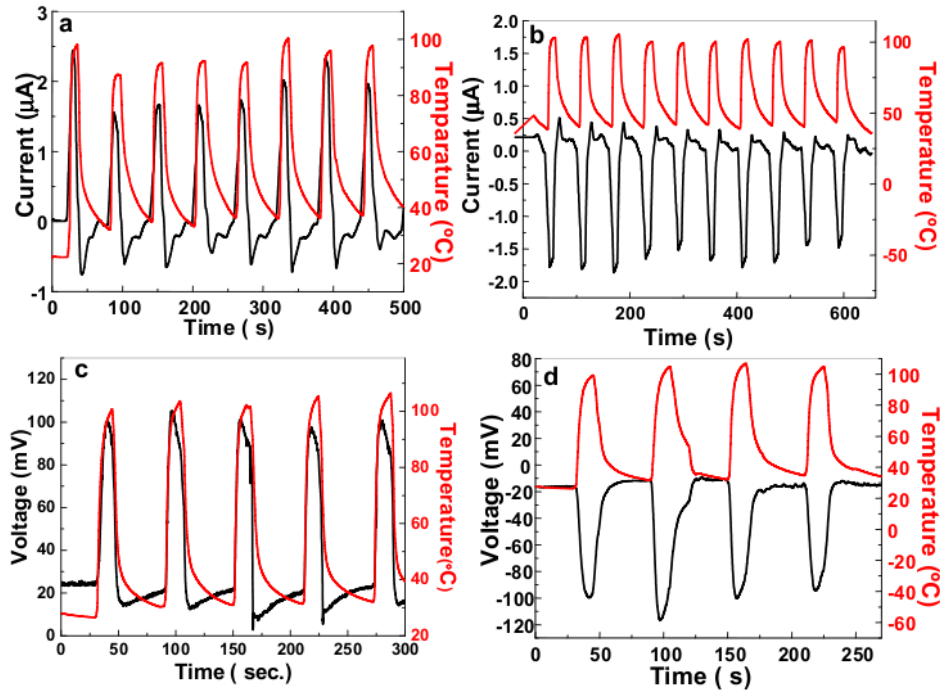
than the reported values, yet comparable; however, the piezo-paper is quite easy to synthesize by inexpensive processes and can transform more both mechanical and thermal energy into electricity which makes our approach appealing.

2.3.5. PYROELECTRIC RESPONSE

A cement-on type K thermocouple from Omega was attached to a 1 cm^2 piezo-paper and laminated to measure the temperature of the device. The temperature was monitored by Lakeshore 331 temperature controller. The closed circuit current and open circuit voltage of ZnO paper were measured by placing the device on heating plate maintained at 120°C for 15 seconds and allowed to cool for 45 seconds in air.

Figure 2.7a shows the device temperature T, the rate of change of temperature (dT/dt) and the pyroelectric current (Ip) on common time scale. Figure 2.7b shows the pyroelectric voltage (Vp) with device temperature T and rate of temperature change (dT/dt). The pyroelectric voltage (Vp) and current (Ip) respond well to the steps in temperature time derivative and increase in amplitude with time. Voltage and current follow the temperature and are proportional to the rate of change in temperature. The sign of measured current or voltage is consistent with the sign associated with the temperature derivative which is characteristic of the pyroelectric effect. Both Ip and Vp were measured at relatively-high temperature rate, where the maximum was 5.8 °Cs^{-1}over a temperature range between 22 and 98°C. The peak Ip and Vp were ~1.5- 2.5 μA (figure 2.7a) and ~80-100mV (figure 2.7b), respectively. Figure 2.8a shows the closed circuit current of devices with repetitive heating cooling cycles and corresponding temperature profile. The data clearly indicate that the current output was originated from ZnO paper as a result of

Figure 2.8: (a) Closed circuit current of 1cm² devices as a function of temperature during heating-cooling cycles. The current response is consistent in forward and reverse polarity. (b) shows the open circuit voltage during cooling-heating cycles.

heating, as the output coincided with the working cycle (figure 2.8a). Furthermore, the output signal switched in sign from positive to negative when the measured polarity was switched from forward to reversed connection (figure 2.8b). A similar pattern in the open circuit voltage output was also observed, as shown in (figure 2.8c and d). The theoretical current density of pyroelectric device can be calculated classically by $I = A \cdot p \cdot \dfrac{dT}{dt}$, where, A, p and dT/dt are the effective area of device, pyroelectric coefficient and rate of change of temperature. The pyroelectric coefficient of bulk ZnO is 14 µCm⁻²K⁻¹ and rate of heating of ZnO paper is 5.8 °Cs⁻¹ [87]. Therefore, according to this model, the theoretical estimated current output for 1cm² thin film of ZnO should be 8.12 nA. However the observed output of 1cm² ZnO paper is 1.5 µA which is ~180 times higher than same size of thin crystalline ZnO film.

At first sight, there is an apparent increase in the pyroelectric response but it can be seen that there is no such effect. The factors that influence the pyroelectric properties of thin films can be categorized into two groups: 1) surface and size effects, 2) residual stress due to mismatch in the lattice parameters and the

thermal expansion coefficient between the film and the substrate [30, 31]. Here the ZnO film was grown in a highly porous paper composed of micron size fibers. These fibers are covered completely with crystalline continuous ZnO thin film, and with ZnO nanorods. The surface area can be estimated to be at least a couple of orders of magnitude larger than the one proposed above (*e.g.* 800 cm^2). This would yield a theoretically estimated current of 6.4 µA/cm^2 at 5.8°Cs^{-1}. The measured current is comparable to maximum estimated current for ZnO film.

In order to verify this hypothesis, current measurements were carried out as a function of the area of piezo-paper device. The maximum theoretical current is estimated to increase as 25.6 µA and 57.6 µA for a 4 cm^2 and 9 cm^2 device respectively. The measured current output from these devices were ~20 µA and ~46 µA, respectively, which are comparable to theoretical estimated values and confirm the enhanced power output is due to high surface area of ZnO film. The ZnO film is poorly bonded with cellulose fiber therefore residual stress is negligible hence its contribution in output current is ruled out.

The maximum power output for our typical single layer devices presented in this work is *c.a.* 750 nW/cm^2 for temperature rate of approximately 5.8°Cs^{-1}. Recent studies show a peak power density for thin film of PZT and thin-film lead scandium tantalate is 0.23 µWcm^{-2} and 125 µWcm^{-2} respectively for a maximum temperature rate of approximately 15°Cs^{-1}. The pyroelectric coefficient of PZT and thin-film lead scandium tantalate are 238 µCm^{-2} K^{-1} and 6000µCm^{-2} K^{-1} which are much higher than the pyroelectric coefficient of ZnO (14 µCm^{-2}K^{-1}) [14,30]. The device was tested under continuous heating for 30 minutes showing an initial increase in voltage to 100 mV and a decrease in the response voltage of ~40% was observed over the time tested.

2.3.6. A MULTIFUNCTIONAL DEVICE

The piezo-paper devices presented here can in principle, be used to transform mechanical and thermal energy into useful electrical energy. However, its applications are rather restricted by the power outlet. For instance, to power a 10mW small motor, our approach would require around ~13 m^2 of paper based on pyroelectric power output and 88m^2 based on piezoelectric power output which still is economically viable, while for other reported nanowires based devices would require around 12 m^2 of Si or GaN wafer grown nanowire arrays which is difficult to

implement. None of these are practical; still, one can think of applications where a small scale device could be helpful.

The low cost of paper, its light weight, ease of fabrication and mechanical flexibility should make our piezo-paper based devices quite competitive in applications compared to previously reported nanogenerator technologies. Moreover, by using thinner paper matrices, we could improve the performance, although this might compromise the mechanical flexibility of the devices.

2.4. Conclusions

We have presented the synthesis and performance of a low cost ZnO based paper device for the generation of electrical current when exposed to mechanical excitation or thermal energy. ZnO is embedded in commercial paper, using a simple and scalable synthesis method, producing a multifunctional piezo-paper which can be integrated with a wide variety of structures. The scalability of the device has been proven by stacking these in parallel, which scales the current to higher values. The feasibility of using this paper as energy harvesting devices is demonstrated. Our results open up new fabrication approaches for the realization of low cost flexible energy generators and sensors that could power devices from at different scales.

The purpose of this work has been to contribute with the development of ZnO nanoscale science through a nanocomposite based on ZnO nanorods and nanostructured film. This composite presents several advantages over the devices that were reported before our work was carried out: 1) It is synthesized through a low-cost low temperature method; 2) on top of a low cost substrate; 3) the whole device is, in principle, bio-degrabable and environmentally benign, given its components. In fact, it has been shown that ZnO nanowires dissolve to less than 50% of their volume in different bio-fluids after 6 to 12 hours [32], which opens the possibility of having a dispensable device for specific functions inside the body. However, the output of our device is somewhat below the output of the all-solid-state devices that have been proposed before. Nevertheless, the possibility of a lower cost and a broader set of applications due to the bio-compatibility could make this kind of devices more attractive.

As it has been stated in the text, the piezoelectric contribution to the ZnO

53

nanorods is negligible, and instead the ZnO thin film is responsible for the formation of the dipole and the final current collection. In this sense, the device presented here does is not nanotechnology, according to the definition given in the introduction. However, it should be possible to find other scaffold structures which would favor the collection of pyroelectric or piezoelectric currents from the nanorods. This should be explored keeping in mind that the low cost of the substrate is what make this kind of device attractive. For instance, an aligned array of nanorods placed between two low cost substrates which could be compressed would be ideal, since this kind of device would make use of the highest piezoelectric coefficient of the nanorods.

2.5. Related published work

U.S. Provitional Patent 61/146,421: "Multifunctional Integrated Composite Unit For Energy Generator, Storage and Strain Sensor and Method of Use Thereof". Filed January 22, 2009 by P. M. Ajayan and Ashavani Kumar of Rice University and A. R. Botello-Méndez, Mauricio Terrones and Humberto Terrones of IPICYT.

Ashavani Kumar, Andres Botello-Mendez, Hemtej Gullapalli, Robert Vajtai Mauricio Terrones, Pulickel M. Ajayan. Low cost, multifunctional, piezoelectric paper for energy harvesting. Nano Lett. (submitted)

2.6. References

[1]. Wang, Z. L. Zinc oxide nanostructures: growth, properties and applications. *J. Phys. Condens. Matter*. **16**, R829-R858 (2004).

[2]. Koch, U., Fojtik, A., Weller, H. & Henglein, A. Photochemistry of semiconductor colloids. Preparation of extremely small ZnO particles, fluorescence phenomena and size quantization effects. *Chem. Phys. Lett.* **122**, 507-510 (1985).

[3]. Bahnemann, D.W., Kormann, C. & Hoffmann, M.R. Preparation and characterization of quantum size zinc oxide: a detailed spectroscopic study. *J. Phys. Chem.* **91**, 3789-3798 (1987).

[4]. Haase, M., Weller, H. & Henglein, A. Photochemistry and radiation chemistry of colloidal semiconductors. 23. Electron storage on zinc oxide particles and size quantization. *J. Phys. Chem.* **92**, 482-487 (1988).

[5]. Hu, Z., Oskam, G., Lee Penn, R., Periska, N., & Searson, P. The Influence of Anion on the Coarsing Kinetics of ZnO Nanoparticles. *J. Phys. Chem. B.* **107**, 3124 (2003).

[6]. Viswanatha, R., Amenitsch, H., & Sarma, D.D. Growth Kinetics of ZnO Nanocrystals: A Few Surprises. *J. Am. Chem. Soc.* **129**, 4470 (2007).

[7]. Hu, Z., Escamilla Ramírez, D.J., Herdia Cervera, B.E., Oskam, G., & Searson, P. Synthesis of ZnO Nanoparticles in 2-Propanol by Reaction with Water. *J. Phys. Chem. B.* **109**, 11209 (2005).

[8]. Yang, C., Li, Y., Xu, G., & Ma, X. Microstructure Characterization of Single-crystal ZnO Nanorods Synthesized by Solvothermal at Low Temperatures. *J. Mater. Scil Technol.* **23**, 583 (2007).

[9]. García, S. P. & Semancik, S. Controlling the Morphology of Zinc Oxide Nanorods Crystallized from Aqueous Solutions: The Effect of Crystal Growth Modifiers on Aspect Ratio. *Chem. Mater.* **19**, 4016 (2007).

[10]. Beeby, S. P., Tudor, M. J., White, N. M. Energy harvesting vibration sources for Microsystems applications. *Meas. Sci. Technol.* **17**, R175-R195 (2006).

[11]. Hochbaum, A. I., Chen, R., Delgado, R. D., Liang, W., Garnett, E. C., Najarian, M., Majumdar, A., Yang, P. Enhanced thermoelectric performance of rough silicon nanowires *Nature* **451**, 163-167 (2008).

[12]. Nickel, N. H.; Terukov, E. *Zinc Oxide – A Material for Micro- and Optoelectronic Applications*. Springer, The Netherlands, 2005, Chapter 1.

[13]. Elmer, K.; Klein, A.; Rech, B. *Transparent Conductive Zinc Oxide: Basics and Applications in Thin Film Solar Cells*. Springer-Verlag Berlin Heidelberg 2008, Chapter 1.

[14]. Polla, D.L., Francis, L. F. Processing and Characterization of Piezoelectric Materials and Integration into Microelectromechanical Systems. *Annu. Rev. Mater. Sci.* **28**, 563-597(1998).

[15]. Hill, N. A., Waghmare, U. First-principles study of strain -electronic interplay in ZnO: Stress and temperature dependence of the piezoelectric constants. *Phys. Rev. B* **62**, 8802 (2000).

[16]. Paradiso, J. A., and Starner, T., Energy scavenging for mobile and wireless electronics. *Prevasive Computing*, January - March, 18 – 27 (2005).

[17]. Boukai, A.I. et al. Silicon nanowires as efficient thermoelectric materials. *Nature* **451**, 168-171 (2008).

[18]. Whatmore, R. W. Pyroelectric devices and materials. *Rep. Prog. Phys.* **49**, 1335-1386 (1986).

[19]. Zhou, J., Xu, N., Wang, Z.L. Dissolving Behavior and Stability of ZnO Wires in Biofluids: A Study on Biodegradability and Biocompatibility of ZnO Nanostructures *Adv. Mater.* **18**, 2432-2435 (2006).

[20]. Wang, X., Song, J., Liu, J., Wang, Z. L. Direct Current Nanogenerator Driven by Ultrasonic Waves. *Science* **316**, 102-105 (2007).

[21]. Qin, Y., Wang, X., Wang, Z. L. Microfibre-nanowire hybrid structure for energy scavening. *Nature* **451**, 809-813 (2008).

[22]. Liu, J., Fei, P., Zhou, J., Tummala, Rao., Wang, Z. L. Toward high output-power nanogenerator. *Appl. Phys. Lett.* **92**, 173105-07 (2008).

[23]. Wu, X., Vanderbilt, D., Hamann, D. R. Systematic treatment of displacements, strains, and electric fields in density functional perturbation theory. *Phys. Rev. B* **72**, 035105-18 (2005).

[24]. Ye, C. P., Tamagawa, T., Polla, D. L. Experimental studies on primary and secondary

pyroelectric effects in Pb(Zr$_x$,Ti$_{1-x}$)O$_3$, PbTiO$_3$, and ZnO thin films *J. Appl. Phys.* **70**, 5538-5543(1991).

[25]. Klemm, D., Heublein, B., Fink, H.-P., Bohn, A. Cellulose: Fascinating Biopolymer and Sustainable Raw Material. *Angew. Chem., Int. Ed.*, **44**, 3358-3393 (2005).

[26]. Fukada, E. History and Recent. Progress in. Piezoelectric Polymers*IEEE Trans. Ultrason. Ferro. Freq. Contr*. **47**, 1277-1290 (2000).

[27]. Kim, J., Yun, S. Discovery of cellulose as a smart material. *Material Macromolecules* **39**, 4202-4206 (2006).

[28]. Pushparaj, V. L., Shaijumon, M. M., Kumar, A., Murugesan, S., Ci, L., Vajtai, R., Linhardt, R., Nalamasu, O., Ajayan, P. M. Flexible energy storage devices based on nanocomposite paper. *Proc. Nat. Acad. Sci.* **104**, 13574-77(2007).

[29]. Alexe, M., Senz, S., Schubert, M. A., Hesse, D., & Gösele, U. Energy Harvesting Using Nanowires *Adv. Mater.*, **20**, 4021-4026 (2008).

[30]. Huang, H., Sun, C. Q. and Hing, P. Surface bond contraction and its effect on the nanometric sized lead zirconate titanate *J. Phys: Condens. Mater.* **12**, L127-L132 (2000).

[31]. Xie, J., Mane, P.P., Green, C.W., Mossi, K.M., & Leang, K. ASME Conference on Smart Materials, Adaptive Structures and Intelligent Systems

[32]. Zhou, J., Xu, N.S. & Wang, Z.L. Dissolving behavior and stability of ZnO wires in biofluids: A study on biodegradability and biocompatibility of ZnO nanostructures. *Adv. Mater* **18**, 2432–2435 (2006).

Chapter 3

# Theoretical Calculations Of Various ZnO Systems

CONTENTS

3.1. INTRODUCTION

The applications of ZnO have received a new twist with the synthesis of a rich family of nanoscale structures ranging from nanowires and nanorods, to nanobelts, nanodisks, nanotubes, nanoribbons, nanoparticles, tetrapods, etc (see §1.3) The properties of these nanostructured materials differ from the bulk counterpart, and thus open the possibility for a new range of applications. In particular, ZnO nanoparticles can exhibit interesting magnetic properties which is the subject of the work presented in §3.2.

ZnO usually crystallizes in the Wurtzite structure. However, it is possible to synthesize ZnO in the Zinc-blende structure on top of an adequate substrate or in the Rocksalt structure at high pressures. In 2007, it was found that ZnO could be observed in a new Hexagonal planar phase. While the electronic, magnetic and mechanical properties of the Wurtzite, Zinc-Blende and Rocksalt structure have been studied for some time, the properties of the Hexagonal phase are relatively unknown. §3.3 and §3.4 are devoted to the study of the Hexagonal phase of ZnO, paying particular attention on the edges and edge states that arise when one considers a finite system. The electronic and magnetic properties of ZnO nanoribbons are analyzed in detailed, and constitute the most original result of this work, which eventually links to §6 of this thesis.

3.2. ELECTRONIC AND MAGNETIC PROPERTIES OF ZnO NANOSTRUCTURES

Recently, efforts have been carried out in order to understand, from experiments, the growth mechanisms of ZnO nanoparticles so that their size, morphology, number of defects and impurities are controlled [1-5]. Despite of these efforts, the effect of impurities and defects on the properties of ZnO nanoparticles remains unclear. Dietl and coworkers predicted that ZnO nanoparticles doped with transition metals (the so-called dilute magnetic semiconductors) would exhibit ferromagnetism above room temperature [6]. Ever since, much effort has been focused towards synthesizing and probing the magnetic properties of such systems. The recent observation of ferromagnetism in un-doped semiconductor oxide nanoparticles (TiO_2, ZnO, In_2O_3, SnO_2, and CeO_2) [7], and other unusual
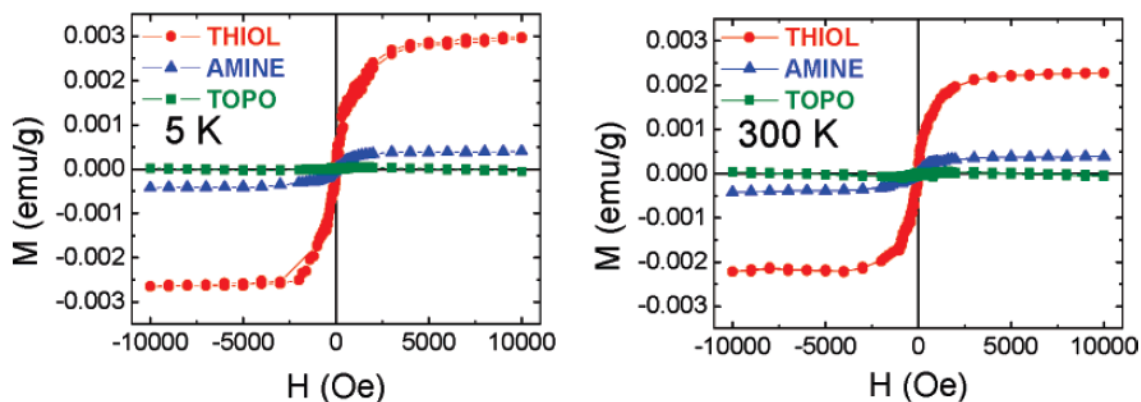
Figure 3.1: Magnetization curve loops for ZnO nanoparticles capped with different organic molecules at 5K and at room temperature [8].

magnetic responses in ZnO doped with transition metals [5], have created excitement in order to answer questions regarding the origin of magnetism in these systems. However, the observations are controversial, and the origin of the ferromagnetism in these ZnO systems is still under debate.

In this context, Sundaresan *et al.* found ferromagnetism experimentally as a general feature for nanoparticles of several oxide semiconductors [7]. In addition, García et al. have found a magnetic behavior in undoped ZnO nanoparticles with organic passivation [8]. They report that the nanoparticles grown in a dodecanethiol environment present a large ferromagnetic response (see figure 3.1). This response is not observed when the nanoparticles are capped with amine or phosphine groups. Banerjee *et al.* observed an enhancement of ferromagnetism upon thermal annealing in ZnO nanoparticles grown by a micellar method from a sulfur based compound [9]. Magnetism has also been found in ZnO systems doped with non-magnetic atoms. Recently, Pan *et al.* reported ferromagnetism in ZnO thin films doped with carbon, from both experiment and theory [10]. Despite the fact that doping and/or passivating ZnO with non-magnetic ions results in the presence of magnetic properties, it is far from clear the nature of this unusual effect. Therefore, efforts for understanding the origin of the ferromagnetic behavior in these systems are still needed and further research should be carried out.

Several theoretical calculations of the geometry and electronic structure of clusters and nanoparticles have been carried out for ZnO and other semiconductors[11-18]. The magnetism experimentally observed for these systems has been attributed to O vacancies, Zn vacancies, intrinsic defects and interstitials.
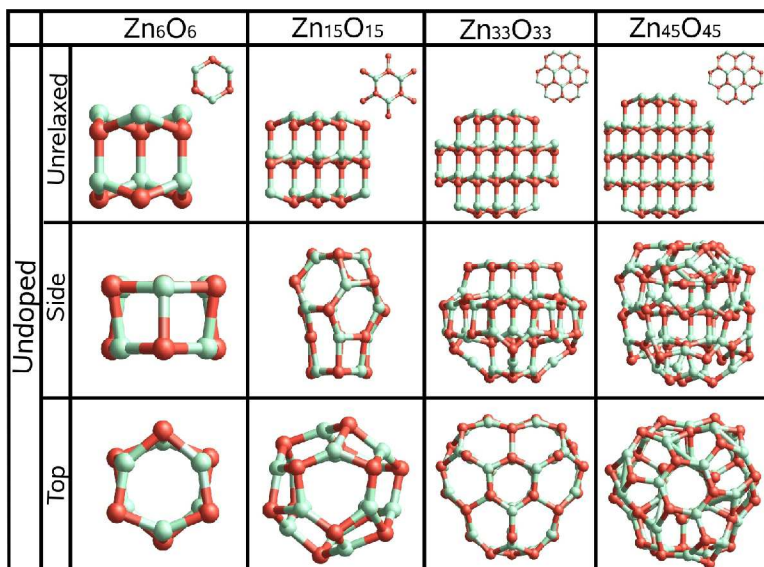
Figure 3.2: Geometry of pure ZnO clusters (zinc atoms in green, oxygen atoms in red). The unrelaxed systems were constructed from the ZnO Wurtzite crystal and it has been used as starting geometry in our calculations of the relaxed systems. The optimal structures have been obtained using the conjugate gradient algorithm in the framework of density functional theory and the local spin density approximation.

In this context, Dalpian and co-workers have recently studied the magnetic properties of undoped ZnO clusters [19]. These authors claimed that ferromagnetism should be mediated through extended surface states, since no single kind of defect is found to be responsible of the obtained magnetic moment [19]. Coey *et al.* suggested an alternative charge-transfer mechanism from the core of the nanocrystal to its surface to explain ferromagnetism in oxide nanoparticles [20].

We have reported the structural, electronic, and magnetic properties of carbon-(C-) sulfur (S-) and non-doped ZnO clusters calculated using first principles. In addition, the effect of sulfur passivation was evaluated. The impurity addition is carried out by the substitution of an O atom by C or sulfur impurities on the surface of the ZnO nanoparticles. On the other hand, sulfur passivation is carried out by attaching sulfur atoms to Zn atoms that have low coordination number (<3). We find that for undoped ZnO clusters, the magnetic state is located at the surface, where the atoms rearrange in a planar-like fashion, but this behavior is not extended beyond this surface. For C-doped ZnO systems, we found a magnetic moment only when the C atom is located at the outer part of the surface of the ZnO nanoparticle. The S-doped ZnO systems studied here (S replacing a Zn or O atom), are nonmagnetic and exhibit a large HOMO-LUMO gap. However, if a stoichiometric ZnO cluster is capped with S (*e.g.* S bonded to Zn), the cluster exhibits a ferromagnetic response.

The effect of geometrical relaxation of the ZnO clusters is depicted in figure 3.2,

61

where the comparison of the relaxed geometry of the clusters with their Wurtzite-like counterparts is shown. For the Zn_6O_6 cluster, it is evident in the side view that the structure flattens, forming two connected hexagonal rings, in agreement with previous results [16-18]. From the top view, it can be noted that the O atoms tend to locate in the outer part of the hexagonal rings. The $Zn_{15}O_{15}$ cluster structure is heavily changed after relaxation. The optimized geometry is a cage-like structure where all the atoms are on the surface. The angles of the bonds are considerably different showing hexagonal and square rings as can be seen on the side view. It can be observed (from the top view) that the O atoms tend to be on the outer part of the structure as in the previous case. The $Zn_{33}O_{33}$ cluster is less modified after relaxation. A three-fold symmetry axis is preserved, (see top view). From the side view, one could notice that the middle layers preserve somewhat the Wurtzite structure, however, in the first layer, the O and Zn atoms show an inward relaxation, and both atomic species share the same plane. The $Zn_{45}O_{45}$ cluster exhibits a large atomic rearrangement, and tends to be more spherical. The O atoms tend to occupy the outer part of the cluster. In general, all optimized clusters exhibit a surface self-reconstruction, thus avoiding low coordination atoms. Similar results were obtained by Puzder, *et al.* using first-principles calculations for CdSe nanoparticles [21].

Figure 3.3 depicts the electronic density of states (or a sum of Lorentzians with a broadening of 0.08eV centered at each energy level) with up and down spins for pure ZnO clusters. Note that almost all clusters exhibit a wide highest occupied molecular orbital (HOMO) – lowest unoccupied molecular orbital (LUMO) gap (see figure 3.3a, 3.3b, and 3.3d); except the $Zn_{33}O_{33}$ cluster which shows states with spin up and down at the Fermi level as shown in figure 3.3c. In this cluster, we observe a shift between the spin up and down density of states. The magnetic moment obtained is $1.87\mu_B$. The density of states of the Wurtzite-like clusters (i.e. before relaxation) showed midgap states (not shown here) that were removed after relaxation. These midgap states were also reported by Puzder, *et al.* in CdSe nanoparticles [21].

According to the Mulliken population analysis, the bonding in the Zn_6O_6 cluster is relatively more ionic (*i.e.*, there is more charge transfer between the ions) than the bonding in bulk ZnO. After charge rearrangement, all the O atoms are equivalent and all the Zn atoms are equivalent. This ionic character can be expected, since
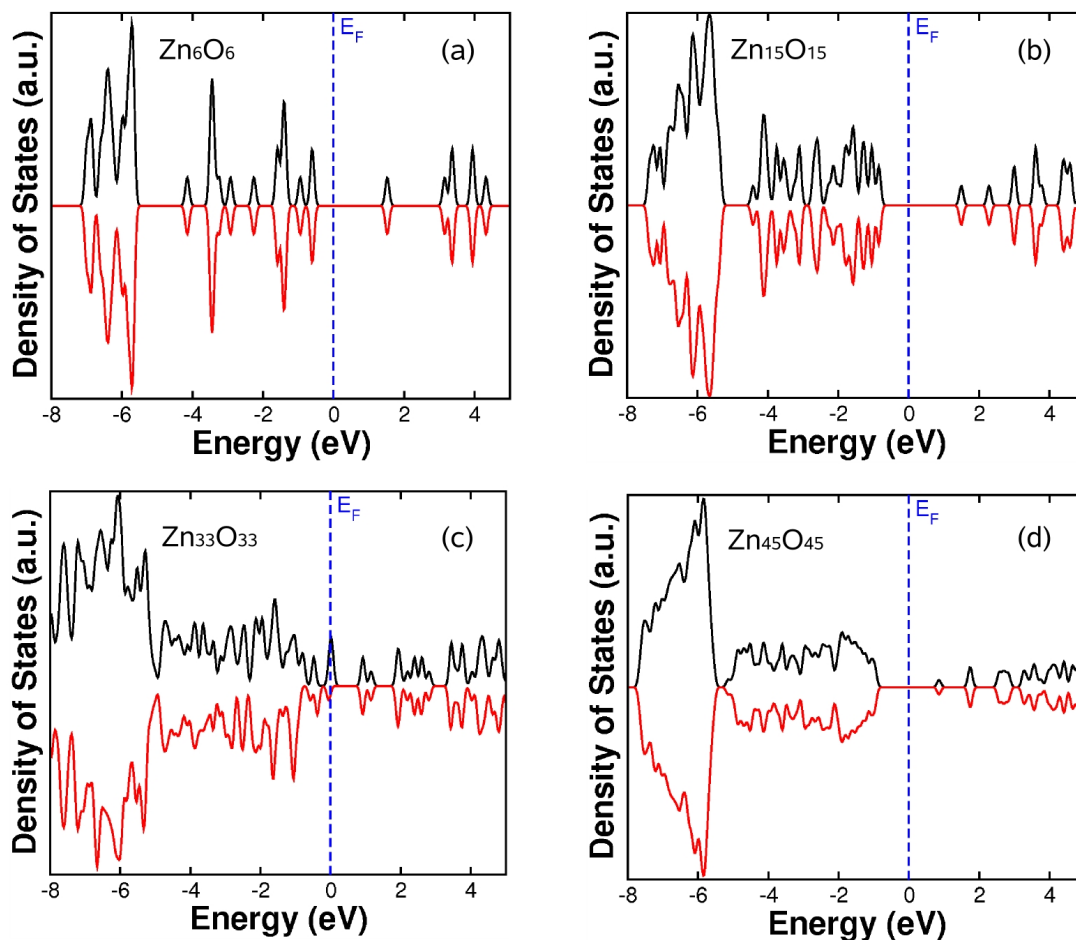
Figure 3.3: Total spin-polarized electronic density of states (DOS) for pure Zn_mO_m clusters (m=6, 15, 33, and 45) after an atomic relaxation. The Fermi energy is set in zero (see the vertical dashed line). In each plot, the upper and lower panel corresponds to the DOS with spin up and down respectively. Amount the considered clusters; it has found that the $Zn_{33}O_{33}$ cluster exhibits a magnetic moment of $1.87\mu_B$. In our calculations, all starting cluster geometries have been obtained from the Wurtzite structure and they have been relaxed using a conjugate gradient algorithm.

the Zn_6O_6 cluster resembles the RS structure. For the $Zn_{15}O_{15}$ cluster almost all atoms are equivalent with an ionicity similar to the Zn_6O_6 cluster, except for three atoms located in the square rings which show an even more ionic character. For $Zn_{45}O_{45}$, the bonding of the atoms at the surface have an ionicity close to the observed in the Zn_6O_6 cluster, and the inside atoms have a bond nature very close to the bulk case.

In order to understand the origin of the magnetism found in $Zn_{33}O_{33}$ clusters, we have calculated the local density of states averaged on O and Zn atoms. It is observed that both types of atoms of the cluster exhibit unpaired spins, although
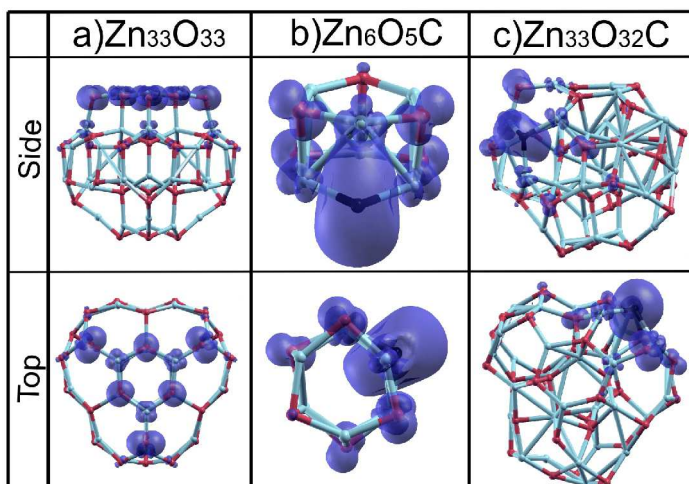
Figure 3.4: Spin density (i.e. density up – density down) of three systems exhibiting a magnetic moment. The $Zn_{33}O_{33}$ non-doped (a) cluster exhibits a magnetic state at the planar graphitic-like surface. b) Carbon-doped clusters (b, c) exhibit with a magnetic state at the C impurity, which extended to its neighbors at the surface.
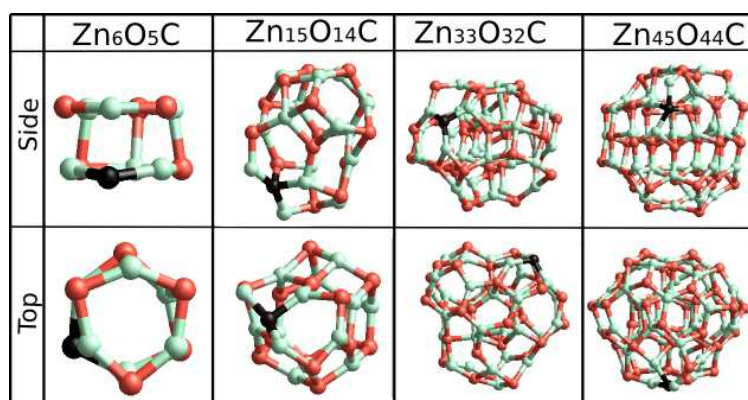
the contribution of the O atoms is more important. Specifically, the contribution to the magnetic moment is mainly due to the O atoms located at the top flat layer where the O and Zn atoms share the same plane. The six O atoms contribute, but the double-coordinated O atoms exhibit larger magnetic moments. Dalpin *et al.* have proposed that magnetism in undoped ZnO systems arise from a delocalized surface state [19]. In agreement with their work, we find that the magnetic state is found at the surface, and that is only found when there is some kind of order inside the cluster. However, in our case, this state is not extended (see figure 3.4a). It is also important to emphasize that the cases where Dalpin et al. find a magnetic moment are those in which planar or graphitic-like reconstruction has been achieved [19]. Comparing their results to ours, we conclude that this graphitic-like reconstruction is necessary for a magnetic moment to be observed (see figure 3.4a). Certainly, this behavior is not unique for nanoparticle systems. Later, in §3.4 we will show that ZnO nanoribbons with graphitic-like structure with zigzag edges could be metallic and ferromagnetic. In that case, unpaired spins emerge in O atoms localized in one-side of the ribbons (O-dominated edge). In addition, new electronic properties have been observed for other semiconductor systems when edges or surface effects are introduced. For instance, Zhang *et al.* [22] have recently found ferromagnetism in nanosheet films made of molybdenum disulfide due to edge effects (see §6.5).

When ZnO clusters contain a C impurity (figure 3.5), the systems exhibit either states at the Fermi level, or a reduction in the HOMO-LUMO gap, as can be confirmed from the electronic density of states (see figure 3.6). In this context, recent experimental studies on C-doped ZnO thin films have revealed a reduction

in the resistivity when compared to the undoped case [23].

In order to understand the effect of a C impurity, we compared the Mulliken populations of the different clusters. For the Zn_6O_5C cluster (see figure 3.5), our calculations reveal that the Zn-C bonding is more ionic than the Zn-O bond. In addition, the length of the Zn-C bond is larger than that of Zn-O. The Zn-O bond distance and character of the three nearest O atoms is affected. The farthest O atoms behave like an O atom on the pure Zn_6O_6 cluster. The C atom displays an electronic charge of 2.993 electrons with spin up and 1.392 electrons with spin down, thus leading to a magnetic moment of $1.6\mu_B$. Therefore, it can be concluded that the spin polarization observed in figure 3.6a is mainly due to the C spin polarization (see figure 3.4b). Similarly, the spin polarization found in the spin density of states of $Zn_{33}O_{32}C$ (see figures 3.4c and 3.6c), was due to the C site polarization. For C-doped ZnO nanosystems, the magnetic state is localized at the C impurity, and extended along its neighbors located on the surface. The atom rearrangement shown in figure 3.4 suggests that the

Figure 3.5: Optimized geometries for ZnO clusters with a carbon impurity. An oxygen atom on the surface was replaced by a carbon atom.

magnetic behavior in C-doped systems occur only when the C atom "pops out" from its surface, but not when the C atom "pops into" the cluster. This in turn suggests that the magnetic behavior of C-doped ZnO systems depend heavily on the bonding environment of the C atom.

The effect of the substitution of an O atom by a S atom in the geometry of $Zn_mO_{m-1}S$ clusters is shown in figure 3.7. Similar to the C impurity case, the difference in the Zn-S and the Zn-O bond length displaces the S atom outwardly from the hexagonal rings of the Zn_6O_5S cluster. For the $Zn_{15}O_{14}S$ cluster, the cage geometry is very similar to that found in the pure case (compare with figure 3.2). The two next cases, as in the previous section, do not show any traces of symmetry, and the clusters tend to be more spherical.
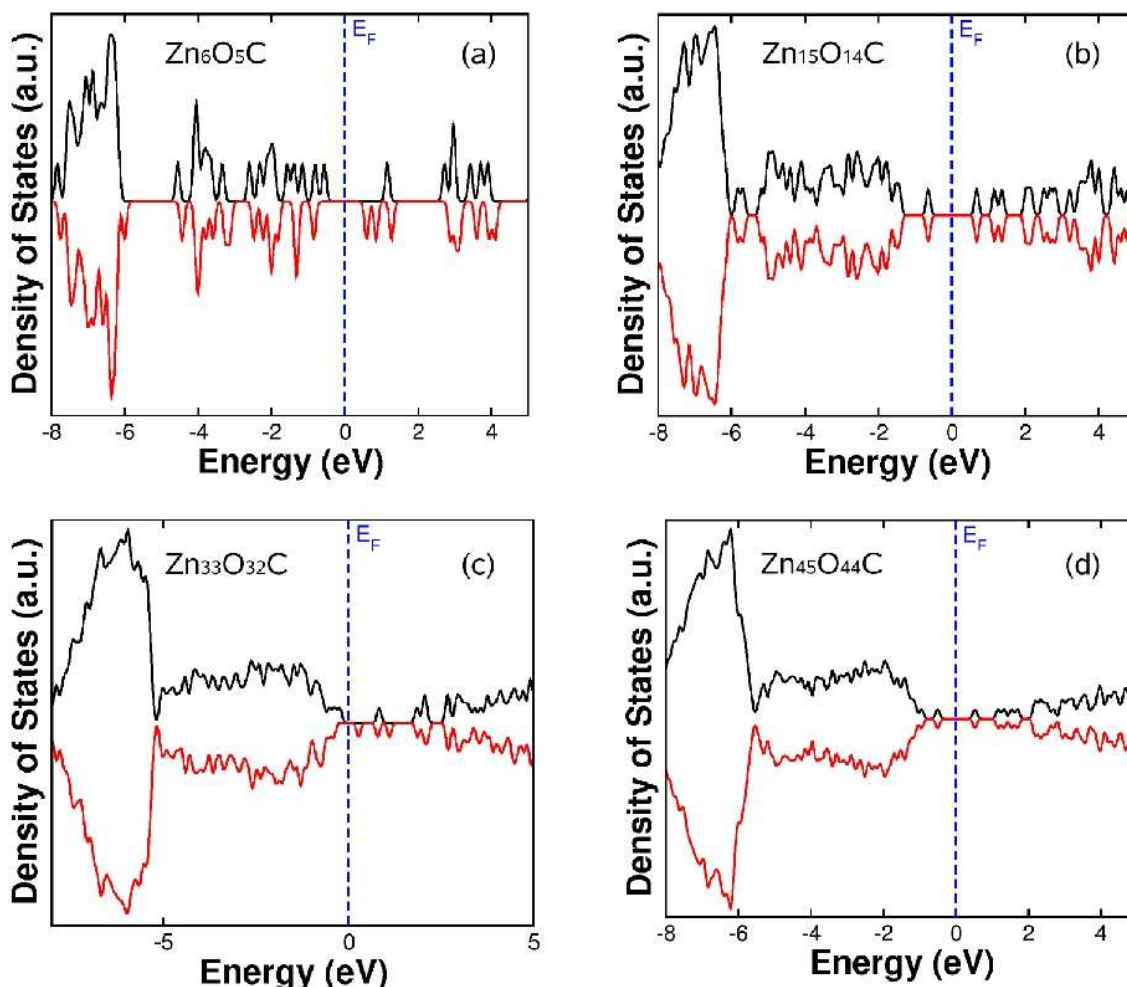
Figure 3.6: Total spin-polarized electronic density of states (DOS) for carbon impurity ZnO clusters ($Zn_mO_{m-1}C$, with m=6, 15, 33, and 45) after an atomic relaxation. The Fermi energy is set in zero (see the vertical dashed line). In each plot, the upper and lower panel corresponds to the DOS with spin up and down respectively. The Zn_6O_5C and the $Zn_{33}O_{32}C$ clusters exhibit a magnetic moment of approx. $2.0\mu_B$. In our calculations, all starting cluster geometries have been obtained of the Wurtzite structure and they have been relaxed using a conjugate gradient algorithm.

From the density of states shown in figure 3.8, it is noteworthy that all the S-impurity clusters reveal a large HOMO-LUMO gap with a null magnetic moment. The magnetic moment observed in the $Zn_{33}O_{33}$ cluster vanishes after a S impurity is added. The nature of the Zn-O bonding is the same as in the pure case, but the Zn-S bond is more ionic. At first sight, these findings seem in contradiction with the experimental results of Garcia *et al.*, where thiol capped ZnO nanoparticles are found to have a ferromagnetic response [8]. However, we will show below that by capping a ZnO cluster with S atoms (*i.e.,* adding a S atom to a Zn atom with coordination less than three), a strong magnetic moment could be created.

	Zn$_6$O$_5$S	Zn$_{15}$O$_{14}$S	Zn$_{33}$O$_{32}$S	Zn$_{45}$O$_{45}$S
Side				
Top				
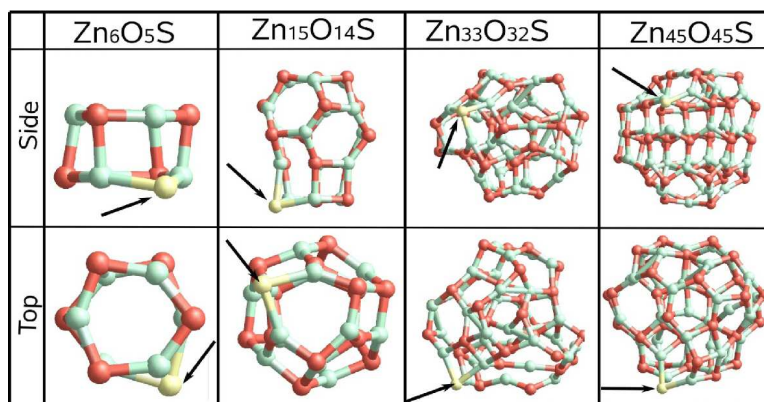
Figure 3.7: Optimized geometries for ZnO clusters with a sulfur impurity. An oxygen atom on the surface was replaced by a sulfur atom. Arrows indicate the position of the sulfur atoms.

Therefore, we conclude that the incorporation of S atoms *into* ZnO nanoparticles reduces the magnetic properties of ZnO nanoparticles, while passivation or capping of ZnO nanoparticles with S atoms enhances the magnetic properties of such ZnO nanosystems.

Table 3.1 presents the Eg for the different ZnO clusters. For the pure case, there is no clear correlation between the Eg and size, as reported earlier [12-14]. For C-impurities, the Eg is in general, reduced with respect to the pure case. However, the Zn$_{33}$O$_{32}$C exhibits a rather strange behavior. It exhibits both a spin up and down Eg, but a spin polarization. The S-doped case shows a bigger Eg than the pure case, except for the case of Zn$_{45}$O$_{44}$S. Albeit, the projected density of states reveals that the S is not contributing states around the Fermi level.

García *et al.,* demonstrated that thiol passivated nanoparticles exhibit a ferromagnetic response [8] (see figure 3.1). Therefore, we also investigated the effect of passivating a ZnO nanocluster with S atoms. We performed spin-polarized calculations on a Zn$_{15}$O$_{15}$ cluster constructed from the Wurtzite crystal, and attached S atoms to each of the Zn atoms with coordination number less than four (see the unrelaxed cluster in figure 3.9). The whole structure was then energetically minimized. In this case, although the unpassivated Zn$_{15}$O$_{15}$ showed a zero magnetic moment without states at the Fermi level (see figure 3.3), the S-passivated cluster exhibits a huge magnetic moment (μ = 5.5 μ_B) and states at the Fermi level (see figure 3.9). The magnetic moment arises mainly from the S atoms. We note from the relaxed molecule that the S atoms tend to bond with other S atoms and with Zn atoms rather than with O atoms. The results for this particular cluster clearly confirm that S atoms play a crucial role in determining the ferromagnetic properties, but only when passivating the surface, as opposed as doping. The DOS of the Zn$_{15}$O$_{15}$ cluster is interesting because it exhibits only spin-

Pure system	Zn$_6$O$_6$	Zn$_{15}$O$_{15}$	Zn$_{33}$O$_{33}$	Zn$_{45}$O$_{45}$
Eg (eV)	2.1243	2.3401	0.0000	1.8175
C-impurity	Zn$_6$O$_5$C	Zn$_{15}$O$_{14}$C	Zn$_{33}$O$_{32}$C	Zn$_{45}$O$_{44}$C
Eg (eV)	1.1504	1.3212	0.5038	1.0298
S-impurity	Zn$_6$O$_5$S	Zn$_{15}$O$_{14}$S	Zn$_{33}$O$_{32}$S	Zn$_{45}$O$_{44}$S
Eg (eV)	2.3061	2.4431	0.8409	1.4671

Table 3.1: HOMO-LUMO gap (Eg) in eV units for the different clusters. All the clusters exhibit a large HOMO-LUMO gap, except for the Zn$_{33}$O$_{33}$. In general, the Eg of the carbon-impurity clusters is smaller than the Eg of the pure case. Oppositely, the S-impurity clusters exhibit, in general, a larger HOMO-LUMO gap.
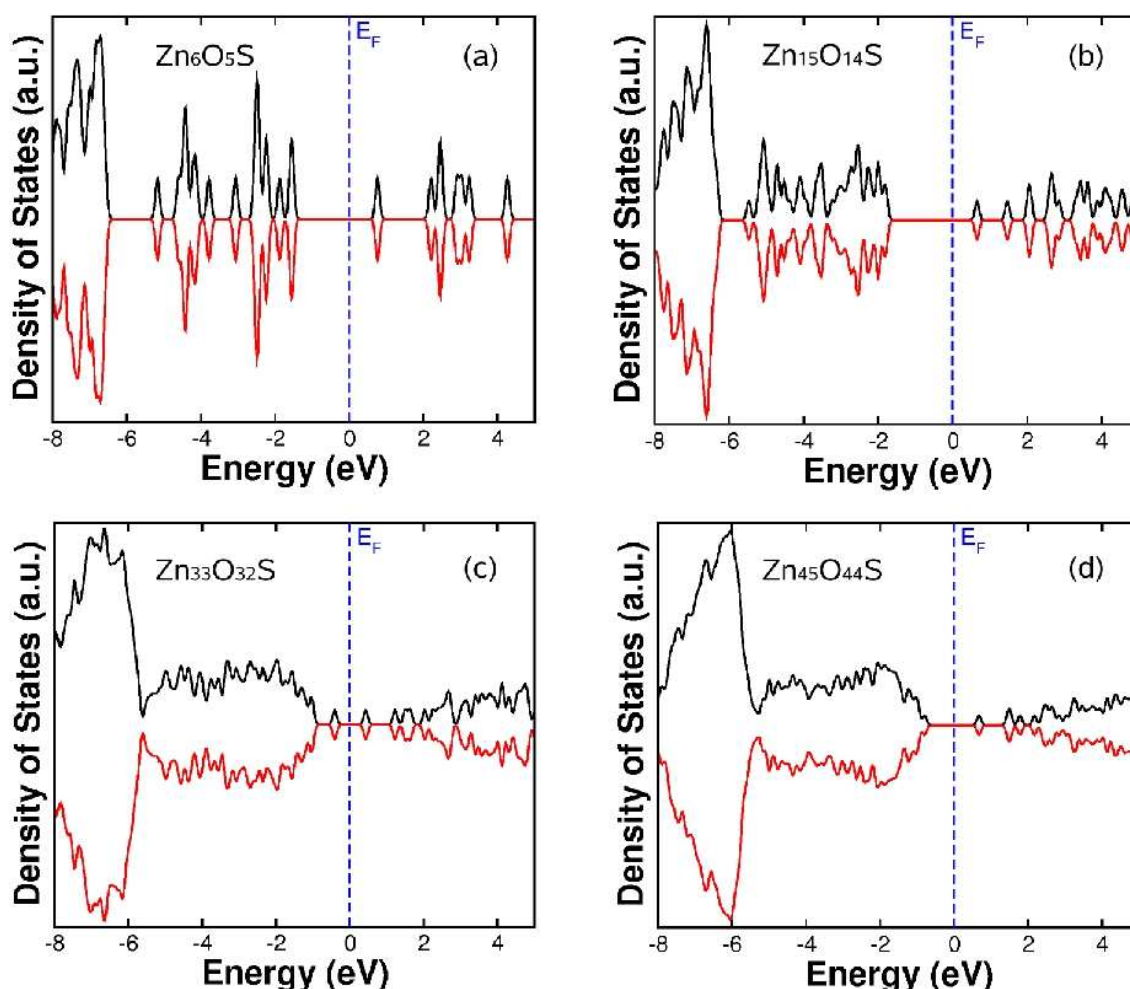
Figure 3.8: Total spin-polarized electronic density of states (DOS) for sulfur-impurity ZnO clusters (Zn$_m$O$_{m-1}$S, with m=6, 15, 33, and 45) after an atomic relaxation. The Fermi energy is set in zero (see the vertical dashed line). In each plot, the upper and lower panel corresponds to the DOS with spin up and down respectively. Note that all systems exhibit a large HOMO-LUMO gap. In our calculations, all starting cluster geometries have been obtained of the Wurtzite structure and they have been relaxed using a conjugate gradient algorithm.
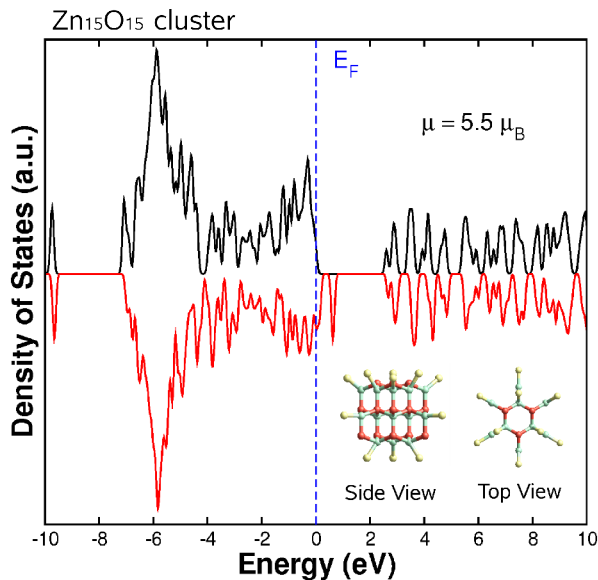
Figure 3.9: Spin-polarized electronic density of states of the $Zn_{15}O_{15}$ cluster passivated with sulfur on the surface. Here, the S atoms are attached to Zn atoms with low coordination number (2 or 3 nearest neighbors). The molecular structure can be seen in the inset. The Fermi level is set to zero. The cluster exhibits high spin moment (5.5 μ_B). The structure was relaxed using the conjugate gradient method. It is important to remark that the pure ZnO cluster exhibits a null magnetic moment.

down excitation states. This kind of material would be very interesting for spintronic applications, since a spin coherent excitation could be used for different channels of electronic transport.

In summary, the electronic and magnetic properties of C-, S- and non-doped ZnO nanoparticles were studied using first principles calculations under the local spin density approximation. From this work, it is possible to conclude that: 1) For undoped ZnO systems, a planar graphitic-like reconstruction is necessary for the observation of a magnetic moment, and the magnetic states will be located on this surface; 2) C impurities could induce a magnetic state if the C atom is located at the surface, and "pops out" from the surface. This magnetic state is located around the C-impurity and extended to its neighbors. If C-impurities at the surface "pop into" the ZnO cluster, then states around the Fermi level appear; and 3) S- impurities at the surface but as *a part of* the ZnO lattice, hamper any magnetic state and open the HOMO-LUMO gap, while S atoms *capping* the low coordinated Zn atoms, enhance a magnetic response. In any case, the environment of the impurity seems to be very important. These findings suggest that the observed magnetic properties of ZnO systems are driven by competition of the structural conformation and are extremely sensitive to the surface and interfaces. We believe that these simple observations could help chemists to achieve more control on the magnetic properties of ZnO nanostructures.

3.3. Planar ZnO: beyond the Wurtzite structure

The WZ structure of ZnO is formed by alternating planes of O and Zn ions

stacked along the *c*-axis, so that any cut of the crystal perpendicular to this direction would result in a single-ion dominated surface. Hence, a polar surface occurs. However, according to the Tasker ionic model, this arrangement would result in a dipole that drives to a divergence in energy as the number of planes increases [24]. In the quest for an explanation, as explained in §1.2.1.4, Claeyssens *et al.,* proposed a boron-nitride (BN) like transition to remove the dipole [25]. In this transition, the Zn and O atoms share the same plane, thus eliminating the dipole.

Tusche and collaborators synthesized for the first time this predicted planar ZnO [26]. They have grown 2-5 layers of ZnO using laser ablation on a silver (111) substrate (see figure 1.3). Their surface x-ray diffraction and scanning tunneling microscopy studies reveal that when the number of layer is less than 4, the structure suffers a severe inward relaxation, changing the bulk four-fold tetrahedral for a trigonal planar coordination. Our calculations, as well as those reported before confirm this theoretically (see figure 1.2).

The polar surfaces of ZnO with finite thickness have intrinsically an electric dipole due to the presence of single ion dominated faces, which yield to an electric field in the layered system causing divergence on the energy values. This artifact can be avoided by rearranging the surface O and Zn atoms, thus reducing the ionicity [27]. Previous studies indicate that a removal of one fourth of the charge on the surface would eliminate the dipole [28]. It is also well known that any charge rearrangement is tightly related to ionic accommodation.

Number of Layers	Distance (d_{Zn-O})	Angle (α)
1	-	-
2	2.441 Å	92.85º
3	2.402 Å	91.26º
4	2.132 Å	104.85º
5	2.056 Å	106.96º
6	2.022 Å	107.90º
Bulk	1.941 Å	109.51º

Table 3.2: Values for the angle (α) and distance (d_{Zn-O}) between Zn and O atoms for the most external layers located in systems ranging from 1 to 6 layers. For systems with four or less layers, the structure is planar (both ions share the same plane), resembling a honeycomb hexagonal structure. The molecular model is shown in Figure 14.
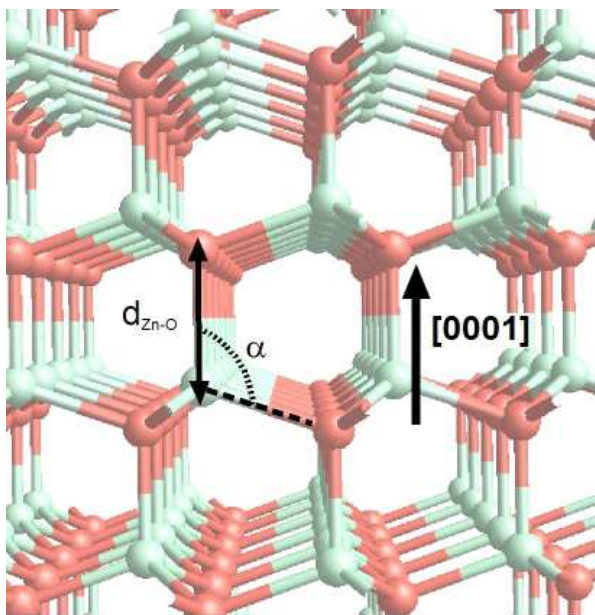
Figure 3.10: Molecular model of Wurtzite-type ZnO showing the angle (α) and the distance (d_{znO}). Note that d_{znO} and α determine the geometry of the layered structure after relaxation with respect to the bulk parameters (d_{znO} = 1.940Å, α = 109.512°). The different values obtained for d_{znO} and α are shown in Table 4.

In order to study the effects of the charge rearrangement and geometric relaxations for different ZnO layered systems, we constructed these systems by cutting the crystal Wurtzite-type structure perpendicular to the c-axis. Here, one layer is defined as the set of the zigzag planes constituted by O and Zn atoms; figure 3.10 shows a cross-section of four layers of the Wurtzite structure. The atomic geometry optimization essentially modifies the distance between two zigzag consecutive layers (d_{Zn-O}) and the angle α between this bond (if any) and the next ion (figure 3.10). For a ZnO monolayer, we noted that the most stable geometry corresponds to a flat hexagonal ZnO system. When the number of consecutive ZnO layers corresponds to N = 2 and 3, the interlayer distance is much larger than the bond length of the bulk Wurtzite-type structure (~2.4Å vs. 1.941Å), so the layers barely interact with each other. For these cases, the angle is approximately 90°, meaning that all the atoms also lie on the same plane and exhibit a planar honeycomb hexagonal-like structure. For N=4, the average distance d_{Zn-O} decreases substantially and the average angle increases by more than 12 degrees, thus recovering the Wurtzite-type structure. For N>4, the parameters slowly approach the bulk values of the Wurtzite structure. The data shown on table 3.2 summarizes the variations of d_{Zn-O} and α as the number of layers increase in the system.

The stability of the different ZnO layered systems was evaluated with respect to the binding energy of the bulk ZnO structure. For the monolayer, the binding energy is -9.86 eV/ZnO, however, for the next system (N=2), the binding energy increases to -10.25 eV/ZnO. We noted that when the layered system changes from planar (*i.e.*, hexagonal) to the Wurtzite-type structure, there is a decrease in the binding

energy (Figure 1.2). This is probably due to the charge recombination necessary for the stabilization of the polar surfaces. It is expected that as the number of layers increase, the binding energy approaches to the bulk energy.

When the number of ZnO layers is < 4, the surface is stabilized by a rearrangement of ions, being now both (Zn and O) lying on the same plane. Therefore, this is not a polar surface. In this case, the surface becomes semiconducting. Strikingly, for systems containing more than four ZnO layers, the stabilization consists of a charge rearrangement resulting in a metallic system. This metallic system is probably not observed experimentally because of the triangular rearrangement proposed before.

For planar hexagonal ZnO systems, we found from the geometry optimization that they are energetically favorable and since both the anion and the cation lie on the same plane the system is insulating. The band structures shown in figure 3.11 depict correspond to the planar systems (semiconducting). As mentioned earlier, the LDA band gap for the bulk WZ ZnO structure is 0.78eV. For the planar systems, the band structures show a direct band gap of 2.013, 1.749 and 1.584eV for one, two, and three layers respectively. Recently, Tu studied the properties of the HX-ZnO and found that the quasiparticle band gap is of 3.576 eV [29].

Our calculations show that the ZnO layered systems are energetically favorable. We have also studied the stability and properties of a layered system with AA stacking, *i.e.*, each Zn is surrounded by two O in the same plane and one Zn in the next layer, as opposed to the Wurtzite based structure or AB stacking, in which each Zn is surrounded by two O in the same plane and one O in the neighboring layer. These structures show always a semiconducting behavior, and a lower binding energy, and thus, less stable than the AB stacked layers. For example, for four layers, the AB stacked layers have a binding energy of -10.46 eV, while the corresponding AA stacked system has a value of -9.94 eV. When the crystal based on the AA stacking is constructed and relaxed a structure close to the ZB ZnO structure with binding energy of -10.74 eV is obtained.

The electronic properties of this new phase of ZnO are quite different from the other phases. As opposed to the RS case, in the HX phase the bond length is decreased and the bond is significantly more covalent. The band gap increases considerably with respect to the other phases. The band structure shows that the
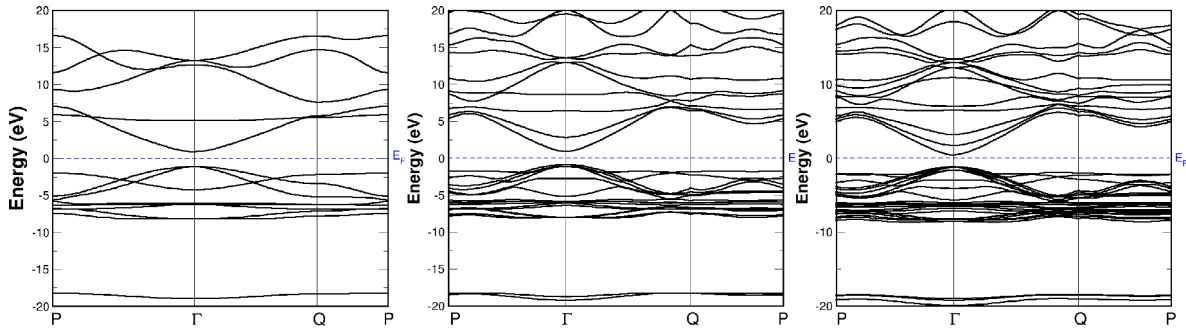
Figure 3.11: LDA bands structure for the three different HX ZnO structures. The gaps are Eg= 2.013, 1.749, and 1.584eV for the monolayer (left), bilayer (center) and trilayer (right), respectively.

electron and hole effective masses have a similar value.

3.3.1. STRUCTURAL DEFECTS IN PLANAR ZNO

The idea of structural defects in planar systems has been very useful to understand the formation of curved C systems such as fullerenes and nanotubes from graphene layers. Both fullerenes and nanotubes incorporate defects in the form of pentagons to close the structure. The presence of other types of rings, such as heptagons, is also possible. For BN nanotubes and fullerenes, squares and octagons are required to close the structure keeping the stoichiometry. Terrones *et al.,* have shown that for C, such structural defects can be arranged in a completely planar structure being more stable than C_{60} [30]. Their study includes planar sheets formed by heptagons and pentagons (labeled R_{57}), and heptagons, pentagons and hexagons, (labeled H_{567}, and O_{567}). The unintentional inclusion of defects can change the electronic properties of materials. However, a good understanding of these defects can become useful to change selectively the physico-chemical properties for specific applications.

In the case of ZnO, structural defects could help to understand the surface properties of small nanoparticles and very narrow nanobelts and nanowires.

A hypothetical planar structure with structural defects can be constructed with octagons and squares (labeled H_{48}), or with octagons, hexagons and squares (labeled H_{468}), keeping the stoichiometry (see Figure 3.12). The H_{48} structure lies close to the HX phase by 0.25eV/ZnO. The difference in stability remains practically constant as the number of layers of H_{48} increases, and even in the limit case of an infinite H_{48} crystal, in which its stability is close to the WZ phase

73
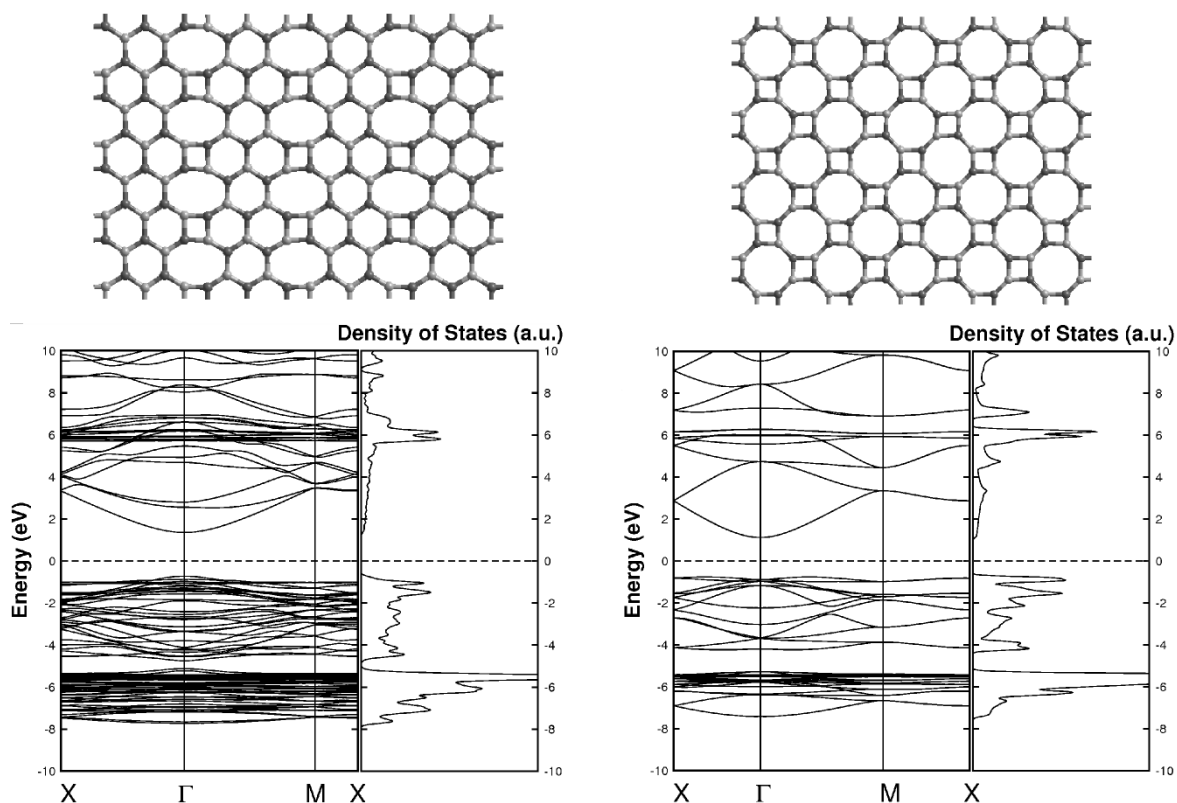
Figure 3.12: Molecular model of ZnO Haeckelite sheets with octagons hexagons and squares (left) and octagons and squares(right), along with their respective band structure and density of states.

(0.24eV/ZnO above WZ). The calculated band gaps for the H_{48} and H_{468} systems are 2.00 (indirect X-Γ) and 2.07eV, respectively. This value is very close to that observed in the HX phase. However, a difference arises in the effective particle masses of the top valence band and the lowest conduction band. The H_{48} system has an electron effective mass of $0.21m_0$, very similar to the hole effective mass of $0.28m_0$. In addition, the ion distance is close to the one on the HX phase. On the other hand, the H_{468} system exhibits a very different electron and hole effective masses, ca. 0.18 and $1.8m_0$, respectively. The nature of the bond, and the ion distance is much closer to the WZ or ZB phase than to the HX phase. The study of the stability of these systems is interesting and could be relevant to study the formation of very small ZnO nanostructures such as small clusters, as has been shown before specially when there is a cage-like structure (see figure 3.2)

3.4. EDGES IN PLANAR ZNO

Since the theoretical prediction by Clayessens *et al.,* [25], and furthermore, after

the experimental confirmation of the existence of planar ZnO [26], there have been various studies regarding the electronic and mechanical properties of hypothetical ZnO single wall nanotubes [31-33]. However, the experimental realization of these structures is rather difficult. The realization of a ZnO one-dimensional is appealing, and could be achieved by controlling the dimensions of the already synthesized planar ultrathin films of ZnO forming the so-called nanoribbons. As in the case of graphene and boron nitride, the effect of the edges in such system is important for the electronic properties of such systems, and could be used for tailoring a specific application. We have thoroughly studied the electronic and magnetic properties of the edges on planar ZnO, and a summary of our results are presented next.

As in the case of graphene or boron nitride, depending on the crystallographic orientation, there are two types of edges: armchair and zigzag. These different types of nanoribbons show different electronic and magnetic properties.

For ZnO, one-dimensional structures such as nanowires, nanoribbons and nanobelts are currently the most investigated because of the wide spectrum of technological applications. These structures have been successfully synthesized with different characteristics for several specific purposes. However, the understanding of their electronic properties is still far from clear. Although theoretical work has been carried out to understand the electronic and mechanical properties of bulk ZnO, little has been done for one-dimensional nanostructures. Xiang and co-workers have studied, using first principles calculations, the energy band gap, the Young modulus and the piezoelectric constant as a function of the diameter for ZnO nanowires [34]. Several groups have reported *ab-initio* calculations for ZnO single-walled nanotubes [31-33]. In addition, Kulkarni and co-workers investigated the effect of tensile loading on ZnO nanowires and nanobelts using molecular dynamics simulations [35]. To the best of our knowledge, no report has addressed *ab-initio* calculations on the electronic properties of ZnO nanobelts or nanoribbons.

ZnO nanoribbons are crystalline nanostructures exhibiting well defined facets. The growth direction of the synthesized nanobelts has been found to be along the [0001], [2110], and [0110] directions, leading to flat surfaces of $\pm(0110)$ or $\pm(0001)$. Several experimental studies have demonstrated that there is a dependence of the width of the ZnO nanoribbons with respect to the electronic properties. For example, Wang's group found a blue shift on the photoluminescence spectra as the

width of the nanoribbons decreases [36].

Here, we have studied using first principles calculations, the electronic structure of ZnO nanoribbons grown perpendicular to the [0001] direction showing flat ±(0001) surfaces. Nanoribbons grown along this direction reveal two possible edge terminations (zigzag and armchair). We have investigated the effect of the geometric relaxation on both configurations. The electronic properties were also thoroughly studied as a function of the nanoribbon's widths. In addition, we calculated the effect of the thickness (number of layers) on the electronic properties for both zigzag and armchair ZnO nanoribbons
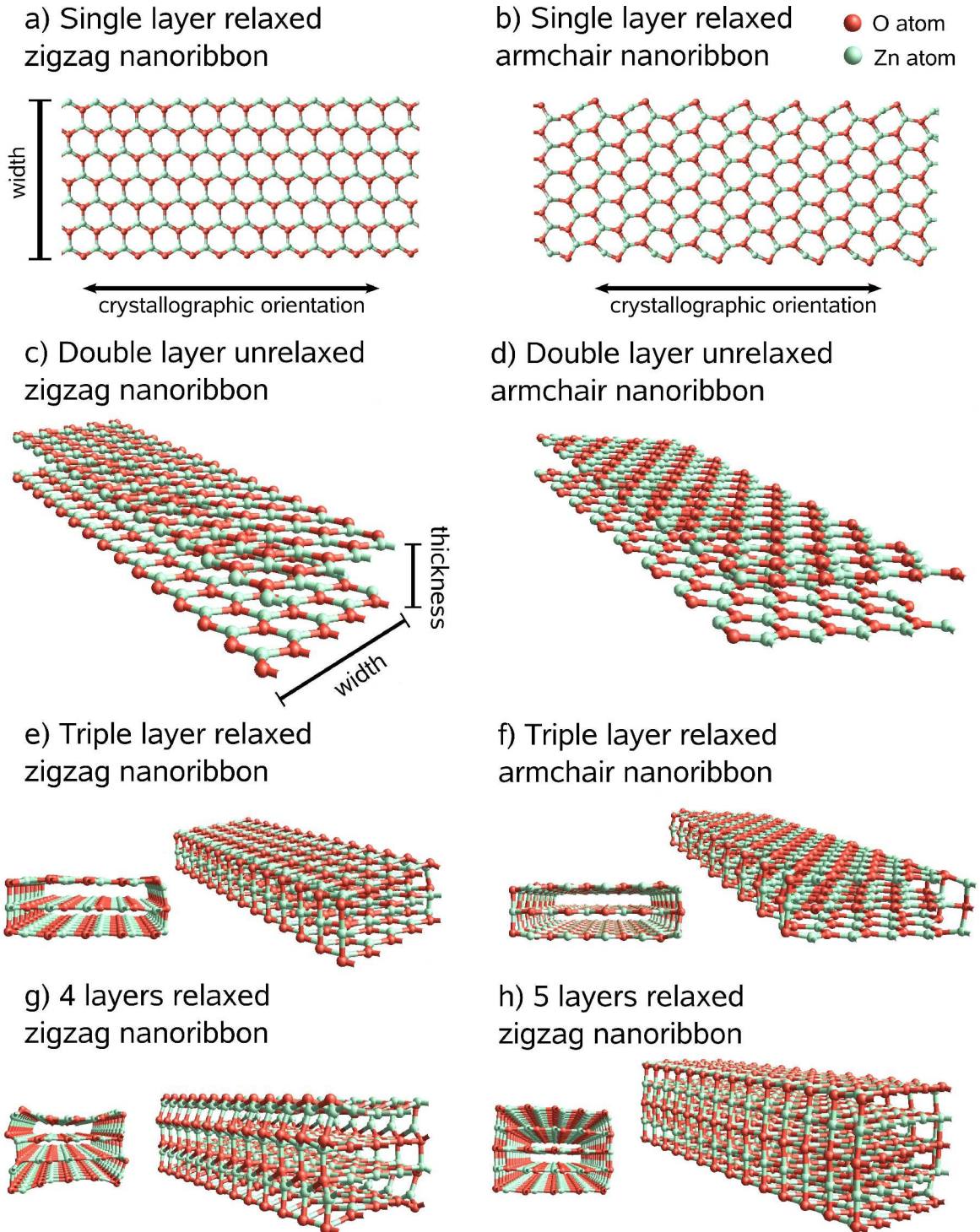
The structures were originally constructed from a set of cuts obtained from the ZnO Wurtzite crystal. The first cuts were made perpendicular to the c-axis in order to form layers. For a monolayer, it has been recently observed that after relaxation the layer prefers a planar configuration in which both the cation and the anion share the same plane. Our calculations for the monolayer result on a binding energy of -9.86eV/ZnO and a band gap of 2.01eV. From the planar monolayer, two different cuts can be performed in order to obtain zigzag and armchair ribbons (figure 3.13a-b).

For ZnO zigzag ribbons one can observe that on one side the surface ions consist of O atoms (two coordinated), whereas the hidden ions represent Zn atoms (three coordinated); the opposite edge of the ribbon shows an inverse atomic configuration (see figure 3.13a). We observed that the zigzag ribbon structures constructed from a ZnO monolayer reveal no significant changes after the atomic relaxation.

The armchair ribbons are characterized by a couple of ions (Zn:cation and O:anion) located on the far edge (two coordinated atoms) and another couple of ions on the inner edge (three coordinated atoms), both alternating along the [1120] direction (see figure 3.13b). After relaxation, we noted that the far edge O ions tend to shift outwards on both sides of the ribbon (see figure 3.13b).

In addition, other ZnO ribbons that resemble experimentally observed nanobelts were constructed. These structures were obtained from planar ZnO layers. Theoretical studies have revealed that ZnO thin films exhibiting a few layers prefer a planar graphitic-like structure. Here, we have started from stacked planar structures as is indicated in figures 3.13 c & d. For zigzag nanoribbons (see figure

76

a) Single layer relaxed
zigzag nanoribbon

b) Single layer relaxed
armchair nanoribbon

● O atom
● Zn atom

width

crystallographic orientation

crystallographic orientation

c) Double layer unrelaxed
zigzag nanoribbon

d) Double layer unrelaxed
armchair nanoribbon

thickness

width

e) Triple layer relaxed
zigzag nanoribbon

f) Triple layer relaxed
armchair nanoribbon

g) 4 layers relaxed
zigzag nanoribbon

h) 5 layers relaxed
zigzag nanoribbon

Figure 3.13: Geometry of different zinc oxide nanoribbons and nanobelts. a) and b) show the geometry of the relaxed structure for the zigzag and armchair nanoribbons respectively. A typical construction (two layers) of ZnO nanobelts from the stacking of layered nanoribbons before geometric relaxation is shown for both the zigzag (c) and the armchair (d) case. After geometric relaxation, the edges of the zigzag ribbons are deformed and joined between consecutive layers (e), while in the armchair the edges remain the same as in the single layer, but are also joined together between consecutive layers (f).

3.13e), the triple-layered zigzag ribbon shows a slight deformation on the edges after atomic relaxation. We observe that the Zn dominated edge of the top layer has bent downwards to form a bond with the O dominated edge of the bottom layer, whereas the Zn dominated edge of the bottom layer has lifted towards the O dominated edge of the top layer. A little movement of the O dominated edges towards the cations was also observed. Similar behavior was witnessed for two and four layers. However, for an odd number of layers, the bottom layer is maintained almost unchanged and the upper layers tend to cluster in pairs (see figure 3.13g & h). For armchair nanoribbons, a similar, but less pronounced rearrangement of atoms on the edges was observed (see figure 3.13f).

The energetic stability of the ZnO ribbons with one layer was studied. The binding energy for both the zigzag and the armchair structures were computed as a function of the ribbon width (figure 3.14a). The armchair ribbons were found to be more stable (~0.4eV/ZnO greater) than the zigzag ribbons despite the significant rearrangement of O ions on the edges.

3.4.1. ELECTRONIC PROPERTIES

The electronic density of states (DOS) of the ZnO monolayer ribbons and their dependence as a function of the width is shown in figure 3.14b-c. In this case, all the zigzag ribbons reveal states located at and close to the Fermi level (see figure 3.14b). An overall metallic behavior indicated by the presence of electronic states at the Fermi level, is similar as the ribbon width is increased. We believe that this effect is mainly due to the O atoms located on the zigzag edges because they increase significantly the states close to the Fermi level. Although Zn atoms located on the edges increase the number of states close to the Fermi level, their effect is minimal when compared to the O dominated edges. Interestingly, Fujita and coworkers have found a metallic behavior for zigzag carbon ribbons. They attributed these states not to dangling bonds, but to the edge zigzag states. Recently, structurally induced metallic active edge states have been found on nanoscale MoS_2. Therefore, the appearance of these boundary states is not unique for ZnO.

The electronic DOS of the monolayer armchair as a function of width (from 1.4 to 3.4 nm) is shown in figure 3.14c. The electronic properties of these structures seem to be independent of the width of the ribbon. All the structures reveal a
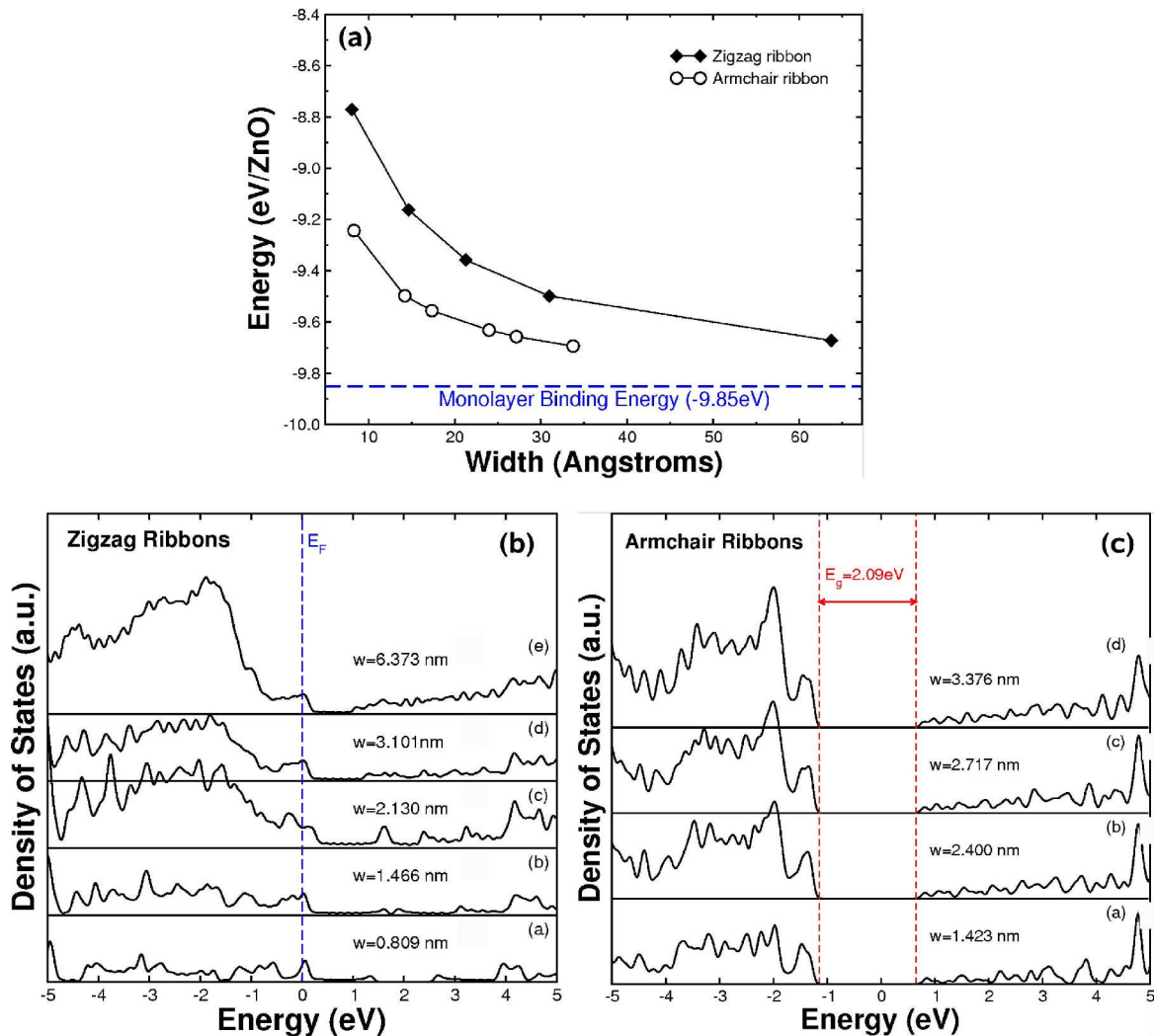
Figure 3.14: (a) Plot representing the binding energies for different ZnO nanoribbons that exhibit zigzag and armchair edges with different widths. Notice that, the armchair ribbons are more stable than the zigzag ribbons. The binding energy of the ribbons approaches the binding energy of a single ZnO monolayer. The corresponding infinite two-dimensional system (monolayer) shows a graphite-like structure, in which the Zn and O atoms share the same plane; (b) and (c) electronic density of states (DOS) for ZnO single layer nanoribbons with different widths (w) and edge terminations (zigzag and armchair): (b) the zigzag structures show states at the Fermi level (E_F); (c) note that all armchair ribbons reveal a semiconducting behavior with a band gap that is independent of the ribbon width, and corresponds to the band gap of the infinite 2D monolayer.

semiconducting behavior with a constant band gap of 2.09 eV (note that the calculated band gap for bulk ZnO exhibiting the Wurtzite structure is 0.76 eV). This band gap is very similar to that found in an infinite two dimensional (2D) ZnO planar monolayer (*e.g.,* 2.01 eV), thus we expect that the band gap will remain almost constant with increasing the width of the ribbon.

The electronic DOS for zigzag ribbons with a fixed width of 1.466 nm for up to 5
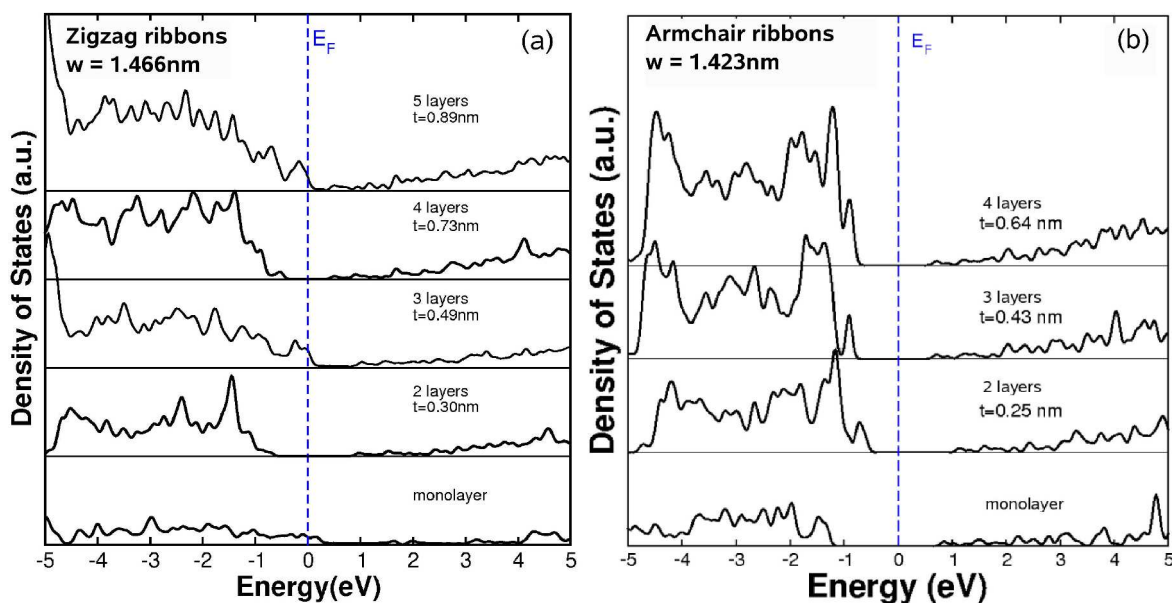
Figure 3.15: Plots of the electronic density of states (DOS) of ZnO nanoribbons with fixed width (w) and different thicknesses (t): (a) the single layered zigzag ribbon shows states close to the Fermi level; however, these states disappear when the thickness is increased. Interestingly, the states close to the Fermi level only appear when the system contains an odd number of layers; (b) note that all armchair nanoribbons always exhibit a semiconducting behavior.

layers (from 0 to 0.83 nm) is shown in figure 3.15a. As stated before, for an even number of ZnO layers the cations rearrange to bind with the anions of the next layer (surface reconstruction). This atomic rearrangement seems to avoid the formation of states close to the Fermi level (results shown in figure 3.15a for 2 and 4 layers respectively). However for an odd number of ZnO layers (3 & 5), we noted that the local DOS for the O atoms located on one side of the nanoribbon results in a significant number of states close to the Fermi level (figure 3.16). These results in the metallic behavior of odd layer nanoribbons (see Figure 3.15a). It is therefore clear that the number of stacked ZnO layers within the ribbons could result in either semiconducting or metallic materials (figure 3.15a).

The effect of thickness on the electronic properties of the armchair ribbons has also been addressed in this study. All these structures are always semiconducting with very similar band gaps (figure 3.15b).

The electronic band structures for a characteristic zigzag nanoribbons is shown in figure 3.17. The zigzag ribbons with metallic behavior exhibit band crossing the Fermi level. However, there is a clear difference between the monolayer (figure 3.11a) and the nanoribbons with odd number of layers. In the first case the edge

(a)3 layer zigzag ribbon   **(b)**5 layer zigzag ribbon
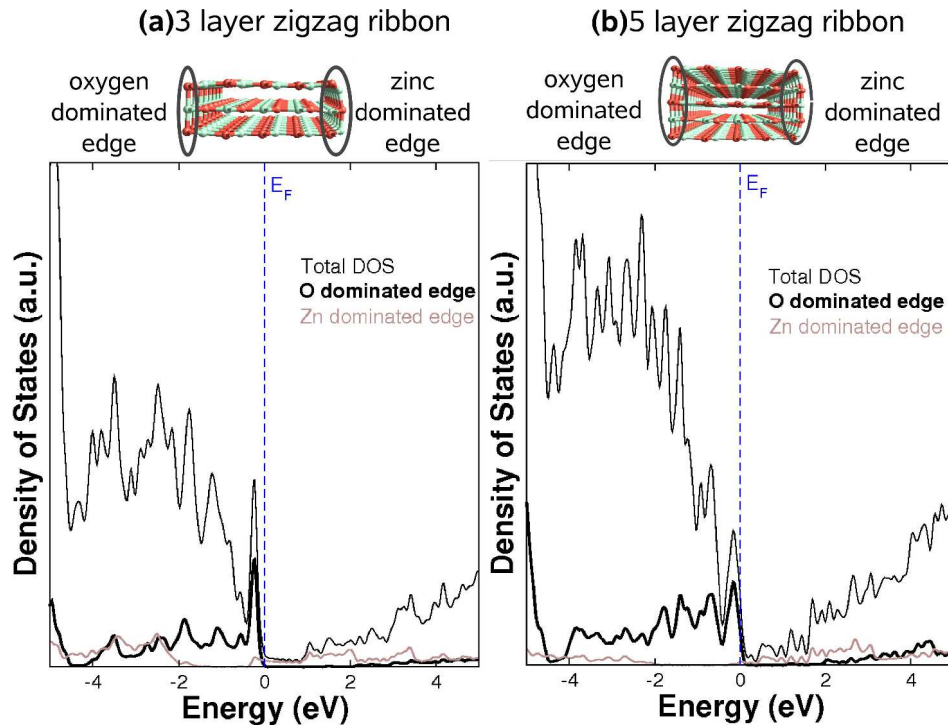
Figure 3.16: Plots of the local densities of states (LDOS) from different edges of ZnO nanoribbons, compared with the total density of states for: (a) a three layered zigzag ZnO nanoribbon, and (b) a five layered zigzag ZnO nanoribbon. The states close to the Fermi level are clearly arising by the oxygen dominated edges, whereas the zinc dominated edges do not contribute significantly to the states close to the Fermi level.

states are localized on the O atoms. However, the slight slope of the band crossing the Fermi level in the second case, indicate that these edge states are delocalized, and the electrons have higher mobility along one face of the thick ribbon (e.g., the O dominated edge for 3 & 5 layers; see figure 17). For armchair ribbons, the electronic band structure always exhibit a direct band gap of ca. 2 eV (figure 18).

Our results demonstrate that the electronic properties of ZnO nanoribbons can be tuned depending on the width, thickness and growth direction. Based on our calculations, the different electronic properties observed experimentally for ZnO ribbons (*e.g.*, a blue shift on the photoluminescence) could be explained due to
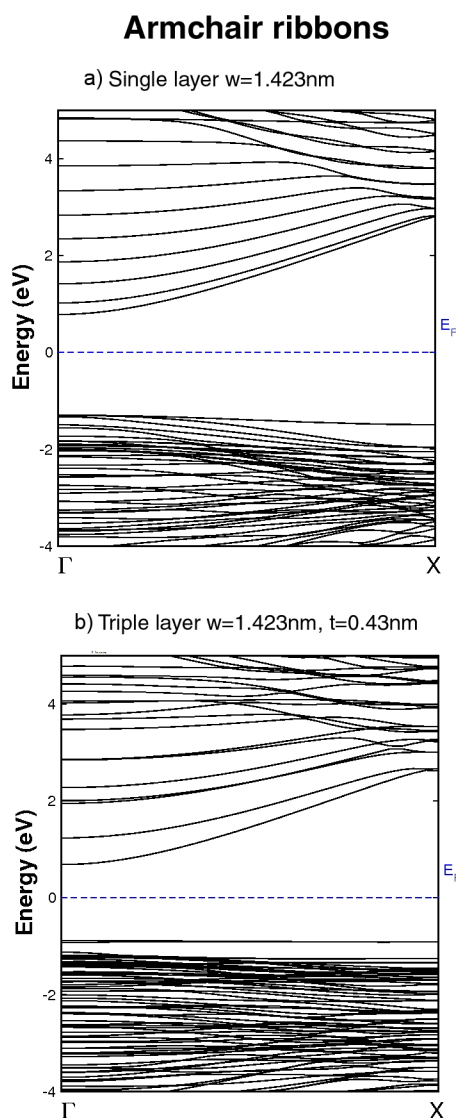
Zigzag ribbons

Triple layer w=1.466nm, t=0.49nm
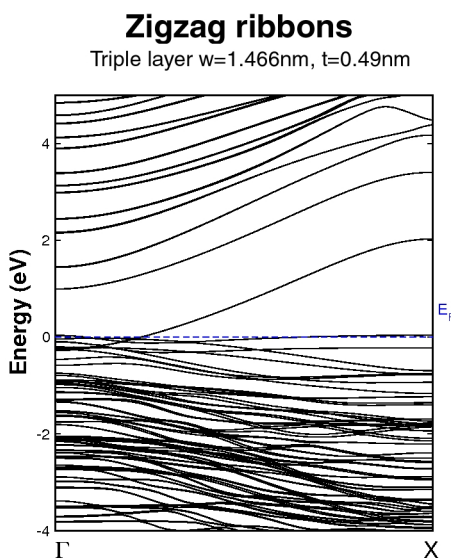
Figure 3.17: Band structure for a triple layer zigzag ZnO nanoribbon exhibiting states at the Fermi level.

changes in the thickness of the ribbons (number of layers), and not necessarily to the ribbon widths. The possibility of tuning the edge states based on the crystallographic orientation of the ribbon edges and size could lead to highly selective reactive materials.

In this case, we performed DFT calculations within the LDA+U approximation using a plane wave basis as implemented in the Quantum-ESPRESSO package [55] (see appendix B.3). The energy cut-off of the plane waves was set to 65Ry and 8 K-points were used for the sampling of the Broullin Zone. For the determination of the Hubbard U parameter, we adopted the proposal of Janotti, *et al.*, described above where the U parameter is defined as the energy interaction between the d electrons on the same atom screened by the macroscopic optical dielectric constant [18]. For a nanoribbon or monolayer, the screening would be very different from the bulk. Therefore, using the same U as in the bulk would not be a very accurate approximation. To address this, we calculated the dielectric constant for a monolayer, which would be a better estimate for the nanoribbons dielectric constant. The resulting value for U is 11.6eV. Using this effective on site Coulomb correlation

Armchair ribbons

a) Single layer w=1.423nm

b) Triple layer w=1.423nm, t=0.43nm

Figure 3.18: Band structure for armchair nanoribbons of different thickness, always showing a semiconducting behavior
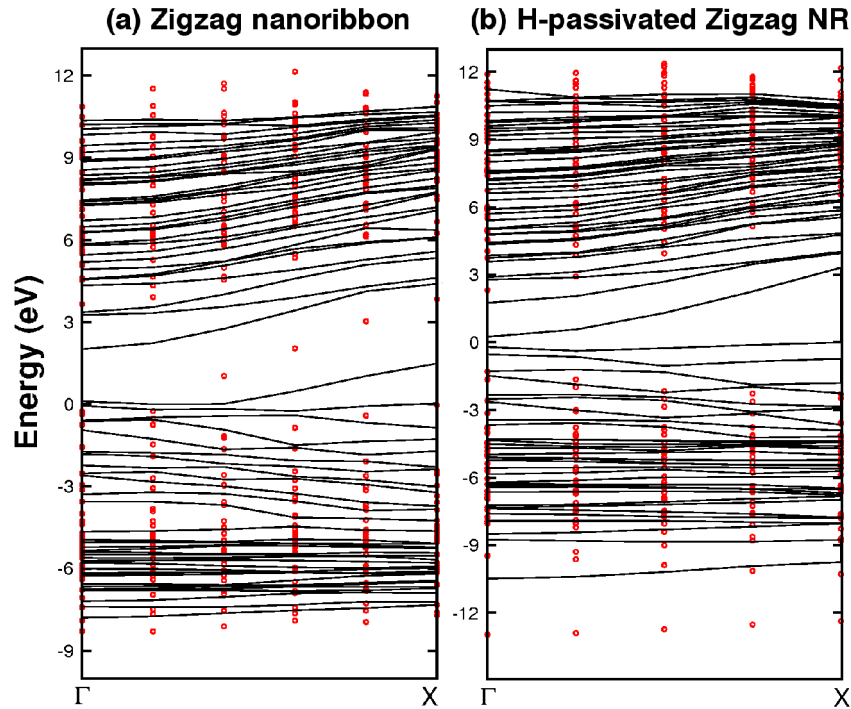
Figure 3.19: LDA-DFT band structure (solid lines) and quasiparticle energies (red dots) for a zigzag ZnO nanoribbon and a hydrogen passivated zigzag ZnO nanoribbon. The results confirm the DFT prediction of metallicity of zigzag ZnO nanoribbon, and show that hydrogen passivated zigzag ZnO nanoribbons are wide band gap semiconductors

interaction, we found that the correction performed by LDA+U changes the position of the *d* bands, shifting them several eV below the valence band maximum, thus leading to a decreased interaction with the O *p* bands. Despite the difference in the lower valence bands, the description of LDA is qualitative the same, since the LDA+U result exhibits states at the Fermi level, and a magnetic moment of $0.25\mu_B$ for the unpassivated zigzag nanoribbon.

Additionally, we have carried out non-self-consistent quasiparticle GW calculations (see appendix B.4) in order to verify that the electron electron interactions do not change the electronic properties of these nanoribbons. The calculations were done on top of LDA-DFT using the QE package and the YAMBO code [37,38]. The results are shown in figure 3.19. It can be noted that the introduction of electron-electron interactions do not change the edge states in ZnO zigzag nanoribbons. However, when the nanoribbon is passivated with hydrogen then the band gap opens considerably.

3.4.2. MAGNETIC PROPERTIES

The possibility of using the intrinsic charge transfer of semiconductors along with the spin information of the carriers makes ferromagnetic semiconductors the most promising materials for spintronics. The ultimate material for real sustainable applications should be cheap, bio-friendly and should have a Curie temperature (T_C) well above room temperature. As mentioned in Section 3, ZnO is a candidate for spintronic applications, and surface states can lead to magnetic moments, we have studied the magnetic properties of ZnO nanoribbons.

Figure 3.20 shows the total density of states for ZnO zigzag nanoribbons with different width (w). In all cases, we observed states at the Fermi level, and shifts in the spin density of states. The resultant magnetic moment corresponded to 0.55, 0.59, 0.62, and 0.65μ_B for ribbons exhibiting widths (w) of 1.466, 2.130, 3.101, and 6.373 nm respectively. We have also compared the binding energy between the LDA and LSDA calculations; the energy differences were of the order of 10^{-2} eV in which the energies calculated with the LSDA appeared more stable.

The effect of the thickness on the electronic and magnetic properties of the ZnO nanoribbons was also addressed in this study. When a second layer is stacked on top of the single layer, the system becomes semiconductor, and no spin shift is observed (figure 3.21a). However, when a third layer is stacked on top, the states at the Fermi level reappear with the presence of significant shifts between the spin densities of states (up and down; figure 3.21b). Nevertheless, when a fourth layer is stacked again, the states at the Fermi level vanish, and the structure becomes a semiconductor (figure 3.21c). As the number of layers increases to five, the states at the Fermi level are again observed, however, without shifts on the spin density of states (figure 3.21d).

The origin of this magnetic behavior was further studied using the charge density and spin density distribution (plotted in figure 3.22a), which shows the total charge distribution (up+down) for a single layer ribbon with w=2.130nm with the same orientation as that depicted in figure 3.13a. We note that the major contribution to the states on the Fermi level is due to edge states, and specifically to the O dominated edge. On this border, the charge distribution, and thus, the bond are significantly different to the charge distribution in the rest of the ribbon. The Zn-O bond on the edge is stronger and exhibits an excess of charge.

84
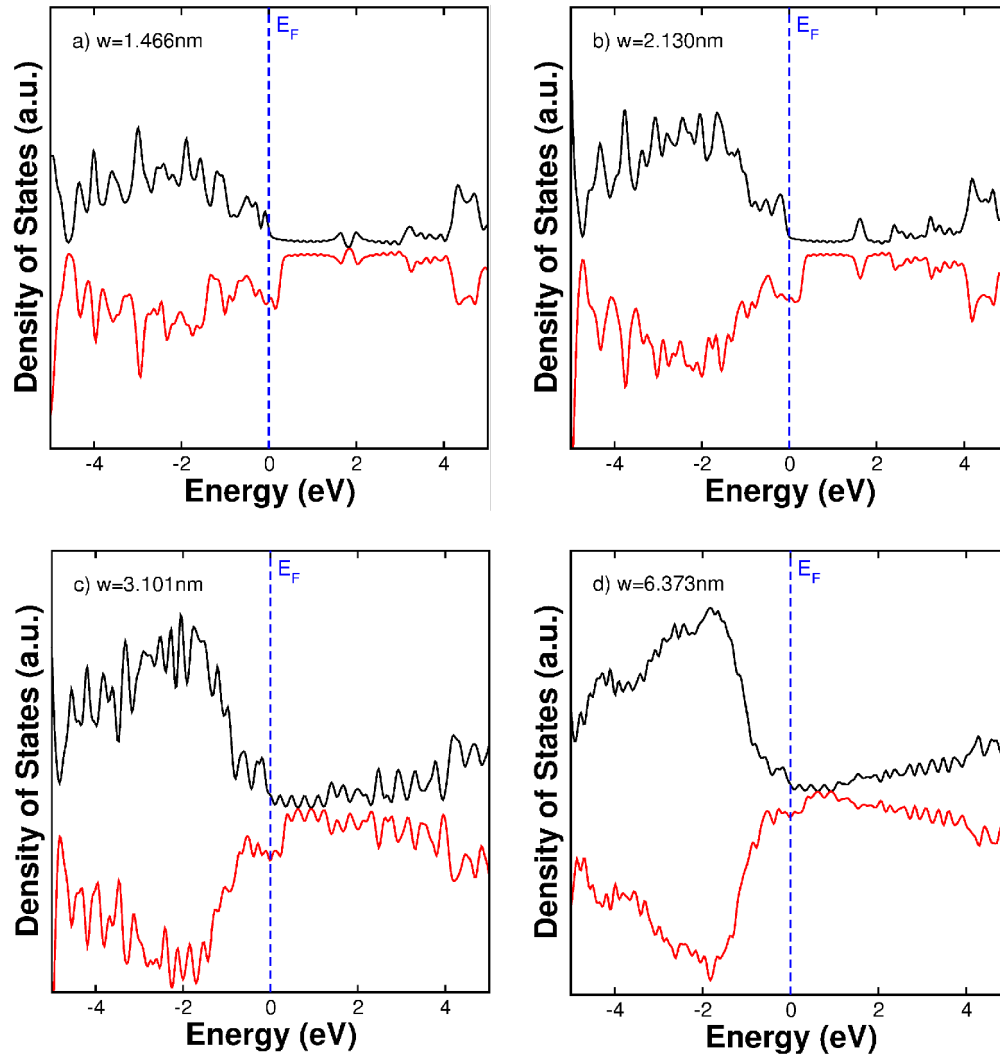
Figure 3.20: Plots of the electronic density of states (DOS) for the majority and minority spin of zinc oxide zigzag nanoribbons. Different values of the width of the ribbon are shown in (a), (b), (c) and (d). All systems exhibit a non-null magnetic moment. The Fermi level has been set to zero.

Our results clearly demonstrate that ZnO is able to possess magnetic end even ferromagnetic behavior without the introduction of metal impurities. As Garcia *et al.,* have concluded from experimental results, these properties arise only from changes in the electronic structure [8]. Therefore, the results showed here open up the possibility of having ferromagnetism at room temperature in finite layered ZnO systems.

Recently, Chen and coworkers found that zigzag ZnO nanoribbons will turn half-metallic when the Zn atoms at the edge are passivated with hydrogen [39]. Moreover, they find the half-metallicity only emerges in the ribbons with relatively
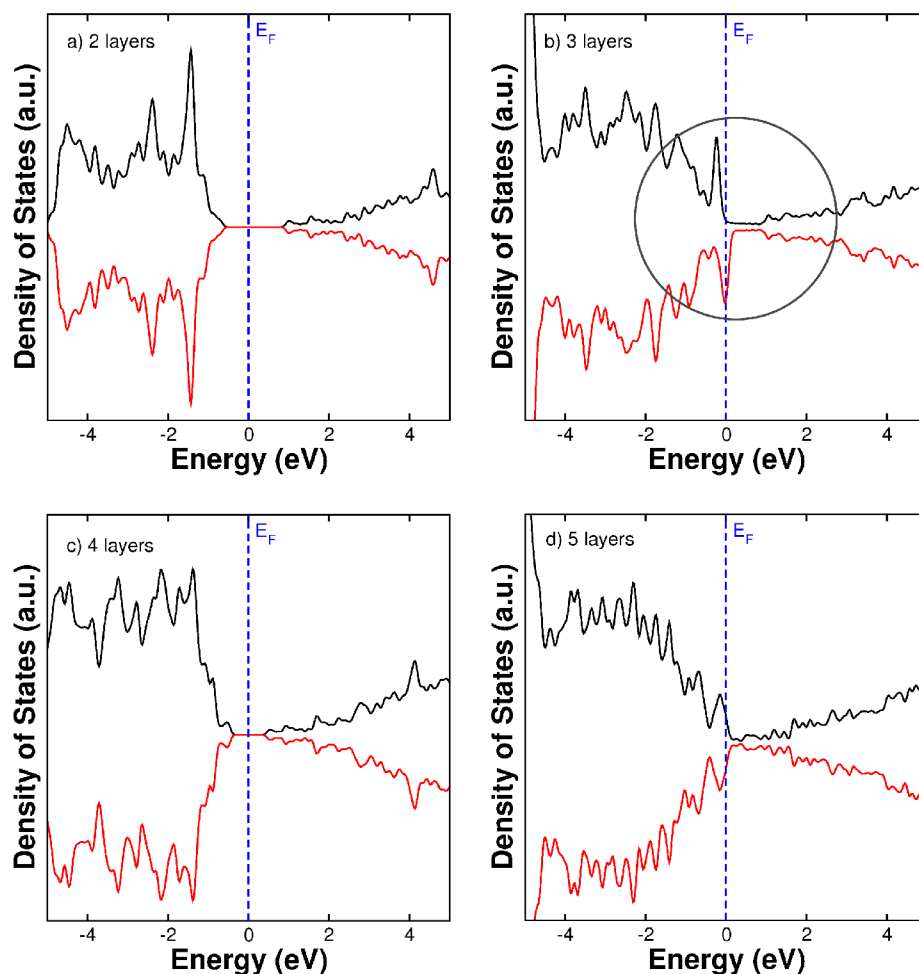
Figure 3.21: Plots of the electronic density of states (DOS) for the majority and minority spin of zinc oxide zigzag nanoribbons. Different values of the thickness or layers of the ribbon are shown in (a), (b), (c) and (d). The width of the ribbons is fixed to w=1.466 nm. Notice that the system with 3-layers exhibits a shift in the majority and minority spin density of states and consequence a magnetic moment is obtained. The Fermi level has been set to zero.

large width. However, the passivation of Zn atoms with hydrogen is not very favorable. Nevertheless, they show that the half-metallicity can also be achieved when the saturation is done with CH_3 or NH_2 molecules [39].

However, there is still need to shed some light on the effect of S atoms in the magnetic properties of ZnO systems. We demonstrate below that the S-passivation in ZnO systems promotes strong ferromagnetism. This finding is remarkable due to possible technological applications regarding information storage, processing devices and spintronics. Using density functional theory, we predict ferromagnetism enhancement in two ZnO systems: nanoparticles and nanoribbons when passivated with S or thiol groups. Recent experimental results, related to the
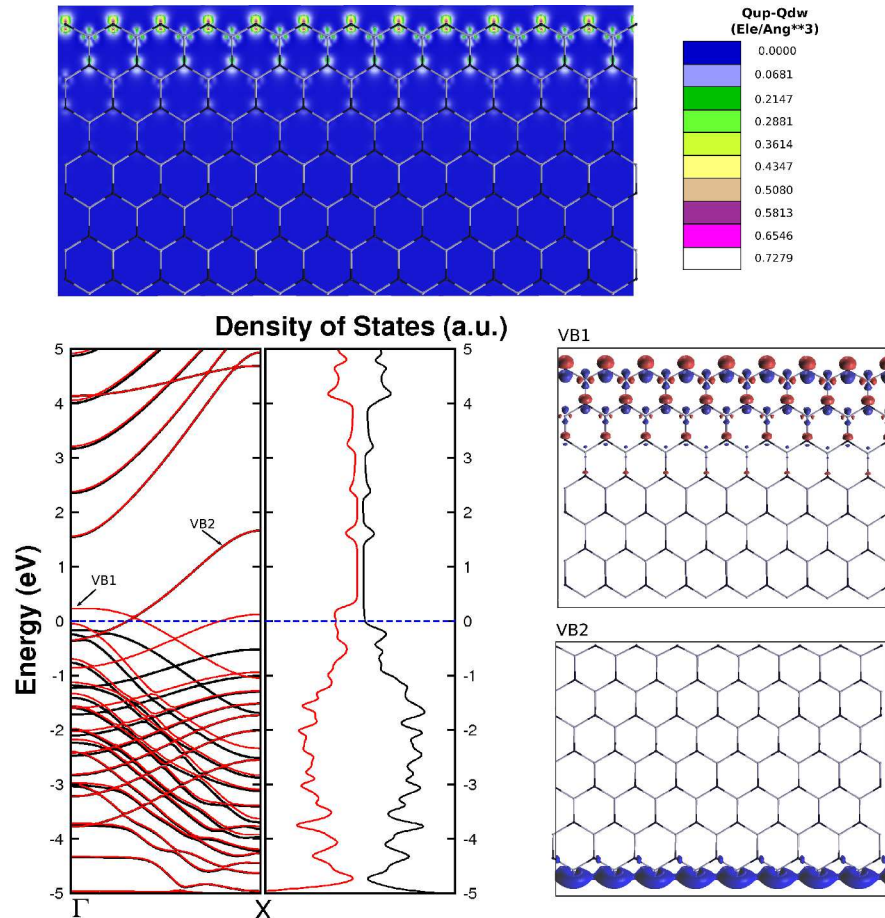
Figure 3.22: (Top): Difference in charge energy density (up-down) for a zinc oxide nanoribbon with zigzag edges, showing that the magnetic moment is due to the oxygen dominated edges. (bottom) Band structure, density of states, and wavefunctions of the top valence

production of very thin films of ZnO adopting a boron-nitride-like planar structure, have inspired our choice for one of the systems studied here [26]. Above, we have observed using first principles calculations that one-dimensional undoped ZnO nanostructures, and in particular zigzag nanoribbons, are metallic and could exhibit small ferromagnetic responses. However, when these ribbons are passivated with S or methanethiol (CH_3S), the magnetic moment increases significantly. Local density of states (LDOS) calculated on the S, Zn and O atoms within the ZnO nanoribbon's unit cell, indicate that the main contribution to the total magnetic moment arises from the S atoms. Similarly, we have also found that ZnO clusters could exhibit enhanced ferromagnetism when they are passivated with S atoms; a high magnetic moment is obtained. The ferromagnetic behavior found in these S-passivated ZnO nanoparticles is attributed to weak coordinated atoms located on the cluster surface.
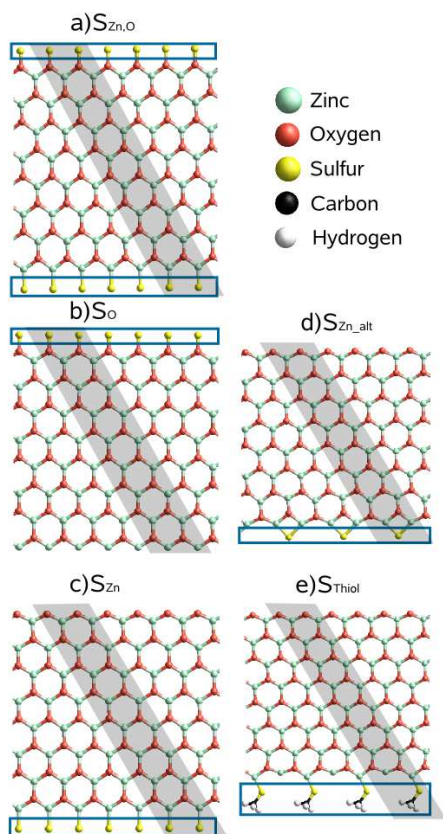
Figure 3.23: Molecular models of ZnO nanoribbons passivated with sulfur. (a) Both the Zn and the O dominated edges are passivated. (b) Only the Zn dominated edge is passivated. (c) Only the O dominated edge is passivated. (d) Sulfur alternated passivation of the Zn dominated edge. All the structures were relaxed using a conjugate gradient method. Note that for (d), the sulfur atoms are binded to two zinc atoms.

In figure 3.23, we show five different forms of S-passivated ZnO zigzag nanoribbons that were constructed by cutting a planar monolayer along two parallel zigzag lines. The ribbons are periodic in the "x" direction with the width defined in the "y" direction. Note that if the ribbons were periodic in the "y" direction, these would exhibit armchair edges. However, we are not interested in this kind of ribbons since as mentioned above, they are semiconducting and do not exhibit a ferromagnetic behavior. For all zigzag nanoribbons, the S or thiol groups are attached to the ribbon atoms located on the edges. The shaded regions in figure 3.23 schematically represent the unit cell.

We have studied nanoribbons passivated with S on the both edges (label $S_{Zn,O}$, see figure 3.23a). Here, a S atom is attached to a Zn or O atom. The spin-resolved density of states (figure 3.24a) shows a shift of the spin up and spin down densities with a reduction of approximately 10% ($0.59\mu_B$) of the magnetic moment with respect to the corresponding unpassivated system ($0.65\mu_B$). We have determined that the main contribution to the total magnetic moment comes from the O-dominated edge. Therefore, the addition of S-passivation on both edges does not affect considerably the electronic and magnetic properties of the nanoribbons. However, the magnetic moment of the nanoribbons varies depending on how the S atoms are attached to the edges (see below).

Figures 3.23b and 3.23c depict the morphology of the ZnO zigzag nanoribbons passivated on the O-terminated edge (label S_O), and Zn-terminated edge (label S_{Zn}) respectively. In both cases, the spin resolved density of states reveal a shift in the
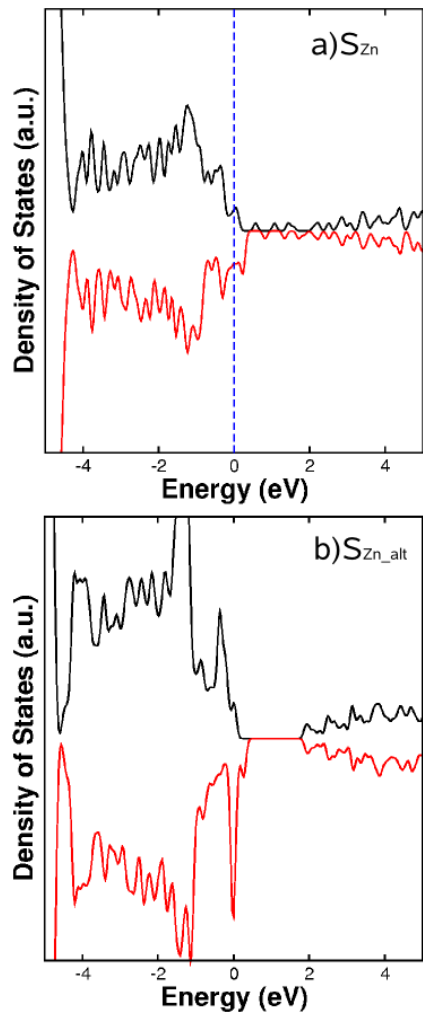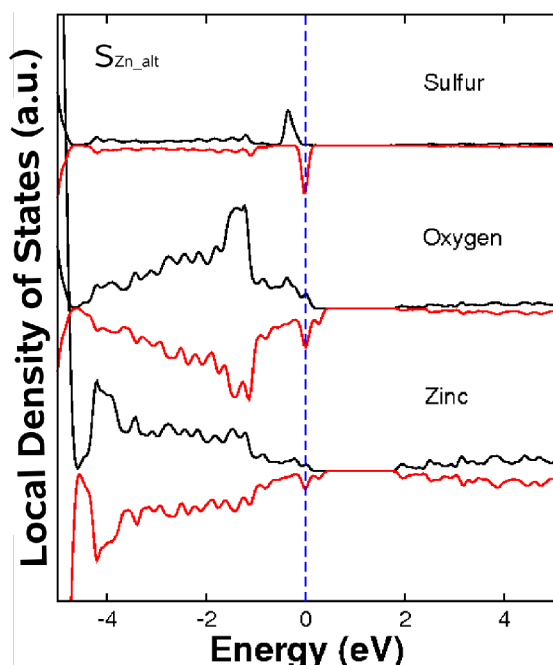
Figure 3.24: Spin-polarized electronic density of states of ZnO nanoribbons passivated with sulfur. Note that all systems show a shift in the density of states, and consequently a magnetic moment is obtained. (a) Nanoribbon passivated on the Zn-terminated edge showing μ=0.72 μ_B (the structure can be seen in Fig. 3.23c). (b) Nanoribbon passivated on the Zn-terminated edge in an alternating form, showing an increased magnetic moment of 1.4 μ_B (the structure can be seen in Fig. 3.23d). The magnetic moment of the unpassivated ribbon is 0.65 μ_B.

up and down spins, although it is substantially less in the first case. The magnetic moment of the S_O ribbon is only 18% of the magnetic moment of the unpassivated ZnO nanoribbon (0.12μ_B), while the magnetic moment of the S_{Zn} ribbon is increased by approximately 10% (0.72μ_B). In addition, the S_{Zn} ribbon is more energetically stable than S_O ribbons, and S tends to bind preferentially to Zn instead of O.

From the experimental point of view, it is difficult to have S passivating each of the two coordinated atoms (O and Zn) within the nanoribbon. Moreover, S has several oxidation numbers. Therefore, we tried to passivate the Zn-dominated edge with a single S every two Zn atoms (alternated passivation), label S_{Zn_alt} in figure 3.23d. The S_{Zn_alt} nanoribbon still exhibits states at the Fermi level, and a shift in the DOS, as shown in figure 3.24b. Here, the magnetic moment is enhanced more than twice when compared to the unpassivated ribbon (0.65μ_B), thus resulting in a total magnetic moment of 1.4μ_B.

Figure 3.25 depicts the local density of states (LDOS) for the S_{Zn_alt} nanoribbon. The DOS was calculated in all the Zn sites, and then added. Similar procedure was followed for the S and O case. It can be observed that all types of atoms (Zn,O, and S) exhibit states at the Fermi level, and a shift in the spin up and down. For S, only states with spin down can be observed at the Fermi level with almost zero states in the conduction band, contrary to the O and Zn atoms. From magnetic moment calculations, we note that the S-atoms exhibit a major contribution to the total magnetic moment.

Additionally, the effect of passivating a ZnO zigzag

Figure 3.25: Spin-polarized local electronic density of states for the nanoribbons with alternating S atoms along to the Zn-terminated edges (the structure can be seen in figure 3.23d). Results for sulfur, zinc, and oxygen atoms are shown. Notice that all atoms exhibit a shift between the spin-up and spin-down density of states, and consequently all atoms contribute to the total magnetic moment.

nanoribbon with a thiol molecule was investigated. In this case, a methanethiol molecule (CH_3S) was attached to two Zn atoms on the Zn dominated edge of the zigzag nanoribbons (figure 3.23d; label S_{Thiol}). After geometric optimization, the S atom is not bound to two Zn atoms. The DOS of this system (not shown here) displays a shift in the spin up and spins down, and exhibits a magnetic moment of approximately $1\mu_B$. Since the calculations of the ribbons with the thiol molecules are very expensive in terms of computational time, we only performed one case. However, it is clear from this exercise, that the effect of passivating with thiol molecules is qualitatively the same as with pure S passivation.

García et al. demonstrated that thiol passivated nanoparticles exhibit a ferromagnetic response [8] (see figure 3.1). Therefore, we also investigated the effect of passivating a ZnO nanocluster with S atoms. We performed spin-polarized calculations in a $Zn_{15}O_{15}$ cluster constructed from the Wurtzite crystal, and attached S atoms to each of the Zn atoms coordinated less than four times (see the unrelaxed cluster in figure 3.9). The whole structure was then energetically minimized. In this case, even when the unpassivated $Zn_{15}O_{15}$ showed a zero magnetic moment without states at the Fermi level (see §3.2), the S-passivated cluster exhibits a huge magnetic moment (μ = $5.5\mu_B$) and states at the Fermi level. As in the case of the nanoribbons, the magnetic moment comes mainly from the S atoms. We note from the relaxed molecule that the S atoms tend to bond with other S atoms and with Zn atoms rather than with O atoms. This observation is consistent with the nanoribbon case in which the S_{Zn} is more stable than S_O. The results of this particular cluster clearly

confirm that S atoms play a crucial role in the ferromagnetic properties. The DOS of the $Zn_{15}O_{15}$ cluster is interesting because it exhibits only spin down excitation states. This kind of materials would be very interesting for spintronic applications, since a spin coherent excitation could be used for different channels of electronic transport.

Certainly, the idea of magnetism in systems containing non magnetic atoms (or d_0 ferromagnetism), challenges our understanding because exchange mechanisms cannot be responsible for this behavior. Coey has reviewed different systems exhibiting d_0 ferromagnetism, and he has proposed that this behavior can be induced by lattice defects and impurities giving rise to magnetic moments associated with molecular orbitals localized in the vicinity of the defects [40]. In the systems studied here, the major components to the magnetic moment are *p* orbital magnetic moments (shown in figure 3.25) of the atoms localized in the vicinity of the S impurities. The contribution to the total DOS of the *p* orbitals are the sum of the O *2p*, S *3p* and Zn *4p* orbitals. These orbitals are also the major contribution to the conduction states.

We have demonstrated the importance of the S- and thiol-passivation in ZnO nanoribbons and clusters. We believe that our results could explain the recent experimental results of the ferromagnetism observed in ZnO nanoparticles, because the presence of S plays a crucial role in the magnetic properties of the different systems investigated in this work. For example, pure $Zn_{15}O_{15}$ cluster exhibits a null magnetic moment, however if the same cluster is passivated with S atoms, a large magnetic moment is obtained ($5.5\mu_B$). In addition, zigzag nanoribbons are excellent candidates for ferromagnetic materials. We found that when the S atoms are attached to Zn atoms in an alternated way along one edge, the magnetic moment is increased significantly. In summary, the findings related to ferromagnetism in nanostructures doped with non-magnetic elements becomes novel and interesting due to potential applications of these new magnetic materials for the data storage industry.

3.5. CONCLUSIONS

In this work, we have contributed to the development of nanoscale ZnO science. The calculations of the magnetic properties of ZnO nanoparticles with different

environments should help experimentalists to plan and direct future work in order to improve the magnetic response of their samples. As we have shown, it is very important to control the environment of the surface atoms. For S as capping agent as has been done experimentally [8], it is very important that the nanoparticle remains crystalline, and that there is no migration of S into the nanoparticle. These structures could be very interesting for information storage and spintronic applications.

After the observation of a new hexagonal planar phase of ZnO by Tusche [26], there have been some works regarding the properties of hypothetical ZnO single walled nanotubes [31-33]. However, we have proposed that a more achievable 1D nanostructure based on such HX phase would be the ZnO nanoribbons described above. We have demonstrated that this novel and original idea could have interesting technological applications. For instance, armchair ZnO nanoribbons could be used as optoelectronic components in a new kind of 2D electronics which will be discussed in §6. Zigzag ZnO nanoribbons either with S or without passivation could be used in spintronic devices, with the advantage over ZnO nanoparticles that the connection to the leads seems significantly easier.

There are many open questions that should be addressed in order to make this calculations reach their intended applications. For the magnetic response of the ZnO nanoparticles, it would be interesting to study larger systems. This could not be done in a reasonable time in this work due to time constrains. However, as the nanoparticles grow larger, the effect of capping or doping concentrations could be studied and should play an important role. *Ab-initio* based semi-empirical approaches could be very helpful for this matter. In addition, as for any application this systems must be coupled with an electronic device, it would be very interesting to study the magnetic, electronic and transport properties of ensembles of ZnO nanoparticles.

It is clear that the most important question to address in the case of ZnO nanoribbons is whether these edge states are observed experimentally. For that, it would be important to first reproduce the experiment of Tusche [26], and then follow one of several techniques that have been applied for other 2D layered materials (see §6). In principle, as in other 2D layered materials, electron lithography could be used to pattern sheets of ZnO to produce arrays of nanoribbons in any shape. Another issue that remains open is the effect of

substrates on the electronic and magnetic properties of ZnO nanoribbons, as such effects have been important in other 2D systems, such as graphene (see §4). As in the case of nanoparticles, it would be interesting to study and understand the coupling of these systems to contacts for an eventual electronic device. These contacts or electronic probes could be conventional ones, such as gold or silver, or more oriented to the novel 2D electronics, such as graphene nanoribbons. In any case, the understanding of the transport properties of such systems could dictate the direction and the role of ZnO in the future of 2D electronics.

3.6. COMPUTATIONAL DETAILS

The electronic calculations have been carried out using the density functional theory in the framework of local spin density approximation (LSDA) with the Ceperley Alder parametrization [41] and a basis of linear combination of atomic orbitals (LCAO) as implemented in the SIESTA code [42]. We use a double-ζ basis set with additional polarization orbitals. The pseudo-potentials (pp's) were constructed from 12, 6, 6, and 4 valence electrons for the Zn, O, S, and C ions respectively (Zn: $4s^2 3d^{10}$, O: $2s^2 2p^4$, S: $3s^2 3p^4$, C: $2s^2 2p^2$). The Troullier-Martins scheme was used [43]. The basis and the pp's were tested on the bulk zinc oxide Wurtzite structure showing an energy gap (Eg) of 0.76 eV, and cell parameters that are consistent with previous LDA calculations. No spin polarization was observed for the bulk Wurtzite case.

We have verified that the approximations used in our work do not give artificial metallicity or spin polarization, using a plane wave basis and hybrid functionals. We have performed two more calculations for the 1.466nm zigzag nanoribbon to make sure the magnetic properties do not disappear upon the inclusion of different functionals. We used a generailzed gradient approximation (GGA) functional (BLYP)[44,45], and a hybrid functional with 50% LDA and 50% GGA for both exchange and correlation. The results are summarized in the following table:

Functional	Magnetic Moment
LDA (CA)	0.550845
GGA (BLYP)	0.584264
HYBRID (50% CA, 50% BLYP)	0.525172

We also verified that neglecting the electron-electron interaction due to local density approximations, does not change the qualitatively results presented here. We performed DFT calculations within the LDA+U approximation using a plane wave basis as implemented in the Quantum-ESPRESSO package [37]. The energy cut-off of the plane waves was set to 65Ry and 8 K-points were used for the sampling of the Broullin Zone. The determination of the Hubbard U was carried out using the approach of Janotti, *et al.* [46]. The resulting value for U is 11.6eV.

The nanoribbon structures in this work were constructed from planar ZnO, and calculations were carried out on large periodic unit cells that prevent unrealistic interactions. The clusters were constructed from segments of the Wurtzite structure. All the structures were relaxed using a congugate gradient (CG) algorithm with variable cell and with a force threshold of 0.04eV/Å.

3.7. RELATED PUBLISHED WORK

Botello-Méndez, A. R.; Martínez-Martínez, M. T.; López Urías, F.; Terrones, M.; Terrones, H. Metallic edges in zinc oxide nanoribbons. *Chem. Phys. Lett.* **448** 258 (2007).

Botello-Méndez, A. R.; López Urías, F.; Terrones, M.; Terrones, H. Magnetic behavior in zinc oxide zigzag nanoribbons. *Nano Lett.* **8**, 1562 (2008).

Botello-Mendez, A. R.; López Urías, F.; Terrones, M.; Terrones, H. Enhanced ferromagnetism in ZnO nanoribbons and clusters passivated with sulfur. *Nano Res.* **1** 420 (2008).

Botello-Mendez, A. R.; López Urías, F.; Terrones, M.; Terrones, H. Carbon and Sulfur Impurities in Zinc Oxide Nanostructures could Taylor their Electronic and Magnetic Properties *J. Phys. Chem. C (submitted)*
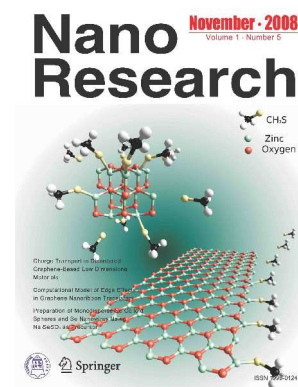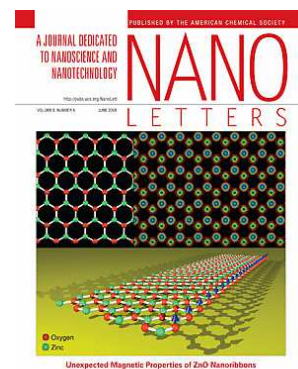
3.8. REFERENCES

[1]. Xiong, G., Pal, U. & Serrano, J.G. Correlations among size, defects, and photoluminescence in ZnO nanoparticles. *J. Appl. Phys.* **101**, 024317-6 (2007).

[2]. Viswanatha, R., Amenitsch, H., & Sarma, D. D. Growth Kinetics of ZnO Nanocrystals: A

Few Surprises. *J. Am. Chem. Soc.* **129**, 4470 (2007).

[3]. Viswanatha, R., Santra, P.K., Dasgupta, C. & Sarma, D.D. Growth Mechanism of Nanocrystals in Solution: ZnO, a Case Study. *Phys. Rev. Lett.* **98**, 255501-4 (2007).

[4]. Zhang, J., Liu, H., Wang, Z. & Ming, N. Synthesis and band gap of ZnO particles with hexagonal bilayer structure. *Appl. Phys. Lett.* **90**, 113117-3 (2007).

[5]. Brehm, J.U., Winterer, M. & Hahn, H. Synthesis and local structure of doped nanocrystalline zinc oxides. *J. Appl. Phys.* **100**, 064311-9 (2006).

[6]. Dietl, T., Ohno, H., Matsukura, F., Cibert, J. & Ferrand, D. Zener Model Description of Ferromagnetism in Zinc-Blende Magnetic Semiconductors. *Science* **287**, 1019-1022 (2000).

[7]. Sundaresan, A., Bhargavi, R., Rangarajan, N., Siddesh, U. & Rao, C.N.R. Ferromagnetism as a universal feature of nanoparticles of the otherwise nonmagnetic oxides. *Phys. Rev. B* **74**, 161306-4 (2006).

[8]. García, M. A.; Merino, J. M.; Fernández Pinel, E.; Quesada, A.; de la Venta, J.; Ruíz González, M. L.; Castro, G. R.; Crespo, P.; Llopis, J.; González Calbet, J. M.; Hernando, A. Magnetic Properties of ZnO Nanoparticles. *Nano Lett.* **7**, 1489-1494 (2007).

[9]. Banerjee, S., Mandal, M., Gayathri, N., & Sardar, M. Enhancement of ferromagnetism upon termal annealing in pure ZnO. *Appl. Phys. Lett.* **91**, 182501(2007).

[10]. Pan, H. et al. Room-Temperature Ferromagnetism in Carbon-Doped ZnO. *Phys. Rev. Lett.* **99**, 127201-4 (2007).

[11]. Joswig, J., Roy, S., Sarkar, P. & Springborg, M. Stability and bandgap of semiconductor clusters. *Chem. Phys. Lett.* **365**, 75-81 (2002).

[12]. Wang, B., Wang, X., Chen, G., Nagase, S. & Zhao, J. Cage and tube structures of medium-sized zinc oxide clusters (ZnO)[sub n] (n = 24, 28, 36, and 48). *J. Chem. Phys.* **128**, 144710-6 (2008).

[13]. Wang, B., Nagase, S., Zhao, J. & Wang, G. Structural Growth Sequences and Electronic Properties of Zinc Oxide Clusters (ZnO)n (n=2-18). *J. Phys. Chem. C* **111**, 4956-4963 (2007).

[14]. Jain, A., Kumar, V. & Kawazoe, Y. Ring structures of small ZnO clusters. *Comp. Mater. Science* **36**, 258-262 (2006).

[15]. Li, C., Guo, W., Kong, Y. & Gao, H. First-principles study of the dependence of ground-state structural properties on the dimensionality and size of ZnO nanostructures. *Phys. Rev. B* **76**, 035322-8 (2007).

[16]. Li, C., Guo, W., Kong, Y. & Gao, H. First-principles study on ZnO nanoclusters with hexagonal prism structures. *Appl. Phys. Lett.* **90**, 223102-3 (2007).

[17]. Zhang, L. & Huang, H. Structural transformation of ZnO nanostructures. *Appl. Phys. Lett.* **90**, 023115-3 (2007).

[18]. Zhao, M., Xia, Y., Tan, Z., Liu, X. & Mei, L. Design and energetic characterization of ZnO clusters from first-principles calculations. *Phys. Lett. A* **372**, 39-43 (2007).

[19]. Schoenhalz, A.L., Arantes, J.T., Fazzio, A. & Dalpian, G.M. Surface magnetization in non-doped ZnO nanostructures. *Appl. Phys. Lett.* **94**, 162503-3 (2009).

[20]. Coey, J.M.D., Wongsaprom, K., Alaria, J. & Venkatesan, M. Charge-transfer ferromagnetism in oxide nanoparticles. *J. Phys. D-Appl.* **41**, 134012 (2008).

[21]. Puzder, A., Williamson, A.J., Gygi, F. & Galli, G. Self-Healing of CdSe Nanocrystals: First-Principles Calculations. *Phys. Rev. Lett.* **92**, 217401 (2004).

[22]. Zhang, J. et al. Magnetic Molybdenum Disulfide Nanosheet Films. *Nano Lett.* **7**, 2370-2376 (2007).

[23]. Tan, S.T. et al. p-type conduction in unintentional carbon-doped ZnO thin films. *Appl. Phys. Lett.* **91**, 072101-3 (2007).

[24]. Tasker, P.W. The stability of ionic crystal surfaces. *J. Phys. C: Solid State Phys.* **12**, 4977-4984 (1979).

[25]. Freeman, C.L., Claeyssens, F., Allan, N.L. & Harding, J.H. Graphitic Nanofilms as Precursors to Wurtzite Films: Theory. *Phys. Rev. Lett.* **96**, 066102-4 (2006).

[26]. Tusche, C., Meyerheim, H.L. & Kirschner, J. Observation of Depolarized ZnO(0001) Monolayers: Formation of Unreconstructed Planar Sheets. *Phys. Rev. Lett.* **99**, 026102-4 (2007).

[27]. Wander, A. et al. Stability of Polar Oxide Surfaces. *Phys. Rev. Lett.* **86**, 3811 (2001).

[28]. Dulub, O., Boatner, L.A. & Diebold, U. STM study of the geometric and electronic structure of ZnO (0001)-Zn,(0001)-O,(1010), and (1120) surfaces. *Surf. Sci.* **519**, 201-217 (2002).

[29]. Tu, Z.C. First-principles study on physical properties of a single ZnO monolayer with graphene-like structure. ArXiv 0901.1112 (2009).at <http://arxiv.org/abs/0901.1112>

[30]. Terrones, H. et al. New Metallic Allotropes of Planar and Tubular Carbon. *Phys. Rev. Lett.* **84**, 1716 (2000).

[31]. Tu, Z.C. & Hu, X. Elasticity and piezoelectricity of zinc oxide crystals, single layers, and possible single-walled nanotubes. *Phys. Rev. B* **74**, 035434-6 (2006).

[32]. Erkoç, S. & Kökten, H. Structural and electronic properties of single-walled ZnO nanotubes. *Physica E.* **28**, 162-170 (2005).

[33]. Wang, B., Nagase, S., Zhao, J. & Wang, G. The stability and electronic structure of single-walled ZnO nanotubes by density functional theory. *Nanotechnol.* **18**, 345706 (2007).

[34]. Xiang, H. J., Yang, J., Hou, J. G., & Zhu, Q. Piezoelectricity in ZnO nanowires: A first-principles study. *Appl. Phys. Lett.* **89**, 223111 (2006).

[35]. Kulkarni, A.J., Zhou, M., Sarasamak, K. & Limpijumnong, S. Novel Phase Transformation in ZnO Nanowires under Tensile Loading. *Phys. Rev. Lett.* **97**, 105502-4 (2006).

[36]. Wang, X., Ding, Y., Summers, C.J. & Wang, Z.L. Large-Scale Synthesis of Six-Nanometer-Wide ZnO Nanobelts. *J. Phys. Chem. B* **108**, 8773-8777 (2004).

[37]. Giannozzi, P. et al. QUANTUM ESPRESSO: a modular and open-source software project for quantum simulations of materials. *J. Phys.: Condens. Matter* **21**, 395502 (2009).

[38]. Marini, A., Hogan, C., Grüning, M. & Varsano, D. yambo: An ab initio tool for excited state calculations. *Comp. Phys. Commun.* **180**, 1392-1403 (2009).

[39]. Chen, Q., Zhu, L. & Wang, J. Edge-passivation induced half-metallicity of zigzag zinc oxide nanoribbons. *Appl. Phys. Lett.* **95**, 133116-3 (2009).

[40]. Coey, J. d0 ferromagnetism. *Solid State Sci.* **7**, 660-667 (2005).

[41]. Ceperley, D.M. & Alder, B.J. Ground State of the Electron Gas by a Stochastic Method. *Phys. Rev. Lett.* **45**, 566 (1980).

[42]. Soler, J.M. et al. The SIESTA method for ab initio order-N materials simulation. *J. Phys.: Condens. Matter* **14**, 2745-2779 (2002).

[43]. Troullier, N. & Martins, J.L. Efficient pseudopotentials for plane-wave calculations. *Phys. Rev. B* **43**, 1993 (1991).

[44]. Becke, A.D. Density-functional exchange-energy approximation with correct asymptotic behavior. *Phys. Rev. A* **38**, 3098 (1988)

[45]. Lee, C., Yang, W., Parr, R. G. Development of the Colle-Salvetti correlation-energy formula into a functional of the electron density. *Phys. Rev. B* **37**, 785 (1988)

[46]. Janotti, A., Segev, D. & Van de Walle, C.G. Effects of cation d states on the structural and electronic properties of III-nitride and II-oxide wide-band-gap semiconductors. *Phys. Rev. B* **74**, 045202-9 (2006).

Chapter 4

Nanoscale Carbon

CONTENTS

4.1. INTRODUCTION

It is well known that the properties of carbon materials heavily depend on the environment of each of the carbon atoms in its structure. The four valence electrons in carbon atoms ($2s^2 2p^2$) give rise to $2s$, $2p_x$, $2p_y$, and $2p_z$ orbitals which can mix forming the strong covalent bonds in carbon structures. Several possibilities for electron configuration or hybridization of the atomic orbitals can arise, leading to different properties of carbon materials.

The flexibility of the carbon-carbon bond results in a large family of nanoscale carbon materials which can exhibit a different kind of hybridization yielding different properties (see figure 4.1). For instance, a carbon nanotube can be thought of as a single graphite sheet (or graphene) rolled to form a cylinder of nanometer size diameter. The curvature of the nanotubes lead to a small amount of sp^3-like bonding such that the bonds in the circumferential direction are slightly weaker than those along the nanotube axis. The effect of curvature and the mixing of sp^2 and sp^3 bonding is also true for fullerenes. In this case, additional hybridization occurs due to the introduction of pentagon rings. In contrast, nano-diamond clusters and particles exhibit an admixing of sp^2 bonding. Carbon nanoribbons are finite graphene sheets exhibiting edges. The hybridization in these edges depend on the shape of the edge, and can lead to different electronic and chemical properties.

In this work, we present the properties of nanoscale carbon materials. We first briefly introduce the properties of the widely studied family of fullerenes and carbon nanotubes. Then we present the characteristics of the recently synthesized graphene and graphene nanoribbons, which have interesting new properties. In the next two chapters, we will describe different synthesis methods focused on large-scale production of graphene sheets and graphene nanoribbons, some of which were developed at our laboratory (§5), and some of the new properties of nanoribbons and other materials (§6). This chapter introduces the state of the art nanoscale carbon and sets the background for our perspectives on how the interesting field of nanocarbon materials will evolve in the next years based on the current technological needs and the problems for assessing them.
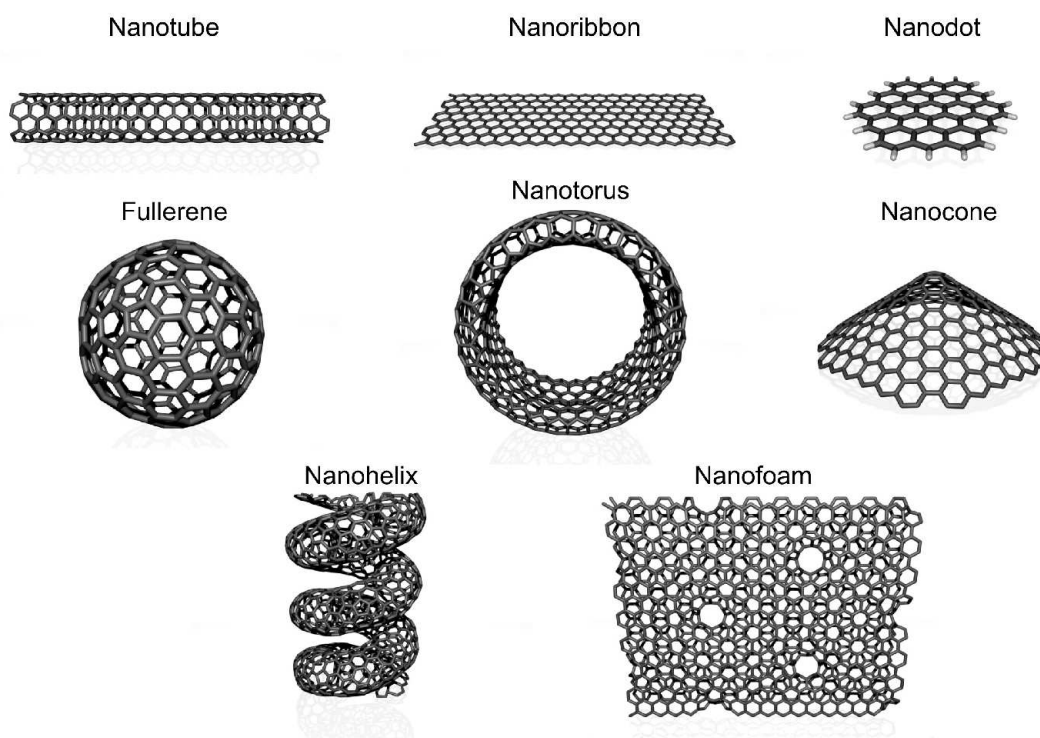
Figure 4.1: The family of graphene-based carbon materials. As graphene is rolled up and joined it forms a nanotube. Nanoribbons are formed when cutting graphene along two parallel lines. If two other cuts on perpendicular direction are made to graphene nanoribbons, a graphene nanodot is obtained. Pentagons and heptagons in graphene create curvature and can us form nanocones or if completely closed (e.g. with 12 pentagons), a fullerene is obtained. Nanohelixes and nanotori can be obtained by rolling nanotubes. Graphene layers joined by nanotube segments can form a nanofoam. All these structures can be formed with bilayer, trilayer or multilayer graphene, forming, for instance, multi-walled nanotubes, multiple layer nanoribbons, onions, etc.

4.2. FULLERENES AND NANOTUBES

Science of fullerenes was boosted when the synthesis of such structures was made available in macroscopic quantities [1,2]. Since then, a large number of studies have appeared, and several applications have been proposed. For example, fullerenes are now considered as versatile building blocks in organic chemistry, introducing new chemical, geometric, electronic, photophysical, and photochemical properties [3]. The most intensively studied fullerene is the buckminsterfullerene C_{60}. The spherical cage of C_{60} makes it and its higher family members unique. Fullerenes can be considered as three-dimensional analogues of benzene and other planar aromatics, but in contrast to such systems, fullerenes have no boundaries, and therefore no hydrogen atoms are needed to saturate

dangling bonds. This change in topology alone changes the reactivity of the fullerenes and makes it significantly different from that of classical planar aromatics, and has established a new chemistry called fullerene chemistry [3].

The icosahedral C_{60} consists of 12 pentagons and 20 hexagons (see figure 4.2b). This structure obeys Euler's theorem predicting that exactly 12 pentagons are required for the closure of a carbon network consisting of n hexagons. The isolated pentagon rule predicts that fullerene structures with all the pentagons isolated by hexagons are more stable when compared to structures with adjacent pentagons.

Due to the spherical shape, C_{60} has several consequences. a) The deviation from planarity introduces a large amount of strain energy; for instance, thermodynamically, C_{60} is less stable than the planar graphite. b)The curvature and the deviation from planarity causes re-hybridization of the sp^2 *s* and *p* orbitals and deviates from strictly planar situations [4].

In fact, C_{60} has an average s bond hybridization of $sp^{2.278}$ and a fractional *s* character of 0.085 [5–10]. As a consequence, of the π-orbitals extend further beyond the outer surface than into the interior of C_{60}. This implies that C_{60} is a fairly electronegative molecule [11,12] since due to the rehybridization low lying π* orbitals it also exhibits considerable *s* character. Also, the bonds at the junctions of two hexagons are shorter than the bonds at the junctions of a hexagon and a pentagon [13–20]. As a consequence, the double bonds are placed at the junctions of the hexagons and there are no double bonds in the pentagonal rings. Therefore, the atoms at the pentagon rings are more reactive.

As mentioned above, in general, fullerenes consist of closed (~sp^2 hybridized) carbon networks, organized on the basis of 12 pentagons and any number of hexagons except one. This definition includes elongated fullerenes, better known as nanotubes [21] (Figure 2c). In 1991, Iijima reported the existence of such structures, consisting of concentric graphite tubes [22]. A few months after Iijima's publication, Ebbesen and Ajayan described the bulk synthesis of nanotubes [23] formed as an inner core cathode deposit generated by arcing graphite electrodes in an inert atmosphere; a similar procedure to that used for fullerenes.

However, on another approach, carbon nanotubes (CNTs) can be visualized as rolled hexagonal carbon networks that are capped by pentagonal carbon rings. There are two types of carbon tubes: single-walled (SWNTs) and multi-walled
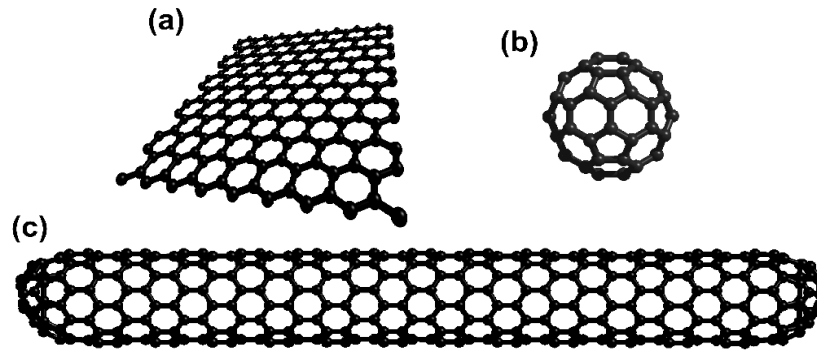
Figure 4.2: Ball and stick models of (a) a finite graphene layer (b) a Buckminster fullerene C_{60}, and (c) a carbon nanotube.

(MWNTs).

In the early 1990s, two research groups calculated the electronic properties of individual SWNTs for the first time [24-26]. They predicted that SWNTs might be metallic or semiconducting, depending upon their chirality (the way the hexagons are arranged along the tube axis) and diameter [24-26]. By the end of that decade, these particular predictions where confirmed experimentally [27,28].

Later, other experimental groups conducted transport measurements on bulk nanotube samples [29], individual multilayered tubes [30, 31], and ropes of single-walled tubules [32]. These reports revealed that the conducting properties of the tubes are extremely sensitive to the degree of graphitization, chirality, and diameter. It is important to stress that the transport response among different bulk samples of MWNTs strongly depends on the preparation and method used. The best way to determine the conductivity mechanism of MWNTs and SWNTs is direct 4-probe (or 2-probe) measurements on crystalline individual tubes, thus avoiding some contact problems: in a two probe measurement one also measures the resistance of the contact point of the wires to the sample. Typically the contact resistance is smaller than the resistance of the sample, and can thus be ignored. However, when one is measuring a very small sample resistance, the contact resistance can dominate and completely obscure changes in the resistance of the sample itself. In this context, individual MWNT conductivity measurements demonstrated that each MWNT exhibits unique conductivity properties [30,31] that can lead to both metallic and semiconducting behavior (resistivities at room temperature of ~1.2×10^{-4}–5.1×10^{-6} ohm·cm; activation energies <300 meV for semiconducting tubes). These results were the first to suggest that the geometric differences (*e.g.*, defects,

chirality, diameter, etc.) and degree of crystallinity (hexagonal lattice perfection) of the tubular structures play a key role in the electronic response. Bundles of SWNTs have been shown to behave as metals with resistivities in the 0.34×10^{-4} and 1.0×10^{-4} ohm·cm range [32].

Carbon-carbon bond observed in graphite is one of the strongest in nature, thus, CNTs are excellent candidates to be the stiffest and most robust structures ever synthesized. In observing MWNTs and SWMTs under a transmission electron microscope (TEM), it is remarkable that the tubes are flexible and do not break upon bending [33,34–37]. Early theoretical calculations predicted these properties [38–40], noting that the carbon tubes would soften with decreasing radius and by varying their chirality. First Young's moduli measurements demonstrated that multilayered CNTs are mechanically much stronger than conventional carbon fibers [41,42], and are extraordinarily flexible when subjected to large strain [43]. The values are dependent on the crystallinity of the material and the number of defects (*e.g.*, pentagon-heptagon pairs, vacancies, interstitials, etc.) present within the structure. For instance, pyrolytically grown CNTs possess more defects when compared with arc-discharge nanotubes due to the temperatures involved during processing.

The thermal conductivity of the well-known carbon allotropes such as diamond and graphite (in-plane) is extremely high. Therefore, the thermal conductivity of CNTs (dominated by phonons) along the tube axis is expected to be one of the highest ever when compared to other materials. Kim et al. determined that the thermal conductivity for individual MWNTs is higher than that of graphite (3000 W/K) at room temperature, and two orders of magnitude higher than those obtained for bulk MWNTs [44]. These studies revealed that the phonon mean free path is ~500 nm, and temperature dependence of the thermal conductivity exhibits a peak at 320 K due to the onset of umklapp phonon scattering [44]. The thermoelectric power shows an expected linear T dependence, which was absent in previous bulk measurements. Smalley and coworkers carried out thermal conductivity measurements on bulk samples composed of SWNTs produced using laser techniques [32]. The results show different temperature dependence of k, thus implying the presence of smaller crystalline sizes within the graphitic domains when compared with those of MWNTs. Hone [45] measured the thermal conductivity of randomly oriented SWNTs (35 W/m K) and aligned SWNTs (>200

105

W/m K). Hone *et al.,* [46] also described the thermal conductivity of SWNTs at low temperatures and noticed a linear dependence of k as a function of temperature, reflecting the one-dimensional band structure of individual SWNTs, with linear acoustic bands contributing to the thermal transport at the lowest temperatures and optical subbands entering at higher temperatures [47].

Nowadays, CNTs can be produced using a wide variety of processes such as arc-discharge, pyrolysis of hydrocarbons over metal particles, laser vaporization of graphite targets, solar carbon vaporization, and electrolysis of carbon electrodes in molten ionic salts.

Applications include the use of nanotubes as (a) gas storage components of Ar [48], N_2 [49], and H_2 [50,51]; (b) STM probes [52] and field emission sources [53–55]; (c) high-power electrochemical capacitors [56, 57]; (d) electronic nanoswitches [58]; (e) chemical sensors [59,60]; (f) magnetic data storage devices (e.g., Fe-filled nanotubes) [61]; (g) nanocomposites [62–64]; (h) the production of nanorods (e.g., TiC, NbC, Fe_3C, GaN, SiC, and BC_x) using CNTs as reacting templates [65, 66], etc. [67]. However, in order to employ CNTs or nanocomposites on a commercial basis, it is necessary to control their growth, length, diameter, and crystallinity at accessible costs. In the following sections, the structure, growth, and applications of CNTs and related materials are discussed in detail.

4.3. GRAPHENE

Although carbon is one of the best known materials, the two dimensional allotrope called graphene was isolated only recently by Geim and Novoselov [68]. This novel material exhibits interesting electronic behavior very different from graphite, diamond, or even more recently discovered allotropes, such as nanotubes or fullerenes (see §4.2).

Graphene has been studied for a long time theoretically, because it is the starting point for understanding more complicated systems. Graphene can be thought of as the building block of other forms of sp^2 carbon: it can be stacked to form graphite (3D), or cut to be rolled to form nanotubes (1D) or wrapped up into fullerenes (0D) (see figures 1 and 2). However, it was considered that graphene was a hypothetical material that could not be conceived experimentally because of Mermin-Wagner theorem: there should be no long-range order in two dimensions; dislocations
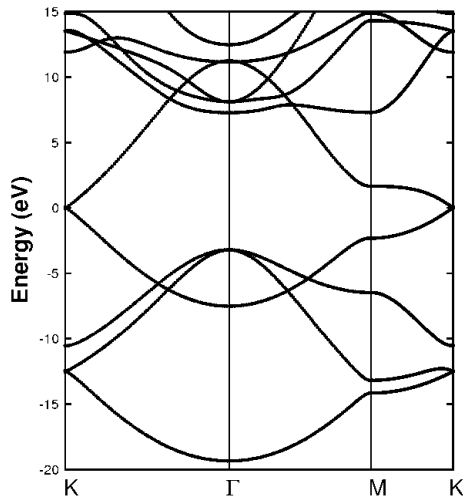
Figure 4.3: Band structure for graphene calculated with density functional theory under the local density approximation. Note the linear band dispersion close to K.

should appear in two dimensional crystals at any finite temperature [69]. The interest on graphene is largely due to its unique electronic properties and new physics. In the next sections, we present a brief review of such properties.

4.3.1. ELECTRONIC PROPERTIES OF GRAPHENE

Graphene crystal structure can be thought of as two equivalent carbon sub-lattices. Due to symmetry considerations, the electronic hopping between the sub-lattices leads to the formation of two energy bands, which intersect at K and K' (see figure 4.3) [70]. Near these crossing points, the electron energy is linearly dependent on the wave vector. Because of the linear dispersion, very different electronic behavior of graphene from that of conventional metals and semiconductors, where the electron behavior can be approximated by a free-electron can be observed. In fact, this linear dispersion results in massless excitations, with velocities on the order of 10^6m/s, which are described by the Dirac equation. Dirac fermions exhibit very different and unusual properties than ordinary electrons, leading to new phenomena. For example, anomalous integer quantum Hall effect can be observed in graphene even at room temperature [71,72]. Other interesting properties of graphene include insensitivity to external electrostatic potentials (Klein paradox), jittery motion of the wave function under confining potentials, and large mean free paths. For a comprehensive review of the properties of graphene, see [73].

When two or more graphene layers are stacked upon each other, the electronic properties change notably. The relative position of neighboring layers, or stacking order, can be varied, and affect the electronic properties. For bilayer graphene, the stacking order can be either AA with each atom on top of another atom or AB, where a set of atoms in the second layer sits on top of the empty center of a hexagon in the first layer. As the number of layers increase, the stacking order can become more complicated. However, for graphite, there are three common types of stacking: AB or Bernal stacking, ABC or rhombohedral stacking and no discernible stacking order or turbostratic stacking. For graphite, the most stable stacking is AB,
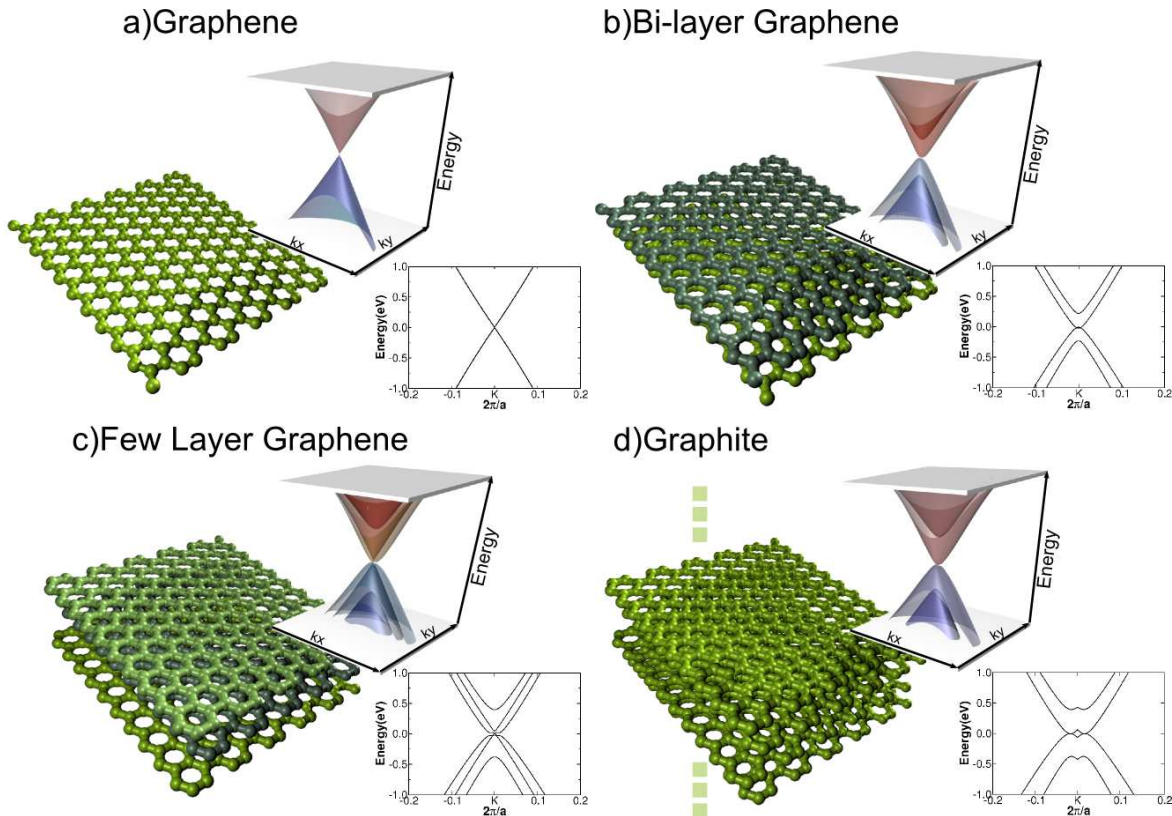
Figure 4.4: Low energy DFT 3D band structure and its projection on kx close to k-point K (π/a*[2/3, 0.0 0.0]) for (a) graphene, (b) bilayer graphene, (c) trilayer graphene and (d) graphite. (a) shows the characteristic Dirac point of graphene. The Dirac point (i.e. relativistic fermion characteristic) is lost in bilayer graphene (b), but appears again in trilayer graphene (c). (d) shows the Graphite structure which exhibits a semimetallic band structure with parabolic-like bands. The Fermi level has been set at zero in all cases.

and therefore has become the most studied stacking for other graphene based stacks. However, the other stacking orders are certainly possible, specially in few layer graphenes, and there is no clear indication why AB stacking should be the most stable, and therefore different configurations should be studied.

The limit of thickness at which graphene can be considered as such can be determined by the rapid change in the electronic structure as the number of layers increase. In fact, the first 3 AB stacks of graphene show very different electronic spectra (see figure 4.4). The bilayer (figure 4.4b) shows parabolic bands (thus, no Dirac electrons) which touch at the Fermi level. Under the presence of an electric field the gap on bilayer graphene can be opened, and therefore, it is very interesting for technological applications [72]. The trilayer shows an interesting band structure which is in some sense the combination of the monolayer and the bilayer. In general, for few layer graphene with N layers (AB stacking), there will be

a linear band (Dirac fermions) if N is odd [74]. As the number of layers increases the band structure becomes more complicated: several charge carriers appear [68,75], and the conduction and valence bands start notably overlapping [68,76]. Therefore three different types of 2D crystals are distinguished: graphene, and double- and few- layer graphene. Thicker structures can be considered as thin films of graphite [77].

The stacking order or disorder has been found to dramatically change the electronic properties of multilayer graphene, introducing Dirac fermions due to the symmetry breaking even in graphite [78,79].

A finite layer of graphene will inevitably have borders (thus forming graphene nanoribbons), which can exhibit edge states and different electronic and magnetic properties depending on the size and type of border. The most studied chiral angles 0°, and 30° lead to armchair and zigzag edges, or armchair and zigzag nanoribbons (A-GNRs, Z-GNRs), respectively (see figure 4.5 left). Experimental results indicate that these are the most common type of edges in nanoribbons [80], although edge reconstruction with pentagonal and heptagonal carbon rings has also been observed [81,82].

Z-GNRs exhibit edge states not present in the armchair case [83,84] (see figure 4.5 right). These edge states are present as a flat band around the Fermi level, but extended along the ribbon's edge, leading to a metallic nanoribbon if the width is large enough [85-87]. Furthermore, Z-GNRs exhibit interesting magnetic properties of relevance for spintronics [88-91]. A-GNRs have a peculiar dependence on the width.

Effect of thickness (*i.e.*, more than one layer) has also been studied. According to these studies GNRs have increased numbers of zigzag edge states, and decreased armchair band gaps, when multilayered [92]. Although Eg of a bilayer A-GNR (b-A-GNR), in general, is smaller than that of A-GNR, bilayer A-GNR exhibits two distinct groups, metal and semiconductor, while AGNR displays purely semiconducting behavior. Moreover, Eg of b-A-GNR is highly sensitive to the interplanar distance [93]. Other studies have shown that A-GNRs exhibit three classes of bilayer gaps which decrease with increasing ribbon width [94].

The edge states in graphene and multilayer graphene nanoribbons are highly reactive sites. The modulation of the electrical and magnetic properties of

graphene and multilayer graphene nanoribbons from the attachment of different atoms or molecules has been proposed for applications such as sensors, memories and processing devices.

4.3.2. ELECTRONIC PROPERTIES OF GRAPHENE NANORIBBONS

The study of the electronic properties of GNRs started with the work of Fujita et al. in 1996 [83,84]. The different properties of nanoribbons with different chiralities, similar to carbon nanotubes, were then revealed. According to the first studies based on orthogonal π tight binding (π-TB) calculations, it was predicted that Z-GNRs would exhibit edge states not present in the armchair case. Furthermore, these edge states were present as a flat band around the Fermi level (see figure 4.5 right). These states are localized at the edges, but extended along the ribbon's edge, leading to a metallic nanoribbon. More accurate Density Functional Theory (DFT) within the Local Density Approximation (LDA) calculations have revealed that the Z-GNRs exhibit a finite band gap when the structures are relaxed or spin polarization is considered [95,86]. Calculations beyond local interactions such as GW quasiparticle (GW-QP) calculations agree qualitatively with the LDA results; however, the electron-electron interaction correction induces an increase of the band gap for all cases [87]. Recent transport experiments have revealed that the existence of an energy gap in GNRs may be understood in terms of Coulomb blockade [95]. It is important to note that most calculations have been done with the edges saturated with hydrogen, otherwise, dangling bonds appear. These dangling bonds are very reactive, and thus normally not feasible under ambient conditions, where they would get saturated with some ambient molecule or atom. However, under vacuum and at high temperatures, these saturating atoms or molecules could be removed.

The electronic properties of GNRs have a peculiar dependence on the width. According to π-TB calculations, A-GNRs can be divided in two families: semimetallic if the width N_A = 3p+2, where p is an integer; or semiconductor otherwise. DFT calculations indicate that A-GNRs can be grouped in three families according to N_A = 3p, N_A = 3p+1 and N_A=3p+2, all with different band gaps (Eg) such that $\Delta Eg^{3p+1} > \Delta Eg^{3p} > \Delta Eg^{3p+2}$. Barone et al. predict that in order to produce materials with band gaps similar to Ge or InN, the width of the ribbons must be between 2 and 3 nm. If larger bang gap ribbons are needed (like Si, InP, or GaAs),
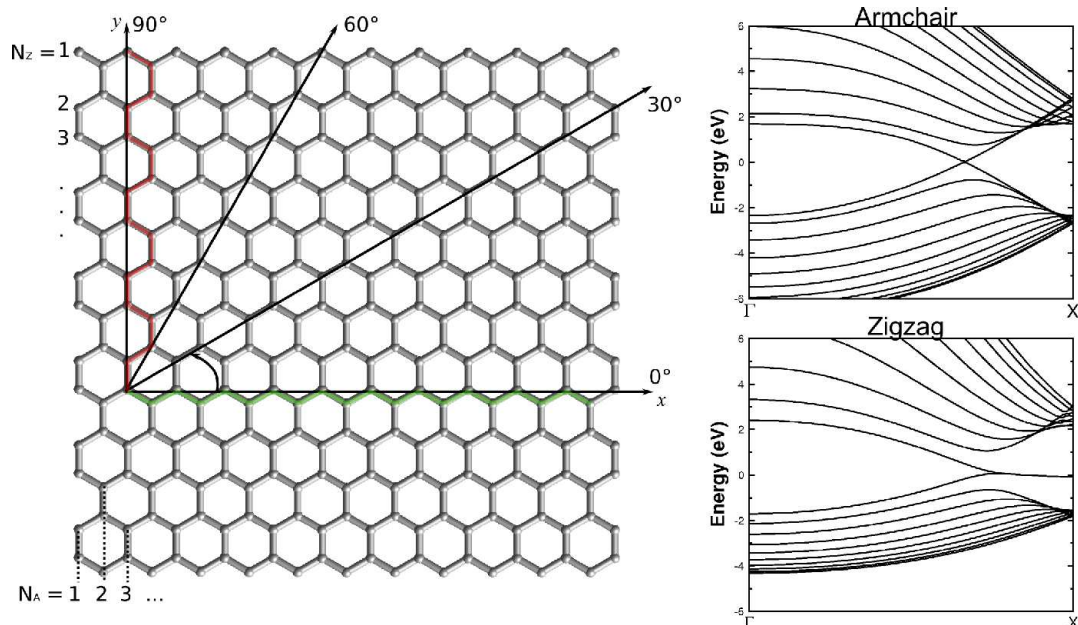
Figure 4.5: Left: Molecular model of graphene showing the different angles defining the zigzag and armchair edges. The convention for labeling the width of GNRs with N_A and N_Z is shown. Right: third nearest neighbors tight binding structure for an armchair (top) and zigzag (bottom) nanoribbon.

their width must be reduced to 1-2 nm [86].

Zero dimensional systems (*I,.e.* finite width and length) have also been studied [96-98]. Shemella *et al.,* have found that in addition to quantum confinement along the width of the ribbon, an additional finite size effect emerges along the length of ribbons only for metallic armchair ribbons [96]. However, most of the physical features appearing in the density of states of an infinite GNR are recovered at a length of 40 nm [97]. Nevertheless, even for the long edge effects appear in the vicinity of the Fermi energy. The weight of these edge states scales inversely with the length of the ribbon, and they are expected to become negligible only at ribbon lengths of the order of micrometers [97].

Other morphologies have been studied, such as Möbius strips, and twisted graphene nanoribbons [99,100]. A high number of twists leads to a sharp increase of the HOMO -> LUMO transition energy [101]. Yakobson *et al.,* have recently showed that graphene nanoribbons with small width will tend to form helically shaped twists, while nanoribbons with larger width will show ripples [101].

4.3.3. MAGNETIC PROPERTIES OF GRAPHENE NANORIBBONS

Since the first studies by Nakada and Fujita [83,84] it was realized that edge states in Z-GNRs could exhibit interesting magnetic properties. Later, it was showed that Z-GNRs exhibit an antiferromagnetic configuration between ferromagnetically coupled edge states at each edge, and this configuration is energetically favored over the configuration with same spin orientation between the two edges [29]. Thus, Z-GNRs have a null total magnetic moment. These findings were confirmed using non-collinear spin calculations [102]. The magnetism of the graphitic edge is well understood by considering the magnetic tails' interaction and the antiferromagnetic interlayer coupling. As for the inter-edge interactions, the antiferromagnetic coupling between the edge states is favored, but the energy lowering relative to the ferromagnetic coupling decreases as the strip width increases [88].

In spite of these findings, GNRs found their way with interesting spin properties. Wimmer *et al.,* find that nanoribbons symmetric edges show zero spin conductance but nonzero spin Hall conductance, and only nanoribbons with asymmetrically shaped edges give rise to a finite spin conductance and can be used for spin injection into graphene [103].

Son, Cohen and Louie proposed that the effects of external transverse fields would be significant on the edge states [104]. They found that Z-GNRs would become half-metallic upon the effect of a transverse electric field. The half-metallicity of the Z-GNRs originates from the fact that the applied electric fields induce energy-level shifts of opposite signs for the spatially separated spin-ordered edge states [104]. Other studies using hybrid functionals have suggested that finite graphene ribbons behave as half-semiconductors [105]. At B3LYP level of theory, it was confirmed that the half-metallicity in Z-GNR can be realized when an external electric field is applied across the ribbon [106]. The critical electric field decreases with the increase of the ribbon width to induce the half-metallicity. Both the spin polarization and half-metallicity are removed when the edge state electrons fully transferred from one side to the other under very strong electric fields. The electric field range under which Z-GNR remains half-metallic increases with the ribbon width [106].

In addition, first-principles simulations predict that spin-valve devices based on

GNRs will exhibit magnetoresistance values that are thousands of times higher than previously reported experimental values, due to the unique symmetry of the band structure in the nanoribbons [107]. It has been showed that it is possible to manipulate the band structure of the nanoribbons to generate highly spin-polarized currents [106].

4.3.4. Optical properties of graphene nanoribbons

The optical properties of graphene nanoribbons are also interesting. The optical absorption of Z-GNRs is qualitatively different from that of armchair nanotubes. Unlike the selection rule for nanotubes, when the incident beam is polarized along the longitudinal direction, the interband transitions at direct gaps are forbidden for GNRs. This selection rule is due to the finite width of graphene nanoribbons [108].

Also, GNRs exhibit strongly bound bright and dark excitons dominating the optical spectra [109,110]. It has been shown that the absorption and luminescence properties of nanoribbons can be controlled by changing both width family and edge termination [109,110]. For instance, the optical response of the Z-GNRs is found to be dominated by magnetic edge-state-derived excitons with large binding energy [111].   Also, photo-assisted inter-subband transitions could lead to interesting optoelectronic properties [112].

The vibrational properties and Raman spectra of GNRs studied DFT-LDA indicates that for all GNRs there are three typical Raman-active modes, *i.e.*, the radial-breathing-like mode (RBLM), the localized mode and the graphene E-2g-like one, which are helpful to identify different GNRs in the Raman experiments. Among them, the RBLM is the most characteristic one, whose frequency decreases with the increasing GNR width in a linear proportion to the inverse square root of the width, making it very useful to determine the GNR width experimentally [113].

4.3.5. Doping effects

The vast majority of the nanoribbons studied in the literature have the edges saturated with hydrogen to avoid dangling bonds which usually introduce states around the Fermi level. The non-saturated edges are highly reactive sites, and are unlikely to be stable at ambient conditions. However, they could remain non-saturated after a heat treatment, and under vacuum or inert atmosphere. In any

case, the effect of saturation is equivalent to doping in classic semiconductors, as could be a way to change the electronic and magnetic properties of nanoribbons.

It has been found that the C-C bond lengths and bond angles near the graphene nanoribbon (GNR) edge have considerable changes when edge carbon atoms are bounded to different atoms [114]. Pati and Datta found that saturating the edges with boron atoms stabilizes zigzag nanoribbons into a ferromagnetic ground state, and the system exhibits half-metallicity under finite electric fields at any width [115]. Rosales et al. study the effect of lineal organic molecules attached to graphene nanoribbons [116]. They found that the conductance exhibits an even-odd parity effect as a function of the length of the attached molecules. Kudin has studied the effect of edge saturation with two H or F atoms [117]. According to their calculation, there is a significant alteration of the carbon bond across the ribbons, and the most stable state is a closed shell configuration. According to Cervantes-Sodi and co-workers, N and B produce different effects, depending on the position of the substitutional site [118]. In particular, edge substitutions at low density do not significantly alter the band gap, while bulk substitution promotes the onset of semiconducting-metal transitions. Pyridine-like defects induce a semiconducting-metal transition.

The magnetic properties are also sensitive to edge modification. Huang, et al. found that the stability of the spin state and its magnetic moments is found to continuously decrease with increasing the concentration of the defects or impurities [119]. The system generally becomes nonmagnetic at the concentration of one edge defect (impurity) for every *c.a.* 10 Å. Doping the edge by Mg and B can turn the semiconducting armchair ribbon into a metal [120]. The formation of a spin-paired C-O bond drastically reduces the local atomic magnetic moment of carbon at the edge of the ferromagnetic zigzag ribbon [121].

The absorption of different gas molecules on the edges of GNRs has also been investigated. The electronic and transport properties of the GNR edges are sensitive to the adsorption of different gases, and depending on the type of gas molecule the system could exhibit n- or p-type semiconducting behavior [122-124]. The change of the electronic properties upon gas adsorption could be used to make p-type or n-type semiconductors by means of finite concentration adsorption of gas molecules or a gas sensor [123].

Adding transition metal atoms at the edges of carbon nanoribbons has also been studied. Depending on the ribbon width and adsorbed TM atom species, A-GNR, which are nonmagnetic semiconductors, can either be a metal or a semiconductor with ferromagnetic or antiferromagnetic spin alignment, and in the case of Ti and Fe could exhibit half metallicity [125,126]. Armchair edge doping with Fe and Mn change it into a ferromagnet with a large magnetic moment [127,128].

Kan, *et al.,* and Dalosto *et al.*, separately, have proved that half metallicity can be achieved by selectively adding polar molecules at the edges of carbon nanoribbons [129,130]. In the first case, attaching NO_2 to one edge and CH_3 groups to the other edge.

Although substitutional doping on these nanoribbons seems rather difficult form the experimental standpoint, there have been several studies of graphene nanoribbons doped with boron [85,118,131,132], and nitrogen [85,118,133]. These studies show that these impurities induce localized states around the Fermi level, which act as scattering sites.

Other reactive sites are structural defects. OuYang *et al.,* have studied the functionalization of graphene nanoribbons by carboxyl groups on Stone-Wales (SW) defects [134]. With the increase of the axial concentration of SW defects, the system would transform from semiconducting behavior to p-type metallic behavior.

4.3.6. EFFECT OF EDGE DISORDER

Since many of the potential applications of GNRs arise from the possibility of tuning the properties with the edge type and family, a natural question is what happens when the chiral angle is different from the armchair or zigzag angle. This question was already addressed by Nakada, *et al.,* [84], and they determined that for a ribbon of a width of a few nanometers, the edge states would prevail even for the inclusion of an armchair-type edge for every three zigzag-type edge (see figure 4.5). It has been shown that a moderate degree of edge disorder can explain the fact that the experimentally measured bandgaps of GNRs do not depend on orientation [135].

Edge disorder has proved to be significant in transport properties in transistor devices. For example, it was found that the presence of edge roughness decreases the ratio between the on-current and minimal leakage current [136]. It has been

noted that if the impurity scattering does not connect the two valleys, *i.e.*, there is a long-range potentials due to the impurities at the edges, then the channel is a good conductor [137]. The addition of edge disorder significantly reduces on-state currents and increases off-state currents, and introduces wide variability across devices. These effects decrease as ribbon widths increase and as edges become smoother. However, the band gap decreases with increasing width, thereby increasing the band-to-band tunneling mediated subthreshold leakage current even with perfect nanoribbons [138].

Other defects, such as edge vacancies have been also studied. For the case of A-GNRs, edge vacancies induce a reduction of Eg leading to a semiconductor-metal transition [139]. Though the electronic band structure of Z-GNRs may be affected by the edge-vacancy defects, their metallic characteristic remains. On transport calculations, a single edge defect induces quasi-localized states and consequently causes zero-conductance dips. The center energies and breadths of such dips are strongly dependent on the geometry of GNRs. A-GNRs are more sensitive to a vacancy than Z-GNRs, but are less sensitive to a weak scatter [140].

The stability of the spin state and its magnetic moments is found to continuously decrease with increasing the concentration of the defects or impurities. The system generally becomes nonmagnetic when the concentration of defects is larger than one for each 10 Å [141]. The presence of certain kinds of defects at the edges of monohydrogenated Z-GNRs changes dramatically the charge transport properties inducing a spin-polarized conductance. There are two different classes of defects depending on their distinct transport properties: (i) sigma-defects, which do not affect the transmittance close to the Fermi energy; and (ii) pi-defects, which cause a spin polarization of the transmittance and that can be further divided into either electron or hole defects if the spin transport polarization results in larger transmittance for the up or down spin channel, respectively [142].

4.4. CONCLUSIONS

The four valence electrons in carbon atoms ($2s^2\,2p^2$) give rise to $2s$, $2p_x$, $2p_y$, and $2p_z$ orbitals which can mix forming the strong covalent bonds in carbon structures. Several possibilities for electron configuration or hybridization of the atomic orbitals can arise, leading to different properties of carbon materials. In this chapter we

have reviewed the most relevant properties of carbon materials for the next chapters. In particular, the discovery of graphene and consequently, graphene nanoribbons (GNRs) has set a new dimension for nanoscale carbon science. These new material is the subject of study of the following two chapters.

4.5. REFERENCES

[1]. Kroto, H.W., Heath, J.R., O'Brien, S.C., Curl, R.F. & Smalley, R.E. C60: Buckminsterfullerene. *Nature* **318**, 162-163 (1985).

[2]. Kratschmer, W., Lamb, L.D., Fostiropoulos, K. & Huffman, D.R. Solid C60: a new form of carbon. *Nature* **347**, 354-358 (1990).

[3]. Hirsch, A. *Principles of Fullerene Reactivity in Fullerenes and Related Materials*. Springer Berlin 1999.

[4]. Haddon, R.C. Chemistry of the Fullerenes: The Manifestation of Strain in a Class of Continuous Aromatic Molecules. *Science* **261**, 1545-1550 (1993).

[5]. Haddon, R.C. Hybridization and the orientation and alignment of .pi.-orbitals in nonplanar conjugated organic molecules: .pi.-orbital axis vector analysis (POAV2). *J. Am. Chem. Soc.* **108**, 2837-2842 (1986).

[6]. Haddon, R.C. Rehybridization and .pi.-orbital overlap in nonplanar conjugated organic molecules: .pi.-orbital axis vector (POAV) analysis and three-dimensional Hueckel molecular orbital (3D-HMO) theory. *J. Am. Chem. Soc.* **109**, 1676-1685 (1987).

[7]. Haddon, R.C. .pi.-Electrons in three dimensions. *Acc. Chem. Res.* **21**, 243-249 (1988).

[8]. Haddon, R.C. Measure of nonplanarity in conjugated organic molecules: which structurally characterized molecule displays the highest degree of pyramidalization? *J. Am. Chem. Soc.* **112**, 3385-3389 (1990).

[9]. Haddon, R.C. Electronic structure, conductivity and superconductivity of alkali metal doped (C60). *Acc. Chem. Res.* **25**, 127-133 (1992).

[10]. Haddon, R., Brus, L. & Raghavachari, K. Electronic structure and bonding in icosahedral C60. *Chem. Phys. Lett.* **125**, 459-464 (1986).

[11]. Haddon, R.C., Brus, L.E. & Raghavachari, K. Rehybridization and [pi]-orbital alignment: the key to the existence of spheroidal carbon clusters. *Chem. Phys. Lett.* **131**, 165-169 (1986).

[12]. Schulman, J.M., Disch, R.L., Miller, M.A. & Peck, R.C. Symmetrical clusters of carbon atoms: The C24 and C60 molecules. *Chem. Phys. Lett.* **141**, 45-48 (1987).

[13]. Lüthi, H.P. & Almlöf, J. AB initio studies on the thermodynamic stability of the icosahedral C60 molecule "buckminsterfullerene". *Chem. Phys. Lett.* **135**, 357-360 (1987).

[14]. Dunlap DI (1988) *Int J Quantum Chem Symp* 22:257

[15]. Scuseria, G.E. Ab initio theoretical predictions of the equilibrium geometries of C60, C60H60 and C60F60. *Chem. Phys. Lett.* **176**, 423-427 (1991).

[16]. Häser, M., Almlöf, J. & Scuseria, G.E. The equilibrium geometry of C60 as predicted by

second-order (MP2) perturbation theory. *Chem. Phys. Lett.* **181**, 497-500 (1991).

[17]. Yannoni, C.S., Bernier, P.P., Bethune, D.S., Meijer, G. & Salem, J.R. NMR determination of the bond lengths in C60. *J. Am. Chem. Soc.* **113**, 3190-3192 (1991).

[18]. David, W.I.F. et al. Crystal strcture and bonding of ordered C60. *Nature* **353**, 147-149 (1991).

[19]. Hedberg, K. et al. Bond Lengths in Free Molecules of Buckminsterfullerene, C60, from Gas-Phase Electron Diffraction. *Science* **254**, 410-412 (1991).

[20]. Liu, S., Lu, Y., Kappes, M.M. & Ibers, J.A. The Structure of the C60 Molecule: X-Ray Crystal Structure Determination of a Twin at 110 K. *Science* **254**, 408-410 (1991).

[21]. Endo, M. & Kroto, H.W. Formation of carbon nanofibers. *J. Phys. Chem.* **96**, 6941-6944 (1992).

[22]. Iijima, S. Helical microtubules of graphitic carbon. *Nature* **354**, 56-58 (1991).

[23]. Ebbesen, T.W. & Ajayan, P.M. Large-scale synthesis of carbon nanotubes. *Nature* **358**, 220-222 (1992).

[24]. Hamada, N., Sawada, S. & Oshiyama, A. New one-dimensional conductors: Graphitic microtubules. *Phys. Rev. Lett.* **68**, 1579 (1992).

[25]. Saito, R., Fujita, M., Dresselhaus, G. & Dresselhaus, M.S. Electronic structure of graphene tubules based on C60. *Phys. Rev. B* **46**, 1804 (1992).

[26]. Saito, R., Fujita, M., Dresselhaus, G. & Dresselhaus, M.S. Electronic structure of chiral graphene tubules. *Appl. Phys. Lett.* **60**, 2204-2206 (1992).

[27]. Wilder, J.W.G., Venema, L.C., Rinzler, A.G., Smalley, R.E. & Dekker, C. Electronic structure of atomically resolved carbon nanotubes. *Nature* **391**, 59-62 (1998).

[28]. Odom, T.W., Huang, J., Kim, P. & Lieber, C.M. Atomic structure and electronic properties of single-walled carbon nanotubes. *Nature* **391**, 62-64 (1998).

[29]. de Heer, W.A., Châtelain, A. & Ugarte, D. A Carbon Nanotube Field-Emission Electron Source. *Science* **270**, 1179-1180 (1995).

[30]. Dai, H., Wong, E.W. & Lieber, C.M. Probing Electrical Transport in Nanomaterials: Conductivity of Individual Carbon Nanotubes. *Science* **272**, 523-526 (1996).

[31]. Ebbesen, T.W. et al. Electrical conductivity of individual carbon nanotubes. *Nature* **382**, 54-56 (1996).

[32]. Thess, A. et al. Crystalline Ropes of Metallic Carbon Nanotubes. *Science* **273**, 483-487 (1996).

[33]. Ajayan, P.M., Stephan, O., Colliex, C. & Trauth, D. Aligned Carbon Nanotube Arrays Formed by Cutting a Polymer Resin--Nanotube Composite. *Science* **265**, 1212-1214 (1994).

[34]. Iijima, S., Brabec, C., Maiti, A. & Bernholc, J. Structural flexibility of carbon nanotubes. *J. Chem. Phys.* **104**, 2089-2092 (1996).

[35]. Chopra, N.G. et al. Fully collapsed carbon nanotubes. *Nature* **377**, 135-138 (1995).

[36]. Ruoff, R.S. & Lorents, D.C. Mechanical and thermal properties of carbon nanotubes. *Carbon* **33**, 925-930 (1995).

[37]. Dresselhaus MS, Dresselhaus G, Eklund, P. 1996. *The Science of Fullerenes and Carbon Nanotubes.* New York: Academic

[38]. Overney, G., Zhong, W. & Tománek, D. Structural rigidity and low frequency vibrational modes of long carbon tubules. *Z. Physik D Atoms, Mol. Clusters* **27**, 93-96 (1993).

[39]. Robertson, D.H., Brenner, D.W. & Mintmire, J.W. Energetics of nanoscale graphitic tubules. *Phys. Rev. B* **45**, 12592 (1992).

[40]. Tersoff, J. Energies of fullerenes. *Phys. Rev. B* **46**, 15546 (1992).

[41]. Treacy, M.M.J., Ebbesen, T.W. & Gibson, J.M. Exceptionally high Young's modulus observed for individual carbon nanotubes. *Nature* **381**, 678-680 (1996).

[42]. Wong, E.W., Sheehan, P.E. & Lieber, C.M. Nanobeam Mechanics: Elasticity, Strength, and Toughness of Nanorods and Nanotubes. *Science* **277**, 1971-1975 (1997).

[43]. Falvo, M.R. et al. Bending and buckling of carbon nanotubes under large strain. *Nature* **389**, 582-584 (1997).

[44]. Kim, P., Shi, L., Majumdar, A. & McEuen, P.L. Thermal Transport Measurements of Individual Multiwalled Nanotubes. *Phys. Rev. Lett.* **8**7, 215502 (2001).

[45]. Hone, J. Phonons and thermal properties of carbon nanotubes. *Carbon Nanotubes* **80**, 273-286 (2001).

[46]. Hone, J., Whitney, M., Piskoti, C. & Zettl, A. Thermal conductivity of single-walled carbon nanotubes. *Phys. Rev. B* **59**, R2514 (1999).

[47]. Hone, J., Batlogg, B., Benes, Z., Johnson, A.T. & Fischer, J.E. Quantized Phonon Spectrum of Single-Wall Carbon Nanotubes. *Science* **289**, 1730-1733 (2000).

[48]. Gadd, G.E. et al. The World's Smallest Gas Cylinders? *Science* **277**, 933-936 (1997).

[49]. Terrones, M., Kamalakaran, R., Seeger, T. & Rühle, M. Novel nanoscale gas containers: encapsulation of N 2 in CN x nanotubes. *Chem. Commun.* **2000**, 2335–2336 (2000).

[50]. Dillon, A.C. et al. Storage of hydrogen in single-walled carbon nanotubes. *Nature* **386**, 377-379 (1997).

[51]. Liu, C. et al. Hydrogen Storage in Single-Walled Carbon Nanotubes at Room Temperature. *Science* **286**, 1127-1129 (1999).

[52]. Dai, H., Hafner, J.H., Rinzler, A.G., Colbert, D.T. & Smalley, R.E. Nanotubes as nanoprobes in scanning probe microscopy. *Nature* **384**, 147-150 (1996).

[53]. de Heer, W.A. et al. Aligned Carbon Nanotube Films: Production and Optical and Electronic Properties. *Science* **268**, 845-847 (1995).

[54]. Rinzler, A.G. et al. Unraveling Nanotubes: Field Emission from an Atomic Wire. *Science* **269**, 1550-1553 (1995).

[55]. Saito, Y. et al. Conical beams from open nanotubes. *Nature* **389**, 554-555 (1997).

[56]. Britto, P., Santhanam, K. & Ajayan, P. Carbon nanotube electrode for oxidation of dopamine. *Bioelectrochem. .Bioenerget.* **41**, 121-125 (1996).

[57]. Niu, C., Sichel, E.K., Hoch, R., Moy, D. & Tennent, H. High power electrochemical capacitors based on carbon nanotube electrodes. *Appl. Phys. Lett.* **70**, 1480-1482 (1997).

[58]. Yao, Z., Postma, H.W.C., Balents, L. & Dekker, C. Carbon nanotube intramolecular junctions. *Nature* **402**, 273-276 (1999).

[59]. Kong, J. et al. Nanotube Molecular Wires as Chemical Sensors. *Science* **287**, 622-625 (2000).

[60]. Collins, P.G., Bradley, K., Ishigami, M. & Zettl, A. Extreme Oxygen Sensitivity of Electronic Properties of Carbon Nanotubes. *Science* **287**, 1801-1804 (2000).

[61]. Grobert, N. et al. Enhanced magnetic coercivities in Fe nanowires. *Appl. Phys. Lett.* **75**, 3363-3365 (1999).

[62]. Kuzumaki, T., Ujiie, O., Ichinose, H. & Ito, K. Mechanical Characteristics and Preparation of Carbon Nanotube Fiber-Reinforced Ti Composite. *Adv. Engineer. Mater.* **2**, 416-418 (2000).

[63]. Kuzumaki, T., Miyazawa, K., Ichinose, H. & Ito, K. Processing of carbon nanotube reinforced aluminum composite. *J. Mater. Res.* **13**, 2445-2449 (1998).

[64]. Musa, I., Baxendale, M., Amaratunga, G. & Eccleston, W. Properties of regioregular poly(3-octylthiophene)/multi-wall carbon nanotube composites. *Synthetic Metals* **102**, 1250 (1999).

[65]. Dai, H., Wong, E.W., Lu, Y.Z., Fan, S. & Lieber, C.M. Synthesis and characterization of carbide nanorods. *Nature* **375**, 769-772 (1995).

[66]. Han, W., Fan, S., Li, Q. & Hu, Y. Synthesis of Gallium Nitride Nanorods Through a Carbon Nanotube-Confined Reaction. *Science* **277**, 1287-1289 (1997).

[67]. Terrones, M., Hsu W.K., Kroto H. W., Walton, D.R.M. 1998. In *Fullerenes and Related Structures*; Topics in Chemistry Series, ed. A Hirsch, 199:189–234. Springer-Verlag

[68]. Novoselov, K.S. et al. Electric Field Effect in Atomically Thin Carbon Films. *Science* **306**, 666-669 (2004).

[69]. Mermin, N.D. Crystalline Order in Two Dimensions. *Phys. Rev.* **176**, 250 (1968).

[70]. Saito, R., Dresselhaus, G., & Dresselhaus, M. S.. *Physical Properties of Carbon Nanotubes.* Imperial College Press. London, 1998

[71]. Novoselov, K.S. et al. Two-dimensional gas of massless Dirac fermions in graphene. *Nature* **438**, 197-200 (2005).

[72]. Zhang, Y. et al. Direct observation of a widely tunable bandgap in bilayer graphene. *Nature* **459**, 820-823 (2009).

[73]. Neto, A.H.C., Guinea, F., Peres, N.M.R., Novoselov, K.S. & Geim, A.K. The electronic properties of graphene. *Rev. Mod. Phys.* **81**, 109-54 (2009).

[74]. Partoens, B. & Peeters, F.M. Normal and Dirac fermions in graphene multilayers: Tight-binding description of the electronic structure. *Phys. Rev. B* **75**, 193402-3 (2007).

[75]. Partoens, B. & Peeters, F.M. From graphene to graphite: Electronic structure around the K point. *Phys. Rev. B* **74**, 075404 (2006).

[76]. Morozov, S.V. et al. Two-dimensional electron and hole gases at the surface of graphite. *Phys. Rev. B* **72**, 201401 (2005).

[77]. Geim, A.K. & Novoselov, K.S. The rise of graphene. *Nat Mater* **6**, 183-191 (2007).

[78]. Luk'yanchuk, I.A. & Kopelevich, Y. Dirac and Normal Fermions in Graphite and Graphene: Implications of the Quantum Hall Effect. *Phys. Rev. Lett.* **97**, 256801-4 (2006).

[79]. Latil, S., Meunier, V. & Henrard, L. Massless fermions in multilayer graphitic systems with misoriented layers: Ab initio calculations and experimental fingerprints. *Phys. Rev. B* **76**, 201402-4 (2007).

[80]. Jia, X. et al. Controlled Formation of Sharp Zigzag and Armchair Edges in Graphitic Nanoribbons. *Science* **323**, 1701-1705 (2009).

[81]. Girit, C.O. et al. Graphene at the Edge: Stability and Dynamics. *Science* **323**, 1705-1708 (2009).

[82]. Koskinen, P., Malola, S. & Hakkinen, H. Evidence for graphene edges beyond zigzag and armchair. *Phys. Rev. B* **80**, 073401-3 (2009).

[83]. Fujita, M., Wakabayashi, K. & Kusakabe, K.N.A.K. Peculiar Localized State at Zigzag Graphite Edge. *J. Phys. Soc. Jpn.* **65**, 1920-1923 (1996).

[84]. Nakada, K., Fujita, M., Dresselhaus, G. & Dresselhaus, M.S. Edge state in graphene ribbons: Nanometer size effect and edge shape dependence. *Phys. Rev. B* **54**, 17954 (1996).

[85]. Owens, F. Electronic and magnetic properties of graphene nanoribbons. *Mol. Phys.* **104**, 3107-3109 (2006).

[86]. Barone, V., Hod, O. & Scuseria, G.E. Electronic Structure and Stability of Semiconducting Graphene Nanoribbons. *Nano Lett.* **6**, 2748-2754 (2006).

[87]. Yang, L., Park, C., Son, Y., Cohen, M.L. & Louie, S.G. Quasiparticle Energies and Band Gaps in Graphene Nanoribbons. *Phys. Rev. Lett.* **99**, 186801-4 (2007).

[88]. Lee, H., Son, Y-W., Park, N., Han, S. & Yu, J. Magnetic ordering at the edges of graphitic fragments: Magnetic tail interactions between the edge-localized states. *Phys. Rev. B* **72**, 174431 (2005)

[89]. Sawada, K., Ishii, F. & Saito, M. Band-Gap Tuning in Magnetic Graphene Nanoribbons. *Appl. Phys. Express* **1**, 064004 (2008).

[90]. Son, Y., Cohen, M.L. & Louie, S.G. Half-metallic graphene nanoribbons. *Nature* **444**, 347-349 (2006).

[91]. Rudberg, E., Salek, P. & Luo, Y. Nonlocal Exchange Interaction Removes Half-Metallicity in Graphene Nanoribbons. *Nano Lett.* **7**, 2211-2213 (2007).

[92]. Finkenstadt, D., Pennington, G. & Mehl, M.J. From graphene to graphite: A general tight-binding approach for nanoribbon carrier transport. *Phys. Rev. B* **76**, 121405-4 (2007).

[93]. Lam, K. & Liang, G. An ab initio study on energy gap of bilayer graphene nanoribbons with armchair edges. *Appl. Phys. Lett.* **92**, 223106-3 (2008).

[94]. Sahu, B., Min, H., MacDonald, A.H. & Banerjee, S.K. Energy gaps, magnetism, and electric-field effects in bilayer graphene nanoribbons. *Phys. Rev. B* **78**, 045404-8 (2008).

[95]. Sols, F., Guinea, F. & Neto, A.H.C. Coulomb Blockade in Graphene Nanoribbons. *Phys. Rev. Lett.* **99**, 166803-4 (2007).

[96]. Shemella, P., Zhang, Y., Mailman, M., Ajayan, P.M. & Nayak, S.K. Energy gaps in zero-dimensional graphene nanoribbons. *Appl. Phys. Lett.* **91**, 042101-3 (2007).

[97]. Hod, O., Peralta, J.E. & Scuseria, G.E. Edge effects in finite elongated graphene nanoribbons. *Phys. Rev. B* **76**, 233401-4 (2007).

[98]. Lopez-Urias, F., Cruz-Silva, E., Munoz-Sandoval, E., Terrones, M. & Terrones, H. Magnetic properties of individual carbon clusters, clusters inside fullerenes and graphitic nanoribbons. *J. Mater. Chem.* **18**, 1535-1541 (2008).

[99]. Jiang, D. & Dai, S. Spin States of Zigzag-Edged Mobius Graphene Nanoribbons from First Principles. *J. Phys. Chem. C* **112**, 5348-5351 (2008).

[100]. Caetano, E.W.S., Freire, V.N., dos Santos, S.G., Galvao, D.S. & Sato, F. Möbius and twisted graphene nanoribbons: Stability, geometry, and electronic properties. *J. Chem. Phys.* **128**, 164719-8 (2008).

[101]. Bets, K. & Yakobson, B. Spontaneous twist and intrinsic instabilities of pristine graphene nanoribbons. *Nano Res.* **2**, 161-166 (2009).

[102]. Sawada, K; Ishii, F; Saito, M. *Appl. Phys. Express* **1**, 1 (2008).

[103]. Wimmer, M., Adagideli, I., Berber, S., Tomanek, D. & Richter, K. Spin Currents in Rough Graphene Nanoribbons: Universal Fluctuations and Spin Injection. *Phys. Rev. Lett.* **100**, 177207-4 (2008).

[104]. Young-Woo Son, Marvin L. Cohen, and Steven G. Louie. Half-metallic graphene nanoribbons. *Nature* **444**, 347 2006.

[105]. Rudberg, E; Salek, P; Luo, Y. *Nano Lett.* **7**, 2211-2213 (2007).

[106]. Kan, E., Li, Z., Yang, J. & Hou, J.G. Will zigzag graphene nanoribbon turn to half metal under electric field? *Appl. Phys. Lett.* **91**, 243116-3 (2007).

[107]. Kim, W. & Kim, K. Prediction of very large values of magnetoresistance in a graphene nanoribbon device. *Nat. Nanotechnol.* **3**, 408-412 (2008).

[108]. Hsu, H. & Reichl, L.E. Selection rule for the optical absorption of graphene nanoribbons. *Phys. Rev. B* **76**, 045418-5 (2007).

[109]. Yang, L., Cohen, M.L. & Louie, S.G. Excitonic Effects in the Optical Spectra of Graphene Nanoribbons. *Nano Lett.* **7**, 3112-3115 (2007).

[110]. Prezzi, D., Varsano, D., Ruini, A., Marini, A. & Molinari, E. Optical properties of graphene nanoribbons: The role of many-body effects. *Phys. Rev. B* **77**, 041404-4 (2008).

[111]. Yang, L., Cohen, M.L. & Louie, S.G. Magnetic Edge-State Excitons in Zigzag Graphene Nanoribbons. *Phys. Rev. Lett.* **101**, 186401-4 (2008).

[112]. Peng, X., Liao, W. & Zhou, G. Optoelectronic properties for armchair-edge graphene nanoribbons. *Chin. Phys. Lett.* **25**, 3436-3439 (2008).

[113]. Zhou, J. & Dong, J. Vibrational property and Raman spectrum of carbon nanoribbon. *Appl. Phys. Lett.* **91**, 173108-3 (2007).

[114]. Wang, Z.F. et al. Tuning the electronic structure of graphene nanoribbons through chemical edge modification: A theoretical study. *Phys. Rev. B* **75**, 113406-4 (2007).

[115]. Dutta, S. & Pati, S.K. Half-Metallicity in Undoped and Boron Doped Graphene Nanoribbons in the Presence of Semilocal Exchange-Correlation Interactions. *J. Phys. Chem. B* **112**, 1333-1335 (2008).

[116]. Rosales, L., Pacheco, M., Barticevic, Z., Latge, A. & Orellana, P.A. Transport properties of graphene nanoribbons with side-attached organic molecules. *Nanotechnol.* **19**, 065402 (2008).

[117]. Kudin, K.N. Zigzag Graphene Nanoribbons with Saturated Edges. *ACS Nano* **2**, 516-522 (2008).

[118]. Cervantes-Sodi, F., Csanyi, G., Piscanec, S. & Ferrari, A.C. Edge-functionalized and substitutionally doped graphene nanoribbons: Electronic and spin properties. *Phys. Rev. B* **77**, 165427-13 (2008).

[119]. Huang, B., Liu, F., Wu, J., Gu, B. & Duan, W. Suppression of spin polarization in graphene nanoribbons by edge defects and impurities. *Phys. Rev. B* **77**, 153411-4 (2008).

[120]. Gorjizadeh, N., Farajian, A.A., Esfarjani, K. & Kawazoe, Y. Spin and band-gap engineering in doped graphene nanoribbons. *Phys. Rev. B* **78**, 155427-6 (2008).

[121]. Veiga, R.G.A., Miwa, R.H. & Srivastava, G.P. Quenching of local magnetic moment in oxygen adsorbed graphene nanoribbons. *J. Chem. Phys.* **128**, 201101-3 (2008).

[122]. Huang, B. et al. Adsorption of Gas Molecules on Graphene Nanoribbons and Its Implication for Nanoscale Molecule Sensor. *J. Phys. Chem. C* **112**, 13442-13446 (2008).

[123]. Moradian, R., Mohammadi, Y. & Ghobadi, N. Investigation of gas sensing properties of armchair graphene nanoribbons. *J. Phys.: Condens. Matt.* **20**, 425211 (2008).

[124]. Yu, S.S., Zheng, W.T. & Jiang, Q. Oxidation of Graphene Nanoribbon by Molecular Oxygen. *IEEE Transact. Nanotechnol.* **7**, 628-635 (2008).

[125]. Sevincli, H., Topsakal, M., Durgun, E. & Ciraci, S. Electronic and magnetic properties of 3d transition-metal atom adsorbed graphene and graphene nanoribbons. *Phys. Rev. B* **77**, 195434-7 (2008).

[126]. Kan, E., Xiang, H.J., Yang, J. & Hou, J.G. Electronic structure of atomic Ti chains on semiconducting graphene nanoribbons: A first-principles study. *J. Chem. Phys.* **127**, 164706-5 (2007).

[127]. Gorjizadeh, N., Farajian, A.A., Esfarjani, K. & Kawazoe, Y. Spin and band-gap engineering in doped graphene nanoribbons. *Phys. Rev. B* **78**, 155427-6 (2008).

[128]. Gorjizadeh, N., & Kawazoe, Y. Magnetic Properties of Mn Doped Armchair Graphene Nanoribbon. *Mater. Trans.* **49**, 2445-2447 (2008).

[129]. Kan, E.J., Li, Z.Y., Yang, J.L., & Hou, JG. Half-Metallicity in Edge-Modified Zigzag Graphene Nanoribbons. *J. Am. Chem. Soc.* **130**, 4224-4225 (2008).

[130]. Dalosto, S.D. & Levine, Z.H. Controlling the Band Gap in Zigzag Graphene Nanoribbons with an Electric Field Induced by a Polar Molecule. *J. Phys. Chem. C* **112**, 8196-8199 (2008).

[131]. Martins, T.B., Miwa, R.H., da Silva, A.J.R. & Fazzio, A. Electronic and Transport Properties of Boron-Doped Graphene Nanoribbons. *Phys. Rev. Lett.* **98**, 196803-4 (2007).

[132]. 1. Huang, B. et al. Making a field effect transistor on a single graphene nanoribbon by selective doping. *Appl. Phys. Lett.* **91**, 253122-3 (2007).

[133]. Yu, S., Zheng, W., Wen, Q. & Jiang, Q. First principle calculations of the electronic properties of nitrogen-doped carbon nanoribbons with zigzag edges. *Carbon* **46**, 537-543 (2008).

[134]. OuYang, F. et al. Chemical Functionalization of Graphene Nanoribbons by Carboxyl Groups on Stone-Wales Defects. *J. Phys. Chem. C* **112**, 12003-12007 (2008).

[135]. Querlioz, D. et al. Suppression of the orientation effects on bandgap in graphene nanoribbons in the presence of edge disorder. *Appl. Phys. Lett.* **92**, 042108-3 (2008).

[136]. Yoon, Y. & Guo, J. Effect of edge roughness in graphene nanoribbon transistors. *Appl. Phys. Lett.* **91**, 073103-3 (2007).

[137]. Wakabayashi, K., Takane, Y. & Sigrist, M. Perfectly Conducting Channel and Universality Crossover in Disordered Graphene Nanoribbons. *Phys. Rev. Lett.* **99**, 036601-4 (2007).

[138]. Basu, D., Gilbert, M.J., Register, L.F., Banerjee, S.K. & MacDonald, A.H. Effect of edge roughness on electronic transport in graphene nanoribbon channel metal-oxide-semiconductor field-effect transistors. *Appl. Phys. Lett.* **92**, 042114-3 (2008).

[139]. Li, X., Wang, X., Zhang, L., Lee, S. & Dai, H. Chemically Derived, Ultrasmooth Graphene Nanoribbon Semiconductors. *Science* **319**, 1229-1232 (2008).

[140]. Li, T.C. & Lu, S. Quantum conductance of graphene nanoribbons with edge defects. *Phys. Rev. B* **77**, 085408-8 (2008).

[141]. Huang, B., Liu, F., Wu, J., Gu, B. & Duan, W. Suppression of spin polarization in graphene nanoribbons by edge defects and impurities. *Phys. Rev. B* **77**, 153411-4 (2008).

[142]. Martins, T.B., da Silva, A.J.R., Miwa, R.H. & Fazzio, A. σ- and π-Defects at Graphene Nanoribbon Edges: Building Spin Filters. *Nano Lett.* **8**, 2293-2298 (2008).

Chapter 5

Synthesis Of Graphene And Graphitic Nanoribbons

CONTENTS

5.1. INTRODUCTION

It is well known that the properties of carbon materials heavily depend on the environment of each of the carbon atoms in its structure. For example, the electrical properties of diamond and graphite are completely different: the first is an insulator, while the second is a conductor. In diamond, each carbon atom is bound to four carbon atoms resulting in a sp^3 hybridization. On the other hand, in graphite, each carbon atom is bound to three carbon atoms forming the sp^2 hybridization leaving an out of plane delocalized p_z orbital. This hybridization allows an electron to move freely, and therefore, leads to conduction.

The hybridization of nanoscale carbon slightly deviates from that of graphite or diamond, due to curvature or to the presence of pentagonal or heptagonal rings. Even without curvature, when graphite becomes single layered (called graphene), interesting properties appear. Furthermore, when graphene becomes finite, and exhibits edges, new properties arise.

In this chapter, the object of study is carbon nanoribbons from an experimental viewpoint. We present two approaches for experimentally achieving carbon nanoribbons, based on the well known technique of chemical vapor deposition. Although the characteristics of the produced samples do not perfectly resemble the ones of graphene nanoribbons, these approaches are a good start for further scaling of a novel carbon nanoribbon based range of applications.

The discovery of graphene and consequently, graphene nanoribbons (GNRs) has set a new dimension for nanoscale carbon science. Now that graphene synthesis has become available, some of its predicted properties have been successfully verified experimentally [1]. Currently, the synthesis of graphene nanoribbons has been achieved using experimental methods with very low yield such as mechanical cleavage followed by lithography, etching and chemical stripping. Nevertheless, important efforts to achieve large scale synthesis of graphene nanoribbons have begun to appear. Chemical vapor deposition (CVD) has been successfully carried out leading to bulk quantities of graphite nanoribbons which may be very useful for composites. This method will be reviewed and analyzed in §5.2. Another novel approach has been reported using carbon nanotubes (CNTs) as starting material, and by unzipping them in a controlled way, nanoribbons of precise dimensions

could result. This approach will be explored in §5.3.

5.2. CVD PRODUCED NANORIBBONS

Chemical vapor deposition (CVD)-based synthesis has been successfully carried out which yield to milligrams of relatively thick carbon nanoribbons which could be very useful for different applications [2]. CVD allows a one-step production of bulk quantities of graphitic ribbons. This material has been carefully characterized by several techniques and is found to have interesting properties.

The synthesis of these carbon nanoribbons (CNRs) was carried out using the aerosol pyrolysis process [3]. Briefly, solutions of ferrocene ($Fe(C_5H_5)_2$) and thiophene (C_4H_4S) in ethanol were used and sprayed as an aerosol and carried by an argon flow into a quartz tube located inside a two-furnace system heated to 1223 K. A black powder material scraped from the walls of the tube located in the first furnace area is the resulting material.

The morphology of the initial black powder consisted of ribbon-like structures exhibiting lengths of several micrometers, widths ranging from 20 to 300 nm and thickness of <15 nm (figure 5.1). The edges of the as-prepared ribbons also displayed relatively sharp cuts that could be related to the presence of either zigzag or armchair edges [4]. Detailed analysis indicates that the CVD nanoribbons are highly crystalline and do not exhibit impurities originated from the synthesis (e.g. Fe or S) [2]. It is interesting to note that the initial ribbons revealed both flat regions and rippled areas. These ripples have been observed to be a consequence of the thermal stability of single graphene layers and its edges [5,6]. This could suggest that the nanoribbons synthesized by this method grow layer by layer. In any case, the complete understanding of the morphology and structure of these CNR materials is imperative for the prediction of its properties and their eventual applications.

Campos-Delgado and co-workers have investigated the effect of high temperature thermal annealing on the morphology and structure of the CNRs. It can be observed from SEM images that the thermal annealing substantially changes the morphology of the CNRs even at low magnification (see figure 5.2) due to the elimination of defects through atom rearrangement and graphitization. At higher magnifications, Campos-Delgado et al. observed the formation of the so-
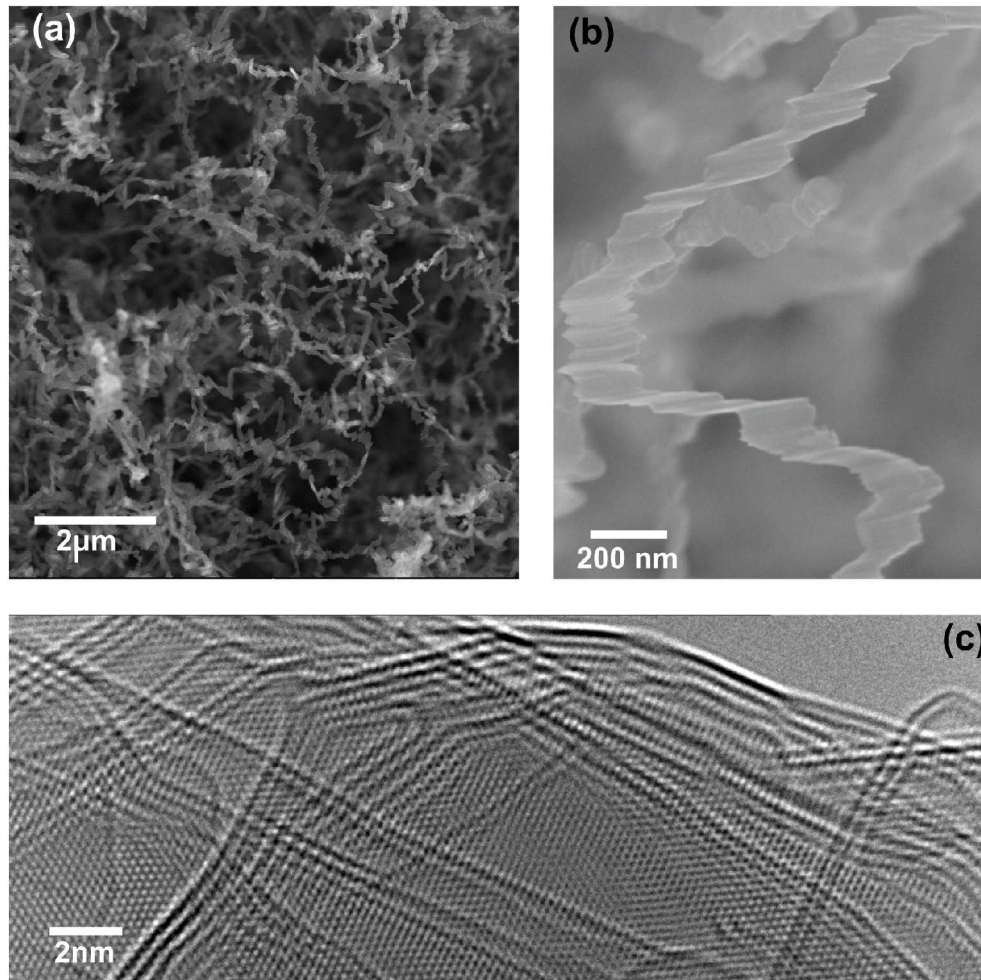
Figure 5.1: (a)Low magnification and (b) high magnification SEM images of CVD produced carbon nanoribbons. (c) edge reconstruction of carbon nanoribbons with joule heating. Courtesy of Campos-Delgado [2,4].

called loops at the edges of the CNRs (see figures 5.3 and 5.4) [7]. These loops are formed to eliminate dangling bonds of the very reactive edges of the nanoribbons when hydrogen is no longer saturating them (*i.e.,* at high temperatures). These loops have been observed before in graphitic fibers [8-11].

As the samples are thermal annealed, interesting features start to emerge. At temperatures below 1500°C, structural changes begin to appear and a well-developed lattice fringe structure can be observed. These fringes start to get aligned as evidence of graphitization (figure 5.4). Above 1500°C, single and double loops start to appear, although open edges are majority. As temperature increases, increasingly straighter lattice fringes are observed, and multi-loop formation emerges, and until being majority in the sample. However, it can be noted from the

129
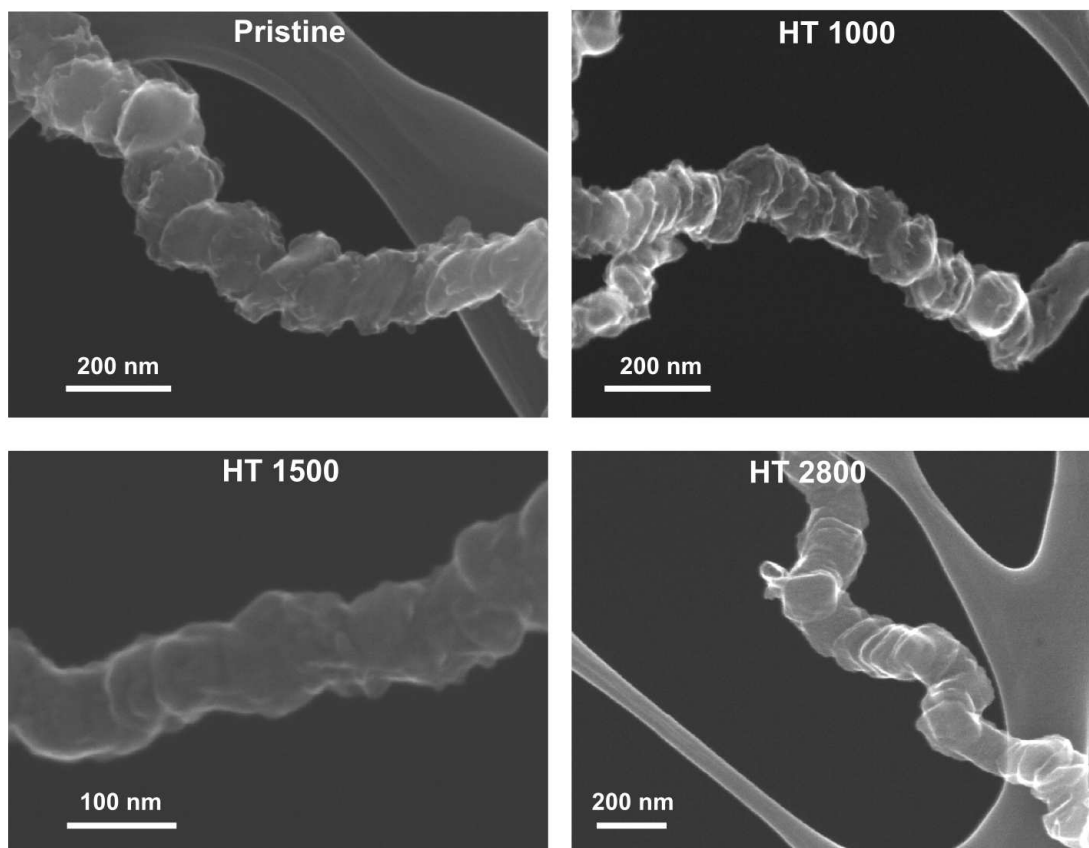
Figure 5.2: Scanning electron micrographs of different carbon nanoribbons after different heat treatment temperatures observed from a top view of the ripples. The effect of heat treatment on the ordering of the graphitic planes is already observed.
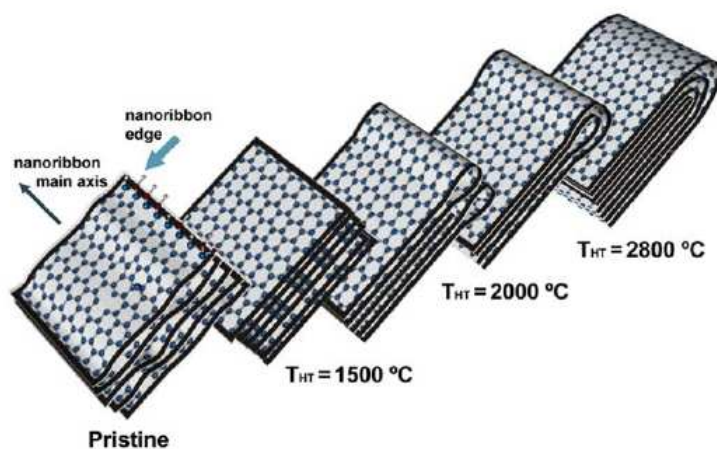
Figure 5.3: Schematic representation of the loop formation upon heat treatment [7].

TEM images that the open edges never cease to appear [7]. A model for loop formation has been proposed, in which two adjacent graphene sheets will tend to

130
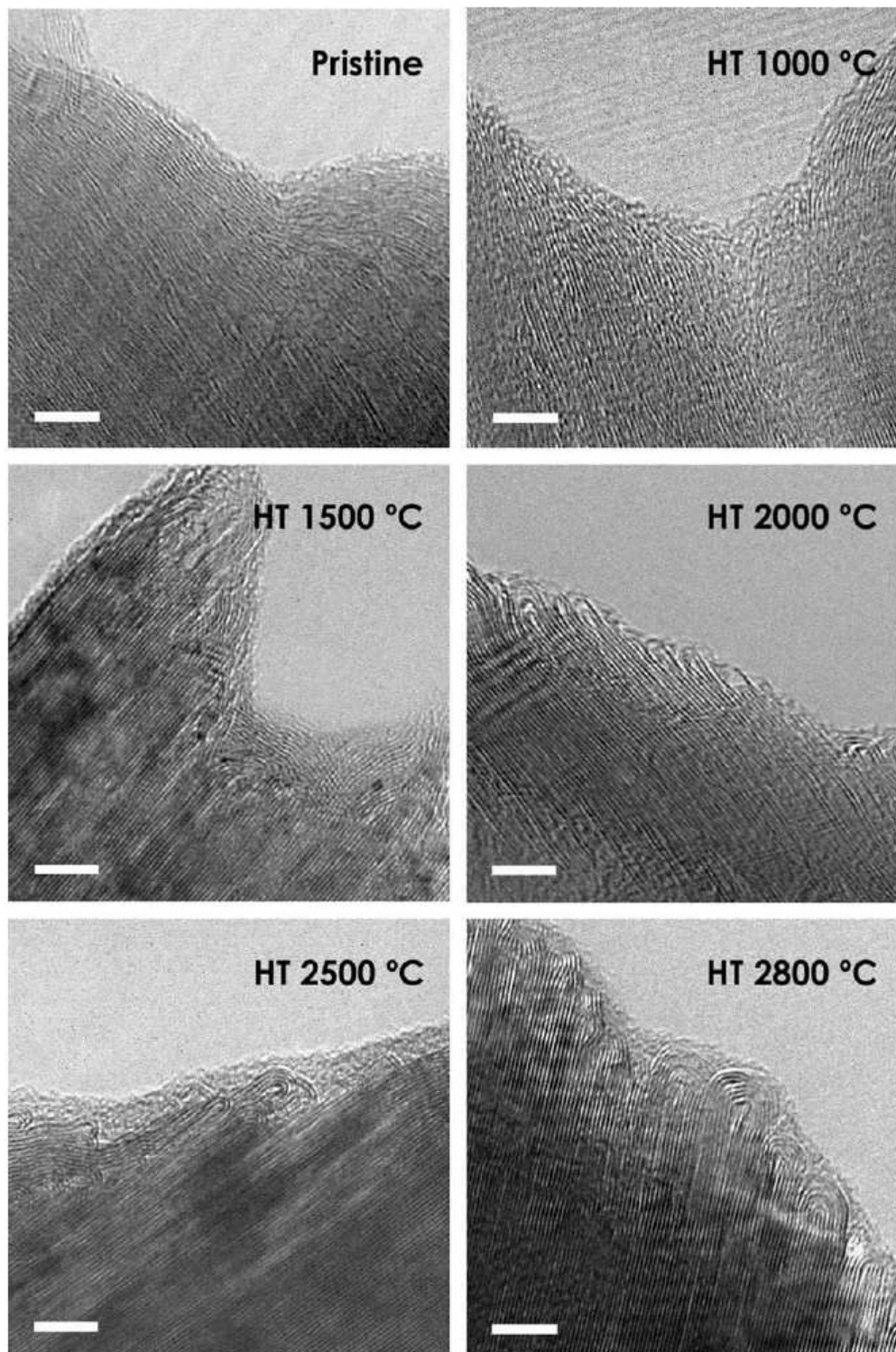
Figure 5.4: Transmission electron micrographs showing the loop formation upon the increase in temperature during heat treatment. Note that at 2000°C the loops are sometimes formed between two consecutive layers. Also, note that even after the 2800°C treatment, there are open edges between some of the loops [7].

join their edges to form a loop, and the radius of curvature will systematically be greater than the separation of the sheets (figure 5.3) [7,12].

5.2.1. X-Ray absorption analysis

It is well known that inner shell excitation probes, such as electron energy loss (EEL) and X-ray absorption spectroscopy, are well suited for studying the structural and electronic properties of carbon materials [13-17]. Therefore, near edge X-ray absorption (NEXAFS) studies were carried out to gain some insight on the structure and the chemical properties of CNRs.

Figure 5.5a shows a typical NEXAFS spectra for a pristine CNR shown in figure 5.5 b. The spectra show the characteristic 1s-π^* transition peak characteristic of sp^2 hybridized C atoms, and a broader peak at 291.5 which is the 1s-σ^* resonance. Additionally, the spectra show a peak at around 288eV and a shoulder close to 290eV. These features have been related to the presence of oxygen and hydrogen at the walls of carbon nanotubes, e.g. functionalization with C==O and COOH (287-289eV) groups or presence of CH$_x$ (289-290eV) species [18-22]. The absorption images (figure 5.5c) at 285.2 eV and 291.9eV show that the samples are significantly more ordered and more graphitic than the carbon grid. In contrast, the images at 288eV and 290eV show that the sample contains as much oxygen species as the carbon grid, but less hydrogenated species. It is important to note that at first sight there is a difference between the edges of the nanoribbon and the inner part of the nanoribbon; however, a point scan at the edge shows no significant differences. The difference shown at the image could rather be a blur-effect, since the size of the edge fringe is very close to the pixel resolution of the method (~20 nm).

Figure 5.6 shows a comparison of the NEXAFS spectra of CNRs after different heat treatment. As mentioned before, the peak at *c.a.* 288 eV can be explained by the introduction of oxygen-containing functional groups at the edges of the open CNRs. As the sample is heated (e.g. at 1500°C), this peak vanishes. However, after further heating (2800°C), a large shoulder appears. Also, a shift toward lower energies of the 1s-π^* transition, and a decrease with respect to the 1s-σ^* resonance is observed after heat treatment. NEXAFS and EELS spectra have been used for determining the ratio of sp^2 to sp^3 bonds in a structure, by taking the
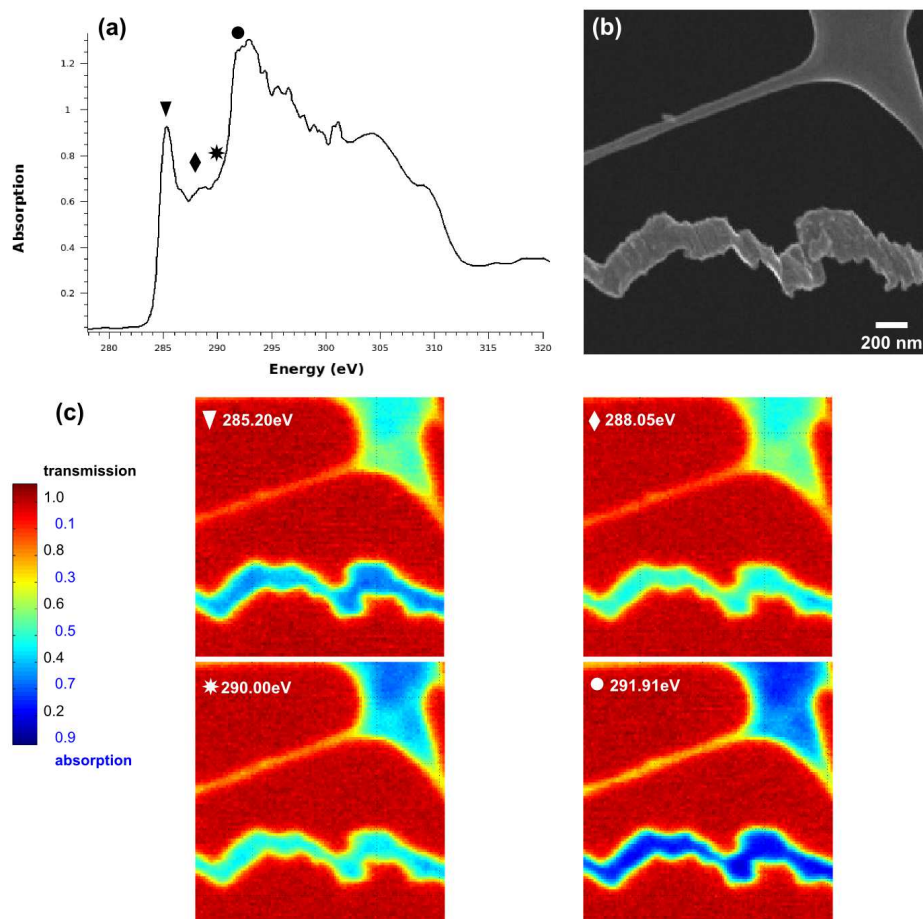
Figure 5.5: (a) NEXAFS absorption spectra for a pristine CNR showing a peak close to 288.05 eV usually attributed to C-H bonds. (b) SEM images of a pristine nanoribbon. (c) STXM images of the same CNR showing that the nanoribbon at four different absorption energies.

area under the 1s-π^* and 1s-σ^* peaks. The sp^2 to sp^3 ratio has been very important for the characterization of amorphous carbon, since the proportion of sp^3 determines the hardness, chemical inertness and friction of the material, which eventually dictates its properties. Figure 5.6 shows that the sp^2 area is reduced as the heat treatment temperature increases. This is rather counter intuitive, and contradicts with the TEM observation of the appearance of fringes as the heat treatment temperature increases (see figure 5.4). However, the quantification of the sp^2 to sp^3 ratio is based on the assumption that the π^* and σ^* bands do not overlap and can be clearly separated [23].

A deconvolution of the spectra of a 2800°C heat treated nanoribbon shows that there are several peaks between the 1s-π^* and 1s-σ^* transitions that contribute to
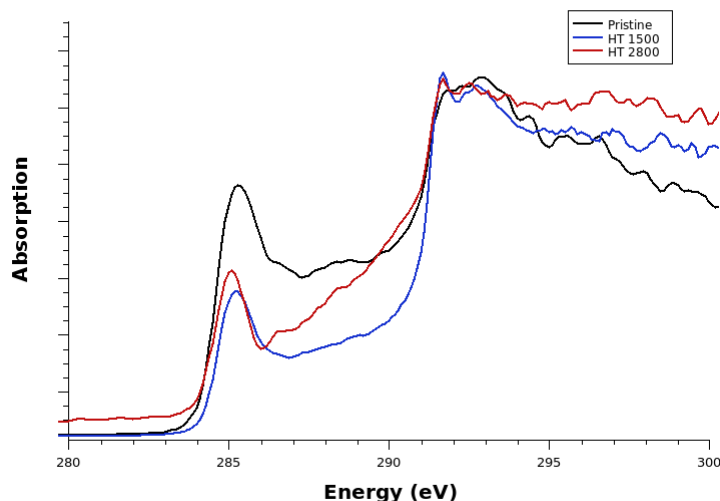
Figure 5.6: NEXAFS spectra for different carbon nanoribbons: pristine, and after heat treatment of 1500°C and 2800°C. The pristine sample exhibits a peak at around 288eV characteristic of oxygen functionalization. This peaks vanishes after thermal annealing, but a pronounced shoulder appears when the sample is treated at 2800°C, in which case cannot be attributed to functionalization.

the extended shoulder, and extends and overlaps with the σ* peak (see figure 5.7). According to this model, the p to s ratio is large and is consistent with the TEM observations.

5.2.2. EELS ANALYSIS

The origin of the peaks in the range between 286-290 eV, as stated before, cannot be attributed to hydrogen or oxygen species. Several theore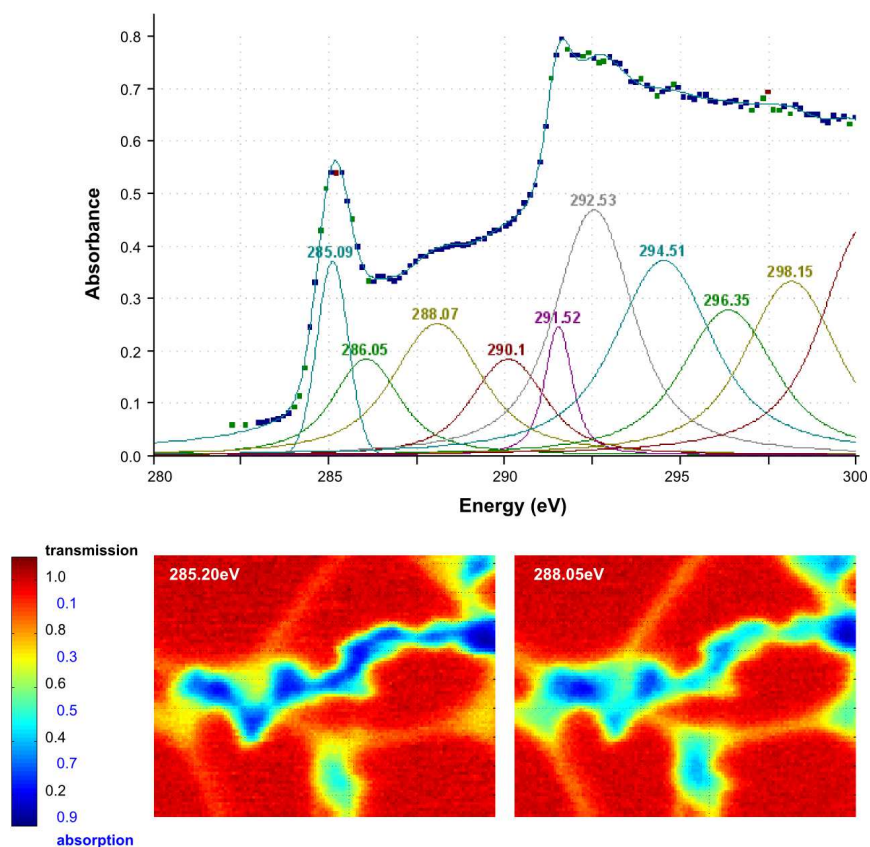tical studies on the EELS spectra of very small diameter carbon nanotubes indicate that the curvature can introduce peaks in this region [24,25].

In order to understand the origin of these peaks, and the shift of the p transition, we carried out Electron Energy Loss function calculations under the Random Phase Approximation of different carbon systems. Figure 5.8 shows the EELS of three different finite carbon systems which have pentagons on their structure. As stated before, pentagon rings on carbon nanostructures are known to be highly reactive sites, and to be responsible for the electronegativity of C_{60}. It is clear that for the case of C_{60}, the large curvature and pentagon sites induce different peaks between the π* and σ* transitions. However this is not that clear in other finite systems, such as nanocones and capped tubes. The effect of the curvature and the pentagonal rings might be suppressed by the presence of hydrogen atoms that were used to avoid dangling bonds during simulation, since a broad s peak is observed, in agreement with the fact that CH_x species introduce transitions close to the s peak. The effect of curvature on the EEL function can be seen more explicitly on the spectra of nanotubes with different diameters. In this case, the peaks

Figure 5.7: Absorption spectra and peak deconvolution of a CNR after heat treatment at 2800°C. Several peaks can be observed between the 1s-π∗ and the 1s-σ∗ transitions, however these cannot be attributed to functionalization groups. The absorption images show that the sample is graphitic, and that the source of the peaks at 288eV is not evenly distributed along the CNR.

between the π* and σ* transitions are more pronounced and left shifted as the curvature increases. This could explain the broad shoulder in the CNR sample treated at 2800°C since there are different curvatures in the overlapping loops (see figures 5.3 and 5.4). Finally figure 5.8c shows the calculated EEL function for looped carbon nanoribbons with different loop diameter, showing consistent results with the previous observations.

In summary, CNRs are a new material that shares several properties with carbon nanotubes and graphite, but it is clear from this analysis that this material also has unique structural and electronic properties. Iijima and co-workers have proposed that loops observed upon heat treatment on highly oriented pyrolitic graphite should have a large amount of heptagonal and pentagonal rings in order to account for the observed rough edges [26]. These sites, or curvature alone, specially the
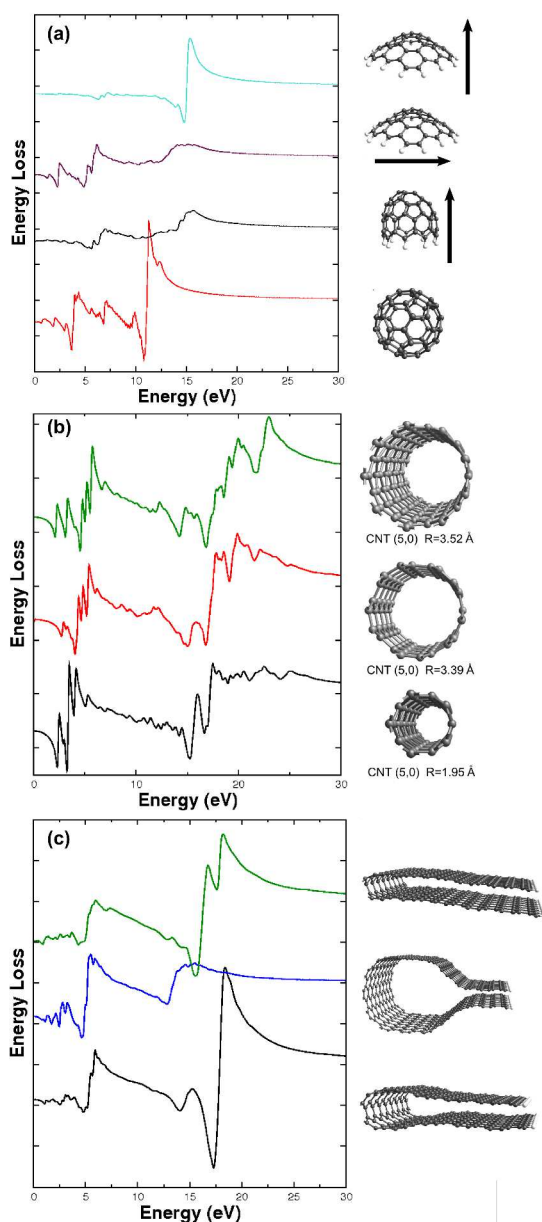
Figure 5.8: Calculated Electron Energy Loss function for different carbon systems. (a) Finite systems: C_{60}, a capped tube and a nanocone exhibit pentagons in their structure showing peaks between the π^* and σ^*. (b) Carbon nanotubes with different diameters. As the diameter decreases, a peak close to the σ^* transition appears, and there is a shift of the π^* transition to lower energies. (c) Looped carbon nanoribbons with different curvature showing peaks between the p and the s transitions.

smallest loops formed at around 2000°C, could introduce new chemistry in one dimensional carbon structures that is only comparable with fullerene chemistry. However, along with the advantages of a robust chemistry, this materials will most probably exhibit the mechanical and electrical properties of carbon nanotubes.

5.3. NANORIBBONS FROM CNTS

In the previous section, we have analyzed a new form of carbon nanoribbons which shares many properties with nanotubes and fullerenes. But it also shows similarities with graphene nanoribbons, since the effect of the shape of their borders determine the properties this materials show; however, in that case what determines the properties is whether the edges form loops or not and the diameter of the loops. However, it is still interesting to try to experimentally achieve materials with closer resemblance with graphene nanoribbons.

Another approach for the production of carbon nanoribbons has been to use carbon nanotubes as starting material, and somehow peel off the walls in a controlled way (see figure 5.9) [27]. Recently, James Tour and coworkers have used a chemical attack based on sulfur acid, potassium permanganate and mild heating that

136
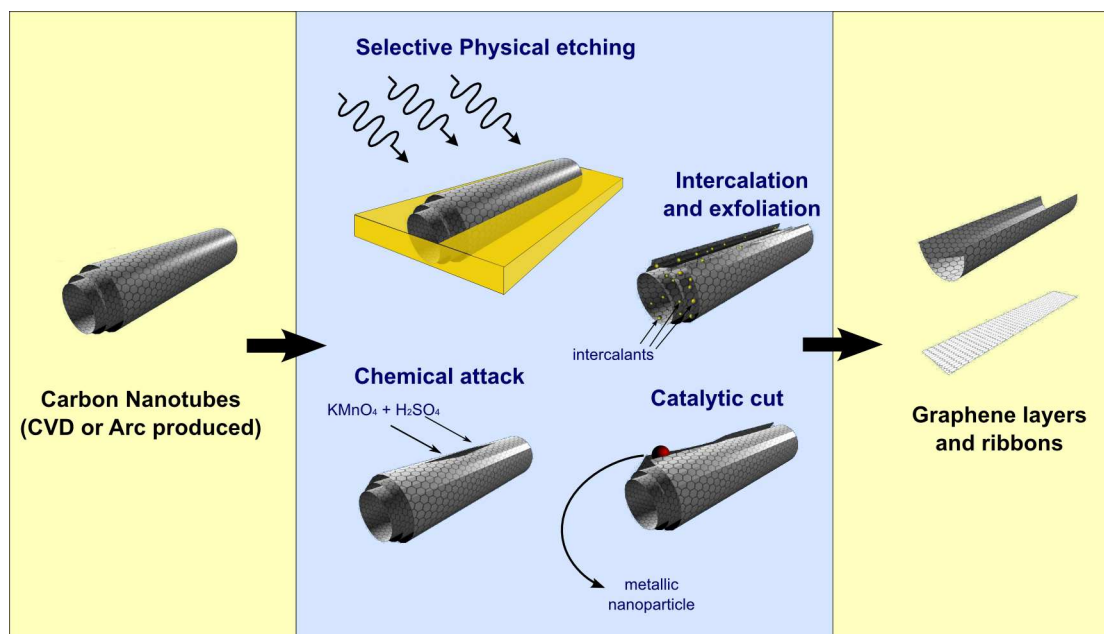
Figure 5.9: Carbon nanotubes can be unzipped by treating them with sulphuric acid and potassium permanganate (anoxidizing agent) to form nanoribbons or graphene sheets (single layers of graphite). A complementary method consists in nanotubes partially embedded in a polymer film which are etched by argon plasma. Another approach is to insert alkali-metal atoms between the concentric cylinders of a multiwalled carbon nanotube, which causes graphene sheets to peel off. The method presented here use catalytic metal nanoparticles to cut along the length of a nanotube like a scalpel.

opens up the tubes longitudinally [28]. Similarly, Cano *et al.,* have opened CNTs by the intercalation of lithium and ammonia [29]. However, in both cases the resulting nanoribbons exhibit impurities at the edges that could affect, for example, their electronic properties. The group of Hongjie Dai has presented a multi-step process in which CNTs partially embedded in a polymer film are etched with argon plasma [30]. Subsequently, the film is removed using solvent vapor followed by a heat treatment of the resulting nanoribbons to remove any residual polymer [30]. The key advantage of this technique is that very narrow nanoribbons (< 10nm) can be produced, resulting in a sample of all semiconductor nanoribbons; however, this multi-step method is hardly scalable.

Recently, Datta and co-workers [31], and separately Ci and coworkers [32,33] demonstrated the controlled catalytic cut of graphite by deposited metal nanoparticles. Carbon in graphite diffuses on the metal nanoparticle when the system is heated at approximately 900ºC under an Ar-H atmosphere until the particle gets saturated and then reacts with H_2 to, in a process that has been addressed in the literature as catalytic hydrogenation of carbon [34]. Depending on
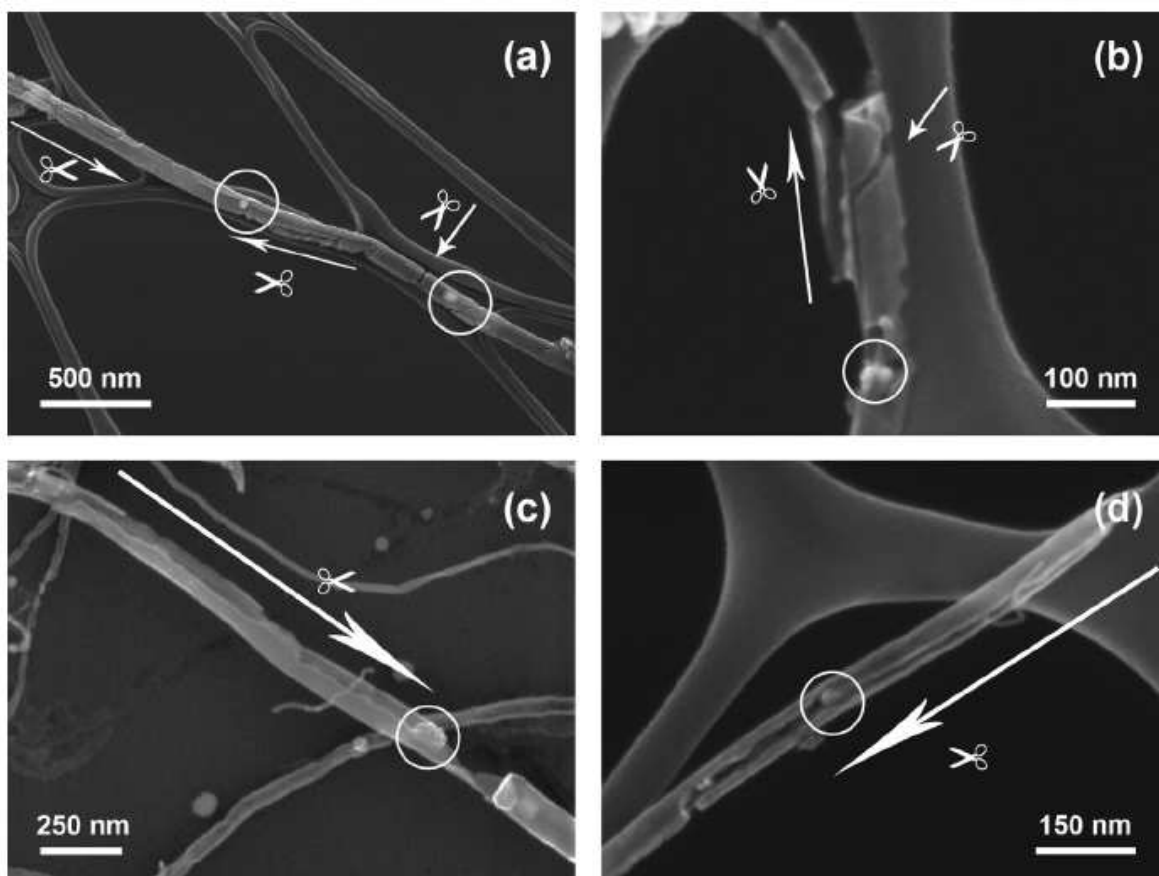
Figure 5.10: SEM micrographs of the prepared samples. (a, b, and d) SEM images of CNxMWNTs cut with Ni nanoparticles. (c) SEM image of a MWNT on a Si substrate, with Co nanoparticles. Arrows guide the eye along the nanocutting and circles mark the presence of metal nanoparticles.

the particle size, the cut can be random, or directed under specific directions, forming armchair or zigzag edges [32,33].

In our laboratory, we have carried out the catalytic cutting of multi-walled carbon nanotubes (MWNTs) and nitrogen-doped multi-walled carbon nanotubes (CNxMWNTs) using either Co or Ni nanoparticles so as to unzip the tubes and form graphene sheets and GNRs (see figure 5.10). As previously reported [32,33], we found that the cutting direction and depth is mostly determined by the particle size and the number of step edges where the nanoparticle nucleates. The experimental process could be understood as a reverse of CVD carbon nanofiber growth.

Metal nanoparticles nucleated on the surface of CNxMWNTs create mostly random cuts on the outer graphitic layers, via catalytic hydrogenation of graphene sheets [32-34]. Larger metal nanoparticles (*c.a.* 40 nm) travel along the axis of
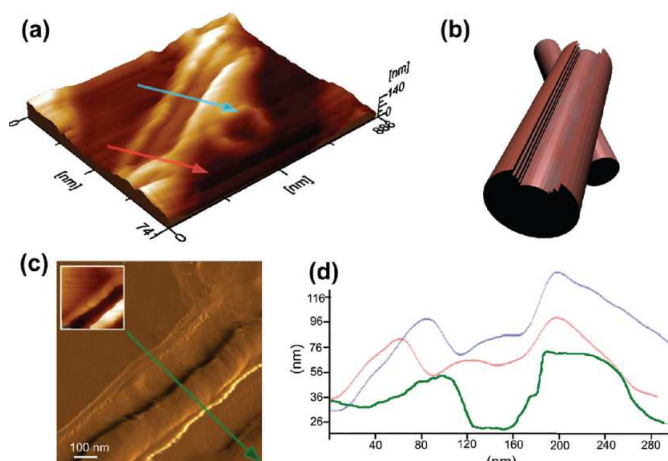
Figure 5.11: (a) AFM image of a CNxMWNT cut along the axis. (b) Schematic model of the cut shown in (a). (c) RMS roughness and topography (inset) AFM images of the detail of a nanotube cut along the axis. (d) Surface profiles along different lines of nanotube cuts shown in (a) and (c).

carbon nanotubes, performing deeper cuts that open MWNTs and CNxMWNTs, thus resulting in the creation of carbon nanoribbons and nanosheets.

After cutting N-doped MWNTs, different sized nanoribbons are produced (typically 15 to 40 nm wide and 100 to 500 nm long). Occasionally, longer nanoribbons are achieved, and most of the time graphitic nanosheets are observed. Most of the tubes are either partially cut or open along the axis.

Si wafers covered with nanotubes and nanoribbons where characterized by AFM in order to get more accurate information on the shape and roughness of the unzipped nanostructures (see figure 5.11). Figure 5.11a depicts an AFM topography image of two overlapped CNx MWNTs and figure 5.11b depicts a model of both nanotubes, in order to better understand the AFM image shown in figure 5.11a. The nanotube on the top has been cut by a metal nanoparticle and we were able to follow the nanoparticle track by analyzing the surface profile along different line scans depicted by arrows (see figure 5.11, panels a and d). Another example of CNx MWNTs unzipped is exhibited in a rootmean- square (rms) roughness image (see figure 5.11c). Here, the line profile (green) shows a deeper cut (see figure 5.11, panels c and d).

The chirality of the nanotubes plays an important role during cutting, especially when the active nanoparticle is 15 nm or smaller. As it has been described in earlier reports for HOPG [32,33], a catalyst particle is able to selectively cut graphene sheets along an armchair or zigzag atomic line. However, it is well known that MWNTs are formed by concentric layers of individual cylinders with very different chiralities. This could be the reason why the active metal particle does not always perform straight cuts on the surface of CNTs. It is important to also consider the amount of defects present on the nanotube surface which were grown by

pyrolisis of hydrocarbons, (vacancies, dopants, etc.), could alter significantly the cuts on the tube surface. For the case of CNxMWNTs, nitrogen is incorporated in the graphitic lattice, and might affect considerably the straight cutting of the tubes. Theoretical simulations on graphene have predicted that defects within the graphitic planes could cause the nanoparticle to turn at a given angle (commonly 60 or 120°) [32,33]. Previous reports for CNxMWNTs predict [35] that nitrogen bonded to the carbon atoms in a pyridinic way certainly induces voids in the graphitic layers, which could be the cause of more turns during the cutting process.

From unzipped MWNTs pure carbon nanoribbons and nanosheets can be produced. On the other hand, in CNxMWNTs nitrogen is incorporated within the graphitic layers and further investigation needs to be performed in order to determine whether nitrogen is present in the produced ribbons. Such case would be very interesting, since it has been predicted in the literature that doping agents (N or B) in graphene nanoribbons could induce remarkable modifications in the electronic and spin properties of such doped structures [36].

5.4. CONCLUSIONS

For a long time, it seemed as if the landscape of the nanoscale carbon science was related only to cage-like objects — spheres and tubes. But recently, flat forms of carbon have gained prominence with the discovery of graphene. The properties of these new flat systems are different from other forms of nanoscale carbon, and therefore set a whole new kind of challenges and opportunities. As it has been exposed in this Chapter, there has been an important progress in order to understand the properties of these systems from a theoretical point of view. However, to realize the practical potential of these newcomers, methods for their mass production are sorely needed.

Some efforts have started to appear. Two pathways have been followed: a bottom-up approach with CVD, and a top-down method with nanotubes as starting points. For the first case, a complete understanding of the resulting product's structure is still needed. However, this work has proved that this systems show characteristics of nanotubes, fullerenes and nanoribbons. For the second approach, more research is needed to find ways of efficiently unwrapping single- and double-walled nanotubes, in order to carefully control the widths and edge

patterns of nanoribbons. In either case, electronic, mechanical, chemical and thermal properties must be probed. Particular attentions should be paid in order to study the properties of synthesized doped few layer nanoribbons, as these systems might hold the key for the realization of the potential applications of graphene and graphene nanoribbons. Once bulk quantities of nanoribbons are available, their toxicological effects and possible biological applications can also be studied. And, last but not least, the potentially unusual magnetic and catalytic properties of these materials can finally be explored.

5.5. RELATED PUBLISHED WORK

- Elias, A.; Botello-Mendez, A; Meneses-Rodriguez, D; Gonzalez, V; Ramírez-González, D; Ci, L; Muñoz-Sandoval, E; Ajayan, P; Terrones, H; Terrones, M. Longitudinal Cutting of Pure and Doped Carbon Nanotubes to Form Graphitic Nanoribbons Using Metal Clusters as Nanoscalpels. *Nano Letters (in press)*
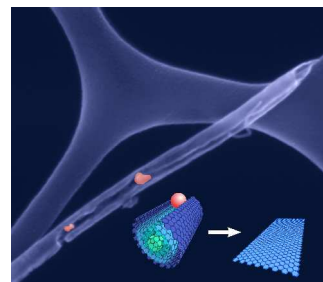
5.6. REFERENCES

[1]. Geim, A.K. & Novoselov, K.S. The rise of graphene. *Nat Mater.* **6**, 183-191 (2007).

[2]. Campos-Delgado, J. et al. Bulk Production of a New Form of sp2 Carbon: Crystalline Graphene Nanoribbons. *Nano Lett.* **8**, 2773-2778 (2008).

[3]. Pinault, M. et al. Carbon nanotubes produced by aerosol pyrolysis: growth mechanisms and post-annealing effects. *Diamond Relat. Mater.* **13**, 1266-1269 (2004).

[4]. Jia, X. et al. Controlled Formation of Sharp Zigzag and Armchair Edges in Graphitic Nanoribbons. *Science* **323**, 1701-1705 (2009).

[5]. Bets, K., & Yakobson, B. Spontaneous twist and intrinsic instabilities of pristine graphene nanoribbons. *Nano Res.* **2**, 161-166 (2009).

[6]. Shenoy, V. B., Redy, C. D., Ramasubramaniam, A., & Zhang, Y. W. Edge-Stress-Induced Warping of Graphene Sheets and Nanoribbons. *Phys. Rev. Lett.* **101**, 245501 (2008).

[7]. Campos-Delgado, J. et al. Thermal stability studies of CVD-grown graphene nanoribbons: Defect annealing and loop formation. *Chem. Phys. Lett.* **469**, 177-182 (2009).

[8]. Murayama, H. & Maeda, T. A novel form of filamentous graphite. *Nature* **345**, 791-793 (1990).

[9]. Gogotsi, Y., Libera, J.A., Kalashnikov, N. & Yoshimura, M. Graphite Polyhedral Crystals.

Science **290**, 317-320 (2000).

[10]. Endo, M. et al. Structural characterization of cup-stacked-type nanofibers with an entirely hollow core. *Appl. Phys. Lett.* **80**, 1267-1269 (2002).

[11]. Endo, M. et al. Transitional behaviour in the transformation from active end planes to stable loops caused by annealing. *New J. Phys.* **5**, 121 (2003).

[12]. Rotkin, S. V. SWNT Nucleation: Energetics of Zipping Edge Mechanism. *Mat. Res. Soc. Symp. Proc.* **675**, W291 (2001) .

[13]. Stephan, O. et al. Electron energy-loss spectroscopy on individual nanotubes. *J. Electron Spectrosc. Relat. Phenom.* **114**, 209-217 (2001).

[14]. Zhong, J. et al. X-ray absorption near-edge structure and photoelectron spectroscopy of single-walled carbon nanotubes modified by a HBr solution. *Carbon* **44**, 866-872 (2006).

[15]. Tang, Y.H., Sham, T.K., Hu, Y.F., Lee, C.S. & Lee, S.T. Near-edge X-ray absorption fine structure study of helicity and defects in carbon nanotubes. *Chem. Phys. Lett.* **366**, 636-641 (2002).

[16]. Banerjee, S. et al. Near-Edge X-ray Absorption Fine Structure Investigations of Order in Carbon Nanotube-Based Systems. *J. Phys. Chem. B* **109**, 8489-8495 (2005).

[17]. Watts, B., Thomsen, L. & Dastoor, P. Methods in carbon K-edge NEXAFS: Experiment and analysis. *J. Electron Spectrosc. Relat. Phenom.* 151, 105-120 (2006).

[18]. Felten, A.; Hody, H.; Bittencourt, C.; Pireaux, J.-J.; Hernandez-Cruz, D.; Hitchcock, A. P. Scanning transmission X-ray microscipy of isolated multiwall carbon nanotubes. *Appl. Phys. Lett.* **89**, 093123 (2006).

[19]. Braun, A. et al. Advantages of soft X-ray absorption over TEM-EELS for solid carbon studies--a comparative study on diesel soot with EELS and NEXAFS. *Carbon* **43**, 117-124 (2005).

[20]. Warwick, T. et al. A new bend-magnet beamline for scanning transmission X-ray microscopy at the Advanced Light Source. *J. Synchrotron Rad.* **9**, 254-257 (2002).

[21]. Kuznetsova, A. et al. Oxygen-Containing Functional Groups on Single-Wall Carbon Nanotubes: NEXAFS and Vibrational Spectroscopic Studies. *J. Am. Chem. Soc.* **123**, 10699-10704 (2001).

[22]. Grill, A. Diamond-like carbon: state of the art. *Diamond Relat. Mater.* **8**, 428-434 (1999).

[23]. Titantah, J. T., & Lamoen, D. Technique for the sp2/sp3 characterization of carbon materials: Ab initio calculations of near-edge structure in electron-energy-loss spectra. *Phys. Rev B* **70**, 075115 (2004).

[24]. Titantah, J. T., Jorissen, K., & Lamoen, D. Density functional theory calculations of energy-loss carbon near-edge spectra of small diameter armchair and zigzag nanotubes: Core-hole, curvature, and momentum-transfer orientation effects. *Phys. Rev. B* **69**, 125406 (2004).

[25]. Stéphan, O., Ajayan, P. M., Colliex, C., Cyrot-Lackmann, F., & Sandré, E. Curvature-induced bonding changes in carbon nanotubes investigated by electron energy-loss spectrometry. *Phys. Rev. B* **53**, 13824 (1996).

[26]. Liu, Z., Suenaga, K., Harris P. J. F., & Iijima, S. Open and Closed Edges of Graphene Layers. *Phys. Rev. Lett.* **102**, 015501 (2009).

[27]. Terrones, M. Materials Science Nanotubes unzipped. *Nature* **458**, 845-846 (2009).

[28]. Kosynkin, D.V. et al. Longitudinal unzipping of carbon nanotubes to form graphene nanoribbons. *Nature* **458**, 872-876 (2009).

[29]. Cano-Márquez, A.G. et al. Ex-MWNTs: Graphene Sheets and Ribbons Produced by Lithium Intercalation and Exfoliation of Carbon Nanotubes. *Nano Lett.* **9**, 1527-1533 (2009).

[30]. Jiao, L., Zhang, L., Wang, X., Diankov, G. & Dai, H. Narrow graphene nanoribbons from carbon nanotubes. *Nature* **458**, 877-880 (2009).

[31]. Datta, S.S., Strachan, D.R., Khamis, S.M. & Johnson, A.T.C. Crystallographic Etching of Few-Layer Graphene. *Nano Lett.* **8**, 1912-1915 (2008).

[32]. Ci, L. et al. Controlled nanocutting of graphene. Nano Res. **1**, 116-122 (2008).

[33]. Ci, L. et al. Graphene Shape Control by Multistage Cutting and Transfer. *Adv. Mater.* (2009) DOI: 10.1002/adma.200900942.

[34]. Barker, R., Sherwood, R. & Derouane, E. G. Further-Studies of the Nickel-Graphite-Hydrogen Reaction. *J. Catal.* **75**, 382-395 (1982).

[35]. Terrones, M., Kamalakaran, R., Seeger, T. & Rühle, M. Novel nanoscale gas containers: encapsulation of N 2 in CN x nanotubes. *Chem. Commun.* **2000**, 2335–2336 (2000).

[36]. Cervantes-Sodi, F.; Csányi, G.; Piscanec, S.; Ferrari, A. C. Edge-functionalized and substitutionally doped graphene nanoribbons: Electronic and Spin properties. *Phys. Rev. B* **77**, 165427 (2008).

Chapter 6

Finite Layered Materials

CONTENTS

6.1. INTRODUCTION

Carbon nanotubes, graphene and graphene nanoribbons have been considered as possible substitutes for silicon in a new era of carbon-based electronics due to their interesting, and sometimes superior, electronic and magnetic properties [1]. However, carbon nanotubes have shown major drawbacks, such as the lack of control of the electronic properties of the synthesized material [2]. In contrast, tailoring the electronic properties of graphene and graphene nanoribbons has been proved successful with top down and bottom up approaches [3-6].

Graphene is a one layer thick 2D material that exhibits unusual physical phenomena such as integer Quantum Hall effect, Klein Paradox, and Quantum blockade, due to its singular band structure which results in relativistic fermions [7]. A finite layer of graphene will inevitably have borders (thus, forming graphene nanoribbons), which can exhibit edge states and different electronic and magnetic properties depending on the size and type of border. These phenomena could be applied to revolutionize electronics through the use of new variable states (e.g. quantum states, spin, etc) and processing architectures that take advantage of new phenomena. However, for the realization of such carbon-based electronic devices, a deeper understanding of the above mentioned phenomena must be gained.

Another (simpler) approach towards carbon-based electronics is to use this one layer thick material in a similar way as silicon is used in today's electronics (i.e., with electron charge as the variable state, and the concept of transistors for processing units). A one electron transistor has already been proved for a graphene quantum dot exploiting the Coulomb blockade and quantum confinement [8]. However, it might be difficult to use graphene alone under this approach, because graphene and graphene nanoribbons are semimetal or in the case of very narrow nanoribbons, a relatively small gap semiconductor, but current electronics architecture require insulators for processing information. The use of other finite 2D layered materials with other properties could therefore prove useful for the realization of such novel electronics. Recently, other one-layer thick materials have been synthesized [9], and the properties of their borders and edge states are starting to be studied, both from the theoretical and the experimental standpoints.

In this chapter, we review the state of the art of the investigation of edge states in

147

layered materials. The most important layered material is without a doubt graphene. This material was first isolated by Geim and Novoselov through a simple micro cleavage method [10]. The electronic and magnetic properties of graphene and graphene nanoribbons that have been reported so far were outlined in §4.3. In §6.2, we describe some of our contributions for the use of defects in graphene for tailoring the properties of the nanoribbons with the aid of structural defects. Next, in §6.4 and §6.5 the electronic and magnetic properties of other layered materials are exposed. Some of these materials have been isolated by the group of Geim and Novoselov, using the same simple cleavage technique [9]. Such materials include boron nitride, molybdenum disulfide, and niobium selenide [9]. Finally, in §6.6, the properties of other materials, such as ZnO, that become layered only when nanostructured are presented. This variety of materials should give the field new perspectives and more alternatives for the future of electronics.

6.2. Edge defects in graphene nanoribbons

In §4.4 we reviewed the properties of graphene and graphene nanoribbons. In particular, in §4.4.6 we mentioned that edge disorder has strong impact on the electronic and magnetic properties of graphene nanoribbons. We also mentioned that zigzag and armchair edges are the most common edge termination according to experiments. Recently, Koskinen and coworkers have found that edge reconstruction of graphene nanoribbons can occur in which non hexagonal rings occupy the edges [11]. Indeed, these edge reconstructions have been observed experimentally by the same group, and by others and suggest that these are metastable configurations (see figure 6.1) [12,13].

First principles calculations on the edge energies of GNRs indicate that A-GNRs have lower energy than Z-GNRs [14,15]. However, edge reconstruction by pentagonal and heptagonal carbon rings can bring the stability of the zigzag structure lower than that of armchair. We shall call this new structure Zig-57 GNR. Similarly, one can construct different armchair edge reconstructions labeled as Arm-57, Arm-56 and Arm-5677, depending on the number of sides of the carbon rings at the edge (see figure 6.2).

We have studied the electronic and magnetic properties of the different reconstructed GNRs with and without hydrogen passivation. We have found that
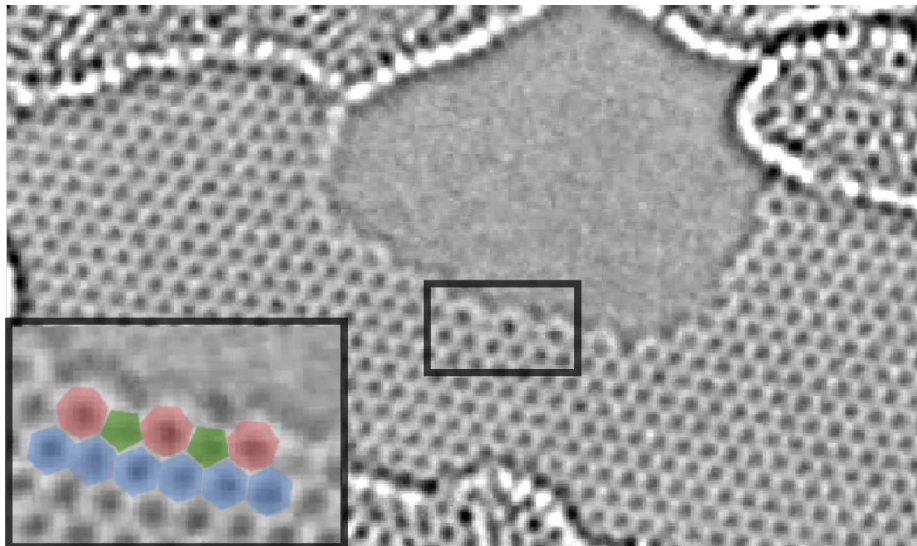
Figure 6.1: Edge reconstruction in graphene observed under an aberration corrected TEM [13].

the electronic properties deviate significantly from the bare armchair and zigzag nanoribbons, and since these reconstructions have been found experimentally their properties should be studied and understood.

Figure 6.3 shows the band structure for the typical reconstructed GNR systems. The Arm-57 (N_A=10) band structure exhibits a magnetic moment of ~1μ_B per edge atom, although a magnetic moment is not always observed in these systems. In any case, the system is metallic; however, when the edges are saturated with hydrogen, a band gap is opened.

The Zig-57 system shows a metallic behavior similar to the zigzag case. When the edges are saturated with hydrogen atoms, the system remains metallic. However, Koskinen and coworkers have demonstrated that in this case, the energy of the hydrogen atoms in the H_2 molecule is lower than in the edges of the Zig-57 GNR, indicating that the system without edge passivation is more probable to be observed. Also, the energy of these systems is significantly lower than the bare Z-GNR and close to the A-GNR.

As in the case of the Arm-57 GNRs, the non-passivated Arm-56 GNRs can exhibit a magnetic moment, and are always metallic, even with the saturation of the edges by hydrogen atoms. In this case, the passivation of hydrogen is favorable with respect to the formation of the H_2 molecule.

The band structure of the Arm-5677 (N_A=10 for the non-passivated case, and
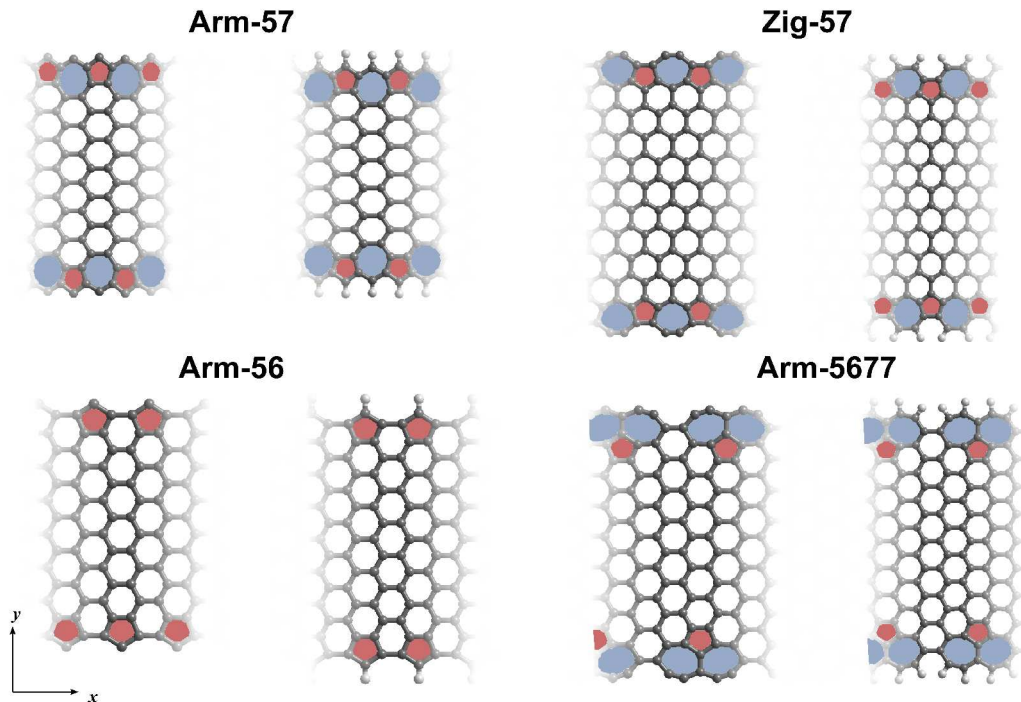
Figure 6.2: Ball and stick models of non-passivated and hydrogen passivated graphene nanoribbons (GNRs) with edge reconstruction, *i.e.,* with edge shape different from zigzag or armchair. The reconstructed GNRs exhibit pentagonal and heptagonal rings (shaded in red and blue, respectively), as has been found experimentally. Note that the armchair edge reconstructions (Arm-57, Arm-56, Arm-5677) show different symmetry depending on the width of the nanoribbon. The GNRs are periodic in the x direction.

N_A=11 for the H-passivated case in figure 6.3) systems can exhibit a band gap. As in the Zig-57 case, the saturation of the edges with hydrogen is unfavorable.

Figure 6.4 shows the dependence of the electronic band gap for the non-passivated Arm-5677 and the hydrogen saturated Arm-5677 and Arm-57 cases. It can be observed that both the hydrogen passivated and the non passivated Arm-5677 cases show a family dependence of the band gap with the width as in the case of the bar A-GNRs. However in this case only one family (N_A=3p+1) exhibit a finite band gap, and the other two families (N_A=3p, N_A=3p+2) have zero band gap. In both cases, the energy gap initially increases, but it is expected to decrease monotonically after some critical width. It is interesting to note that the most stable case for the Arm-5677, *i.e.,* without hydrogen passivation, exhibits a larger band gap. As it has been mentioned before, calculations including electron-electron interactions usually open up the energy gaps, so it would be interesting to calculate the band gaps for these systems under, for example, the GW approximation. The dependence of the band gap of the Arm-57 passivated with hydrogen is somewhat
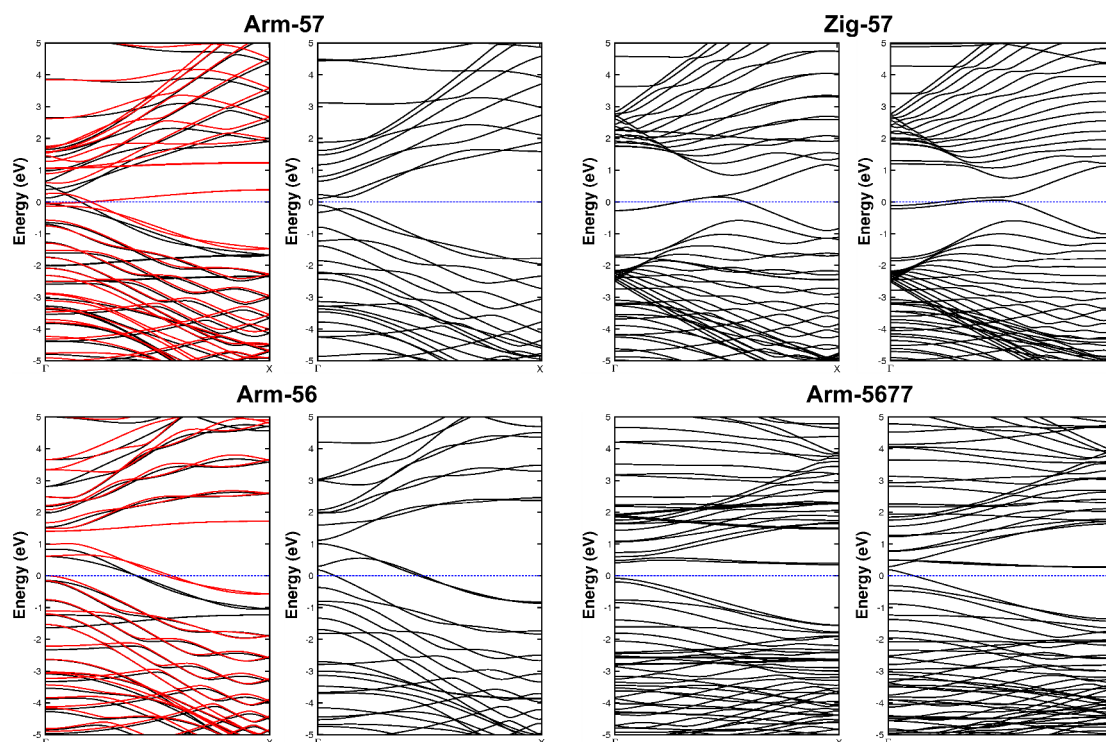
Figure 6.3: Band structure for typical non-passivated (left) and hydrogen-passivated (right) edge-reconstructed GNRs. Note that the non passivated Arm-57 and Arm-56 GNRs can exhibit a magnetic moment (see figure 6.4). In contrast, the hydrogen passivated Arm-57, and Arm-5677, and the non-passivated Arm-5677 cases show a band gap which depend on the width (see figure 6.5). The rest of the systems are always metallic.

irregular, however, as shown in figure 6.5 it follows the same tendency of initially increasing ($N_A < 10$), but then decreasing as the width of the nanoribbon increases.

The magnetic properties of the Arm-56 and Arm-57 are somewhat puzzling. We have calculated the energy of these systems starting from two configurations (see figure 6.5): 1) the spin of atoms at the edges are aligned throughout the edge, *and* aligned parallel between the edges. In this case, called the ferromagnetic case (FM) there is at total magnetic moment (~$1\mu_B$ per edge atom). 2) the spin of the atoms at the edges are aligned throughout the edge, but aligned antiparallel with respect to the opposite edge. In this last case called the anti-ferromagnetic case (AFM) the total magnetic moment is zero, even when the local magnetic moment at the edge atoms is $\pm 1\mu_B$. In the case of the Z-GNRs the energy of the AFM case is always lower, and the difference E_{AFM}-E_{FM} becomes smaller as the width of the GNR increases. Figure 6.5 shows the dependence of the energy difference on the width for these systems. It can be seen that it varies without any obvious pattern.
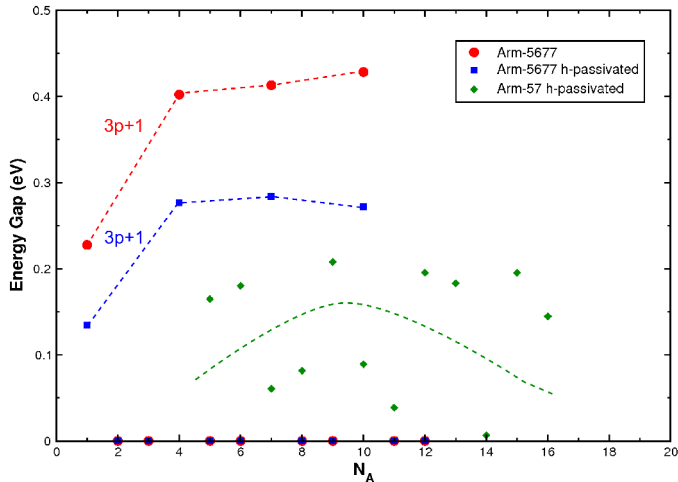
Figure 6.4: Energy band gaps for non-pasivated and hydrogen-passivated Arm-5677 GNRs as a function of width. Note that, as in the case of pure armchair GNRs, there are three families of Arm-5677 and H-passivated Arm-5677. However, in this case, the NA=3p and NA=3p+2 the energy gap is zero, and finite for NA=3p+1. The energy gap of the Hydrogen passivated Arm-57 oscillates around 0.1eV. Dashed lines are guides to the eye.
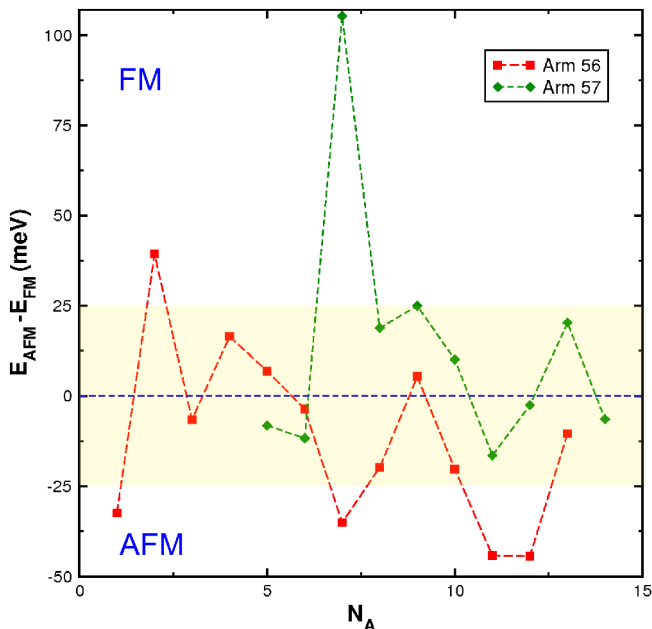
Figure 6.5: Energy difference for the non-passivated Arm-56 and Arm-57 cases as a function of width. The shaded region represents the thermal energy at room temperature, at which most systems could probably be turned to ferromagnetic upon external fields.

However, in most cases the difference between the AFM and FM case is lower than 25meV, which suggest that it could be possible to align the magnetic moments at the edges with an external field.

6.2.1. HYBRID GRAPHENE NANORIBBONS

In 1992 Terrones and Mackay proposed that graphene can exhibit grain boundaries by the inclusion of pentagons and heptagons, preserving the total Gaussian curvature equal to zero at the graphene layer and changing the chirality in such a way that zigzag and armchair edges coexist in the same structure (see figure 6.6) [16]. This kind of grain boundary was studied before [17], and has been observed experimentally by scanning tunneling microscopy (STM) in highly ordered pyrolytic graphite (HOPG) [18]. In addition, it has been shown that this kind of defects could be easily identified experimentally with IR and Raman spectroscopies [19]. A whole new class of finite graphene structures (nanoribbons) could be built following the main idea outlined in

the study of graphitic grain boundaries. When simulating the diffraction pattern of graphene with a 5-7 grain boundary we find that zigzag and armchair features are present in the form of a pattern with twelve spots (see figure 6.6c). Such a fingerprint could be useful for experimentally identifying these systems.

In this Section, we present a linear array of pentagons and heptagons as a grain boundary to rotate a piece of a graphene, and in this way smoothly converting an armchair nanoribbon into a zigzag nanoribbon (see figure 6.6a). In other words, an armchair nanoribbon (blue part in figure 6.6) can be joined to a zigzag nanoribbon (green part in figure 6.6) using a grain boundary formed by a linear array of pentagons and heptagons (called 5-7 chain from here on), thus forming a hybrid nanoribbon (HNR). Similarly, a 2D system can be constructed by merging zigzag and armchair ribbons consecutively (figure 6.6b), thus creating a hybrid graphene (HG). Different systems could be constructed in a systematic way by tweaking the number of armchair dimers (N_A), and the number of zigzag chains (N_Z), resulting in a (N_A,N_Z)-HNR, or a (N_A,N_Z)-HG, for the 1D and 2D cases, respectively. Additionally, more complex 1D systems could be achieved by incorporating more than one 5-7 chain, thus resulting in armchair(N_A)-zigzag(N_Z)-armchair(N_A)-HNRs, or zigzag(N_Z)-armchair(N_A)-zigzag(N_Z) HNRs, and so on.

The incommensurability of the graphene ribbons in the zigzag and armchair directions is manifest in these structures. The armchair segments are under tension, whereas the zigzag segments are under compression. The hexagonal network is deformed, and the angles change from 120° to (114.7°,122.6°,122.6°) for the armchair case, and (113.6°, 123.2°, 123.2°) for the zigzag case. The bond lengths are also distorted, being extended up to 1.54 Å for the armchair section, and compressed up to 1.38 Å in the zigzag case.

It is well established that the electronic properties of armchair ribbons depend on their width, resulting in three families of nanoribbons. In particular, ribbons with N_A = 3p, where p is an integer, are semi-metallic, according to LDA calculations [20], or have a small band gap in calculations including electron-electron interactions [21]. In any case, it is interesting to investigate the effect of width on the electronic properties of the hybrid graphene systems described above.

We have computed the electronic properties of HG with different armchair and zigzag widths. In particular, we have studied (2,4)-(6,4) HG, and (5,8) HG systems.

153
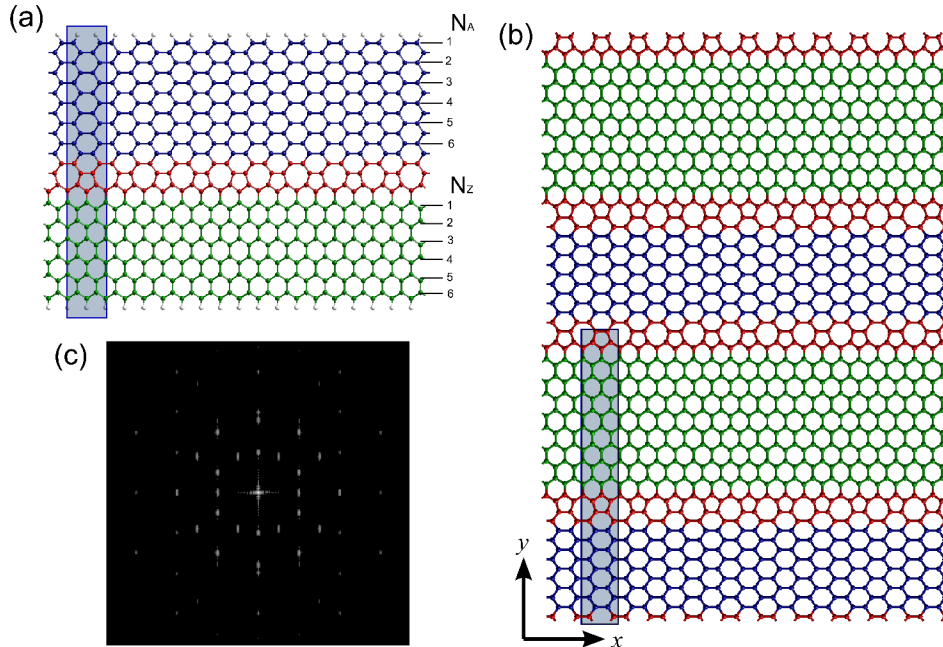
Figure 6.6: Molecular models of ordered arrays of pentagon-heptagon defects on a hybrid-graphene nanoribbon ($N_A = N_Z = 6$) (a) and a $N_A = 5$, $N_Z = 8$ single hybrid-graphene layer (b). The shaded region represents the unit cell for each case; the nanoribbon is periodic on the x direction, while the graphene layer is periodic in x and y. Colors indicate the armchair (blue), zigzag (green) and 5-7 chain region (red) for clarity. (c) Simulated diffraction pattern of graphene with a 5-7 grain boundary.

Despite of the different widths, all the systems show similar behavior. In close similitude to the related Haeckelites systems, all the 2D systems show states at the Fermi level (E_F) [19]. The density of states (DOS) of these systems is shown in figure 6.7a. LSDA calculations revealed a zero magnetic moment. It is important to note that some of the states around the E_F could be induced by symmetry loss due to lattice distortion.

In order to further investigate the properties of the states lying close to the Fermi energy, we represent iso-surface contour plots of three wavefunctions with energies around the Fermi level (see figure 6.7b). The states close to the E_F are localized at the interface between the nanoribbon-regions and the 5-7 chain. The first wavefunction plotted (left plot in figure 6.7b), exhibits states at the zigzag-region edges hybridized with states at the pentagons of the 5-7 chain. In addition, some states in the middle of the armchair-region are present. The second wavefunction (center plot figure 6.7b) shows the typical zigzag edge states found in zigzag nanoribbons. States along the armchair-region similar to those found in armchair nanoribbons are also observed. Finally, the third wavefunction (figure 6.7b
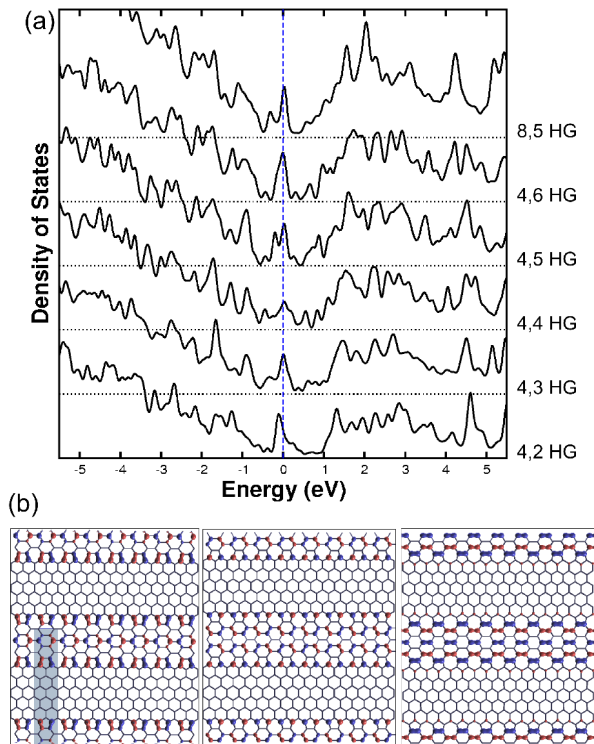
Figure 6.7: (a)Electronic density of states for hybrid-graphene layers with different armchair widths. Note that all the systems exhibit a large density of states around the Fermi level (E_F is set to zero). When the number of armchair dimers N_A is a multiple of 3 there is an increment on the states at the Fermi level. (b) Wavefunctions with energies (E) around the Fermi level plotted at Gamma point: (left) E= -1.2eV (center) E=-0.2eV, (right) E=0.12eV The shaded region in (left) represents the unit cell of the (3,4) hybrid graphene layer.

right) shows states at the armchair-region closely related to the conduction bands of armchair nanoribbons. It can be concluded from the observations above that the general effect of the grain boundary is to shift down the Fermi level of the armchair nanoribbons in order to achieve band alignment.

Our calculations show that HNRs could exhibit unusual electronic and magnetic properties. It can be observed that HNRs are degenerate in most of the energy spectrum, with the exception of the region close to the Fermi level. The spin resolved DOS for a (4,4) HNR shown in figure 6.8 exhibit states at the Fermi level, and a magnetic moment $\mu = 0.35$ μ_B. Figure 6.8a-c shows the total DOS compared to the local DOS projected on the armchair, zigzag, and 5-7 chain regions, respectively. This detailed analysis indicates that the three regions of the HNR contribute to the states at the Fermi level. However, only the zigzag region contributes to the magnetic moment, which is consistent with previous nanoribbon calculations using only zigzag architectures.

The spin-resolved band structure for a (4,4) HNR is shown in figure 6.9 left. It can be noted that there is a small indirect energy gap of ca. 0.2 eV in the minority spin states, which was not observed in the DOS, due to the Gaussian broadening. Table 6.1 shows that for ribbons with an even width, there is a gap in the spin down states, i.e. the systems exhibit half metallicity (spin polarized conduction). We confirmed the presence of this energy gap obtained within the local spin density approximation by using the Perdew-Burke-Ernzerhof functional within the spin
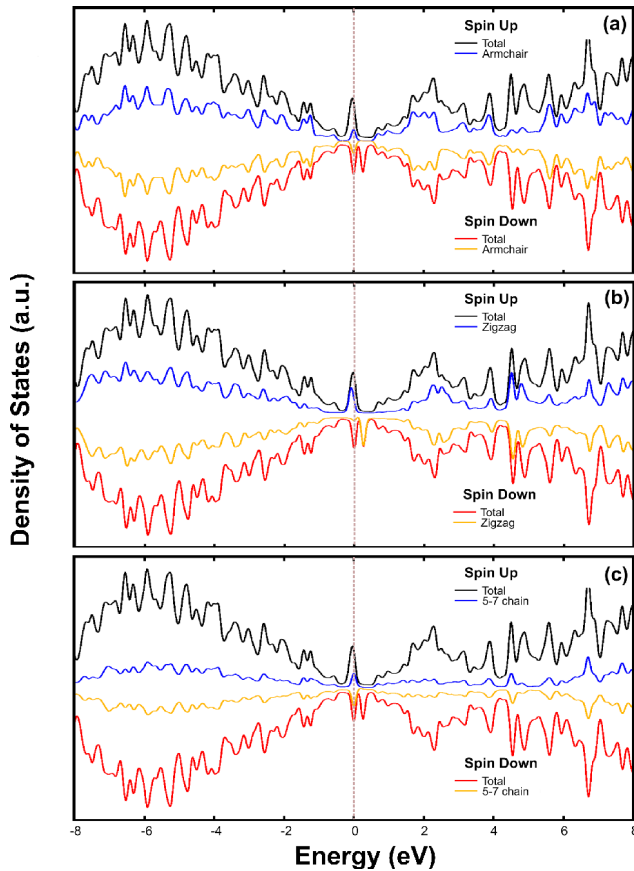
Figure 6.8: Spin resolved total DOS compared to the local DOS on the (a) armchair, (b) zigzag, and (c) 5-7 chain regions of a (4,4) hybrid nanoribbon. Note that all regions contribute to the states near the Fermi level (EF=0); however, only the zigzag region contributes to the magnetic moment.

polarized generalized gradient approximation (s-GGA) for the hybrid nanoribbons obtaining similar results, which are summarized in figure 6.10. In addition, the calculation of the (4,4) hybrid nanoribbon using the hybrid PBE0 functional for exact exchange shows an energy gap of the minority spin at the Γ point.

The isosurface plots of the wavefunctions close to the Fermi level are represented in right panels of figure 6.9. It can be noted that some of these bands (top) are closely related to the zigzag nanoribbon edge states. However, it is important to note that, opposite to a zigzag nanoribbon, there is only one edge state. It has been previously found that for zigzag nanoribbons, an antiferromagnetic configuration between ferromagnetically ordered edge states at each edge is energetically favored over the configuration with same spin orientation between the two edges [22], thus resulting in a null total magnetic moment. However, in this case, since there is only one ferromagnetically ordered edge state, there is always a net magnetic moment.
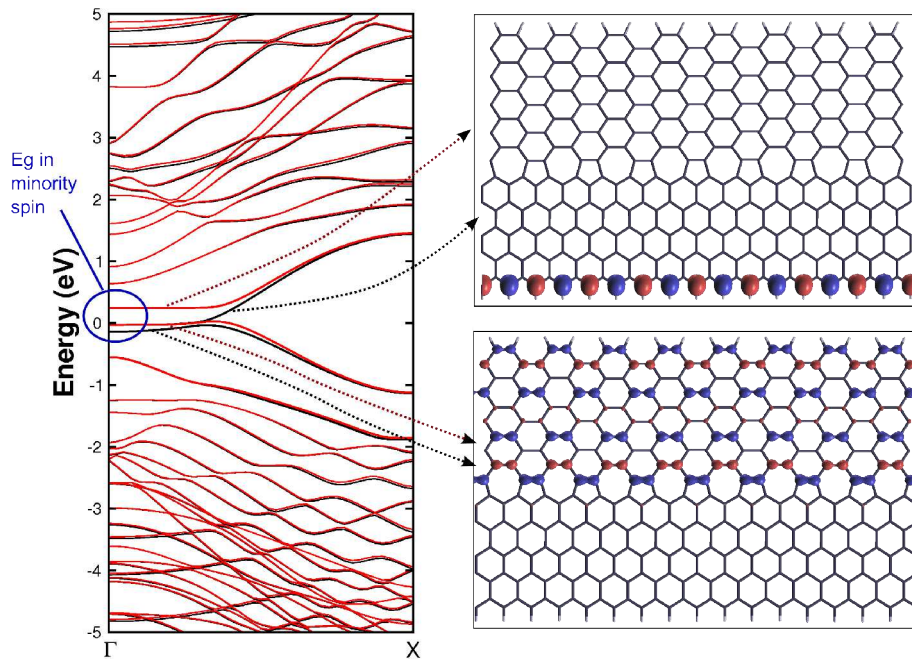
Figure 6.9: (left) Computed spin-polarized band structure for a (4,4) hybrid nanoribbon. Note the energy gap (Eg=0.27 eV) on the minority spin (red). The arrows illustrate the region of the HNR that contributes to the bands marked. Right panels show the wavefunctions of the bands close to the Fermi level plotted at the gamma point.
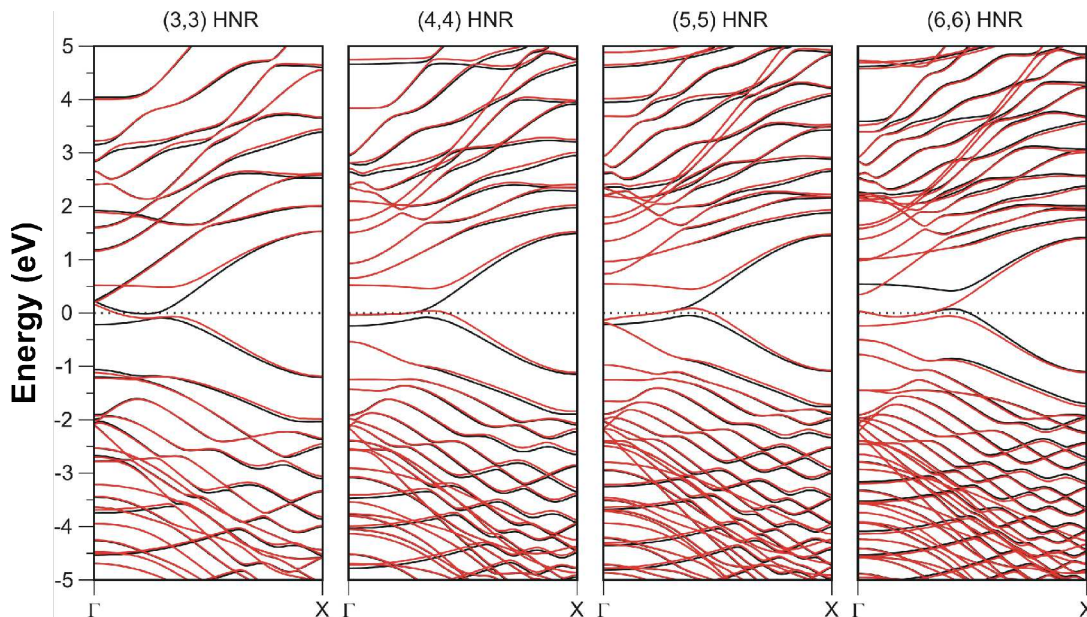
Figure 6.10: Band structure for (3,3), (4,4), (5,5) and (6,6) hybrid nanoribbons obtained using the PBE functional with the s-GGA approximation. It can be observed that in this case, the (5,5) nanoribbon also exhibits an energy gap for the minority carriers. Also, note that for the (6,6) the gap is present in the majority carriers.

| System	Magnetic moment (μ$_B$) LSDA	Spin down E$_g$ (eV) LSDA	Magnetic moment (μB) s-GGA	Spin down E$_g$ (eV) s-GGA
(3,3) HNR	0.27	0.00	0.20	0.04
(4,4) HNR	0.35	0.27	-0.42	0.42
(5,5) HNR	0.02	0.00	-0.43	0.36
(6,6) HNR	0.43	0.22	-0.45	0.34*
N$_Z$=8, N$_A$=5, N$_Z$= 8	0.90	0.00	------	------
N$_Z$=3, N$_A$=8, N$_Z$= 3	0.00	0.00	------	------

Table 6.1: Dependence of the electronic and magnetic properties on the width of the armchair and zigzag regions in HNRs. * Energy gap present in majority carriers.

We have constructed more complicated zigzag-armchair-zigzag HNRs. In this case, there are two zigzag edge states, but they are separated by an armchair segment, and two 5-7 chains. When the armchair segment width is small, there is interaction between the ferromagnetically ordered edges (*e.g.* in the (N$_Z$=8,N$_A$=5,N$_Z$=8) HNR case). However, as the width of the armchair segment is increased, the coupling disappears, and a magnetic moment is again observed (e.g. in the case of (N$_Z$=3,N$_A$=8,N$_Z$=3) HNR). The magnetic moments for the different HNRs calculated are listed in table 6.1.

Quantum conductance calculations were carried out in two different ways. First, a set of (N$_A$,N$_Z$) HNRs were considered as both leads and channels. It can be confirmed that the conductance of these HNRs is obtained straightforwardly from their density of states. The half metallicity of the (4,4) HNR is reflected in the conductance (see figure 6.11), and as expected, in a small region of the energy spectrum, HNRs behave as a spin-polarized conductor.

Another interesting case arises when an armchair segment is placed between two conducting zigzag nanoribbons which are used as leads (see figure 6.12a). In this case, the 5-7 defects are used to join zigzag nanoribbons leads (labeled as Z) to an armchair (N$_A$ = 1 to 5) segment. The results presented in figure 6.12b demonstrate that the conductance near the Fermi level is reduced as the armchair section is increased, denoting a tunneling driven transport across the junction.

Electronic and magnetic properties of hybrid graphene systems consisting of armchair-like and zigzag-like segments joined by a grain boundary formed by a linear array of 5-7-rings were fully examined using DFT calculations. The results showed that these systems exhibit electronic and magnetic properties not observed in graphene. Two dimensional hybrid systems exhibit electronic states at the Fermi
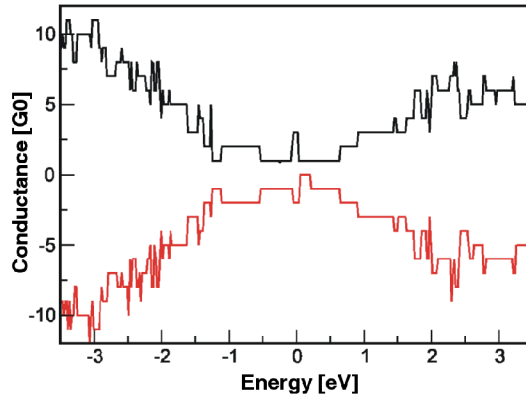
Figure 6.11: Quantum conductance for a typical (4,4) hybrid graphene nanoribbon. The Energy gap in the minority spin for (4,4) observed in the conductance is in accordance to the band structure and the density of states (see figures 6.9 and 6.10). The nanoribbon is spin degenerate in most of the energy spectrum, except for the region close to the Fermi level.
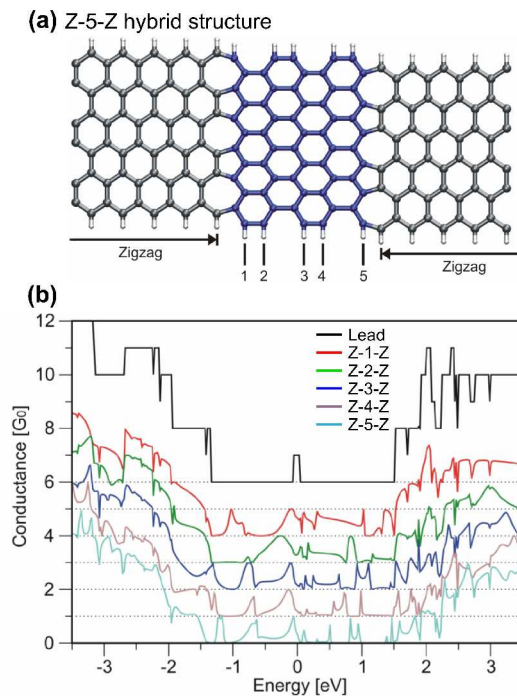
Figure 6.12: (a) Molecular model of a hybrid structure with zigzag leads (Z) connected by 5-7 chains to an armchair segment with N_A=5 (Z-5-Z hybrid structure). (b) Quantum conductance for zigzag – armchair – zigzag devices joined by 5-7 defects. It is observed that the conductance is reduced as the armchair section is increased, revealing a tunneling-driven transport.

level, while one dimensional hybrid nanoribbons (for even widths) can exhibit half metallicity without the use of an external field. Transport calculations reveal that these systems could behave as spin polarized conductors when current is applied along the HNR axis, or could exhibit tunneling driven conduction if current is applied perpendicular to the HNR axis. The grain boundaries of these systems have been found experimentally and a study of their properties is therefore important. In summary, an array of structural defects could be used in favor, and the properties of such systems could find use in electronic devices.

6.3. GRAPHENE NETWORKS

As stated before, numerous theoretical studies have focused on tailoring the electronic properties of graphene and graphene nanoribbons for nanoelectronics applications. Some researchers have adopted an approach similar to that of conventional semiconductor industry, and focused on ion impurities and vacancies (doping) [23,24]. Others have incorporated adsorbed molecules or ions at the edges, or studied the effect of different substrates. Another

159
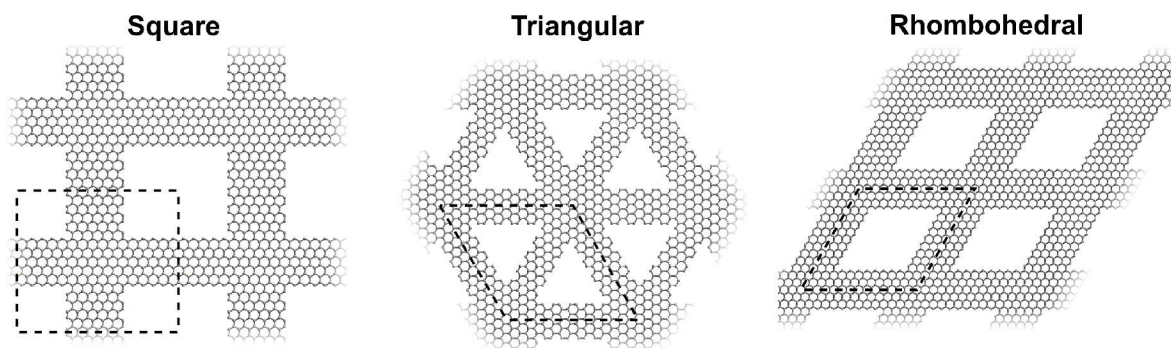
Figure 6.13: Molecular models of simple graphene nanoribbons networks forming square, triangular and rhombohedral lattices. The dashed lines enclose a unit cell of such systems.

promising approach consists of joining an armchair and a zigzag nanoribbon, but instead of using an array of 5-7 defects as in the previous section, by rotating the cutting direction, resulting in Z-shaped [25-28], T-shaped [29,30], L-shaped [31,32], cross shaped [33-35], and arrow-shaped [36-38] graphene nanoribbon intramolecular junctions. This could be done through lithographic techniques as has been proved experimentally. Moreover, one could think of forming complex periodic network structures with segments of armchair and zigzag nanoribbons (see figure 6.13). Similar kinds of networks have already been proposed for carbon nanotubes, and are found to exhibit interesting electronic and mechanical properties which depend on the way the carbon nanotubes are connected to each other [39]. It is important to mention that such structures could be realized through the synthesis of branched carbon nanotubes as building blocks [39]. Graphene based networks, on the other hand, could be achieved with more simple lithographic techniques.

Figure 6.13 shows three different graphene nanoribbon networks, which could also be thought of punched graphene or holey graphene with different symmetries. According to the first viewpoint, a simple square or rectangular network would be defined by four numbers: the width of the armchair and zigzag connecting nanoribbons ($^W N_A$, $^W N_Z$), and their corresponding length ($^L N_Z$, $^L N_A$). Here, we have used the notation depicted in figure 4.3. Note that the width of the armchair segment is measured in terms of dimers along the width ($^W N_A$) and its length is measured in terms of zigzag chains ($^L N_Z$). For example, the square network in figure 6.13 would be denoted as a (12,6)(10,20)-SqGN. Similarly, although the triangular and rhombohedral networks contain nanoribbons of only one type of edge, the connecting segments could have different widths or lengths, therefore
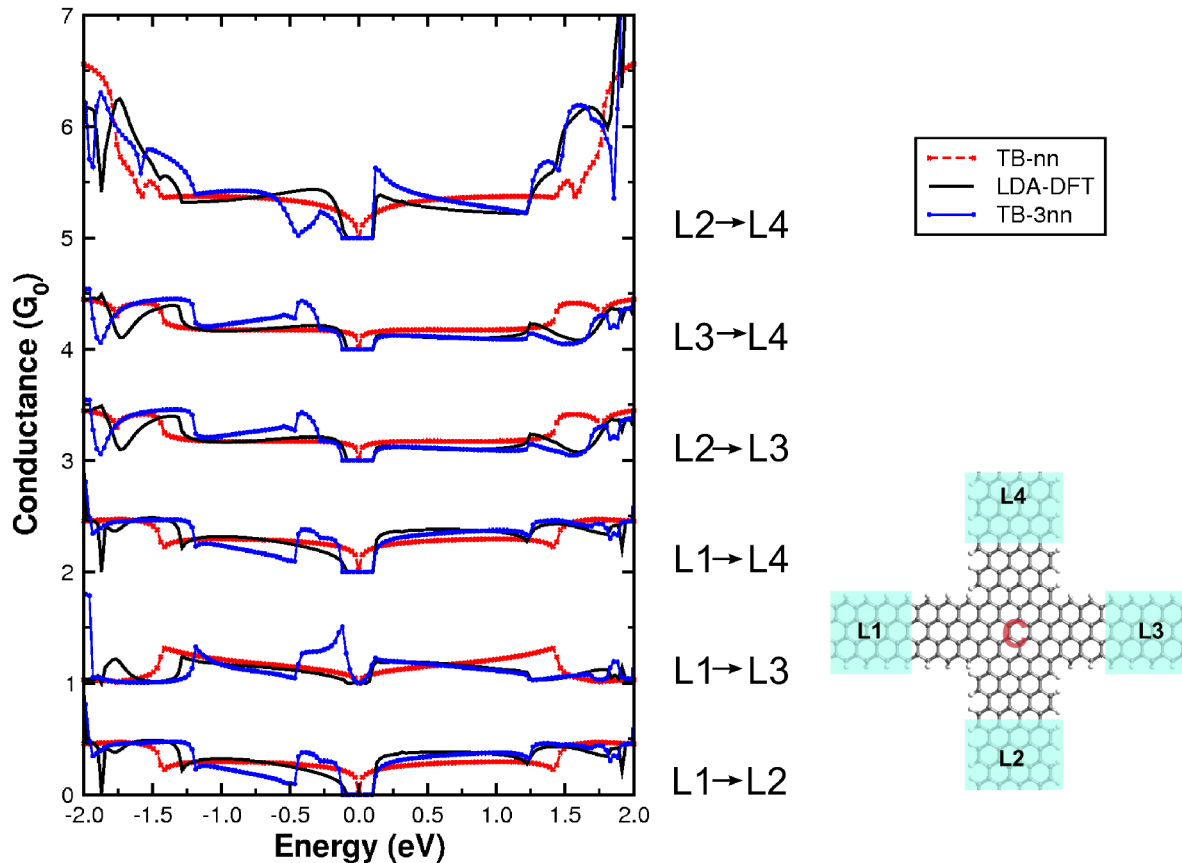
Figure 6.14: Quantum conductance for a multiterminal graphene network (lower right corner) calculated with different approaches. It can be seen that the third nearest neighbor approach has much better agreement with DFT than the nearest neighbor approximation.

the four number notation still applies.

Transport in square networks have already been studied within a first nearest neighbors tight binding approach by Mintmire and Jayasekera [34]. These authors find that the transmission properties of a multiterminal device based on these networks are highly sensitive to the junction region. Here, we investigate the properties of multiterminal and graphene network devices with a combined first-principles and third nearest neighbors tight binding approach.

We calculated the quantum conductance through the node of a (4,4)(12,12)SqGN as depicted in the lower right corner of figure 6.14. Opposite to what was found before [34], the transport through the different leads often show a dip in conductance. This can be due to the band gap opening of narrow nanoribbons, and the fact that there is no continuous zigzag edge across any two leads. On the other hand, the calculated quantum conductance using a third nearest neighbors tight binding (3NNTB) approximation leads very good agreement with the DFT LDA
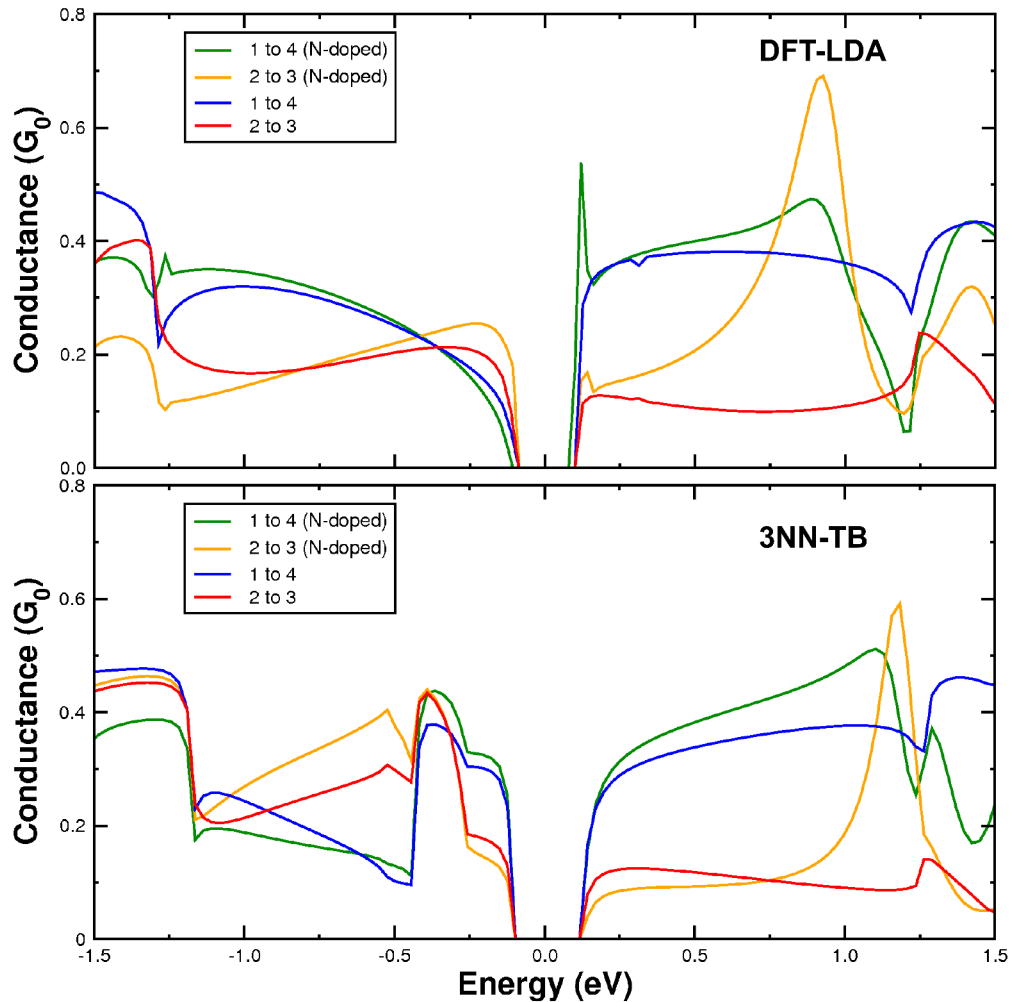
Figure 6.15: Quantum Conductance between leads with different edge shapes of a square graphene network with an impurity. Both the DFT and the third nearest neighbor approaches show a peak in conductance not seen in the pristine case at around 1eV.

approach.

Although it is clear that these graphene networks are very sensitive to the shape of the junction, this could not easily lead to any obvious application. Instead, we analyzed the possibility of changing the transport properties of the nodes by locally modifying the network. We have introduced a nitrogen impurity on the center of the node. Figure 6.15 shows that the quantum conductance across two contiguous leads, which interestingly have different edge shape, change considerably upon nitrogen doping at *c.a.* 0.8eV. The conductance between other combination of leads does not change significantly. We have simulated the doping effect under the 3NNTB scheme by changing the on-site energy at one of the atoms in the node. It can be seen in the bottom panel of figure 6.15 that the effect is very similar to that

found by first principles.

In principle, the effect of local chemical modification of a node should be spotted across a bigger network, and studies of such systems are on their way. These findings suggest that graphene networks could be used as sensors or storage devices, since the position of a given chemical specie could be determined by probing the conductance across different leads in a large square network.

The square network is characterized by exhibiting a combination of zigzag and armchair inner edges. However, the triangular and rhombohedral networks exhibit only one type of inner edge (see figure 6.13). It is particularly interesting to study the effect of this type of ordering on the magnetic properties of the zigzag inner edges. As has been stated before, the atoms at zigzag edges can exhibit a magnetic moment that is aligned in parallel along the edge. Therefore, closed inner edges could exhibit interesting magnetic behavior. Investigations on this direction are currently on their way.

6.4. BORON NITRIDE

Boron nitride (BN) is an insulator (Eg *c.a.* 5.8eV) with many similarities to carbon. It has a polymorph analogous to graphite (hexagonal-BN or h-BN) and a polymorph analogous to diamond (zinc blende BN or z-BN). Other phases like Wurtzite BN and rhombohedral BN can be found. A single sheet of h-BN can be thought of as two hexagonal sub-lattices composed of a boron and a nitrogen atom, respectively. As opposed to graphite, the hexagonal layers eclipse one another forming an aA stacking, where each nitrogen atom lies on top of a boron atom and vice versa. According to calculations, a single sheet of h-BN exhibits a direct band gap of *c.a.* 4.5eV [40]. BN nanotubes, and BN-carbon hybrid nanotubes have been studied. BN nanotubes are always insulating. Only very narrow BN nanotubes are expected to have Eg of around 1.0 eV, but these narrow BN nanotubes are not likely to be stable [40].

Okada and coworkers first studied the edge states of BN nanoribbons using first principles calculations under the LDA [41]. They found that, when terminated with hydrogen atoms, zigzag and armchair nanoribbons were both insulating, with Eg larger than the monolayer for narrow nanoribbons, and converging to the monolayer Eg as the width increases. However, in the zigzag case, the valence and

conduction edge bands show flat dispersion, and are thus found to be edge states. Due to the chemical difference of B and N atoms, the edge state of the conduction band corresponds to the B atom, whereas the edge state of the valence band corresponds to the N atom. Opposite to the zigzag case, the armchair case does not show flat bands [42].

Park and Louie have found that the energy gaps of armchair BNNRs exhibit family dependent oscillations as the width increases, and for ribbons wider than 3nm, converge to a constant value of 0.02eV below the Eg of the monolayer. The band gap of zigzag BNNRs monotonically decreases and converges to a gap 0.7eV smaller than the bulk case [43].

Zigzag edge states on BN nanoribbons exhibit spin-polarized states well localized at and extended along the edges of bare (non saturated) zigzag boron nitride nanoribbons with a magnetic moment of $1\mu_B$ per edge atom. These configurations are accessible at room temperature [44-47].

Half metallicity has also been found for BN nanoribbons. Zheng *et al.,* report first principles calculations within the LSDA showing that BN nanoribbons can turn half metallic when the B edge, but not the N edge of the zigzag BN nanoribbon is saturated with hydrogen. The electrons at the Fermi level are spin-polarized with a half-metal gap of 0.38eV [46].

The electronic structure of BN nanoribbons is strongly modified by transverse electric fields. Due to the asymmetry of the structure, the energy gap of BN nanoribbons can be heavily modulated. Depending on the sign of the field, the Eg is reduced or increased for zigzag nanoribbons, while for the armchair case, it always reduces [43,44,46]. The range of modulation for Eg is from *c.a.* 4eV to less than 1eV for a 46-Z-BNNR, which makes BNNRs excellent candidates for channels in transistors. Furthermore, bare zigzag nanoribbons can exhibit interesting metallic-semiconducting-half-metallic transitions under the influence of an external electric field [44].
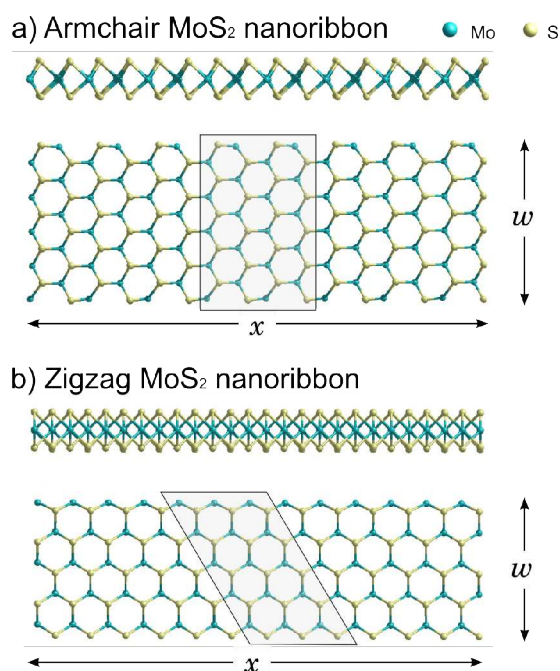
6.5. MOLYBDENUM DISULFIDE

Molybdenum disulfide (MoS_2) is an inorganic layered material with important potential applications as lubricants and catalysts. It belongs to the group of layered chalcogenides. Other compounds belonging to this group are WS_2 NbS_2 $NbSe_2$. In

this material, Mo atoms have a six-fold coordination environment and are hexagonally packed between two trigonal atomic layers of S atoms (see figure 6.16). Similarly to graphite, the S-Mo-S triple layers interact by weak van der-Waals interactions. Bulk MoS_2 is a semiconductor with an indirect band gap of *c.a.* 1eV [48].

Recently, Bollinger *et al.,* observed, using scanning tunneling microscopy, that single-layer MoS_2 nanoparticles exhibit localized states at the borders [49]. They also confirmed these results using density functional calculations and they determined that single-layer MoS_2 stripes are metallic. More recently, Zhang *et al.,* synthesized MoS_2 nanosheets with triangular morphologies that exhibited a ferromagnetic response at room temperature [50]. Tubular structures made of MoS_2 have been already synthesized and have been studied from a theoretical standpoint (see [48]).

Here, we report results on the calculation of the magnetic and electronic properties of 1D MoS_2 nanoribbons with zigzag and armchair edges, emphasizing the effects of the edge passivation. On this respect, a recent report by Chen, et al. presents an Augmented Plane Wave Density Functional study using on the properties of MoS_2 zigzag and armchair nanoribbons [51]; however, the effect of saturation of the edges with hydrogen is not clear, and the magnetic state of the ground state is not investigated. Contrary to the bulk properties of layered MoS_2 and single-layered MoS_2 nanotubes, we found that all zigzag nanoribbons are metallic and exhibit unusual magnetic properties. We observed that this behavior remains even if the ribbons are passivated with H atoms. We should also stress that to the best of our knowledge there is still no direct

a) Armchair MoS_2 nanoribbon   ● Mo   ● S

b) Zigzag MoS_2 nanoribbon

Figure 6.16: Molecular models of the optimized geometries of molybdenum disulfide (MoS_2) nanoribbons (side and top views). The ribbons are periodic in the x direction, and the width is defined as w. The shaded area corresponds to the supercell used in the calculations. (a) armchair and (b) zigzag nanoribbons. In (a) both atoms (Mo and S) share the edges in an alternated way whereas that in (b) one side of the ribbon is dominated by S whereas the Mo dominates the opposite side.

165

experimental evidence of the existence of the nanoribbons discussed in this chapter. However, we believe that these systems could be synthesized by top-down approaches, such as focused ion beam irradiation from the already synthesized triangular islands. For a bottom down-perspective, a passivating agent that could enhance the preferential direction, say zigzag over armchair, would help to generate these systems. In addition, a search for a catalyst that under some conditions could cut MoS_2 layers along specific directions (*e.g.* nano-scissors for graphite [52]), could result in these nanostructures.

In figure 6.16a and b, we show the optimized geometry of the armchair and zigzag nanoribbons respectively. In our calculations, the ribbons are periodic in the x-direction. From the side view, we can observe that the ribbons contain three planes where the Mo atoms are always in the center of the layered system. From the top view, almost perfect hexagonal symmetry can be seen. For the zigzag ribbon, the S dominates one edge whereas the opposite edge is dominated by Mo atoms. For armchair ribbons, both types of atoms (S and Mo) involved in the layered material share the edges. We found that after the structure relaxation, the geometry keeps almost unchanged with a slight reduction of the distance d_{Mo-S} on the borders (3.53% with respect to the bulk Mo-S distance). In table 6.2 a summary of the interatomic distances compared to the bulk case is presented.

	Bulk (experiment)[35]	Zigzag (in)	Zigzag (edge)	Armchair (in)	Armchair (edge)
d_{Mo-S}	2.402 (2.413)	2.400	2.470	2.396	2.43
d_{S-S}	3.137 (3.157)	3.136	3.229	3.136	3.25
d_{Mo-Mo}	3.151 (3.160)	3.148	3.155	3.143	3.158

Table 6.2: Interatomic distances after structure relaxation (Å) for armchair and zigzag nanoribbons both at the middle of the nanoribbon (in) and at the edge (edge) as compared to the bulk distances.

The synthesis of bulk MoS_2 and nanotubes is usually carried out by sulfurizing MoO under an atmosphere of HS_2. Therefore, it is quite probable that the reactive edges get passivated with H atoms. However, hydrogen passivation is not necessarily always the case, since the edges could remain unpassivated by heating treatments [53]. Nevertheless, we studied both the hydrogen passivated case and the non-passivated scenario. The passivation was carried out by attaching hydrogen atoms to the edge atoms so that the coordination number of each atom is kept as in the bulk case (Mo atoms passivated with two H atoms whereas S atoms passivated with one H atom).

Figure 6.17a (top) depicts the spin-resolved density of states (DOS) and the band structure for non-passivated MoS_2 armchair nanoribbons. The DOS reveals a shift between the states with up and down spin that result in a magnetic moment, which is associated to Mo atoms located on the edges (2.2μ_B per Mo atom). The LDA and LSDA calculations show a difference of $\Delta E = E_{LSDA} - E_{LDA} = 0.014eV$. When the armchair ribbon edges are saturated with hydrogen atoms, all the states crossing the Fermi level vanish (presumably, dangling bond states), and the same ribbon exhibits an electronic band gap of 0.67 eV (see figure 6.17 a bottom). The ground state for the hydrogen saturated armchair nanoribbon is a non-magnetic sate, regardless of the calculation (LDA or LSDA).

Figure 6.17 b (top) shows results for the non-passivated MoS_2 zigzag nanoribbon on the polarized electronic DOS and band structure. Here, a shift between the DOS of spin up and down can be clearly noticed. In this case, the LDA and LSDA calculations show a difference of $\Delta E = E_{LSDA} - E_{LDA} = -0.20eV$. When saturating the zigzag nanoribbon edges with hydrogen atoms, the dangling bonds get saturated and the DOS close to the Fermi level decrease. However, there are still bands crossing the Fermi level, and the system exhibits a magnetic moment (see figure 6.17b bottom).

In order to investigate the magnetic couplings between the magnetic moments localized at the edges, we examine two different spin configurations for the hydrogen passivated MoS_2 zigzag nanoribbon: (a) ferromagnetically ordered spins at both edges (FM), and ferromagnetically ordered spins at each edge, but with the opposite spin directions between the edges (AFM). In order to investigate the magnetic state of the ground state, an LSDA calculation starting from an antiferromagntetic configuration was carried out. This calculation leads, after total energy convergence, to a ferromagnetic state with a total magnetic moment $\mu = 0.4\mu_B$ per atom at the edge. An energy difference between these two magnetic states corresponded to $E_{FM} - E_{AFM} = 15meV$. This implies that both configurations could be present at room temperature. Similar magnetic coupling between edges have been observed in the case of zigzag carbon nanoribbons [22]. The band structure of the AFM starting configuration system is very similar to that of the ferromagnetic case (see figure 6.18). However, it can be noted that the bands responsible for the magnetic moment are those located at the Mo dominated edge (see figure 6.18).

167
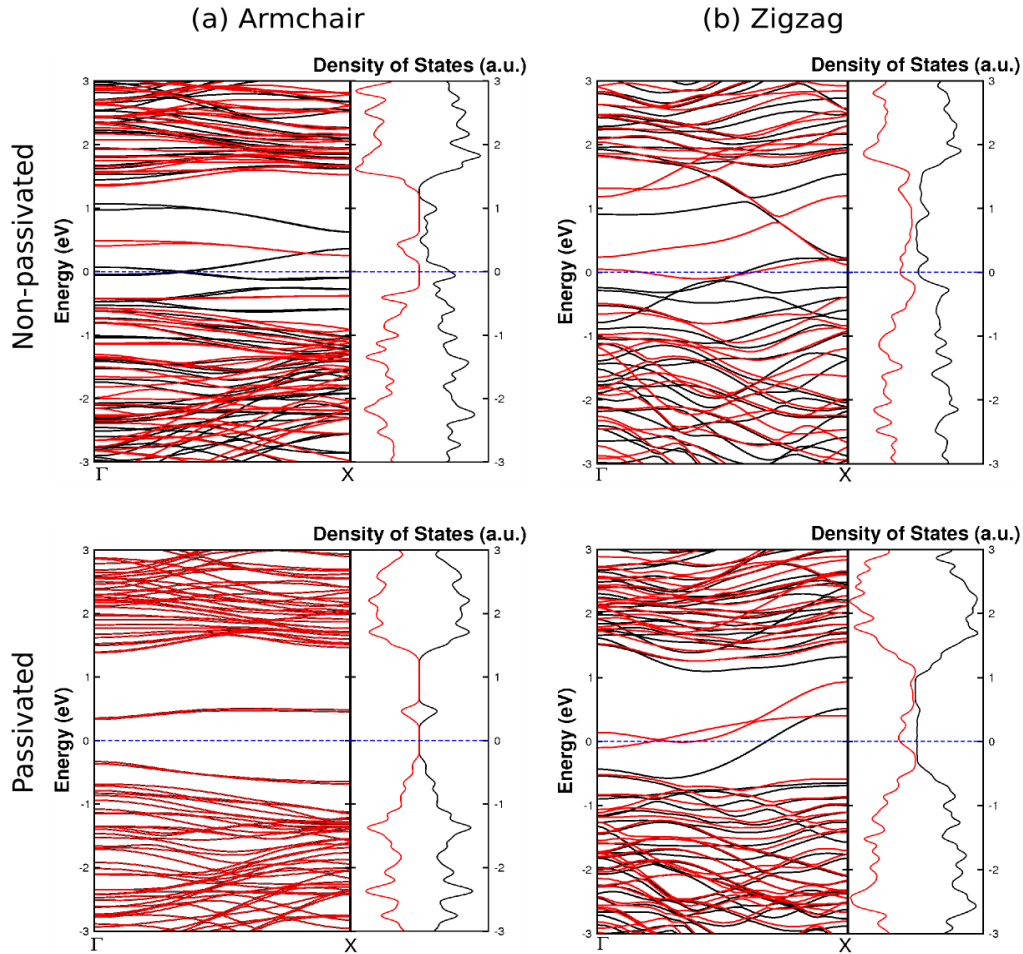
Figure 6.17: Spin-resolved density of states (up:black; down:red) and band-structure calculations for passivated and non-passivated MoS$_2$ nanoribbons with armchair and zigzag edges in (a) and (b) respectively. In all cases, the Fermi level is set at zero (dashed line). Red lines correspond to spin down states whereas the black lines depict spin up states. Note that both non passivated systems exhibit states at the Fermi level. However, as the edges are passivated with hydrogen atoms, the armchair ribbons become semiconducting

The binding energies (E$_b$) were computed as E$_b$ = ET$_{(NR)}$ − ET$_{(A)}$, where ET$_{(NR)}$ is the calculated total energy of the nanoribbon system, and ET$_{(A)}$ is the sum of the free atom energies for all the atoms in the unit cell. As expected, the binding energy of the nanoribbons (both zigzag and armchair) approaches the binding energy of the single 2D MoS$_2$ layer, being the armchair slightly more stable. The energy gap of the passivated armchair nanoribbons is not expected to change significantly, since the edge states will be present as long as the edges are present, and will only disappear in the infinite width case (*i.e.,* the 2D case). increases as the width increases, and it is expected to approach the value of the
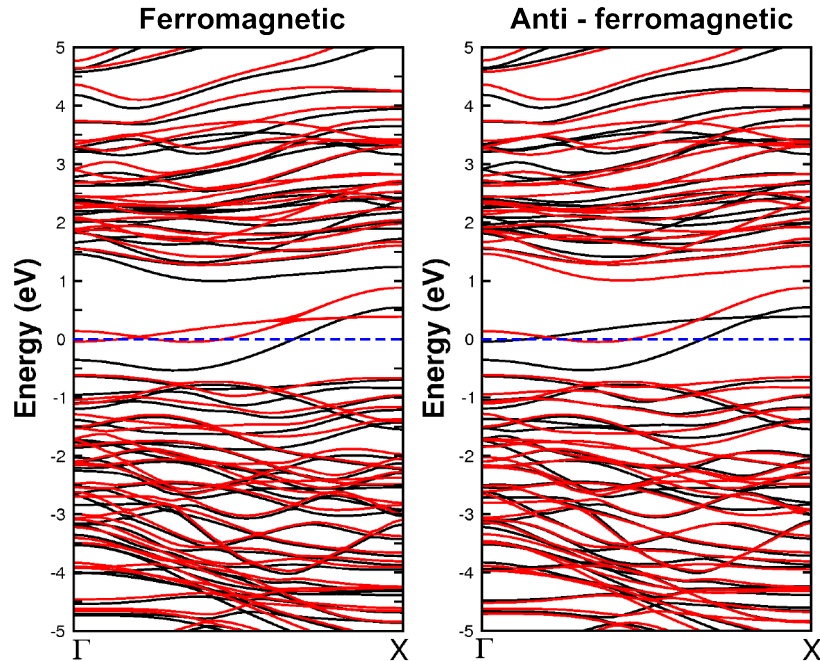
Figure 6.18: Spin polarized band structure (up:black; down:red) calculations of a hydrogen-passivated zigzag MoS2 when the starting spin configuration was taken as ferromagnetic or antiferromagnetic. In both cases, the converged ground-state wave function exhibits a polarized state with a ferromagnetic spin configuration along one of the edges. The Fermi level is set at zero (horizontal dashed line).

2D monolayer (1.8 eV), although very slowly, since for the case of a 3.2nm the value is still far: ca. 0.68eV. The magnetic moment of the passivated zigzag nanoribbons slightly decreases as the ribbon width is increased, although it seems to be stabilized, and remains almost constant at 1.34μ_B (for widths between 20 and 35Å). The number of states close to the Fermi level (*i.e.,* edge states) remains constant as the ribbon width increases, and can be neglected as the width approaches infinitum.

The bands crossing the Fermi level for the passivated zigzag MoS$_2$ nanoribbons were also investigated (see figure 6.19). There are three wave functions crossing the Fermi level. Two of them account for edge states located at the Mo-dominated edge. These wavefunctions overlap with the region where the bonding of the Mo and S atoms is expected to be, so we have identified them as bonding states and are delocalized over the edge and could be a channel for the conduction of electrons. The other wave function is an antibonding state on the S dominated edge since it is clearly located outside the region of interaction between the Mo and
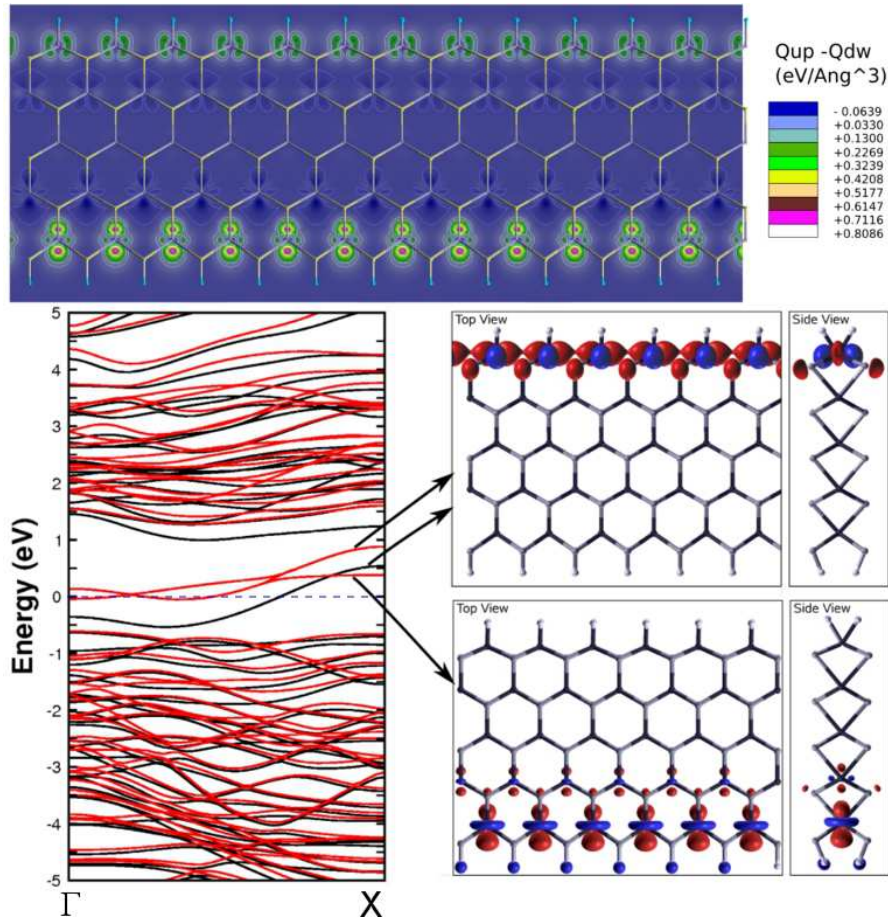
Figure 6.19: (Top) Difference in electronic charge density up and down for the passivated zigzag nanoribbon. Note that the magnetic moment is localized around the Mo atoms close to the edges. (Bottom) The wave functions plotted at the Γ-point close to the Fermi level (set at zero) show that these bands are edge states. Note that two of the bands at the edges are bonding states and one is an antibonding state localized at the opposite edge.

S atoms, and therefore which does not account for any conduction. The difference in charge density with spin up and down is plotted in the top panel of figure 6.19. It is clear that the magnetic moment is due to the Mo atoms located close to both edges. In the ferrimagnetic case, the magnetic moment is only due to the Mo atoms located at the Mo-dominated edge. The properties of the edge states of the passivated armchair MoS_2 nanoribbons are also interesting. The two wavefunctions close to the Fermi level are also edge states (see figure 6.20), and can be thought of as both donor and acceptor states localized at the borders. These edge states could be important for catalysis, and could be photoactivated.

The properties of MoS_2 nanoribbons reveal several advantages over graphene
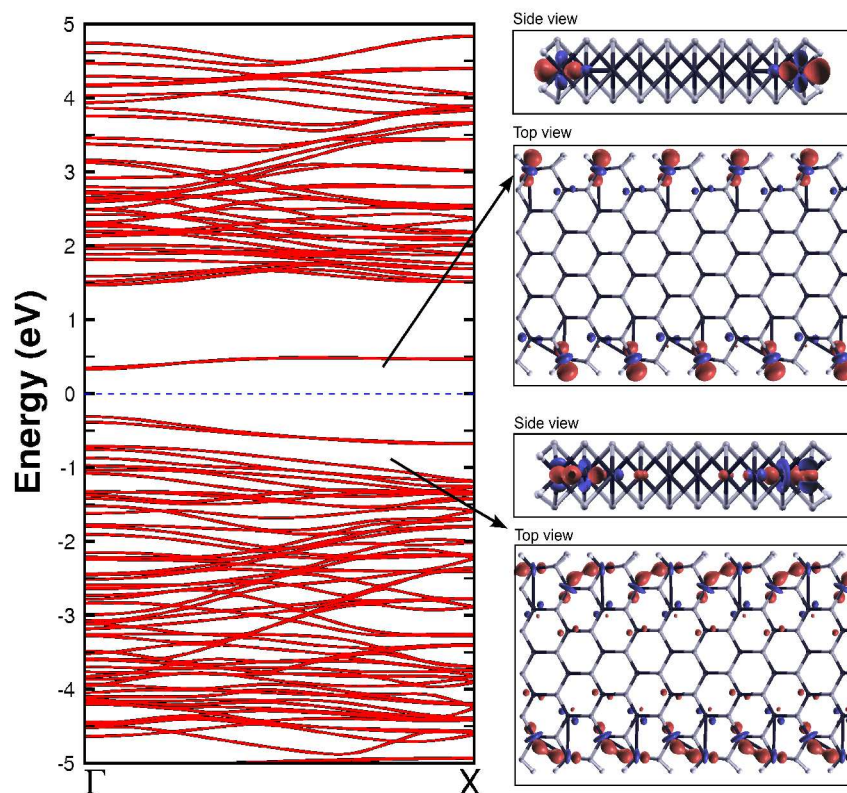
Figure 6.20: Wave functions plotted at the Γ-point of the edge states found on the armchair MoS$_2$ nanoribbons passivated with hydrogen. Note that the Fermi level has been set at zero. These states can be thought of as donor and acceptor states localized at the edges. These states could be interesting for catalysis applications.

nanoribbons. The spin responsible for the magnetic moment of the zigzag graphene nanoribbons is oriented in opposite directions, leading to an antiferromagnetic state. However, for MoS$_2$ systems, the zigzag nanoribbons (passivated and non-passivated) exhibit a magnetic moment only along one edge and are either ferromagnetic or ferrimagnetic. In the case of the armchair nanoribbons, a magnetic moment could be observed if the nanoribbons were not passivated with H atoms. One way to achieve this could be by heating the samples so that the H atoms are removed from the edges.

We have proposed a novel form of 1D MoS$_2$ (nanoribbons) with zigzag and armchair edges, which reveal different electronic and magnetic properties when compared to bulk MoS$_2$. Although MoS$_2$ exhibits a semiconducting behavior in the bulk phase, we found that MoS$_2$ nanoribbons could be metallic and could exhibit a surprising ferromagnetic behavior that has been reported experimentally. Our

results open the possibility for new applications of 1D systems in electronics, because the properties of MoS_2 nanoribbons are significantly different to those found in other 1D systems studied in the past, such as graphene nanoribbons, boron nitride nanoribbons or ZnO nanoribbons.

6.6. ZINC OXIDE

Zinc oxide (ZnO) is a wide band gap semiconductor with a Wurtzite structure which has been investigated as an electronic material for many decades. Recently, basic and applied research on ZnO experienced a renaissance due to the prospective use of ZnO as an optoelectronic material for blue and UV lasers.

Recently, Tusche, Meyerheim, and Kirschner carried out an experimental study of
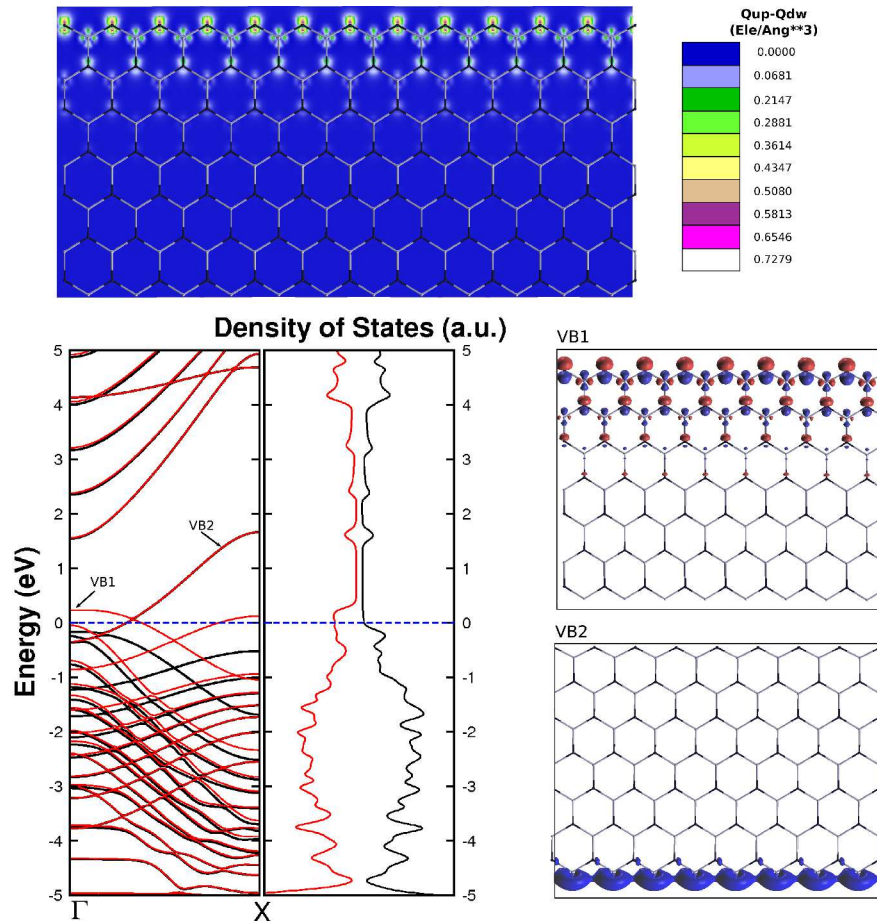
Figure 6.21: (Top): Difference in charge energy density (up-down) for a zinc oxide nanoribbon with zigzag edges, showing that the magnetic moment is due to the oxygen dominated edges. (bottom) Band structure, density of states, and wavefunctions of the top valence band.

172

2–5 monolayer-thick ZnO films deposited on Ag(111) by pulsed laser deposition [54]. While in the bulk Wurtzite structure, Zn and O atoms are arranged in layers separated by a vertical distance of 0.63Å, ultra-thin ZnO films show large inward relaxations of the Zn atoms into the plane of O atoms leading to an almost null polarization. They showed evidence based on scanning tunneling microscopy (STM) and surface X-ray diffraction (SXRD) that ZnO adopts a hexagonal boron-nitride (h-BN)-like structure in which Zn and O atoms are arranged in a trigonal-planar coordination instead of the bulk tetrahedral configuration. According to their study, the transition to the bulk-like Wurtzite structure is in between 3 and 4 monolayers.

The electronic properties of h-ZnO edges have been studied with DFT-LDA (see Chapter 2). The zigzag ZnO nanoribbons containing an odd number of layers were found always metallic (see figure 6.21); however when the thickness or number of layers is even, states close to the Fermi level vanish and the ribbons become semiconducting. All armchair ribbons exhibit a semiconductor behavior with Eg of ca. 2eV. LDA calculations show that the Eg of ZnO nanoribbons can be tuned depending on the width, thickness and edge termination. Also, single layered ZnO nanoribbons with zigzag edges exhibit unpaired spins at the edges dominated by oxygen atoms (see figure 6.21). The emerged magnetic moment increases with the width of the ribbons. For a deeper analysis on the properties of these systems, see Chapter 2.

6.7. CONCLUSIONS

It is clear from what was exposed above, that even though GNRs exhibit numerous interesting characteristics that could be used for next generation electronics, other systems have proved superior for certain specific applications. Table 6.3 summarizes the basic characteristics and phenomena that the different systems presented here exhibit. According to these characteristics, we present in the last column what we envision as the possible application that each of these materials should have for a next generation of electronics based on 2D layered systems. We believe that GNRs are good candidates for contacts because they exhibit good transport. Although it has been proved that GNRs as channels in transistors are achievable, it has also been observed that edge disorder and other scatterers affect considerably the performance. Also, the ON/OFF voltage ratio is
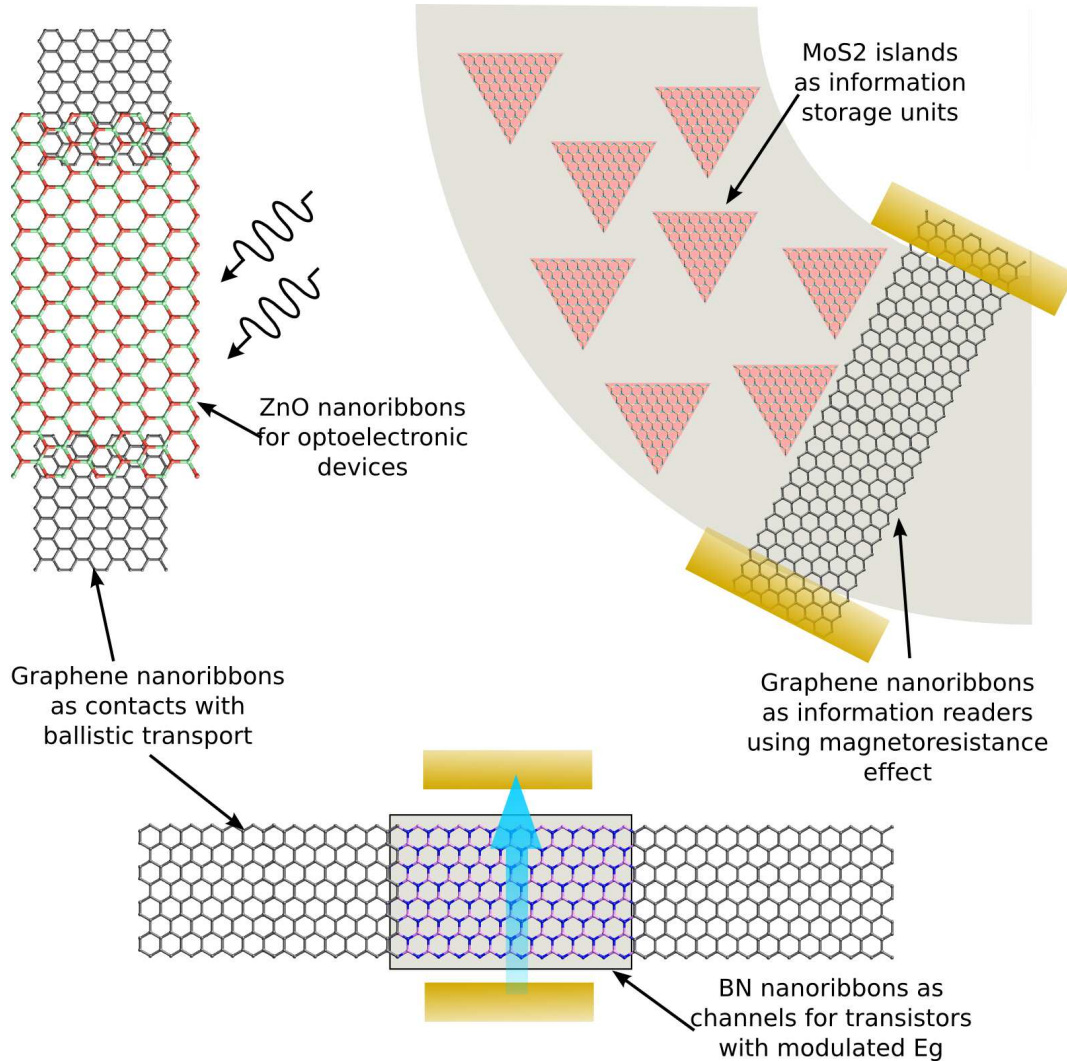
Figure 6.22: Schematic representations of several devices that could be achieved with layered finite materials exploiting the different electronic and magnetic properties of each material.

rather low, and it is difficult to avoid leak currents. In contrast, BN nanoribbons exhibit a large band gap, and the large Eg (from > 4eV to < 1eV with E = 0.1eV/A) modulation due to the Stark effect makes them ideal candidates for channel materials in transistor devices. The magnetoresistance of GNRs can be used for reading form magnetic grains that could be fabricated with MoS_2 nanoislands or nanoribbons. Also, the sensibility of GNRs to edge passivation could be exploited for sensors. Figure 6.22 shows a schematic device where several 2D layered finite materials could be employed, based on the data presented in table 6.3.

System	Eg		Passivation Effect	Electric Field Effect	Magnetic Field Effect	Possible Application
	Armchair	Zigzag				
C	Semi-conductor (3 families)	Semimetal (Eg < 1eV for width > 25nm)	p-, n- doping	Half-metallicity	Magnetore-sistnace	Contacts (ballistic transport) Gas sensors Readers (magnetoresistance)
BN	Insulator	Insulator	-	Stark Effect Large Eg modulation	-	Channel in transitors (processing)
MoS$_2$	Semi-conductor ~1 eV	Metal	-	-	Ferromag-netic	Storage devices, Spin carriers
ZnO	Semi-conductor ~2eV	Metal	Ferromagnetic / Half metallicity	Large Eg modulation	-	Spin carriers, optoelectronic devices

Table 6.3: Comparison of the basic characteristics of different 2D layered finite systems and their possible application on electronic devices.

Much research must be done in order to achieve what we have proposed above. In particular, we highlight the need for spreading the experimental and theoretical studies to other 2D layered systems. A general approach and architecture is desirable over a pure carbon based scenario, so that different materials are explored simultaneously. This would be opposite to the silicon-based electronic era, in which all research and funding was dedicated to Si-based devices and architecture, and now the semiconductor industry is facing the consequences of not having diversity and generalization of devices and architecture.

Much research is still needed in the synthesis of other 2D systems other than GNR. As we have already seen, some methods can be extrapolated, but others must be developed.

6.8. COMPUTATIONAL DETAILS

Electronic calculations were performed using Density Functional Theory within the Local Spin Density Approximation (DFT-LSDA) using the Ceperley-Alder [55] parametrization as implemented in the SIESTA code [56]. The wave functions for the valence electrons were represented by a linear combination of pseudo-atomic numerical orbitals using a double-ζ polarized basis (DZP), while core electrons

were represented by norm-conserving Troullier-Martins pseudopotentials [57]. The real-space grid used for charge and potential integration is equivalent to a planewave cut-off energy of 150 Ry. The pseudo-potentials (pp's) were constructed from 4 valence electrons for the C atoms, and 6 valence electrons for the Mo and S ions (Mo: $5s^14d^5$ and S: $3s^23p^4$). Periodic boundary conditions were used and the inter-ribbons distance was kept to a minimum of 10 Å to avoid lateral interactions. Sampling of the 1D and 2D Brillouin zones were carried out with 16x1x1 and 16x16x1 Monkhorst-Pack grids, respectively. All carbon nanoribbons were saturated with hydrogen atoms to eliminate dangling bonds and relaxed by conjugate gradient minimization until the maximum force was less than 0.04 eV/Å. For the case of Mo and S, the basis and the pp's and convergence on energy shift were tested on the bulk MoS_2 hexagonal structure (space group: Pmmc), and the MoS_2 single layer. Bulk calculations reveal that the binding energy is -16.478 eV/MoS_2, exhibiting an indirect band-gap from Γ to X of 0.88 eV. The single layer has a binding energy of -14.996eV/MoS_2 and a direct band gap of 1.8 eV

Calculations using the spin polarized general gradient approximation (s-GGA) with the Perdew-Burke-Ernzerhof (PBE) functional [58] were performed in the hybrid nanoribbons in order to verify the LSDA results. Exact exchange hybrid PBE0 functional calculations were carried out using the NWChem package [59].

Ab-initio quantum transport properties were calculated by extracting the Hamiltonian and Overlap matrices from SIESTA, and using the Landauer [60,61] formalism and the surface Green's function matching method [62,63].

6.9. RELATED PUBLISHED WORK

Botello-Méndez, Andrés R., Eduardo Cruz-Silva, Florentino López-Urías, Bobby G. Sumpter, Vincent Meunier, Mauricio Terrones, and Humberto Terrones. 2009 Spin Polarized Conductance in Hybrid Graphene Nanoribbons Using 5-7 Defects. ACS Nano. doi:10.1021/nn900614x.

Botello-Méndez, A. R., F. López-Urías, E. Cruz-Silva, B. G. Sumpter, V. Meunier, M. Terrones, and H. Terrones. 2009. The importance of defects for carbon nanoribbon based electronics. physica status solidi (RRL) - Rapid Research Letters 3, 181-183.

Botello-Méndez, A. R., F. López-Urías, M. Terrones, and H. Terrones. 2009.

Metallic and ferromagnetic edges in molybdenum disulfide nanoribbons. Nanotechnology 20, 325703.

Botello-Méndez, A. R., M. T. Martínez-Martínez, F. López-Urías, M. Terrones, and H. Terrones. 2007. Metallic edges in zinc oxide nanoribbons. Chemical Physics Letters. 448, 258-263.

Botello-Méndez, A. R., F. López-Urías, M. Terrones, and H. Terrones. 2008. Magnetic behavior in zinc oxide zigzag nanoribbons. Nano letters 8, 1562.

6.10. REFERENCES

[1]. Emerging Research Materials. International Technology Roadmap for semiconductors 2007. http://www.itrs.net/Links/2007ITRS/2007_Chapters/2007_ERM.pdf

[2]. Arnold, M.S., Green, A.A., Hulvat, J.F., Stupp, S.I. & Hersam, M.C. Sorting carbon nanotubes by electronic structure using density differentiation. *Nat. Nanotechnol.* **1**, 60-65 (2006).

[3]. Tapaszto, L., Dobrik, G., Lambin, P. & Biro, L.P. Tailoring the atomic structure of graphene nanoribbons by scanning tunnelling microscope lithography. *Nat. Nanotechnol.* **3**, 397-401 (2008).

[4]. Duan, H., Xie, E., Han, L. & Xu, Z. Turning PMMA Nanofibers into Graphene Nanoribbons by In Situ Electron Beam Irradiation. *Adv. Mater.* **20**, 3284-3288 (2008).

[5]. Ci, L. et al. Controlled nanocutting of graphene. Nano Res. **1**, 116-122 (2008).

[6]. Datta, S.S., Strachan, D.R., Khamis, S.M. & Johnson, A.T.C. Crystallographic Etching of Few-Layer Graphene. *Nano Lett.* **8**, 1912-1915 (2008).

[7]. Neto, A.H.C., Guinea, F., Peres, N.M.R., Novoselov, K.S. & Geim, A.K. The electronic properties of graphene. *Rev. Mod. Phys.* **81**, 109-54 (2009).

[8]. Ponomarenko, L.A. et al. Chaotic Dirac Billiard in Graphene Quantum Dots. *Science* **320**, 356-358 (2008).

[9]. Novoselov, K.S. et al. Two-dimensional atomic crystals. *Proc. Nat. Acad. Sci.* **102**, 10451-10453 (2005).

[10]. Novoselov, K. S., Geim, A. K., Morozov, S. V., Jiang, D., Zhang, Y., Dubonos, S. V., Grigorieva, I. V. & Firsov, A. A. Electric field effect in atomically thin carbon films. *Science* **306**, 666–669 (2004).

[11]. Jia, X. et al. Controlled Formation of Sharp Zigzag and Armchair Edges in Graphitic Nanoribbons. *Science* **323**, 1701-1705 (2009).

[12]. Koskinen, P., Malola, S. & Hakkinen, H. Evidence for graphene edges beyond zigzag and armchair. *Phys. Rev. B* **80**, 073401-3 (2009).

[13]. Girit, C.O. et al. Graphene at the Edge: Stability and Dynamics. *Science* **323**, 1705-1708 (2009).

[14]. Koskinen, P., Malola, S. & Hakkinen, H. Self-Passivating Edge Reconstructions of Graphene. *Phys. Rev. Lett.* **101**, 115502-4 (2008).

[15]. Wassmann, T., Seitsonen, A.P., Saitta, A.M., Lazzeri, M. & Mauri, F. Structure, Stability, Edge States, and Aromaticity of Graphene Ribbons. *Phys. Rev. Lett.* **101**, 096402-4 (2008).

[16]. Terrones, H. & Mackay, A. The geometry of hypothetical curved graphite structures. *Carbon* **30**, 1251-1260 (1992).

[17]. Thrower, P. A. The study of defects in graphite by transmission electron microscopy. *Chem. Phys. Carbon* **5***,* 217-319 (1969).

[18]. Simonis P. et al. STM study of a grain boundary in graphite. *Surf. Sci.* 511, 319-322 (2002).

[19]. Terrones, H. et al. New Metallic Allotropes of Planar and Tubular Carbon. *Phys. Rev. Lett.* **84**, 1716 (2000).

[20]. Barone, V., Hod, O. & Scuseria, G.E. Electronic Structure and Stability of Semiconducting Graphene Nanoribbons. *Nano Lett.* **6**, 2748-2754 (2006).

[21]. Yang, L., Park, C., Son, Y., Cohen, M.L. & Louie, S.G. Quasiparticle Energies and Band Gaps in Graphene Nanoribbons. *Phys. Rev. Lett.* **99**, 186801-4 (2007).

[22]. Lee, H., Son, Y-W., Park, N., Han, S. & Yu, J. Magnetic ordering at the edges of graphitic fragments: Magnetic tail interactions between the edge-localized states. *Phys. Rev. B* **72**, 174431 (2005)

[23]. Martins, T.B., Miwa, R.H., da Silva, A.J.R. & Fazzio, A. Electronic and Transport Properties of Boron-Doped Graphene Nanoribbons. *Phys. Rev. Lett.* **98**, 196803-4 (2007).

[24]. Peres, N.M.R. et al. Electron waves in chemically substituted graphene. *Europhys. Lett.* **80**, 67007 (2007).

[25]. Wang, Z.F. et al. Z-shaped graphene nanoribbon quantum dot device. *Appl. Phys. Lett.* **91**, 053109-3 (2007).

[26]. Ren, H., Li, Q., Shi, Q. & Yang, J. Quantum Dot Based on Z-shaped Graphene Nanoribbon: First-principles Study. *Chin. J. Chem. Phys.* **20**, 489-494 (2007).

[27]. Wang, Z.F. et al. Ballistic rectification in a Z-shaped graphene nanoribbon junction. *Appl. Phys. Lett.* **92**, 133119-3 (2008).

[28]. Chen, Y.P., Xie, Y.E. & Zhong, J. Resonant transport and quantum bound states in Z-shaped graphene nanoribbons. *Phys. Lett. A* **372**, 5928-5931 (2008).

[29]. Andriotis, A.N. & Menon, M. Transport properties of branched graphene nanoribbons. *Appl. Phys. Lett.* **92**, 042115-3 (2008).

[30]. Chen, Y.P., Xie, Y.E., Sun, L.Z. & Zhong, J. Asymmetric transport in asymmetric T-shaped graphene nanoribbons. *Appl. Phys. Lett.* **93**, 092104-3 (2008).

[31]. Xu, Z., Zheng, Q. & Chen, G. Elementary building blocks of graphene-nanoribbon-based electronic devices. *Appl. Phys. Lett.* **90**, 223115-3 (2007).

[32]. Chen, Y.P., Xie, Y.E. & Yan, X.H. Electron transport of L-shaped graphene nanoribbons. *J. Appl. Phys.* **103**, 063711-4 (2008).

[33]. Jayasekera, T. & Mintmire, J.W. Lattice vacancy effects on electron transport in multiterminal graphene nanodevices. *Int. J. Quant. Chem.* **107**, 3071-3076 (2007).

[34]. Jayasekera, T. & Mintmire, J.W. Transport in multiterminal graphene nanodevices. *Nanotechnol.* **18**, 424033 (2007).

[35]. Laakso, M.A. & Heikkila, T.T. Charge transport in ballistic multiprobe graphene structures. *Phys. Rev. B* **78**, 205420-5 (2008).

[36]. Wakabayashi, K. & Sigrist, M. Zero-Conductance Resonances due to Flux States in Nanographite Ribbon Junctions. *Phys. Rev. Lett.* **84**, 3390 (2000).

[37]. Wakabayashi, K. Electronic transport properties of nanographite ribbon junctions. *Phys. Rev. B* **64**, 125428 (2001).

[38]. Hong, S., Yoon, Y. & Guo, J. Metal-semiconductor junction of graphene nanoribbons. *Appl. Phys. Lett.* **92**, 083107-3 (2008).

[39]. Romo-Herrera, J.M., Terrones, M., Terrones, H., Dag, S. & Meunier, V. Covalent 2D and 3D Networks from 1D Nanostructures: Designing New Materials. *Nano Lett.* **7**, 570-576 (2007).

[40]. Terrones, M. et al. Pure and doped boron nitride nanotubes. *Mater. Today* **10**, 30-38 (2007).

[41]. Okada, S., Igami, M., Nakada, K. & Oshiyama, A. Border states in heterosheets with hexagonal symmetry. *Phys. Rev. B* **62**, 9896 (2000).

[42]. Nakamura, J., Nitta, T. & Natori, A. Electronic and magnetic properties of BNC ribbons. *Phys. Rev. B* **72**, 205429 (2005).

[43]. Park, C. & Louie, S.G. Energy Gaps and Stark Effect in Boron Nitride Nanoribbons. *Nano Lett.* **8**, 2200-2203 (2008).

[44]. Barone, V. & Peralta, J.E. Magnetic Boron Nitride Nanoribbons with Tunable Electronic Properties. *Nano Lett.* **8**, 2210-2214 (2008).

[45]. Okada, S. & Oshiyama, A. Magnetic Ordering in Hexagonally Bonded Sheets with First-Row Elements. *Phys. Rev. Lett.* **87**, 146803 (2001).

[46]. Zheng, F. et al. Half metallicity along the edge of zigzag boron nitride nanoribbons. *Phys. Rev. B* **78**, 205415-5 (2008).

[47]. Zheng, F., Liu, Z., Wu, J., Duan, W. & Gu, B. Scaling law of the giant Stark effect in boron nitride nanoribbons and nanotubes. *Phys. Rev. B* **78**, 085423-5 (2008).

[48]. Enyashin, A., Gemming, S., & Seifert, G. Nanosized allotropes of molybdenum disulfide. *Eur. Phys. J. Special Topics* **149**, 103–125 (2007).

[49]. Bollinger, M.V. et al. One-Dimensional Metallic Edge States in MoS2. *Phys. Rev. Lett.* **87**, 196803 (2001).

[50]. Zhang, J. et al. Magnetic Molybdenum Disulfide Nanosheet Films. *Nano Lett.* **7**, 2370-2376 (2007).

[51]. Li, Y., Zhou, Z., Zhang, S. & Chen, Z. MoS2 Nanoribbons: High Stability and Unusual Electronic and Magnetic Properties. *J. Am. Chem. Soc.* **130**, 16739-16744 (2008).

[52]. Ci, L. et al. Controlled nanocutting of graphene. Nano Res. **1**, 116-122 (2008).

[53]. Hou, P. et al. Hydrogen adsorption/desorption behavior of multi-walled carbon nanotubes with different diameters. *Carbon* **41**, 2471-2476 (2003).

[54]. Tusche, C., Meyerheim, H.L. & Kirschner, J. Observation of Depolarized ZnO(0001) Monolayers: Formation of Unreconstructed Planar Sheets. *Phys. Rev. Lett.* **99**, 026102-4 (2007).

[55]. Ceperley, D.M. & Alder, B.J. Ground State of the Electron Gas by a Stochastic Method. *Phys. Rev. Lett.* **45**, 566 (1980).

[56]. Soler, J.M. et al. The SIESTA method for ab initio order-N materials simulation. *J. Phys.: Condens. Matter* **14**, 2745-2779 (2002).

[57]. Troullier, N. & Martins, J.L. Efficient pseudopotentials for plane-wave calculations. *Phys. Rev. B* **43**, 1993 (1991).

[58]. Perdew, J. P.; Burke, K.; Ernzerhof, M. Generalized Gradient Approximation Made Simple. *Phys. Rev. Lett.* **77**, 3865 (1996).

[59]. Nose, S. A unified formulation of the constant temperature molecular dynamics methods. *J. Chem. Phys.* **81**, 511-519 (1984).

[60]. Landauer, R. Electrical resistance of disordered one-dimensional lattices. *Phil. Mag.* **21**, 863-867 (1970).

[61]. Datta, S., Electronic Transport in Mesoscopic Systems. Cambridge University Press: 1995

[62]. Nardelli, M. B. Electronic transport in extended systems: Application to carbon nanotubes. *Phys. Rev. B* **60**, 7828-7833 (1999).

[63]. Meunier, V.; Sumpter, B. G. Amphoteric doping of carbon nanotubes by encapsulation of organic molecules: Electronic properties and quantum conductance. *J. Chem. Phys.* **123**, 024705 (2005).

Conclusions

CONTENTS

CONTRIBUTIONS

The deepest objective of doing research, at least in academia, is to contribute to the development of humanity. Be it through the development of technologies that directly impact the life quality of individuals, or through the understanding of the laws behind all that surround us which we call Nature. To try to reach that objective in a doctoral thesis is at least pretentious. Instead, the objective is to contribute to a tiny area of research, which collectively might reach the ultimate goal.

In this thesis, we have contributed to the development of mainly two areas: 1) nanoscale zinc oxide science, and 2) nanoscale carbon science. Carbon is, without a doubt, the material which has the most intense research activity in nanoscience and nanotechnology. But also because Carbon chemistry is very flexible, and comes in many flavors (see chapter 4). The second most studied material in Nanoscience and Nanotechnology is probably zinc oxide (ZnO). This is due to the combination of mainly three facts: it is a wide band gap semiconductor with interesting optical properties; it has interesting mechanical; and it is, in principle, innocuous to human health and to the environment.

The contribution to ZnO science was in two different sub areas. The first was through the development of a composite of ZnO and cellulose (chapter 2). This composite can be used as an energy generator making exploiting the piezoelectric and pyroelectric properties of ZnO which are enhanced in the nanoscale. The low efficiency of the device limits its applications to those where it is difficult to power through the grid or through solar power. Due to the presumed bio-compatibility of ZnO and paper, an application for this device could be to power micro or nano sensors working inside the body through an external vibration source. Such devices have been proposed before. However our approach uses a low cost low temperature procedure and the final device involves mostly bio-friendly materials.

The other area in which we have contributed, was through the study of two nanostructured ZnO systems: nanoparticles and nanoribbons (chapter 3). The recent observation of ferromagnetic response in ZnO nanoparticles at room temperature was the main motivation. We have contributed to the understanding of this phenomenon through the calculations of various scenarios at the surface of ZnO nanoclusters of different size, which suggests that the observed properties are

very sensitive to the environment of the atoms at the surface.

Perhaps the most original contribution in this thesis is the introduction of ZnO nanoribbons. When we started the calculations on these systems, we had no idea that a group in Germany would synthesize the ZnO monolayer. Instead, we were motivated by results on the calculations of stability of ZnO polar surfaces carried out by ourselves and others. These results indicated that for a small number of layers the structure would become planar. While others started the calculation of single walled ZnO nanotubes, we focused on the properties of the edges that this new phase of ZnO would exhibit.

When the experimental observations by Tusche and coworkers were reported, the edge effects on ZnO we predicted were no longer purely hypothetical, but became a potentially useful material. This meant that now it would make sense to ask ourselves what could be the potential applications of the different properties of ZnO nanoribbons. These properties are: 1) Edge dependent (but not width dependent) electronic properties: zigzag ZnO nanoribbons are metallic, while armchair ZnO nanoribbons are semiconducting with a constant band gap regardless of the width (*c.a.* 3eV); 2) Edge dependent (only for zigzag) ferromagnetic properties; 3) Half metallicity after proper manipulation of the edges; 4) Gap modulation of armchair ZnO nanoribbons with an electric field. The last two properties were found out by other groups work which was at least partly motivated by our work.

In order to find applications, it was necessary to put these properties in context. We had to look for other materials that had similar edge effects. Nanoribbons made of graphene (a single layer of graphite) is by far the most studied of these systems. By that time, some of my co-workers were already trying to synthesize carbon nanoribbons in a controlled way. We had the opportunity to work with them, and contributed to the understanding of the properties of a CVD approach to carbon nanoribbons, and to the synthesis and characterization of graphene nanoribbons from carbon nanotubes (chapter 5).

While studying the structure and properties of the CVD produced carbon nanoribbons we realized the important role of structural defects. We studied some of these effects both at the edges, and inside the nanoribbon, and we were able to contribute to this fast moving research area (chapter 6).

184

However, graphene nanoribbons were not the only layered materials with interesting edge effects. It has been found that boron nitride (BN) nanoribbons also exhibit interesting edge effects, particularly the band gap (bulk energy gap *c.a.* 5eV) engineering with an external electric field. Furthermore, the sandwich-like layered molybdenum disulfide (MoS_2) nanoribbons and islands exhibit interesting magnetic properties (chapter 6).Although these (graphene, BN, MoS_2, ZnO) are probably not the only layered materials that could exhibit interesting edge effects, the properties of these four were enough to propose a new technology based on edge effects in layered materials. Many authors have proposed the use of graphene nanoribbons for the future of nanoelectronics, but to the best of our knowledge, the idea of nanoelectronics based on the edge effects of different materials is new. The advantage is in the diversity, and the idea would be to take the most robust properties of each.

Although graphene nanoribbons can exhibit interesting optical and magnetic behavior, these properties might be difficult to control. Graphene nanoribbons are more robust at conducting electrons. Boron Nitride nanoribbons are usually insulators, but when an electric field is applied a large band gap modulation is observed and the flow of electrons can be now possible. The on/off ratio of in a device like this is expected to be much larger than in graphene or other layered materials. ZnO nanoribbons have a smaller band gap that BN. The possibility to use light (blue to UV) to make ZnO nanoribbons conductive, put this material as the ideal candidate for, for example, optoelectronic switches. Finally, MoS_2 nanoribbons and islands exhibit spontaneous magnetization which might be more robust than the magnetism observed in graphene or ZnO.

CHALLENGES AND PERSPECTIVES

In science, we appreciate questions. They give us work and motivation for further research. Maybe the greatest contribution of a given work (thesis, article, etc) is the questions it rises. We are glad that the work presented here rises more questions than the ones it has answered (if any). Some of the most obvious challenges are outlined here. They can be divided in two groups depending if they can be addressed immediately or not.

First it would be interesting to understand the properties of the few layered

185

nanoribbons. Some work has already been done for the bilayer of graphene, but little has been done for more than two layers. In the case of ZnO, BN and MoS_2, there is very little known.

In §6.3, we briefly introduced the concept of graphene networks, which can also been seen as graphene with holes. It would be interesting to see what happens when this holes are made in few layer graphene. If two layers are "punched" they would probably form a carbon nanofoam like the one shown in figure 4.1. However it is not clear what would happen when holes are made in a graphene trilayer. It would be also interesting to study the properties of these networks but made of ZnO or BN or MoS_2.

Another important question is the effect of the substrate in the properties of nanoribbons. For the case of graphene, this has been widely studied both from the theoretical and the experimental point of view. However the effect of substrate is not clear in the other systems.

If new electronics based on layered materials are to be pursued, it would be imperative to study and understand the interaction between the different kind of nanoribbons. The easiest case is the BN – graphene nanoribbon interaction. Due to the lattice match one could think that a substitution of carbon atoms for boron or nitrogen would be possible. However, experimentally that could be very difficult to achieve. An easier technique (in principle) would be to transfer somehow the BN nanoribbons into a substrate containing a patterned array of graphene nanoribbons. In this case, the interactions are not covalent, but rather by van der Waals forces, which are very difficult to describe in theoretical calculations, but that should be aimed for. Similarly interactions between graphene nanoribbons and ZnO and MoS_2 systems would be interesting.

Finally, from an experimental point of view, the challenges are many and most of them might require years of work. The most obvious one is how to synthesize all these systems in an efficient, and economically and ecologically cost effective way. The option of unzipping nanotubes seems promising. In this respect, the use of similar technique for single or few layered walled (doped and undoped) nanotubes still needs to be proven.

Appendices

CONTENTS

A. Characterization

The study of nanoscale materials cannot be carried out without the aid of characterization tools. In fact, nanoscience and microscopy and spectroscopy techniques are closely related and often involved in a continuous loop of feedback for research and development. The characterization tools not only aid us for seeing beyond our natural naked eye capabilities, but give us information about the physical and chemical properties of materials. The objective of this section is to briefly describe the physics behind and the information given by the characterization tools used throughout this work.

A.1. Electron microscopy

The naked eye has a spatial resolution (i.e. how small it can still separately identify an object from an adjacent similar object) of around 5µm. This is determined by three factors: size of the reception cells (c.a.4 µm), aberrations, and diffraction of the light at the entrance of the pupil of the eye. When the object of observation has dimensions lower than this, a microscope must be used. Optical microscopes have a spatial resolution of c.a. 0.3µm. In this case, the spatial resolution is limited by diffraction, and in the ideal case of nearly perfect optics, the best resolution is given by just over half the wavelength of light.

The particle-wave duality of quantum mechanics states that a particle can behave like a wave with a wavelength called the *de Broglie wavelength* which is inversely proportional to its momentum. Hence, an electron accelerated at 50keV would have a wavelength of $\lambda=0.005$nm. In the case of electron microscopes, the spatial resolution is limited by the aberration of the electromagnetic lenses.

In a **transmission electron microscope (TEM)**, electrons pass through a rather thin sample and are then imaged by appropriate electromagnetic lenses into a fluorescent screen or a CCD, in analogy to a regular optical microscope. The electrons are accelerated to voltages between 50kV and 300kV. The spatial resolution is around 0.2nm, although recent spherical aberration-corrected TEMs have achieved better resolution at even lower acceleration voltages [1].

Unless the sample is very thin, the electrons of a TEM are strongly scattered within the specimen, or absorbed rather than transmitted. Therefore, for examining

bulk samples it is desirable to use reflected, or secondary electrons (absorbed and then emitted). However, when the electrons are emitted, they do so with a variety of energies and directions, making them difficult to focus and project into a screen. Instead, a scanning approach is used: First, the source electrons are focused into a small-diameter electron probe that is scanned throughout the sample, and then, the secondary electrons of each of the scanning steps or pixels are collected and amplified. The intensity or number of electrons reaching the collector specifies the brightness of a given pixel of an image. This is the principle of a **scanning electron microscope (SEM)**. The acceleration voltage of a SEM is usually between 5 to 30 kV, and the spatial resolution is of c.a. 1nm. In moderate acceleration voltages, the information observed in the SEM image is mostly of the surface of the sample. As the acceleration voltage increases, information of deeper in the sample is obtained. Recently, single atom resolution (c.a. 0.1nm) has been achieved with an aberration corrected SEM [2].

Electron microscopy was used in this work to examine the morphology and crystal structures of the produced nanomaterials presented in Chapter 1 and Chapter 3. In particular, the morphology of the ZnO nanorods synthesized by the solvothermal method was observed with a XL-30 FEI field emission gun SEM. Their crystal structure was observed with a HRTEM 300KV FEI TECNAI F30 STWIN G2. The same equipment was used to characterize the carbon nanoribbons and the catalytic cut carbon nanotubes, along with the DUAL BEAM FEI HELIOS 600 NANOLAB. The morphology of the ZnO-paper composite presented in Chapter 1 was observed with a ESEM FEI QUANTA 400 at Rice University.

A.2. SCANNING PROBE MICROSCOPY

While electron microscopes are an extension of our eyes, scanning-probe microscopes are an extension of our fingertips. In these systems an image is formed using a sharply pointed tip, which mechanically scans in proximity to the surface of the sample in order to sense the local properties. Therefore, the image obtained from scanning probe microscopes represents only the surface properties of the sample.

The **scanning tunneling microscope (STM)** was the first device to achieve atomic spatial resolution. In such system, a conducting tip is brought to about 1nm from a conducting sample, and potential difference is applied. Electrons then move

between the tip and the sample by quantum mechanical tunneling.

When neither the sample or the tip are conducting, if the tip is brought very close to the surface of the sample and the tip essentially *touches* the sample and senses the electrostatic force which can be repulsive or attractive. This is the principle of the **atomic force microscope (AFM)**. In practice, the tip is positioned at the end of a cantilever which deflects as the tip feels the attraction or repulsion from the sample. This deflection is measured by shinning a laser beam to the edge of the cantilever and observing the angular deflection of the reflected beam in a photodetector. Also, with a modified tip the magnetic field of a sample can be monitored. The spatial resolution of an AFM is limited by mechanical control and stability, although, in principle atomic resolution should be accessible.

In Chapter 3 the surface morphology of a multiwalled carbon nanotube cut longitudinally by a cobalt particle through a hydrogenation process was investigated with a JEOL JSPM 5200.

A.3. X-ray diffraction

While electron and probe microscopies give information on the local morphology of the sample, it is usually helpful to have information of the general structure. The structure of a crystal can be studied by the diffraction of a wave as given by Bragg's Law: $2d \sin(\theta)=n\lambda$. An incident wave of wavelength λ is supposed to be reflected elastically at an angle θ by the planes of atoms in a crystal separated by a distance d. In particular, diffraction can only occur for wavelengths $\lambda \leq 2d$, therefore X-Rays are used instead of for instance, visible light. The Bragg Law is a consequence of the periodicity of the lattice, and does not give any information of the composition of the sample. In particular, powder X-Ray diffraction gives averaged information of the different oriented crystals in a sample. The patterns shown in Chapter 1 were acquired with a XRD BRUKER D8 ADVANCE.

A.4. X-ray absorption spectroscopy

In a micrography, it is almost impossible to know what is the composition of the material we are looking at. In particular, in nanotechnology, where the synthesis methods yield to various interesting structures, it is always important not only to know what the structure of this new material is, but what are their physical and

chemical properties.

In particular, in X-ray absorption spectroscopy the transmission of the light source through the sample is studied, similar to optical absorption. However, depending on the energy range of the light source, electrons can be excited into unoccupied energy levels from different shells of the atoms. This means that the absorption of light is a function of the core electron binding energies. The position of these energy levels are element specific, and depend also of the environment of the atoms. Therefore, this method can be used for elemental and chemical analysis.

When light with proper energy hits the sample, an electron absorbs such energy and makes a transition into unoccupied states. The recombination options and the energy absorbed determine the *edge* measured. For instance, in graphite, the energy required for the absorption of a photon by a core C1s electron to reach the Fermi energy is called the absorption K-edge. X-ray absorption spectroscopies are classified according to the range of energy or energy-distance from the edge. Extended X-ray absorption fine structure (EXAFS) covers an energy range of c.a. 500 eV from the edge, and gives information on the interaction between next neighbors and short range order in the lattice. Near edge X-ray absorption fine structure (NEXAFS) covers a smaller range of 30 to 50 eV, and X-ray absorption near edge structure (XANES) covers an even smaller range. Both XANES and NEXAFS give information of the unoccupied levels in the band structure before the electron is ionized out of the crystal [3].

The scanning transmission X-ray micro-spectroscopy (STXM) is a powerful technique that allows the simultaneous (i.e. without unmounting the sample), imaging of a sample through the transmitted X-rays, and the spectral analysis of each of the scanning points through an energy scan or stack. In particular, when using a synchrotron light source, the spectral analysis can be achieve from near the edge (XANES) to the extended X-ray absorption (EXAFS). The measurements presented in Chapter 3 were carried out at the beam 5.3.2 of the Advanced Light Source synchrotron at Lawrence Berkeley National Laboratory.

A.5. Electron energy loss spectroscopy

In the TEM, when the electrons pass through the sample, some may lose energy through inelastic electron-electron collisions. The measurement and analysis of the

energy of electrons as they pass through the sample is called Electron Energy Loss Spectroscopy (EELS). As in the case of the X-Ray spectroscopies, the energy-loss events give information about the chemistry and the electronic structure of the sample's atoms, which in turn reveals details of their bonding, and nearest neighbor atomic structure. The value of energy loss in the incident electrons corresponds to the transferred excitation energy for the inner-shell electrons in a sample.

B. ELECTRONIC STRUCTURE CALCULATIONS

The role of computational calculations in materials science and in nanoscience in particular, has proved to be very important. Computational calculations provide us with tools for a deeper understanding and prediction of the behavior of materials. It is, in principle, a framework for carrying out truly controlled experiments. However, the experiments that are accessible depend mostly on the scales that a given calculation method or approximation is able to achieve. Also, in order to gain knowledge on a specific observed phenomena, there is often need for different degrees of accuracy or different approximations. In this section, a brief description of the different approximations and methods for electronic structure calculations is presented.

All the information of the physical and chemical properties of a material is contained in the way the electrons are arranged and interact, namely in the electronic structure. The Hamiltonian that governs the motion of the electrons and nuclei in a given material is composed by: 1) the sum of the non interacting kinetic energy of electrons and nuclei; 2) the Coulomb interaction between nuclei and electrons; 3) and the Coulomb interaction among electrons, and among nuclei. However, a clever observation that the electrons move much faster than the nuclei, allow us to separate the problem into an electronic Hamiltonian neglecting the kinetic energy of nuclei in what is known as the Born-Oppenheimer approximation. The total energy could then be computed as the sum of the electronic energy and the nuclear energy.

The electronic Hamiltonian then, is composed by 1) the kinetic energy of the electrons; 2) the Coulomb interaction between electrons and nuclei; 3) the Coulomb interaction between electrons; and 4) the Coulomb interaction between
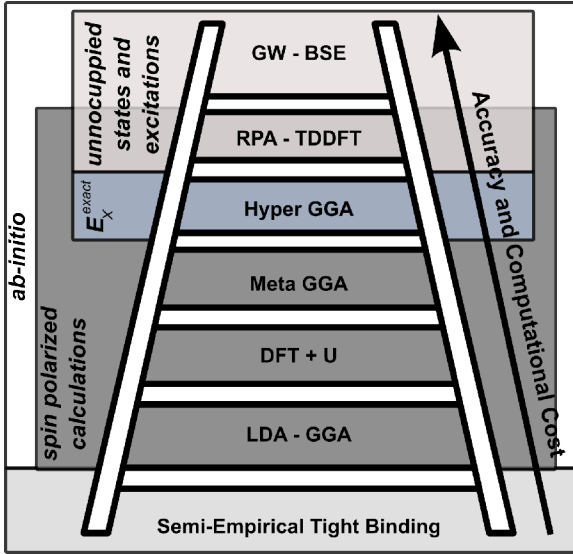
nuclei (in atomic units):

$$H_{elec} = -\sum_i^n \frac{1}{2}\nabla^2 - \sum_A^N \sum_i^n \frac{Z_A}{r_{iA}} + \sum_{i<j}^n \sum_j^n \frac{1}{r_{ij}} + \sum_{B<A}^N \sum_A^N \frac{Z_A Z_B}{R_{AB}}$$

It is important to note that the Coulomb terms are many body interactions; hence, can only be determined exactly for very small systems.

Figure 1: An schematic ladder of electronic calculations

In this Section we will present different approximations to solve this problem, along with their advantages and limitations in terms of computational time and accuracy. In that respect, figure 1 presents an schematic ladder for electronic structure calculations used in this work, and their relative accuracy and computational cost, as well as the properties that are accessible under such approximations.

B.1. SEMI-EMPIRICAL TIGHT BINDING METHOD

In the bottom of the ladder of electronic structure calculations lie the semi-empirical approximations. Although there are other approximations of this kind, the tight binding approximation (TB) is the most relevant for the work presented here.

In the semi-empirical TB approximation, the Schrödinger equation

$$H_{elec}|\psi\rangle = E|\psi\rangle$$

is expressed in its secular form:

$$\left\| \langle\psi|H_{elec}|\psi\rangle - E\langle\psi|\psi\rangle \right\| = 0 \quad,$$

In the case of solids, the wavefunction ψ is expressed as a linear combination of atomic orbitals which are expressed as Bloch sums of the wavevector k:

$$\psi = \sum_i c_i(\vec{k})\Phi_i(\vec{k},\vec{r}) \quad, \text{ where } \quad \Phi_i = \frac{1}{\sqrt{N}}\sum_{t_m} e^{i\vec{k}\cdot\vec{t}_m}\varphi_i(\vec{r}-\vec{t}_m) \quad,$$

and the matrix elements:

$$H_{ij} \equiv \langle \psi | H_{elec} | \psi \rangle \quad , \quad S_{ij} \equiv \langle \psi | \psi \rangle$$

are determined semi-empirically, typically by fitting to experiments or *ab-initio* calculations.

The TB approach makes the following approximations: 1) assumes a local character of atomic orbitals; 2) disregards the crystal field terms, since they represent a rigid shift of the whole band structure; 3) considers the interaction of a small number of neighbors adopting the two-center approximation. The two center interaction integrals can be expressed in terms of a small number of independent parameters. The expressions of the two center integrals for the interaction of different atomic orbitals with different angular momentum were given by Slater and Koster.

In graphene, for instance, a one orbital model is sufficient to describe the band structure close to the Fermi level. This approximation can be done because the π orbitals in graphene are effectively decoupled from the σ orbitals. This simple model, that usually includes only nearest-neighbor interactions, is very successful in describing the properties of single-walled nanotubes despite that it neglects the effects of curvature and assumes all C-C bond lengths to be the same. However, Mintmire et al. showed that for an accurate description of the properties of graphene nanoribbons, particularly the ones with armchair edges, third nearest neighbor interactions must be included [4]. They showed that the two center integral parameter of the nearest neighbor (c.a. 2.6eV) model that works for nanotubes is in fact an effective value of the combination of nearest neighbor (c.a. 3.3eV) and third nearest neighbor interactions (c.a. 0.3eV) [4].

Recently, a more accurate description of the quasiparticle band structure of graphene and graphite has been achieved with a third nearest neighbor tight binding method with overlap fitted to GW calculations [5,6]. However, the introduction of overlap and the extensive fitting procedure shadows the physical interpretations of the different parameters.

In our calculations presented in Chapter 4, the nearest neighbor parameters used were -2.7eV with a zero on site energy. Third nearest neighbor parameters considering overlap and fitted to LDA are listed in table 1.

ε_{2p}	$\gamma 0$	s0	$\gamma 1$	s1	$\gamma 2$	s2
-1.904	-3.012	0.250	-0.633	0.053	0.358	0.030

Table 1: Third nearest neighbors tight binding parameters for carbon fitted to LDA [5].

B.2. DENSITY FUNCTIONAL THEORY

The Density Functional Theory is based on the Hohenberg-Kohn theorems [7-9]. The first theorem states that the electron density $\rho(r)$ corresponds to a unique number of electrons *N* and a unique arrangement of nuclei (number, charge, position), or in other words, external potential $V(r)$. The second theorem introduces a variational approach for determining ρ by minimizing the total Energy of the system. Such ρ is the ground state electron density. Therefore, the total energy is a functional of the electron density and hence, the Hamiltonian.

$$E[\rho]=\int \rho(\vec{r})V(\vec{r})d\vec{r}+T[\rho]+V_{ee}[\rho]$$

Kohn and Sham introduced orbitals into the picture in such a way that the kinetic energy could be computed [10]. The electron density was written as the sum of the squares of an arbitrary number of orhtonormal orbitals. In simple words, the Kohn Sham DFT consists in writing the energy functional in terms of non interacting orbitals, and calculate whatever possible, and leave the rest in a functional called the exchange correlation functional:

$\rho=\sum_{i}^{N}|\Psi_{i}|^{2}$, then the kinetic energy is given by $T[\rho]=\sum_{i}^{N}\langle\Psi_{i}|-\frac{1}{2}\nabla^{2}|\Psi_{i}\rangle$ and

$V_{ee}[\rho]=J[\rho]+E_{XC}[\rho]$, where $J[\rho]=\frac{1}{2}\int\int\frac{\rho(\vec{r})\rho(\vec{r}')}{|\vec{r}-\vec{r}'|}d\vec{r}d\vec{r}'$ is the classical Coulomb interaction energy.

The exchange correlation functional contains the difference between the exact kinetic energy and the kinetic energy of the non interacting orbitals, the non classical part of V_{ee} , and the self interaction correction to the Coulomb term. However, the shape of this exchange correlation functional is unknown and approximations must be made. The approximations are semi-local if the exchange correlation energy depends only on the electron density and orbitals in an infinitesimal neighborhood of the given position, and otherwise they are nonlocal. The local (spin) density approximation employs only the local densities. The

generalized gradient approximation adds the gradients of the local spin densities. The meta-GGA adds the positive kinetic energy density or the Laplacians of the densities. These are all semilocal functionals, and work when the density varies slowly in space. There are also hyper GGAs that add exact exchange energy density [11].

The common semi-local approximations (LDA and GGA) are not successful for describing the properties of all systems, although the exact DFT (meaning knowing the exact E_{XC}) should be capable of obtaining the exact groundstate properties. One example of the failure of the semi-local exchange correlation functionals is the description of the electronic band gaps for semiconductors. In general, LDA or GGA lead underestimated values, and sometimes even erroneous metallic behavior.

As mentioned above, the Kohn-Sham DFT introduces a set of orthonormal basis sets. This basis set can be localized, or extended. An example of the first approach is the linear combination of atomic orbitals (LCAO) approach. This approach has the advantage that fast calculations can be done with minimal basis sets (small number of functions), and very accurate calculations can be achieved with increasing the size of the basis (large number of functions). However, in this method it is often difficult to have a proper description of metals. In contrast, an extended basis, such as a plane wave basis describes very well the delocalized electrons in metals. The cost is that the plane waves are extended all over the simulation space, which in the case of the simulation of nanostructured materials which have at leas one finite direction, translates into a lot of planewaves to fill that space and will give no data.

Since in this work we are interested in nanostructured materials, it was natural to choose an implementation where a LCAO is used as the basis set. We carried out the calculations using the SIESTA code which uses numerical orbitals [12]. The code reads norm conserving pseudopotentials to treat the core electrons. We have used the Troullier-Martins parametrization [13]. Table 2 shows the electronic configurations used for different atoms. In addition to convergence parameters that are common to similar methods (i.e. plane wave codes), the SIESTA method requires that the basis size (number of atomic orbitals), the basis range (radius of the basis orbitals), and the fineness of the real-space integration grid are well converged [12]. We found that a double-ζ with polarization orbitals showed a good

197

compromise between accuracy and speed.

H	1s
C	$2s^2 2p^2$
N	$2s^2 2p^3$
O	$2s^2 2p^4$
S	$3s^2 3p^4$
Zn	$4s^2 3d^{10}$
Mo	$5s^2 4d^4$

Table 2: Valence electrons used for the different elements studied in this work.

For the case of zinc oxide systems, we used the LDA for the exchange correlation functional with the Ceperley Alder approach [14], since the GGA calculations showed a underestimation of the cell parameters and the same underestimation of the energy band gap. For carbon, we used both the CA-LDA and often verified our results under the GGA with the Perdew-Burke-Ernzerhof functional [15].

While the LCAO approach requires the convergence of different parameters described above, the plane-wave basis set monotonically converges as the energy cut off (the number of plane waves) is increased. We often checked that qualitatively our LCAO results were consistent with plane-wave results, unless the calculations became prohibitive, as in the case of the calculation of ZnO clusters. For this, we have used the Quantum-Espresso package [16]. Typically, the cutoff for Zn was 65Ry and for Carbon, Oxygen and Sulfur, c.a. 30Ry.

B.3. DFT+U

In the DFT (LDA or GGA) + U approach, the energy of the strongly correlated orbitals (usually d or f orbitals) is corrected by an orbital dependent Hubbard term such that:

$$E^{DFT+U}[\rho] = E^{DFT}[\rho] + E^{U}[n_i] - E^{dc}[n_i] ,$$

where E^{dc} is a double counting term removed in order to not count twice the contribution from the DFT (LDA or GGA) functional and the Hubbard term, and n_i are elements of the occupation matrix. Then, the energy functional takes the form:

198

$$E^{DFT+U}[\rho] = E^{DFT} + \frac{U}{2}\sum_{i \neq j} n_i n_j - UN(N-1)/2 \quad \text{, where} \quad N = \sum_i n_i \text{.}$$

The determination of U through first principles is rather complicated. Van de Walle and co-workers have proposed the following approach: Since U is defined as the Coulomb energy interaction between the d electrons on the same atoms, an atomic U can be obtained as the energy difference between the addition and removal of an electron from the atomic d subshell [17]. However, when the atoms are assembled in a soli, the atomic Coulomb interaction is screened by the optical dielectric constant, leading to an effective Coulomb correlation interaction [17]:

$$U = \frac{U^{at}}{\epsilon_\infty} \text{.}$$

We carried out LDA+U calculations to correct the overestimated p-d interaction in ZnO, and to verify that our calculations on ZnO nanoribbons were qualitatively correct. We determined the values of U to be 11 and 7 eV for the bulk Wurtzite ZnO and the hexagonal honeycomb monolayer, respectively. The difference is due to the difference in screening (the dielectric constant) of the two systems.

B.4. GW QUASIPARTICLE APPROXIMATION

The third term in the electronic Hamiltonian is the Coulomb interaction between electrons which correlates the motion of the electrons. An exact determination of this problem is not practical since it requires the solution of an equation with 3N coupled spatial degrees of freedom. The common approach as we have seen above is to approximate to two body interactions interacting under an effective potential in which the exchange and correlation of electrons is contained.

Another approach to solve this problem is based on the quasiparticle concept and the Green function method. This concept of quasiparticle is formed by the depletion of negative charge due to Coulomb repulsion between electrons and its surrounding positive screening charge. The mathematical description of the quasiparticles is based on the single-particle Green's function, and its exact determination requires the knowledge of the quasiparticle self energy. The self energy is a non Hermitian, energy-dependent and non local operator that describes the exchange and correlation effects beyond the mean field theory. However, the determination of the self-energy can only be approximate, and is usually carried out

by the dynamically screened interaction or the GW approximation.

The GW approximation gives very good results in agreement with experiments for the calculation of band structures and photo-emission spectra of many semiconductors and insulators. The quasiparticle energies in first order perturbation theory are

$$E_i^{QP} = \epsilon_i^{KS} + \frac{\langle \Sigma(\epsilon_i^{KS}) \rangle - \langle V_{XC}^{LDA} \rangle}{1 - \left\langle \dfrac{\partial \Sigma(\omega)}{\partial \omega} \right\rangle_{\omega = \epsilon_i^{KS}}}$$

In Chapter 2, we have used the GW approximation to verify that our results on the properties of ZnO nanoribbons with zigzag edges were qualitatively correct. The calculations were made with the YAMBO code [18] on top of DFT carried out with the Quantum Espresso package [16] under the LDA (see Appendix 2.2).

C. TRANSPORT CALCULATIONS

The flow of electrons through a device happens because of a difference in the local equilibrium distribution of electrons (Fermi functions) in the source and drain leads. The conductor, which is in the middle of the two leads, seems forced to match two different Fermi functions at its ends, and therefore, its actual steady-state lies in between the two. While the source keeps pumping electrons, the drain keeps pulling them out, each trying to keep equilibrium. However, the conductor does not have an unlimited number of channels through which electrons can travel in and out of the device. Also, the coupling of the conductor with the leads could hamper the flow of electrons.

The rate at which an electron with energy E travels from the source to the drain is given by the transmission function $\bar{T}(E)$. Under the assumption that the electrons travel through the device without changing the state of the conductor (coherent transport), e.g. by causing vibrations in the atomic lattice, the transmission function can be calculated as [19]:

$$\bar{T}(E) = \text{Tr}\left[\Gamma_1 G \Gamma_2 G^+ \right].$$

Where $G = [(E + i0^+)S - H - \Sigma]^{-1}$ is the overall Green's function which includes the interaction with the different leads by the self energy $\Sigma = \sum_j^n \Sigma_j$, where n is the

number of probes or contacts. The coupling functions are expressed by $\Gamma_j = i\left(\Sigma_j - \Sigma_j^+\right)$, where $\Sigma_j = \tau G_C \tau^+$ is the self energy of each contact and includes the interaction of the contacts through the coupling Hamiltonian τ and the conductor's Green's function:

$G_C = [ES_C - H_C + i\eta]^{-1}$, where S_C and H_C are the overlap and Hamiltonian matrices of the isolated conductor.

Then, the current is finally given by

$$I = (q/h) \int_{-\infty}^{+\infty} dE\, \bar{T}(E)(f_1(E) - f_2(E))$$

It can be noted that the calculation of the transmission function and hence the current, can be computed once the Hamiltonian of the system and the coupling Hamiltonians are known. Also, the Green's function approach extension to multiterminal devices is straight forward.

In this work, we have computed the Hamiltonian and overlap matrices within a simple tight binding approach (see Appendix 2.1), or through a first principles approach DFT (see Appendix 2.2). The use of a LCAO basis set is suitable for obtaining these matrices, as opposed to a non localized basis set in which a change of basis set (for instance, into Wannier orbitals) should be done. Therefore, the calculations presented in Chapter 4 were carried out with Hamiltonians obtained with the SIESTA [12] package and the TRANSPLAYER code developed by Meunier [20,21].

D. EELS CALCULATIONS

As stated in Appendix 1.5, in the electron energy loss spectroscopy (EELS), indirect information about excitations form occupied to unoccupied states is gained. The accelerated electrons in a TEM loose energy as they cross the sample. The loss of energy comes from the Coulomb force *eE* of the electron interacting with the medium, and causes the particle to slow down. Therefore, the energy loss gives information on the dielectric function of the sample through the loss function [22,23]:

$$\Im\left[\frac{-1}{\varepsilon(\omega,\vec{q})}\right] = \frac{\varepsilon_2}{\varepsilon_1^2 + \varepsilon_2^2}$$, where $\varepsilon_1 \equiv \Re[\varepsilon]$, and $\varepsilon_2 \equiv \Im[\varepsilon]$ are the real and imaginary

part of the dielectric function, respectively.

Therefore, the energy loss can be computed once the dielectric function is obtained. The calculation of the dielectric function follows that of the response function. Under the Random Phase Approximation (RPA), the response function, which measures the change in the electronic density induced by an external potential, is approximated by a noninteracting system. However, in a real system, the self-energy modifies the electronic density and therefore the RPA is not valid anymore [18]. A more accurate solution is made by the Bethe-Salpeter equation, in which electron-hole interactions are taken into account. However, the calculation is computationally more intense.

The loss functions presented in Chapter 4 were calculated under the RPA within the adiabatic local density approximation as implemented in the YAMBO code [18] on top of DFT eigenvalues and eigenfunctions calculated with the Quantum Espresso package [16].

REFERENCES

[1]. Tanaka, N. Present status and future prospects of spherical aberration corrected TEM/STEM for study of nanomaterials. Sci. Technol. *Adv. Mater.* **9**, 014111 (2008).

[2]. Zhu, Y., Inada, H., Nakamura, K. & Wall, J. Imaging single atoms using secondary electrons with an aberration-corrected electron microscope. *Nat. Mater.* **8**, 808-812 (2009).

[3]. Kuzmany, H. *Ultraviolet and X-Ray Spectroscopy.* Solid-State Spectroscopy 297-332 Springer (2009). http://dx.doi.org/10.1007/978-3-642-01479-6_12

[4]. White, C.T., Li, J., Gunlycke, D. & Mintmire, J.W. Hidden One-Electron Interactions in Carbon Nanotubes Revealed in Graphene Nanostrips. *Nano Lett.* **7**, 825-830 (2007).

[5]. Gruneis, A. et al. Tight-binding description of the quasiparticle dispersion of graphite and few-layer graphene. *Phys. Rev. B* **78**, 205425-16 (2008).

[6]. Reich, S., Maultzsch, J., Thomsen, C. & Ordejón, P. Tight-binding description of graphene. *Phys. Rev. B* **66**, 035412 (2002).

[7]. Hohenberg, P. & Kohn, W. Inhomogeneous Electron Gas. *Phys. Rev.* **136**, B864 (1964).

[8]. Geerlings, P., De Proft, F. & Langenaeker, W. Conceptual density functional theory. *Chem. Rev.* **103**, 1793-1873 (2003).

[9]. Fiolhais, C., Nogueira, F. & Marques, M. *A. primer in density functional theory.* (Springer: 2003).

[10]. Kohn, W. & Sham, L.J. Self-Consistent Equations Including Exchange and Correlation Effects. *Phys. Rev.* **140**, A1133 (1965).

[11]. Perdew, J.P., Ruzsinszky, A., Constantin, L.A., Sun, J. & Csonka, G.I. Some Fundamental

Issues in Ground-State Density Functional Theory: A Guide for the Perplexed. *J. Chem. Theory Comp.* **5**, 902-908 (2009).

[12]. Soler, J.M. et al. The SIESTA method for ab initio order-N materials simulation. *J. Phys.: Condens. Matter* **14**, 2745-2779 (2002).

[13]. Troullier, N. & Martins, J.L. Efficient pseudopotentials for plane-wave calculations. *Phys. Rev. B* **43**, 1993 (1991).

[14]. Ceperley, D.M. & Alder, B.J. Ground State of the Electron Gas by a Stochastic Method. *Phys. Rev. Lett.* **45**, 566 (1980).

[15]. Perdew, J.P., Burke, K. & Ernzerhof, M. Generalized Gradient Approximation Made Simple. *Phys. Rev. Lett.* **77**, 3865 (1996).

[16]. Giannozzi, P. et al. QUANTUM ESPRESSO: a modular and open-source software project for quantum simulations of materials. *J. Phys.: Condens. Matter* **21**, 395502 (2009).

[17]. Janotti, A., Segev, D. & Van de Walle, C.G. Effects of cation d states on the structural and electronic properties of III-nitride and II-oxide wide-band-gap semiconductors. *Phys. Rev. B* **74**, 045202-9 (2006).

[18]. Marini, A., Hogan, C., Grüning, M. & Varsano, D. yambo: An ab initio tool for excited state calculations. *Comp. Phys. Commun.* **180**, 1392-1403 (2009).

[19]. Datta, S. *Quantum Transport: Atom to Transistor.* (Cambridge University Press: 2005).

[20]. Meunier, V. & Sumpter, B.G. Amphoteric doping of carbon nanotubes by encapsulation of organic molecules: Electronic properties and quantum conductance. *J. Chem. Phys.* **123**, 024705-8 (2005).

[21]. Nardelli, M.B. Electronic transport in extended systems: Application to carbon nanotubes. *Phys. Rev. B* **60**, 7828 (1999).

[22]. Smalley , R. E, et al. *Carbon Nanotubes: Synthesis, Structure, Properties and Applications.* (Springer: 2001).

[23]. Kittel, C. *Introduction to Solid State Physics.* (Wiley: 1995).

Contributed Articles